Rock-shape and its role in rockfall dynamics

GLOVER, JAMES,MICHAEL,HARVEY

GLOVER, JAMES,MICHAEL,HARVEY (2015) *Rock-shape and its role in rockfall dynamics*, Durham theses, Durham University. Available at Durham E-Theses Online: http://etheses.dur.ac.uk/10968/

Rock-shape and its role in rockfall dynamics

James GLOVER

A thesis presented for the degree of
Doctor of Philosophy

Durham University

Department of Geography

January 2015

Declaration

The research presented in this thesis was enabled by collaboration between the WSL Institute for Snow and Avalanche Research SLF (Davos Switzerland) and the Department of Geography, Durham University. The thesis presents the original research of the author, and no part of this thesis has been submitted elsewhere for any other degree or qualification.

Abstract

Rockfall threaten infrastructure and people throughout the world. Estimating the runout dynamics of rockfall is commonly performed using models, providing fundamental data for hazard management and mitigation design. Modelling rockfall is made challenging by the complexity of rock-ground impacts. Much research has focused on empirical impact laws that bundle the rock-ground impact into a single parameter, but this approach fails to capture characteristics associated with the impact configuration and, in particular, the effects of rock-shape. While it is apparent that particular geological settings produce characteristic rock-shapes, and that different rock-shapes may produce characteristic runout dynamics, these aspects of rockfall are poorly understood.

This study has focused on investigating the mechanics behind the notion that different rock-shapes produce characteristic runout dynamics and trajectories. The study combines field data on rockfall runout, trajectory and dynamics, laboratory analogue testing in controlled conditions, and numerical modelling of the influence of rock-shape. Initially rock-shape, deposition patterns and rockfall dynamics were documented at rockfall sites in Switzerland and New Zealand. This informed a detailed study of individual rock-ground impacts on planar slopes in which laboratory-scale and numerical rockfall experiments were combined to isolate the role of rock-shape on runout. Innovatively, the physical experiments captured the dynamics of impacts and runout paths using high speed video tracking and a sensor bundle with accelerometers and gyroscopes. Numerical experiments were performed using a 3-D rigid-body rockfall model that considers rock-shape, and has allowed the variability of rockfall behaviour to be explored beyond the limitations of physical experimentation.

The main findings of the study were on understanding rockfall-ground impacts, the influence of rock-shape on rockfall dynamics, and influence of rock sphericity. By measuring velocity, rotational speed, impact and runout character, it has been possible to quantify the variability of individual rock-ground impacts as a function of rock-shape. Investigation of single rebounds reveals that if classical restitution coefficients are applied, R_n values greater than unity are common and rebounds are highly variable regardless of constant contact parameters. It is shown that this variability is rooted in the inherent differences in the magnitudes of the principal moment of inertia of a rock body brought about by rock-shape. Any departure from a perfect sphere induces increased range and variability in rock-ground rebound characteristics. In addition to the popular description of a rock bouncing down slope, rebounds involve the pinning of an exterior edge point on the rock, creating a moment arm which effectively levers the rock into ballistic trajectory as it rotates. Observations reveal that the angle of the impact configuration plays a key role in the resulting rebound, whereby low angles produce highly arched rebounds, while large impact angles produce low flat rebounds. The type of rebound produced has a strong bearing on the mobility of the rocks and their ability to maintain motion over a long runout. The mobility of rocks is also shown to be related to rotation, which is governed by the differences in the principal inertial axes as a function of rock-shape. Angular velocity measurements about each principal inertial axis indicate that rocks have a tendency to seek rotation about the axis of largest inertia, as the most stable state. Rotations about intermediate and small axes of inertia and transitions between rotational axes are shown to be unstable and responsible for the dispersive nature of runout trajectories, which are inherent characteristics of different rock-shapes.

The findings of this research demonstrate the importance of rock-shape in rockfall runout dynamics and illustrate how it is essential that the rock-shape is included in rockfall modelling approaches if the variability of rockfall behaviour is to be simulated.

Acknowledgements

There is something quite capturing about releasing a rocks potential energy to watch it bound down a slope crashing to a halt at the bottom. Growing up on the Somerset levels the closest we got to rockfall was dropping a scrap bike from the Chilthorne Domer Old Rectory roof watching it free-fall to a shattering impact with the pavement. Thanks to my brothers Chris, Rich and Will and best friends Ali, Mads and Claire for these formative 'rockfall' years. Little did I know that I would later engage in similar experiments dropping large 20 tonne rocks into rockfall barriers in Switzerland as I started my internship with Geobrugg AG. Thanks to Nick Rosser for suggesting that I apply for an internship with whom are arguably "the Rolls Royce of rockfall protection". Hiermit möchte ich Andrea Roth, Corinna Wendeler und dem ganzen Geobrugg Team herzlich danken für das tolle Praktikum am Anfang meiner Zeit in der Schweiz, insbesondere die vielen genialen Erlebnisse bei der Zusammenarbeit in den verschiedenen Versuchsanlagen weltweit. Further to this, thanks to Kazuhito Shimojo, Tatsuo Watanabe and Nobuhito Nishimura for the Japanese rockfall experience and demonstrating the multi-functionality of Japanese hire cars.

It was during my time with Geobrugg that my research into rockfalls began as we embarked upon a joint project investigating rockfall attenuator systems with the WSL institute for avalanche and snow research SLF. Many thanks to the Swiss Commission for Technology and Innovation CTI for providing funding for this project which has partly financed this thesis. Et pour la réussite des essais avec les systems de protection de chute de bloc dans la MTA Carriére de St-Lèonard, je remerci Marc-André Tissières, Josiane Tissières, Vincent Tissières, Gerrard Genolet et leur équipe. Et pour sont expert assistance avec l'organisation des essais de chute de bloc en Valais, je remerci François Dufour.

Similar to the unpredictability of rockfall trajectories, the path of this thesis was deflected from rockfall attenuator nets toward the role of rock-shape in runout dynamics. This led to many scrambles amongst the Alps to observe rockfalls, I would like to thank all those who assisted me in these passages. Es grosses merci an Werner Gerber, der mit viel Geduld mir alles über Steinschlag, und Video Aufnahme gelernt hat, und für Pimm's o'clock! Herzlichen Dank an Marc Christen, der alle unsere verrückten Steinschlagerfindungen und Wünsche in das RAMMS::Rockfall Model umgesetzt hat, und natürlich auch alle genialen Powdertage in Davos. Special thanks are to: Remco Leine and Adrian Schweizer for the detailed discussion over the mechanics of rock-ground impacts and the collaboration developing Adrian's rockfall code into the RAMMS::Rockfall model applied in this work; Käthi Leichti, Georgie Bennett, Daniel Oertig, Martin Sieler, Johanna Scheidegger and all others who helped me count and locate rocks; Axel Volkwein, Barbara Krummenacher, Brian McArdell, Christoph Graph, and Yves Bühler for rockfall experimentation and field work assistance; Melanie Heinrich, Anja Schwyzer and Paloma Paleo for the assistance rolling rocks in sub zero conditions; John Duffy and Ryan Turner for Highway 1 rockfall, the Ranch and bowl-n-coke; Whilly Whinston for smartly getting me to the airport on time; Louise Vick, Tim Davies, Chris Massey, Garth Archibald, and David Bell for skink rock rolling on the Port Hills and detailed insights into the runout dynamics of basalt columns; M. Imran for the LaTeX template used for this thesis; WUJ, WUS and crew for support and encouragement along the way; My parents Dave and Tiggy Glover for your financial support with this research and for your detailed edits and advice helping me separate the variables; DoktorandInnen-Davos@slf.ch and A215 for the great research atmosphere amid the many outings into Davoser powder peaks; Den Lenin Mountaineers für eure Kameradschaft und dem Projekt ab in die Höhe mit Blick über dieses rock-n-roll mountain.

Alongside the numerous outings into rockfall terrain and the tedious hours capturing tortuous rockfall trajectories in the laboratory, particular thanks are to my academic supervisors. Each in their own way, has expertly guided the runout trajectory of this thesis. Many thanks to Dave Petley for giving me the opportunity and space to conduct this thesis through the remote Durham-Davos connection, your positive and challenging critique has ensured this thesis remained on course and has contained its initial unpredictable potential. To Nick Rosser, many thanks for your omnipresent support: from laser scanning rockfalls in Randa, Switzerland; to detailed discussion on the methods of capturing rockfall behaviour in the field, the lab, and in writing, you have been a constant amid the variable terrain of this thesis. Many thanks to Perry Bartelt for encouraging me to avoid avalanche powder clouds and keep it all things rock, teaching me the Dasein of large and small numbers, expanding my knowledge of English history and literature, and fish and chips in Scarborough. Your visionary discussions over mass-movements and $\vec{\jmath}$, along with opportunities for international rockfall exchange have been fundamental to the content of this thesis.

Contents

List of Figures

List of Tables

To my Bros.

"It's Only Rock 'n Roll (But I Like It)"

Mick Jagger and Keith Richards, The Rolling Stones, 1973.

Chapter 1

Introduction

Figure 1.1: Rockfall on road way in Vitznau Vierwaldstättersee lake Luzern, Switzerland. The event occurred on November the 20th 2003 and resulted in fragmentation of the block and impact cratering on the road with damage to infrastructure. Picture W. Gerber, Swiss Federal Institute for Forest, Snow and Landscape Research WSL.

1.1 Rockfall

Rockfalls are a frequent and hazardous process which result from the progressive weathering (Calcaterra et al., 2010), failure of rock-masses (Rosser et al., 2013), and are an important contributor to mountain sediment transport budgets (Bennett et al., 2013). Figure 1.1 gives an example of the potential consequences of rockfalls. Between 2011 and 2012 alone there were over 66 rockfalls in Switzerland that lead to; human fatality, structural damage, or closure of traffic lines. Rockfalls are initiated when rock blocks become detached from a rock mass under the action of gravity (Selby, 1982). Rockfalls are distinguished from other mass movements such as rock slides or rock avalanches (Petley, 2013) by their volume, typically between 10^{-2} to 10^{2} m^3, but can be up to 10^5 m^3 (McPherson, 1999, Rochet, 1987). Although rockfalls are classified to belong to the general category of landslides (Cruden and Varnes, 1996, Figure, 1.2) their dynamics are fundamentally different from rock slides and avalanches, as single rocks and boulders whose motion is governed by discrete ground impacts (Hutchinson, 1988). Rock-mass instabilities which result in rockfall can pose a severe threat to infrastructure (Petley, 2012), and rockfall mitigation is an important task in all countries with mountainous terrain or engineered rock slopes.

The release mechanism, shape and sizes of rockfalls is governed by failure along joint planes or discontinuities (Jaboyedoff, 2011, Lambert and Nicot, 2011) and fracture of intact rock, which is preconditioned by rock properties and their structures within the rock-mass. Therefore, the shapes and sizes of rockfalls can be associated with the specific geological settings in the rock masses in which they are formed (Fityus et al., 2013). Detachment is primarily driven by weathering processes such as acting upon the rock-mass (Calcaterra et al., 2010). Triggering factors can be intense rainfall, rapid snowmelt, seismic or anthropogenic influences (e.g. Eberhardt, 2006). Following release, rockfall motion consists of falling, bouncing, rolling or sliding (Dorren, 2003, Erismann and Abele, 2001, Hungr et al., 2001, Keefer, 1984), and the combination of these modes of motion defines the runout path and the area affected by rockfalls. Rockfall motion is influenced by numerous spatially variable parameters including the material properties of the rock itself and the terrain characteristics (Crosta and Agliardi, 2004, Volkwein et al., 2011). These influences can be divided into:

i) Rock and terrain material properties, including friction, stiffness and strength

ii) Impact configuration, defined by the combination of terrain morphology, rock-shape and size, in addition to the rock orientation and kinematics (translational and rotational velocity) at the point of impact.

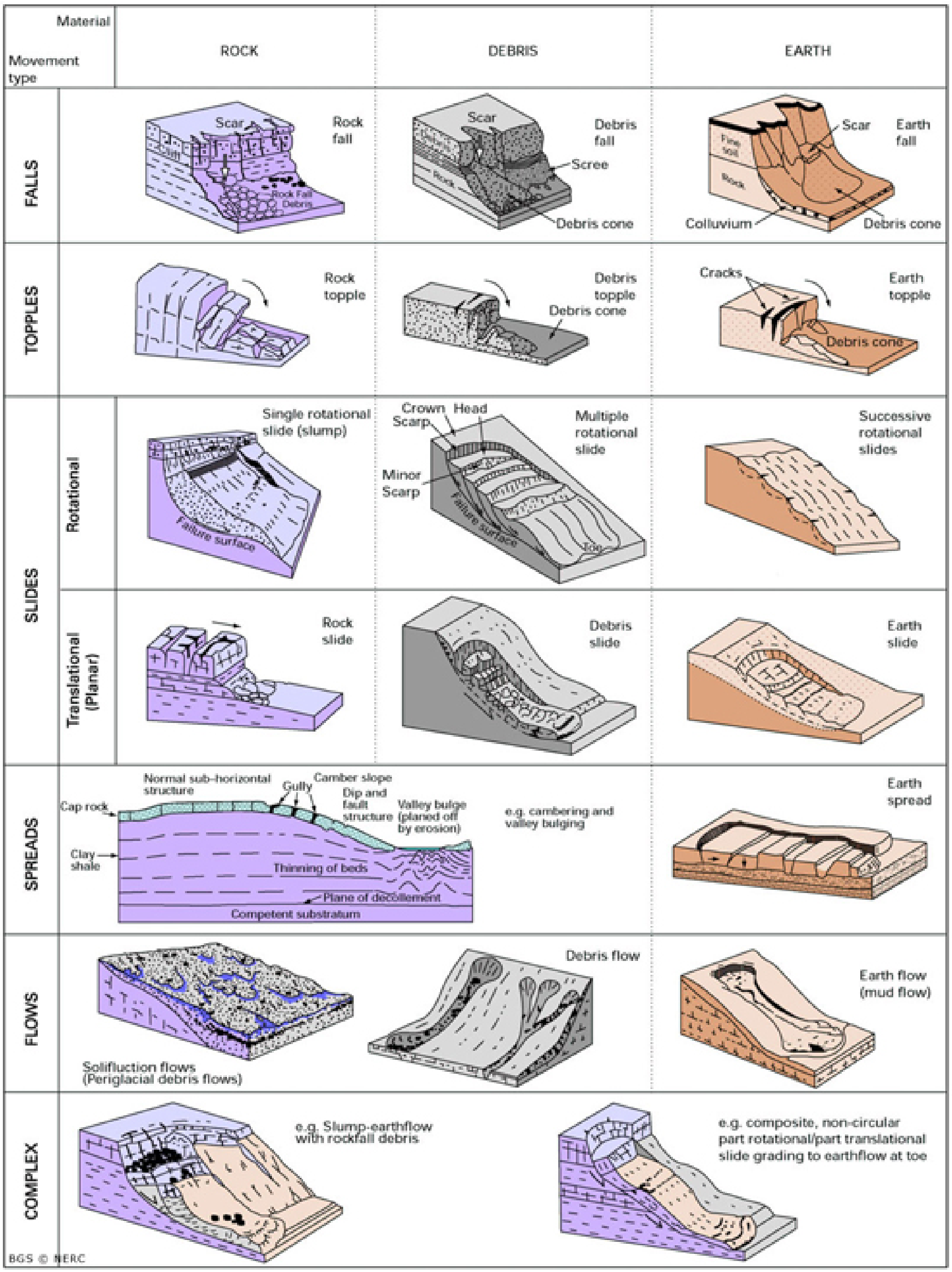

FIGURE 1.2: Landslide classification scheme from Cruden and Varnes (1996)

iii) Vegetation and its density, this is the strength, size and frequency of tree cover in forested areas, along with bushes and thickets.

1.1.1 The rockfall problem

Managing rockfalls can be divided into three main themes, each of which has lead to a great deal of research and engineering:

i) Predicting and monitoring potential instabilities (Santi et al., 2009, Frattini et al., 2008, Baillifard et al., 2003, Chau et al., 2003).

ii) Predicting their runout paths and delineating hazard zones (Baillifard et al., 2003, Volkwein et al., 2011).

iii) Estimating the dynamics of their runout behaviour for the design of mitigation structures to guide and catch dangerous rockfalls that threaten infrastructure and buildings (Ritchie, 1963, Pierson et al., 2001, Duffy, 1992, Gerber, 2001, ASTRA, 1998).

This thesis spans all three themes, attempting to link the characteristic rock shapes that are produced from unstable rock-masses to their runout behaviour. The thesis focuses on runout dynamics and the patterns of runout paths as determined by rock-shape, this approach requires an understanding of:

i) The detailed mechanics of rock-ground impacts.

ii) The dynamics of rockfall motion and trajectories.

iii) Links between rockfall deposition pattern and rock-mass characteristics in more accurate prediction of rockfall behaviour.

Addressing these questions is centred on the problem of finding an improved mechanical description of rock-terrain interaction, involving geology, geomorphology, physics and mathematics. Importantly any method that results, and is to be used in hazard analysis and mitigation, must be validated against a sound understanding of impact mechanics.

1.2 Context and Motivation

The dynamics of rock-ground interaction (Figure. 1.3) and trajectories are a fundamentally complex process (Crosta and Agliardi, 2004), and therefore requires a degree of simplification. Rockfall runout can be considered as a series of individual trajectories (Azzoni et al., 1995), which together form a runout path. The popular approach considers a rock's kinetic losses through ground impact as restitution coefficient reflecting the energy or velocity ratio between impact and rebound (Volkwein et al., 2011).

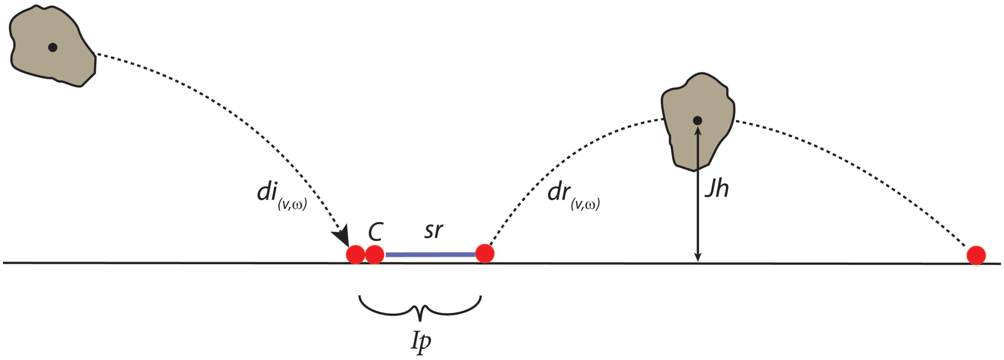

FIGURE 1.3: Sketch of the rock-ground impact-rebound process. The incident dynamics $di_{(v,\omega)}$ of the rock at initial ground contact C are altered through the impact phase Ip which can consist of contacts C, sliding and rolling sr. Rebound of the rock is characterised by its rebound dynamics $dr_{(v,\omega)}$ following the impact phase once the rock loses contact with the ground. It is the rebound dynamics that determine the jump heights Jh relative to the terrain.

In rockfall research a great deal of effort has been placed on defining restitution coefficients which attempt to bundle rock-ground impacts and the influence on runout into a single value describing the rebound characteristics such as terrain material (Chau et al., 2002, Fornaro and Nebbia, 1990) and terrain roughness (Bourrier, 2008). While this approach has been successful in many rockfall modelling approaches (Bourrier et al., 2009b, Spang and Sönser, 1995), it generalises the mechanical features of rock-ground impacts that concern both rock-shape and impact configuration. The expense and effort involved in experimentally measuring restitution coefficients often restricts studies to single impact testing (e.g. Cross, 2002, Labiouse and Heidenreich, 2009) or large scale rock rolling which yields only limited data (e.g. Dorren et al., 2006).

The inconsistent definition of how to measure restitution coefficients has lead to great uncertainty in guideline values (Chau et al., 1999), making the pursuit of parameterizing rockfall models particularly challenging when considering the number of terrain variables (Lambert and Nicot, 2011) and the stochastic nature of rebounds (Bourrier et al., 2009b). Rock-shape is often cited as influential in controlling rock-ground rebounds and the dynamics of rockfall motion (Bourrier et al., 2013, Crosta et al., 2004, Lambert and Nicot, 2011, Volkwein et al., 2011). There have however been limited attempts to quantify the role of rock-shape (e.g. Chau et al., 1999).

In both research and practice there is a strong need to: (i) quantify how rock-shape influences rock-ground impacts; (ii) observe how these affect rockfall runout motion; (iii) explain the characteristic deposit patterns of rockfalls according to rock-shape.

1.3 Research aim and objectives

The aim of this research is to advance the understanding of how the shape of rock particles involved in rockfalls influences their runout dynamics and trajectory. In pursuit of this aim the following research objectives have been outlined:

1. Use a physical model of rockfall to record and quantify the dynamic motion of three end-member rock shapes (*equant*, *platy* and *elongate*), from single impacts to entire runout trajectories.
2. Use a numerical rockfall model in which arbitrary rock shapes can be simulated to explore further aspects of rock-shape such as sphericity, and provide the link between small scale rockfall experiments and full scale field observations of rockfalls.
3. Compare the observed dynamics of physical and numerical experiments with field data collected from full scale rockfall experiments and detailed case studies of real rockfall events.

1.4 Structure of thesis

This thesis comprises of seven chapters. Chapter 1 defines the research need for understanding the mechanics of different rock-shapes during runout and outlines the research aims and objectives.

Chapter 2 reviews past research, providing an overview of the key themes that control rockfall runout, considering rock motion, impacts, fragmentation and interaction with objects that obstruct the runout path such as trees and rockfall protection structures. Work dealing with the characterisation of rock shapes highlights the significance and variability of rock-shape in geological rock masses. The chapter then provides an overview of studies on the dynamics of sporting balls and projectiles, comparing this with rockfall behaviour, followed by a review of rockfall modelling theories used for simulating rockfall runout and mechanics. Finally, a summary of current rockfall protection measures is presented, illustrating the application of detailed case studies on rockfall dynamics.

Chapter 3, provides details of the experimental design developed to achieve the research aims and objectives. Here an overview of the experimental set up of the physical experiments is described including a description of the measurement techniques used to quantify impact configurations, velocities, rotations and deposition patterns both in the physical and numerical experiments. A novel rotation and accelerometer module produced for the laboratory experiments is presented, in addition to data processing techniques which have been devised to provide metrics of the rotational behaviour. The chapter finishes with an explanation of the three-dimensional rigid-body rockfall simulation program RAMMS::Rockfall and first parameter and calibration studies are presented exploring the applicability to the study of the trajectories of rock shapes.

Chapter 4 summaries the results of physical experiments which have been devised explicitly to investigate the dynamics and runout patterns as a function of rock shapes. Data are presented on the translational and rebound behaviour of the different rock-shapes, along with measurements of single impact configurations. The chapter finishes with data describing the rotational behaviour of the test rocks during runout, and deposition patterns observed.

Chapter 5 presents the results from numerical modelling into the dynamics of rock-shape using the three dimensional rigid-body rockfall model. The results include a parameter sensitivity study of the rockfall model, and a one-to-one back calculation of the laboratory experiments presented in Chapter 4. Model results are then presented from investigations into the effects of a rock's *sphericity*, followed by two case studies of rockfall trajectory and runout. The first of the case studies presents rockfalls on road side rock-cut slopes performing a back analysis of full-scale rock rolling experiments in Valais, Switzerland. The second considers rockfalls in natural terrain, presenting a study of the Earthquake induced rockfall in Christchurch, New Zealand.

Chapter 6 discusses the findings in the context of previous literature, illustrating the contribution of this work to the understanding of rockfall mechanics and hazard assessment, highlighting applications to engineering practice and mitigation design. In particular this work demonstrates the significance of the variability of rock-ground impacts according to rock-shape for rockfall modelling.

The thesis closes with conclusions in Chapter 7 where the findings are summarised and recommendations for further research are made.

Chapter 2

Rockfall, Shape, Ballistics, and Modelling

2.1 Rockfall mechanics

The focus of this work concerns the movement behaviour of different rock shapes that leads to their runout paths which define hazard zones and its magnitude. The process of rockfall starts from the *release zone* where rock blocks are dislodged and enter into down slope motion, runout through the *transition zone* where peak dynamic activity is observed, and into the *deposit zone* where rocks slow and come to a stop (Figure. 2.1).

In this review of the literature dealing with rockfalls, a summary of research conducted on all aspects concerning the rockfall process is first presented. It begins with studies on release zones, covering individual processes in the transition zone such as tree impacts and rock fragmentation; and then covers deposit zones and rockfall protection structures along with mitigation processes.

Following the general overview of rockfall, the review focuses on the rock-shapes. The principal question is how different rock-shapes are generated in different geological and geomorphological settings. The review discusses the genesis of rockfalls and the variety of different rock-shapes that can be produced from rock-mass instabilities and denuding aggregates. It covers how rock shapes and sizes can be predicted from discontinuities which characterise a rock-mass.

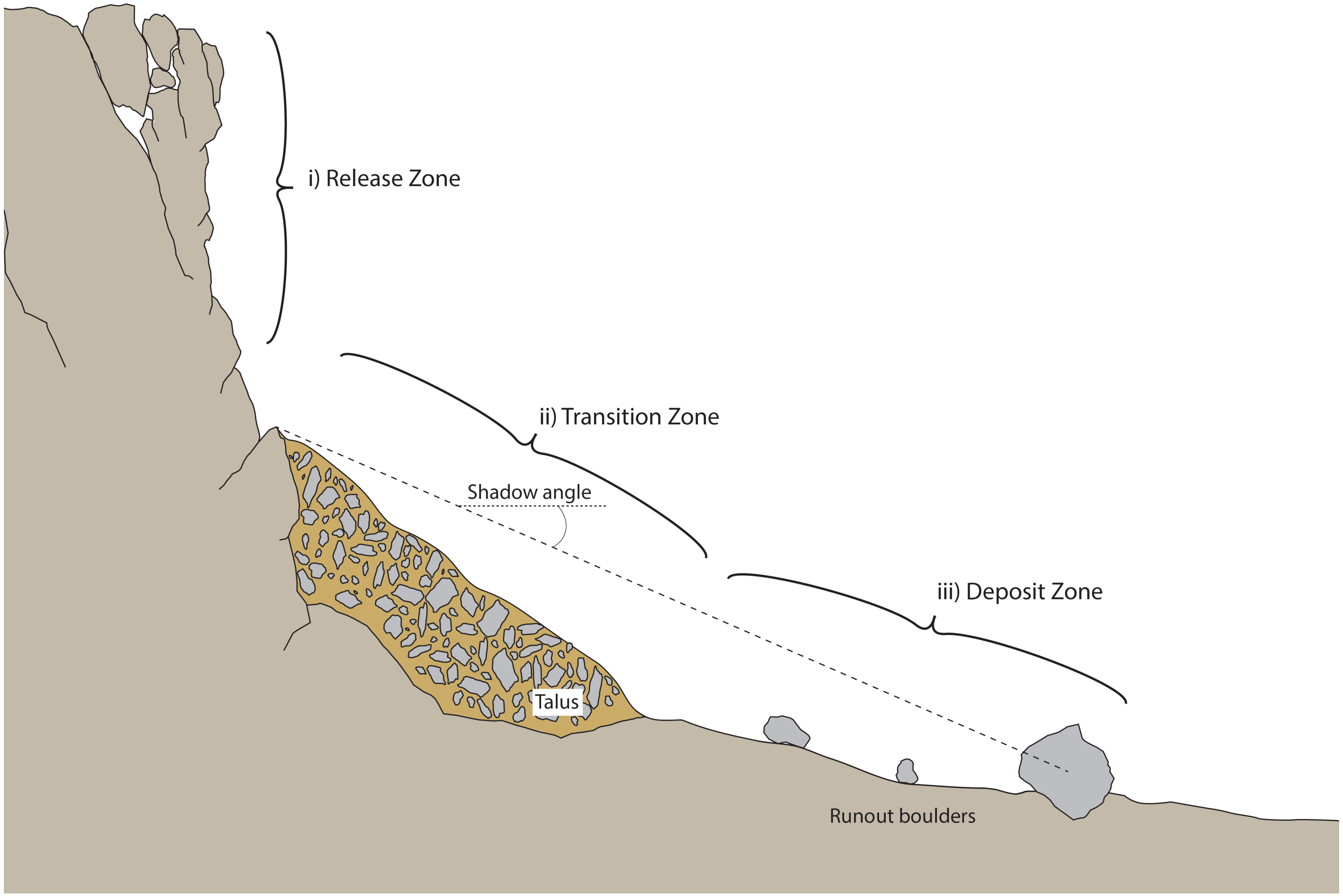

FIGURE 2.1: Sketch of rockfall activity zones composed of the i) Rock release zone, ii) Transition zone, and iii) the Deposit zone.

Following this there is a section on the dynamics of arbitrary shapes in the fields of missile ballistics, sporting balls and rockfalls; in particular with regard to individual ground surface impacts. This leads into an inspection of how single impacts are modelled. Importantly it is questioned if the concept of apparent restitution coefficients for modelling rebounds, which are widely used in rockfall mechanics, is adequate. The review then covers the rock-ground impact problem from a rigid-body perspective and explains the important aspects of rock-ground impact mechanics that are neglected in the rebound approach.

Finally there is a review of the numerous rockfall modelling approaches that are currently available for rockfall mitigation studies. The key mechanics behind their codes are identified, illustrating the different processes of rockfall which they attempt to model.

2.2 Rockfall motion

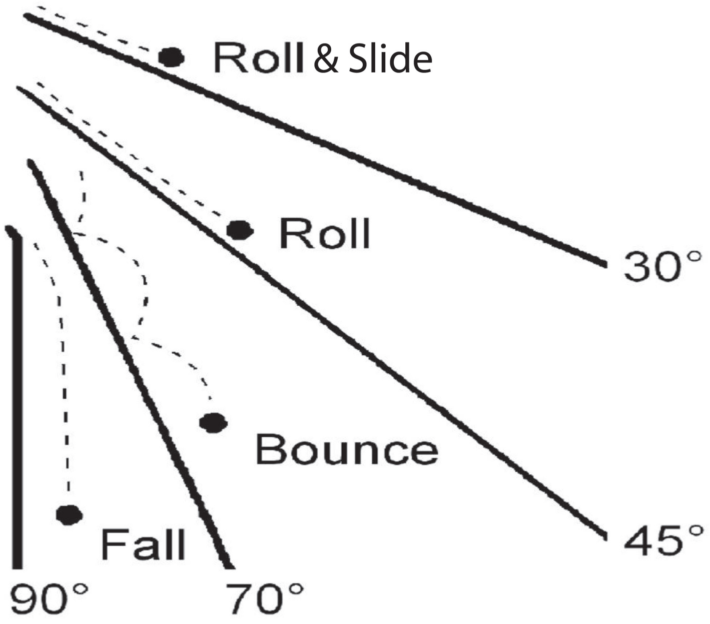

FIGURE 2.2: Suggested modes of rockfall motion according to slope angle (slide, roll, bounce, and fall). Taken from Dorren (2003) who modified Ritchie (1963) depiction of rockfall transport modes.

The characteristic runout behaviour of rockfalls according to terrain slope angle has been described by Ritchie (1963), defining four modes of motion (Figure. 2.2). The combination of all the modes of rockfall motion from the release to deposit compose a rockfall runout path (Figure. 2.3). This was one of the first comprehensive works on rockfall based on field observations of rocks rolled over roadside rock cuts. This work was intended as an engineering guide for the design of rockfall catch ditches.

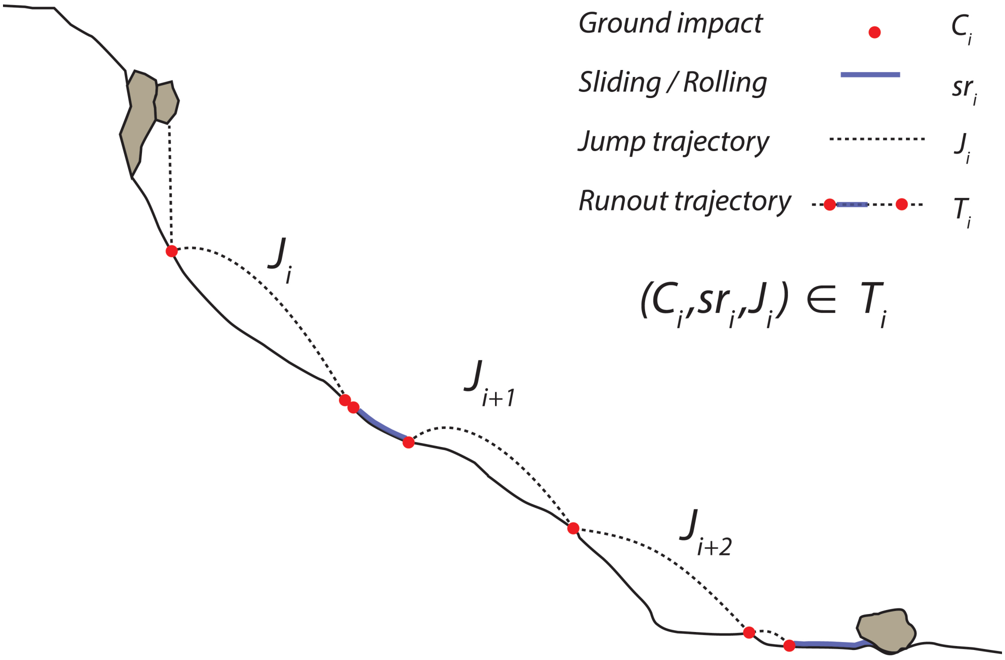

FIGURE 2.3: A rockfall trajectory T_i consists of jumps J_i, ground impacts C_i and contact phases of rolling and sliding sr_i.

2.2.1 Rolling

Several rockfall models account for rolling and sliding as separate phases of motion (e.g. Crosta et al., 2004, Spang and Sönser, 1995). These models apply dynamic rolling and sliding friction to define velocity thresholds at which the transitions between modes of motion are implemented. A problem arises such that the empirical threshold value defining the transition between sliding, rolling and jumping has a strong influence on jump height and is largely designed without physical foundation. Erismann and Abele (2001) investigated the rolling efficiency of polyhedral blocks in relation to slope angle, finding that with increasing number of rock facets, rolling was achieved at lower slope angles. Erismann and Abele (2001) find that non-spherical shapes display a critical velocity beyond which jumping occurs. Pfeiffer and Bowen (1989) suggested that transitions between modes of rockfall runout motion (jumping, rolling, and sliding) appear to be responsible for variability in rockfall trajectories, and therefore mobility and dispersion.

There is a need to explore this hypothesis, which involves investigating the dynamics of different rock-shapes as they travel down slope.

2.2.2 Ground impacts and restitution

Rockfall ground impact is commonly referred to as bouncing (Dorren, 2003, Erismann and Abele, 2001) despite the association with an elastic process. In most rockfall models (Azzoni et al., 1995, Bourrier et al., 2009a, Chau et al., 2002, Descoeudres and Zimmermann, 1987, Evans and Hungr, 1993, Guzzetti et al., 2002) bouncing is modelled as a rebound of the body's centre of mass as a Newtonian inelastic collisions. Rockfall models employing this method are termed rebound models (Volkwein et al., 2011). The contact is modelled using a restitution coefficient determined from experimental studies and rockfall observations, typically by measuring the ratio of incident V^i and reflected V^r velocity R_v (Eq. 2.1) or energy R_{kE} (Eq. 2.2) (Labiouse and Heidenreich, 2009). The body's rotational speed ω and the bodies inertial moment I define the rotational kinetic energy, and the body's mass m and velocity V define the translational kinetic energy. Combining bothe the translational and rotational kinetic energy the restitution of total kinetic energy R_E can be computed (Eq. 2.3).

The methods for defining restitution include:

$$R_v = \frac{V^r}{V^i}. \tag{2.1}$$

$$R_{kE} = \frac{kE^r}{kE^i} \tag{2.2}$$

and,

$$R_E = \frac{1/2[I(\omega^r)^2 + m(V^r)^2]}{1/2[I(\omega^i)^2 + m(V^i)^2]}. \tag{2.3}$$

For rockfall modelling the restitution coefficients are commonly decomposed into slope normal and tangential components (see (Figure. 2.4) and (Eq. 2.4)):

$$R_n = \frac{V_n^r}{V_n^i} \quad \text{and} \quad R_t = \frac{V_t^r}{V_t^i}. \tag{2.4}$$

The same ratio of rebound over incident velocities is applied simply to each component (Eq. 2.4). This permits the kinetic losses to be given a vector and allows the trajectory of the rock to be influenced.

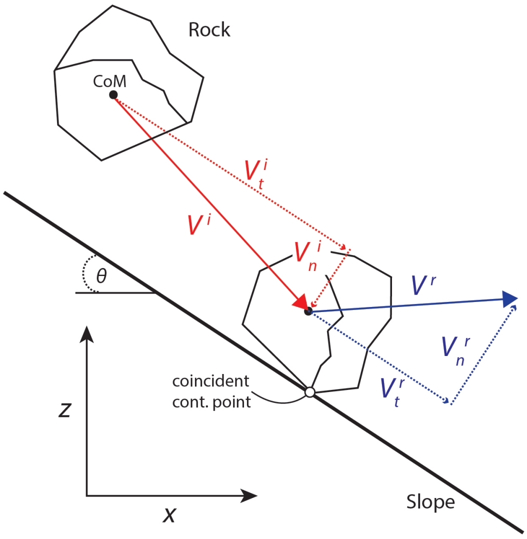

FIGURE 2.4: Apparent restitution coefficient of velocity V measures the ratio of the rebound V^r to the incident velocity V^i vectors. This is decomposed into slope normal (V_n^r, V_n^i) and tangential (V_t^r, V_t^i) components and is measured with respects to the rocks centre of mass (CoM).

If apparent restitution coefficients are to be applied in three dimensions the tangential coefficient of restitution must be given x and y components within the coordinate system of the simulation domain (e.g. Bourrier et al., 2009a, see Figure, 2.5). Rotational velocity restitution have also been included in some rockfall models (Bourrier et al., 2009a) (Figure. 2.5), but there is very limited data on this component of rockfall dynamics due to the difficulties of resolving velocities from videogrammetric measurements.

To date rockfall research has been dedicated to defining normal and tangential impact restitution coefficients to characterise terrain material properties (see Figure, 2.6, Labiouse and Heidenreich, 2009, and references therein) and terrain roughness (Bourrier, 2008, Crosta and Agliardi, 2004). Chau et al. (1999) attempted to relate variations in restitution coefficients to changes in rock-shape, concluding that by increasing shape angularity, normal restitution coefficients are highly sensitive to shape change, whereby spheres remain nominally constant whereas changes toward a hexagonal shape showed

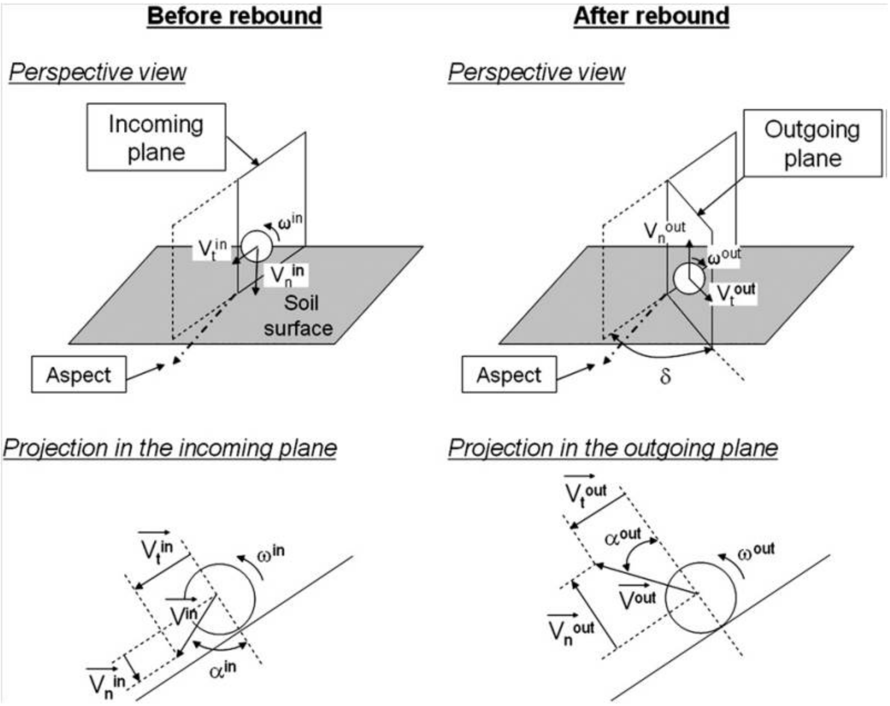

FIGURE 2.5: Depiction of incident and reflected impact indicating the averaged incident velocity and exit velocity used to measure restitution coefficients. Additionally, incident and reflected aspect angle are shown, (Bourrier et al., 2009a).

an increase in normal restitution for the same impact condition. However, tangential coefficients remained largely unchanged. A drawback of these experiments was that only single impacts following free fall were observed, consecutive rebounds during runout were not considered in this study. The effects of rock-shape on the coefficient of normal restitution are also investigated analytically by Vijayakumar et al. (2012) who produced a 2-D rigid body model which demonstrates that increasingly ellipsoidal shapes have increasingly higher coefficients of normal restitution if the body's centre of mass is taken as the datum from which to measure restitution.

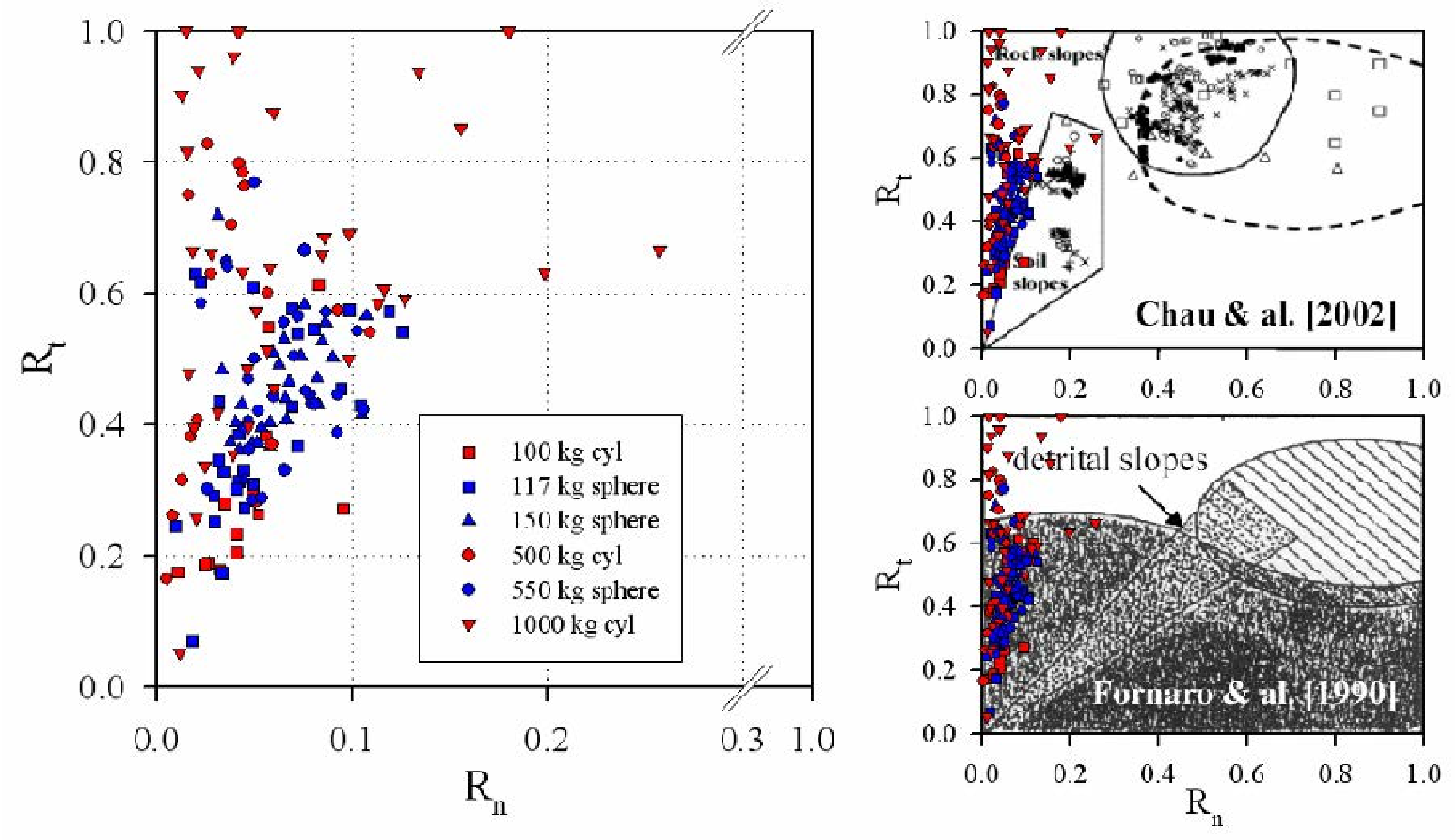

FIGURE 2.6: Summary of restitution coefficients recorded from experimental campaigns in literature. The figure is taken from Labiouse and Heidenreich (2009) in which they experimented with impacts in soft soil. The comparisons are made to previous studies investigating restitution coefficients from Chau et al. (2002) and Fornaro and Nebbia (1990).

2.2.3 Rock-ground impact scars

Rocks impacting softer terrains cause penetration into the soil deforming the ground and altering the topography. This leaves characteristic scaring features in the terrain (Figure. 2.7). Documenting the morphology of scars, Paronuzzi (2009) remarks how the altered terrain geometry is likely to have resulted in a slope normal restitution considerably higher than anticipated for the given terrain material. Thus, rock-ground impact scaring provides another source for uncertainty in the assessment of restitution. This study only inspected two single impact scars in assessing rebound behaviour according to terrain scarring. Zinggeler and Pfeifer (2009) attempt to include the process of soil deformation by altering the selected value of restitution according to the impact dynamics and forcing changes to the rebound angle. Their conceptual model was based on studies of impact scars crater morphology from ballistics research. There is limited research on this phenomenon in rockfall mechanics although often recognised as influential for the rebound. This is most probably because data which includes the impact dynamics of a rockfall in addition to the scar morphology are difficult to obtain experimentally.

Figure 2.7: Examples of rock-ground impact scars in soft soils. A and B) Schwartzhorn Fluelatal Davos, 2011, Photo J. Glover, SLF. C) Rapaki Porthills, Christchurch, 2011, Photo L.Vick, Canterbury University.

One of the biggest issues with modelling rebounds and applying restitution coefficients is that this attempts to bundle multiple rock-ground contacts into a single value of restitution. The rebound model averages the contact over the centre of mass of the rock, which can involve a number of motions such as rotation and sliding. This may provide an explanation for the often reported measures of normal restitution coefficients greater than unity (Buzzi et al., 2012, Spadari et al., 2012).

2.2.4 Interaction with trees

A important method applied to manage rockfalls is the use of forests to break rockfall runout (Stoffel et al., 2006). Trees are natural protective barriers (Figure. 2.8), whereby they serve to dissipate energy through impact and the breaking of tree trunks (Jonsson, 2007). As such small rocks can be caught by forests if the forest is significantly dense (Radtke et al., 2014). Dendrochronological inventories are often used to reconstruct past rockfall activity (Stoffel and Perret, 2006). Whilst the interaction of rockfalls with trees is not considered in this thesis, the general mechanics of rock-tree impacts, including restitution coefficients, provides a useful insight.

FIGURE 2.8: Impact scars on trees found in a rockfall affected area in Grabengufer near Randa in Switerland. Photo J. Glover SLF.

2.2.5 Going ballistic: Trajectory analysis

Once a rock loses contact with the ground its centre of mass takes on a ballistic trajectory between impacts J_i (see Figure 2.3). Gerber (2008) demonstrates a method of rockfall trajectory analysis to extract jump heights and velocities based on the geometric properties of the trajectory parabola, obtained from rockfall scars on the ground and in trees (Fig. 2.7 and 2.8). Note this method is also well docuamented in Volkwein et al. (2011). The method employs a horizontal x and vertical y coordinate system in which the position of the rocks centre of mass can be described using a parabolic function (Eq. 2.5) (see also Fig. 2.9). For rockfall this approach assumes negligible air resistance (Giani, 1992):

$$y_{(x)} = ax^2 + bx + c. \tag{2.5}$$

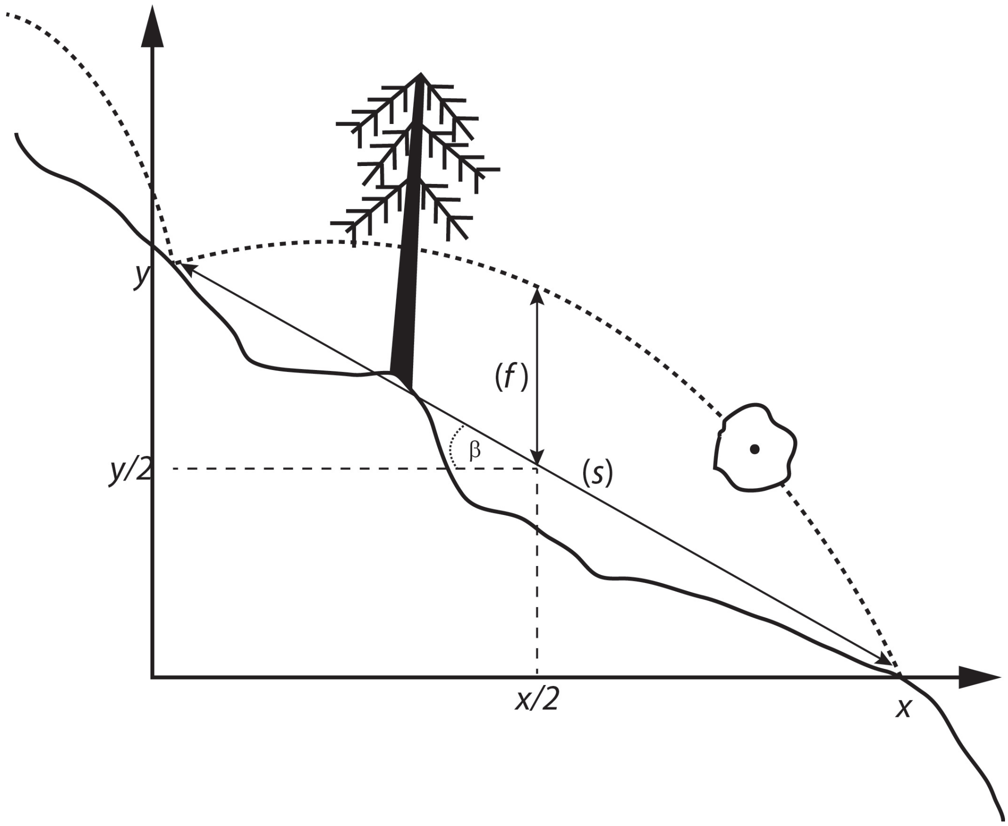

FIGURE 2.9: Rock trajectory parabola between two impact points over terrain that passes a tree leaving height information due to a tree scar. Distances S and f prescribe the form of the parabolic trajectory in the two-dimensional coordinate system (x and y. f is measured at the half distance $x/2$,$y/2$. Adapted after Gerber (2008).

The ballistic parabola of each trajectory J_i have the properties of a slant range s and jump height *f*. The slant range s is the straight line distance between two impact points and has a slope angle β. Note that β is not the terrain slope angle. The jump height f is measured vertically from the mid point of s to the intersect with the trajectory (Figure. 2.9). With information on the parabolic trajectory (*f*, s and β) the parabolic equation for *y(x)* is solved using the following equations (2.6) (Gerber, 2008):

$$a = \frac{-4f}{x^2},$$

$$b = \frac{4f}{x - \frac{y}{x}},$$

$$c = y. \tag{2.6}$$

The jump height f is related to gravity g and the time interval *(t)* between impacts (Eq. 2.7),

$$t = \sqrt{\frac{8f}{g}} \equiv f = \frac{1}{8}gt^2. \tag{2.7}$$

Substituting the velocities of x and z into the parabolic equation (2.5) the position of the rock's centre of mass along its ballistic trajectory is also given with the following equations Eq. (2.8) and Eq. (2.9):

$$x' = Vx_o t + x_o \tag{2.8}$$

$$y' = \frac{1}{2}gt^2 + Vy_o + y_o. \tag{2.9}$$

Where x' and y' denote the momentary position of the rock's centre of mass for a given time t.

In the literature the height obtained by a rock during ballistic trajectory is often referred to as a bounce height (Dorren, 2003), where the ground contact is thought of as a rebound or bounce. This is mainly because in most rebound models currently applied to simulate rock ground-impacts the ground contact is considered to be an instantaneous event, and is modelled with an apparent restitution coefficient (Section. 3.4.2). It is known that rockfall rebounds are influenced by a number of changing conditions in space and time which makes rebounds highly variable events and therefore must be treated stochastically (Bourrier et al., 2009a). The problem with assigning a restitution coefficient to model impacts is that this approach neglects the mechanics of rock-ground impacts which can involve a number of contacts, sliding, and mechanical levering of the rock into a second departure from the terrain surface during a period of impact.

For the aforementioned reason, the result of the rebound process is referred to as a *jump* in this work, in doing so I make reference to the number of additional processes, in addition to bounce that occur during a rebound. Importantly, the entire process of a rebound can affect the trajectory geometry and jump height. Questions arise such as which parabolic geometry is the most efficient for a rock to travel over a slope; e.g.

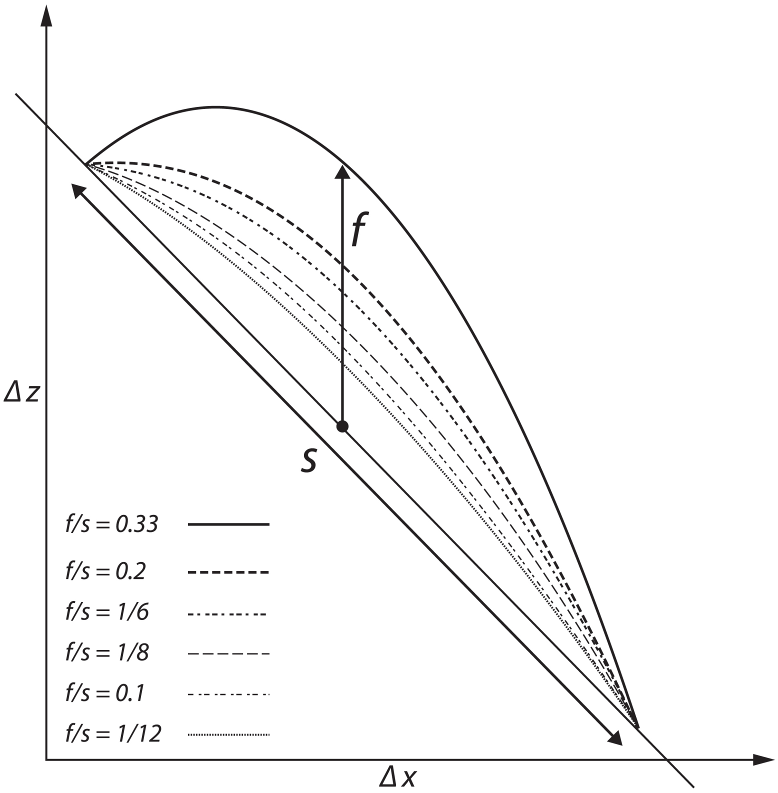

FIGURE 2.10: A range of possible trajectory ratios plotted for a fixed jump distance s and slope angle. The ratios $f/s = 1/12$, $f/s = 1/8$ and $f/s = 1/6$ are suggested by Gerber (2008) and Volkwein et al. (2011) for the estimation of rockfall jump heights and velocities from impact scars.

rebound trajectories that are flat and travel near-parallel to the slope or trajectories that are angled skyward creating a high arcing parabola? Figure 2.10 illustrates a range of typical parabolic rockfall trajectories for a fixed jump distance and slope angle.

2.2.6 Fragmentation

Fragmentation is governed by impact energy, rock strength and impact angle in relation to rock foliations and fabrics (Giacomini et al., 2009). Fragmentation can induce deposition and therefore total dissipation of translational kinetic energy. Bozzolo and Pamini (1986) suggested that most rocks break up on first impact beneath the source, dissipating 75 - 86% of kinetic energy gained during initial freefall (Evans and Hungr, 1993). This is important for hazard analysis and rockfall modelling because the selected "design block" (Crosta et al., 2004, Volkwein et al., 2011) should be representative of those involved during runout. Nocilla et al. (2009) observed how rocks show a decrease in grain size via fragmentation with increasing distance from source, noting this was accentuated in softer lithologies. The role of fragmentation in rockfall motion becomes even more challenging when considering the shape of detached and fragmented clasts. There is a need to explore how detached rock-shapes, which are not conducive to transport, can fragment into more mobile shapes. This equally applies to the stopping process where fragmentation contributes to terminating motion.

2.2.7 Deposit zones

Defining the potential inundation area of falling rocks is an important task in rockfall hazard assessment. The distance a rock will run-out from its release point has been widely studied with metrics such as the rockfall shadow angle (Evans and Hungr, 1993) and the Fahrb´oschung (Dorren and Seijmonsbergen, 2003).

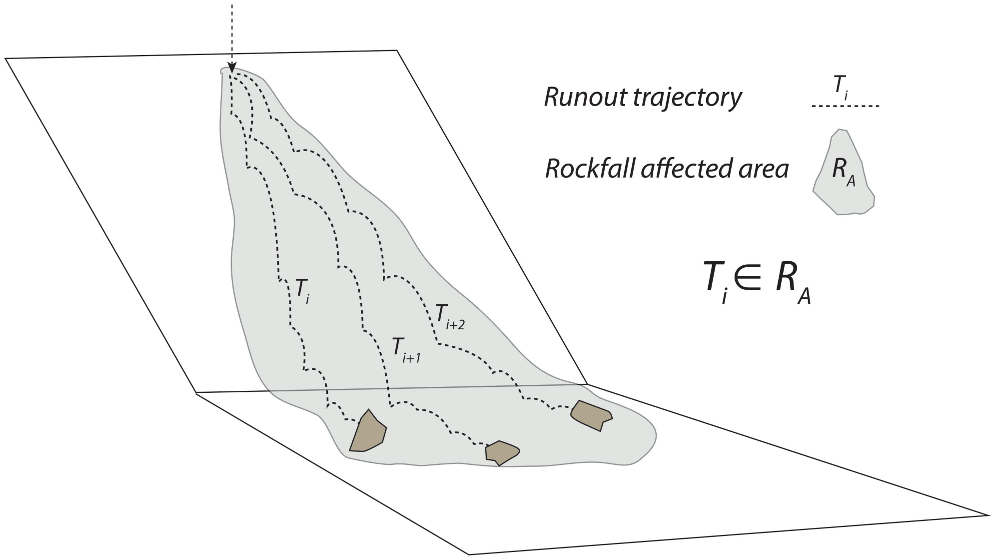

FIGURE 2.11: Deposit zone area R_A is defined by the area below the release zone that is encroached upon by each single rockfall runout trajectory T_i. The member set $T_i \epsilon R_A$ defines the inundation area.

An additional component to the run-out path is the lateral travel distance away from the steepest path of descent, which in many cases is difficult to measure since the exact release point is not always well constrained. Nonetheless the most extreme lateral runout rocks in a rockfall zone define the extent of the rockfall deposit zone (Figure. 2.11). (Evans and Hungr, 1993) define rockfall inundation area by measuring the runout distance and lateral dispersion angle from a single point source. Crosta and Agliardi (2004) measure dispersion as the width to length ratio of the inundation area (Figure. 2.12).

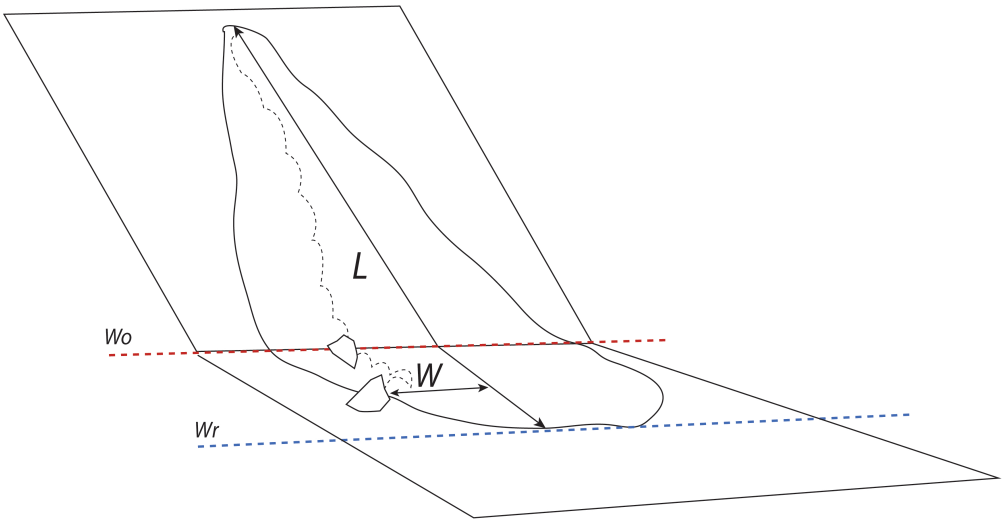

FIGURE 2.12: The measure of the rockfall dispersion W/L, where W is the lateral runout distance from the centeral fall line, and L is the total runout distance from the release source. Acording to Crosta and Agliardi (2004) this is taken as the maximum distances for a rockfall deposit zone e.g. W_r. While the ratio can be applied to measurements taken at specific points of interest along the runout slope e.g. the toe of the slope W_o, and also applied to single runout trajectories.

Crosta and Agliardi (2004) investigated rockfall dispersion in relation to slope angle and surface roughness using a numerical model, suggesting that for shallow slopes dispersion is moderate between 10 and 20°. For rough slopes dispersion is expected to be high; up to a threshold of 45°. For short and steep slopes lateral dispersion is normally low. From experiments Azzoni and Freitas (1995) found rocks runout laterally from the release point up to a maximum of 20% of the runout length, observing a reduction in dispersion with increasing slope angle. This demonstrates a clear dependence on terrain roughness and in some cases wider terrain morphology. However, these numerical experiments performed modelling using a spherical rock and forced the variability of the trajectory by variably adding terrain roughness and contact parameters. There is a need to demonstrate how rock-shape can influence these results.

2.3 Rock-shape

In rockfall analysis and mitigation design, engineers are interested in the 'design block' (Crosta and Agliardi, 2004, Volkwein et al., 2011), representing the maximum rockfall size at any given site. For example, in rockfall barrier testing a standard design rock is used (Gerber, 2001) see Figure, 2.13. While this is an accepted approach in rockfall engineering practice, it neglects the possibility of irregular rock-shapes which could have a strong impact on the behaviour of rockfall barriers and run-out trajectories.

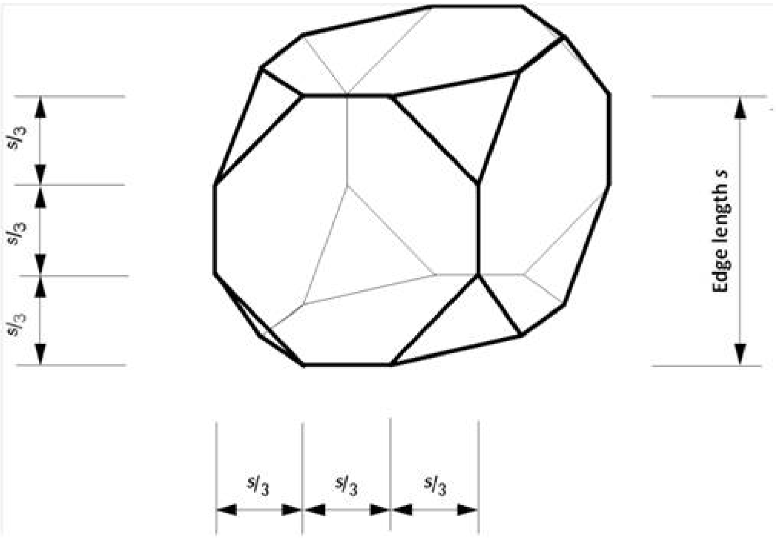

FIGURE 2.13: Standard shape of concrete block used for testing rockfall barriers, from Gerber (2001).

2.3.1 Rock-mass character

Characterising rock-masses is important in rockfall hazard mitigation because of the number of possible rock shapes and sizes that can be generated. The lithology and geological setting have a strong bearing on preconditioning the size and shape of detachable rocks. Over and above weathering processes (Calcaterra et al., 2010), the geometric relationships of rock-mass discontinuities, which include joints, fractures, contacts, bedding, asperities, and schistosity, govern block shape and size (Figure. 2.14) along with the release mechanism of rockfalls (Jaboyedoff, 2011, Lambert and Nicot, 2011). The rock-mass properties of discontinuity orientation, persistence, joint set number, and spacing, are required to define rock-shape and size Wyllie and Mah (2004), (Figure. 2.14).

Rock-mass characterisation is important as it offers the opportunity to predict kinematically permissible block shapes and sizes before release. The field of rock-mass characterisation is advancing by applying both photogrammetric and laser scanning to measure discontinuities (Rosser et al., 2005, Sturzenegger et al., 2007, Sturzenegger and Stead, 2009). With detailed discontinuity data now readily available, predictions of internal rock-mass structure and block size and shape distributions (Kalenchuk et al., 2006, Palmström, 1995, 2005) are being made and incorporated into geotechnical design of

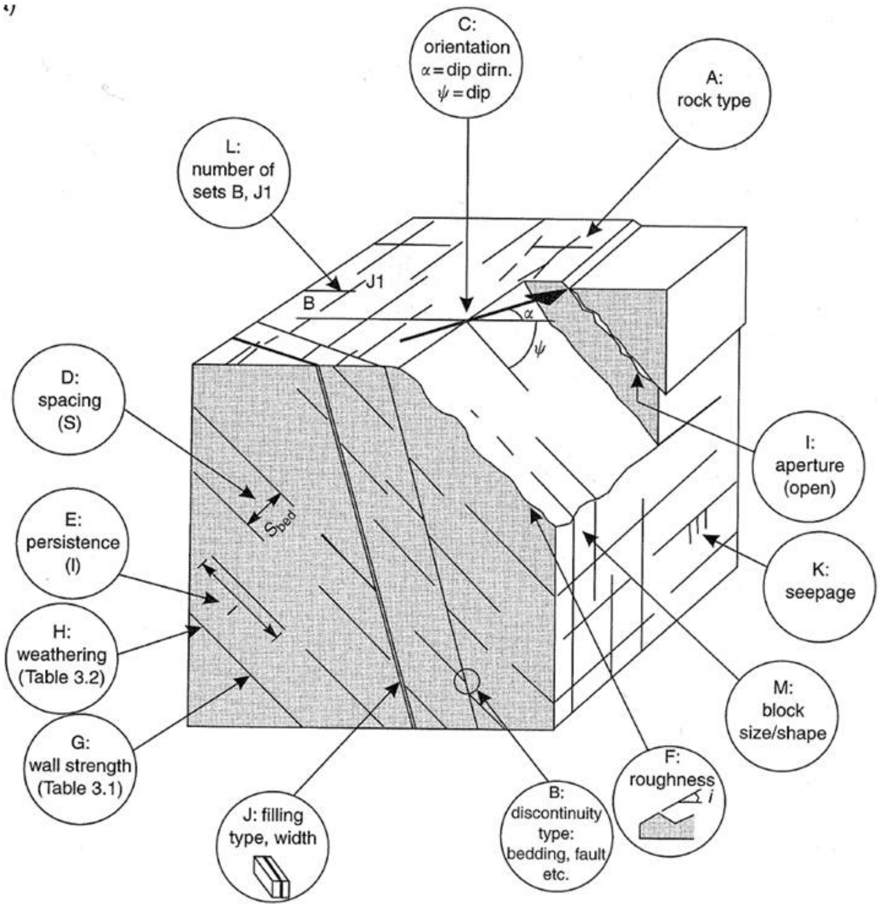

Figure 2.14: Characteristics of discontinuities in rock-masses, from Wyllie and Mah (2004).

excavations (Kalenchuk et al., 2008) and slope stability assessment (Singh et al., 2013). There is much scope to now integrate this information into rockfall runout analysis.

2.3.2 Block shape and size

The shapes, sizes and frequency of detachable rocks are characteristic of a particular lithology and structural architecture off specific geological settings. Kim et al. (2004), for example, find that there is a decreasing block size approaching the core of fault zones due to strain localisation. Coe and Harp (2007) studying limestone fold architecture find a higher susceptibility of rockfalls approaching the hinge of folds which is again attributed to strain localisation and a higher discontinuity density about this point. GIS (Geographic Information System) studies investigating rockfall activity identify a higher frequency of rockfalls in siliceous over calcareous rock-masses with limestones showing greater release volumes (Duarte and Marqunez, 2002, Fischer et al., 2012). The geometric relationship between rock-mass discontinuities which dictate rock-shape and size distribution are a reflection of the geological deformation history of the rock-mass.

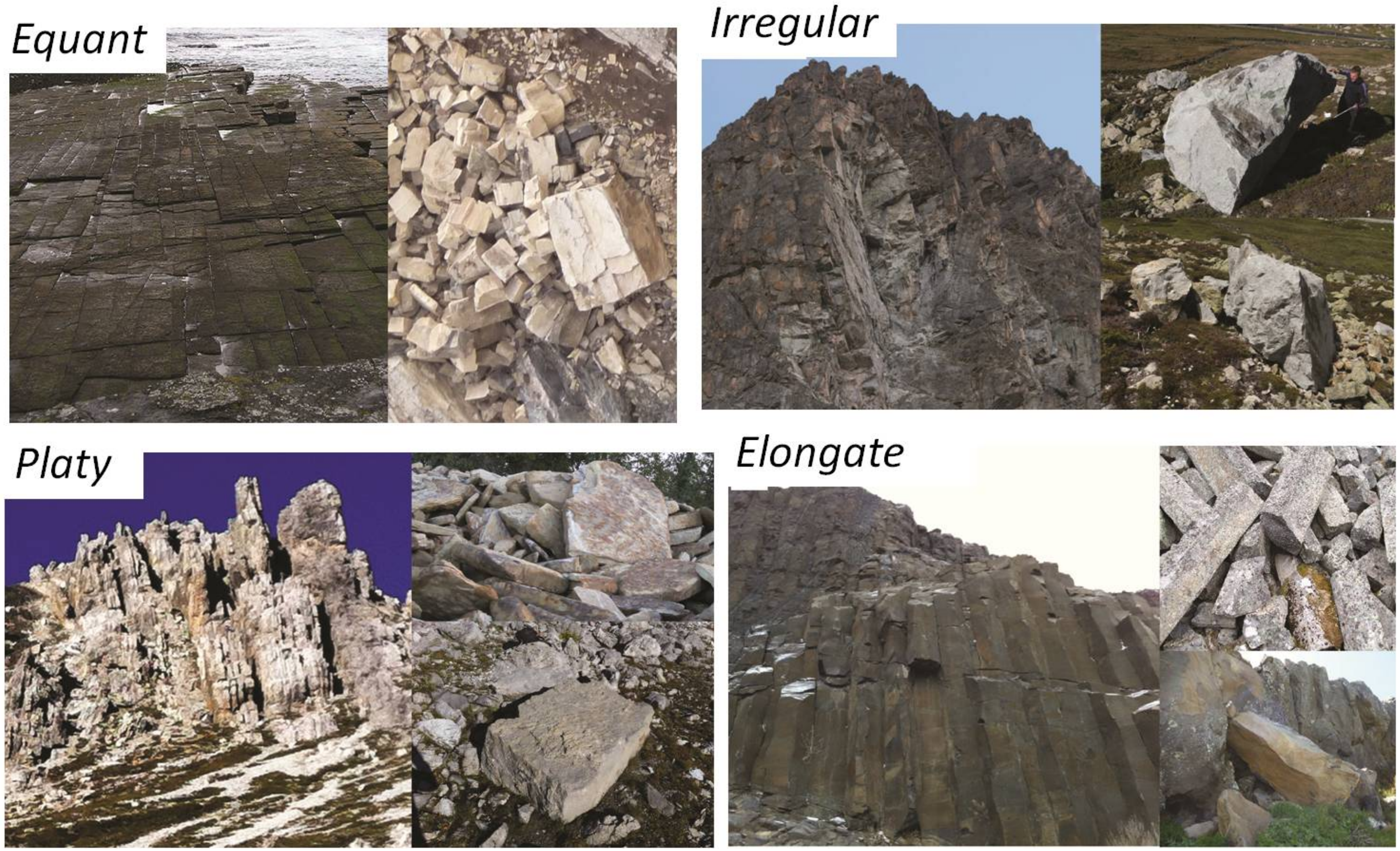

Figure 2.15: Photographs of rock masses and their aggregate forms. (*Top left*) An example of *equant* cubic rock forms generated in a sequence of sandstones exposed to an extensional deformation regime, the primary joint sets are near equally spaced and orthogonal to one another. (*Top right*) The complex over printed joint in of this granodioritic rock mass result in highly irregular and angular rock block forms. (*Bottom left*) The uplifted and folded limestone sequence is well bedded producing distinguished slabs which detach as pronounced *platy* rock forms. (*Bottom right*) Distinguished columnar jointed basalt sequence produces the characteristic *elongate* rock forms.

2.3.3 Failure mechanism

The discontinuities of a rock mass determine the mechanism of failure (Figure. 2.16), predefining the release kinematics and initial orientation of rocks during rockfall initiation. The first contact with the slope holds an important influence on the resultant trajectory and runout path.

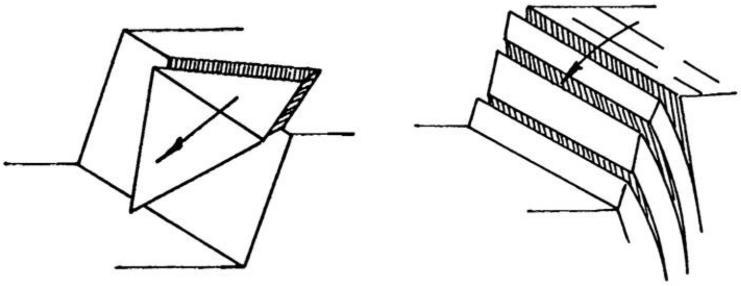

FIGURE 2.16: Example rock-mass failure mechanisms, from Wylie and Mah (2004). (*left*)Wedge failure of a rock mass, topple failure (*right*). The failure mechanisms are dictated to by the discontinuities that dissect the rock-mass.

2.3.4 Particle shape and size

In granular systems the classification and quantification of shape and size are fundamental in the dynamics of the process. For example, in the study of sediment transport of fluvial systems (Demir, 2000, Sneed and Folk, 1958), grain comminution (Djordjevic, 2010), and in grain packing (Latham et al., 2008).

Classifying particle size is a straightforward quantification, with the widely applied Wentworth (1922) classification system the accepted norm. This was extended by McPherson (1999) and includes particle sizes expected of rockfalls (10^{-2} to 10^{2} m^3). Particle shape is, however, a nontrivial task to characterise because the description must incorporate a number of often overlapping features. Blott and Pye (2008) suggest that particle form, roundness, irregularity and sphericity are the four most important shape descriptors, ultimately the method and aspect of shape considered in a classification is driven by the process under investigation in addition to the practicalities of measurement.

2.3.5 Form

Particle form is commonly measured using the three principal geometric axes: length, breadth and width (Figure. 2.17) measured orthogonal to one another (Krumbein, 1941). In the literature a number of different nomenclatures for the length, breadth and width axes have been proposed. Wentworth (1922) labelled them D', D'' and D''' axes, while a, b and c axes were used by Zingg (1935) and Krumbein (1941). A practical solution was developed by Sneed and Folk (1958) who used long L, intermediate I, and shortest S axes, which was independent of the coordinate system.

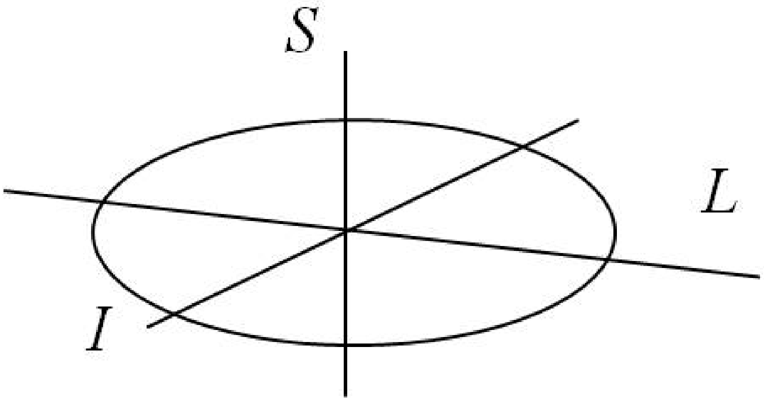

FIGURE 2.17: Principal long L, intermediate I, and shortest S axes according to Sneed and Folk (1958).

From the principal geometric dimensions, form is classified by assessing the aspect ratios of axes. A problem with this approach is that there is no standardised method to determine axis length, for example, whether the axis should be orthogonal. Additionally there is an inherent ambiguity in selecting the geometric axes of a particle (Blott and Pye, 2008). However, for field studies of granular deposits this approach is often selected due to its apparent ease of application.

One of the first particle form classification schemes (Zingg, 1935) developed shape descriptors based on the aspect ratios of the principal axes. The breadth-to-length ratio (b/a or I/L) and width-to-breadth ratio (c/b or S/I) were used to define four end-member shape classes which could be plotted on a square bivariant plot. Classes were *flat*, *spherical*, *flat* and *columnar*, and *columnar*. Various names have been proposed for these four classes by authors (e.g. Brewer, 1965, Krumbein, 1941).

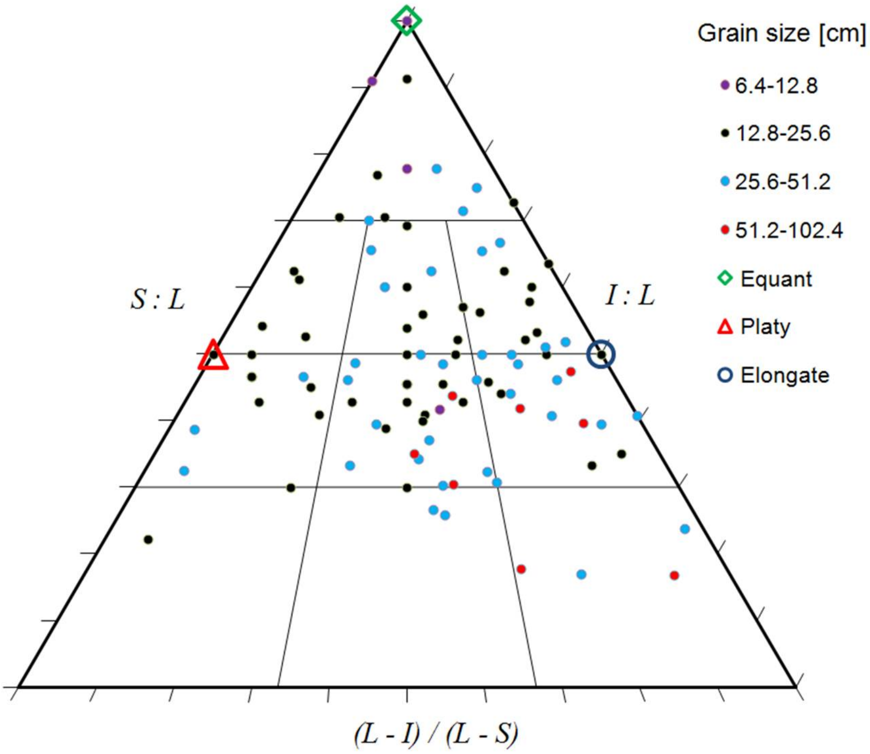

FIGURE 2.18: Triangular plot representing rock-shape in relation to the aspect ratios of the principal length axes (L, I and S). The data are taken from a preliminary survey of rockfall deposits in dolomites along the Julier Pass Kanton Graübunden. The data are also classified using the McPherson (1999) method.

Sneed and Folk (1958) argued that a measurement of three principal axes is best represented on triangular plots. The authors recognised four main shapes in their classification which contained 10 sub-categories (Figure. 2.18). However, they noted within this classification there were three end-member shapes, respecting the mathematical ratios between axis lengths.

$$\begin{aligned} L > I = S \quad (elongate) \\ L = I > S \quad (platy) \\ L = I = S \quad (equant) \end{aligned} \tag{2.10}$$

There have been many variations on these principal classifications of geometric form (for a complete review, see Blott and Pye, 2008). Fundamentally, the methods have been adapted to target a specific feature of form central to the process under investigation. For shape analysis of sediments, Benn and Ballantyne (1993) demonstrate how the ternary diagrams of Sneed and Folk (1958) are the appropriate standard method to represent shape data, because they are without bias or distortion.

In studies of rockfall deposits a measure of the three principal geometric axes is commonly performed, not only for practical reasons in the field, but also because a 3-D size estimate is additionally obtained with this measure. Commonly the three axes method is accompanied with a graphical classification (Figure. 2.19), where an interpretation of the shape is made by the observer (Fityus et al., 2013). The motion dynamics of different shaped rocks are therefore qualitative, because the observed behaviour of a rock in this sense can only be associated to a shape that is selected visually by the observer when using graphical classification schemes.

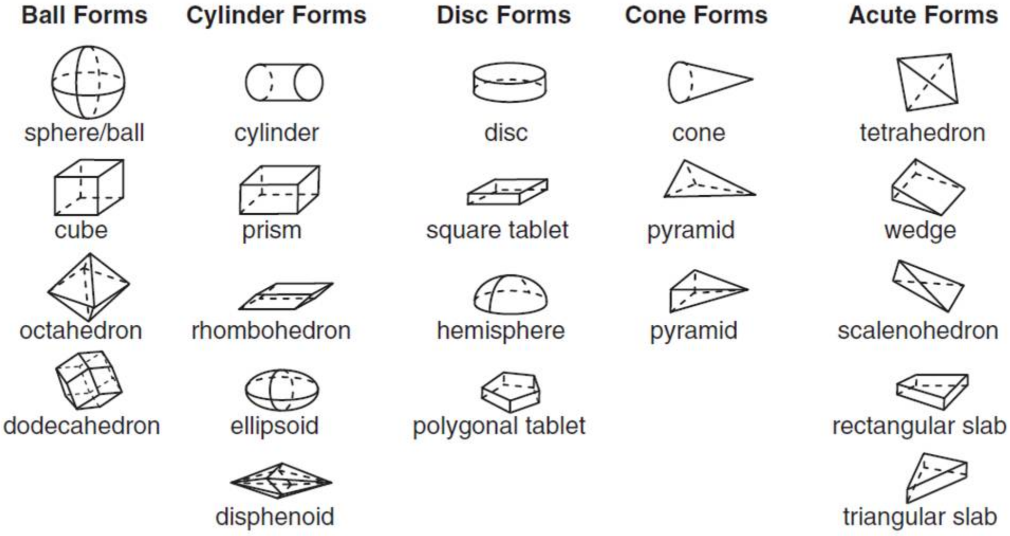

FIGURE 2.19: Graphical shape chart, from (Fityus et al., 2013).

2.3.6 Shape and inertia

Wang et al. (2007) propose to calculate the equivalent ellipsoid based on the moment of inertia tensor of a given particle. This method has the benifit of incourporating a component of the particles dynamics in the classification. The method is based on an adaptation of the aforementioned geometric form classification schemes (Wentworth, 1922, Zingg, 1935, Krumbein, 1941, Sneed and Folk, 1958). However, insetad of measuring the geometric axis lengths, the lengths of the principal inertial axes of an object are measured. This is achieved by computing the ellipsoid that holds the equivalent magnitude inertial axes to the particle. The geometric length breadth and width values of the equivalent ellipsoid are then used as a measure of the objects form. Standard form classifiers in which the aspect ratios of the principal lengths define shapes as either equant, elongate, platy or bladed are applied and are presented on triangular diagrams such as those of Sneed and Folk (1958) (Figure. 2.18). The inertia ellipsoid method is selected because the principal inertial axes are governed by an objects shape and mass distribution, and therefore is able to incorporate irregular rock-shapes into the classification where mass is unevenly distributed due to void space. Additionally, the inertial axes I and rotational velocity Ω about this axis determine the angular kinetic energy T (Eq. 3.14),

$$T = \frac{1}{2} I \Omega^2, \tag{2.11}$$

and angular momentum of a rock-body, and therefore an element of the kinetic behaviour is integrated into the classification. Finally, using this method eliminates the inherent ambiguity associated with selecting the geometric axis of a particle (Blott and Pye, 2008).

The moment of inertia quantifies a body's resistance to change in angular velocity about an arbitrary rotation axis. For a point mass m rotating at a distance r about an axis the moment of inertia is given as:

$$I = mr^2 \tag{2.12}$$

I reflects the mass distribution about an axis of rotation. It is important to note that rotations about different axes within the same body yields different inertial moments. For an arbitrary shaped body, I is calculated by summing I of the mass distributed about the rotation axis (Eq. 2.13),

$$I = \sum_{i=1}^{n} m_i r_i^2. \tag{2.13}$$

Conceptually this can be thought of as an assemblage of mass points about the rotation axis.

The principal inertial axes are the three orthogonal axes that pass through a body's centre of mass and about which rotation takes place. The rotations about the axes of maximum, and minimum moments of inertia are dynamically stable. This meaning, any small perturbation of the body's rotation about this axis is not amplified through time; whilst the rotation about the axis of intermediate moment of inertia is unstable, and perturbations are amplified (Figure. 2.20). In an experiment conducted in space Pettit (2009) demonstrates the stability of rotations of rigid bodies.

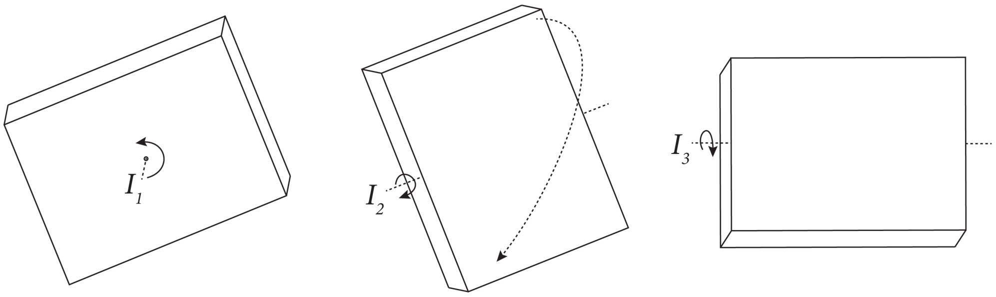

FIGURE 2.20: Sketch showing rotation about I_1 and I_3 are stable, while rotation about I_2 is unstable; its rotation axis oscillates causing the body to flip during rotation. The dotted arrow illustrates one case how the body would flip during rotation. For a video example of this behaviour see Pettit (2009).

With the principal inertial axes, the half-axis lengths a,b and c of the equivalent inertial ellipsoid E are calculated using the mass m and the principal inertial axes I as follows:

$$\begin{aligned} E_a &= \sqrt{(\frac{5}{2m}(I_2 + I_3 - I_1)} \\ E_b &= \sqrt{(\frac{5}{2m}(I_1 + I_3 - I_2)} \\ E_c &= \sqrt{(\frac{5}{2m}(I_1 + I_2 - I_3)}. \end{aligned} \tag{2.14}$$

2.3.7 Angularity and sphericity

The exterior morphology of a rock particle can be described as being angular, rounded or having sphericity. In rockfall, Bourrier (2008) investigate the angularity of particles, investigating how this influences the rebound properties. The quality of sphericity Ψ (2.15), is defined as (see Wadell, 1935):

$$\Psi = \frac{\pi^{\frac{1}{3}}(6V_p)^{\frac{2}{3}}}{A_p}, \tag{2.15}$$

where V_p is the particle volume and A_p the surface area of the particle. The parameter quantifies the departure of a particle from a sphere by taking the ratio between the area of the particle and the smallest enclosing sphere. If this is performed in three dimensions, then the measure includes a degree of angularity. A particles angularity is not the same as its sphericity, as shown graphically in Figure, 2.21. In effect the measure of sphericity if applied in three dimensions offers a crossover between rock *form* and *angularity*.

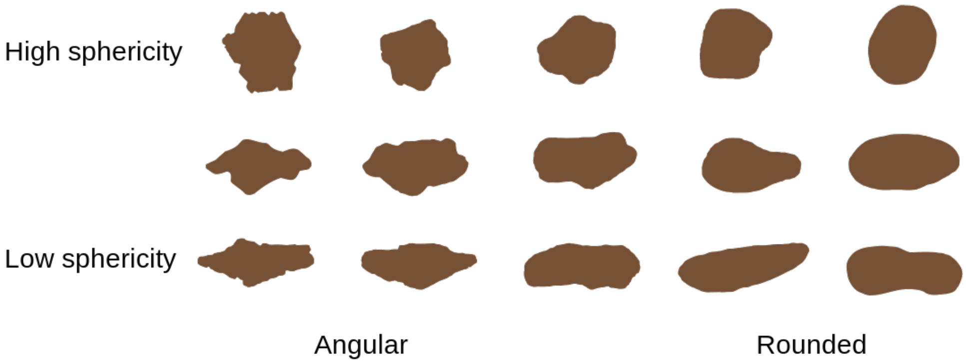

FIGURE 2.21: Graphical identification chart for granular particles angularity and sphericity.

Angularity considers the morphology of edge and corner points of the body. Blott and Pye (2008) summarise a number of techniques for measuring particle angularity and propose a new method. The methods use either ratios between enclosing circles or smallest fitting circles inside the edge and corner points, or angles between corner points (Figure. 2.22).

There has been little research in rockfall which has considered particle sphericity or angularity. The morphology of a rock particle has the potential to influence the impact configuration of rock-ground impacts. For example well rounded rocks have the potential to roll more eaisly than more angular rocks. This was shown by Erismann and Abele (2001), who related the number of facets of a shape to the slope angle at which rolling commenced.

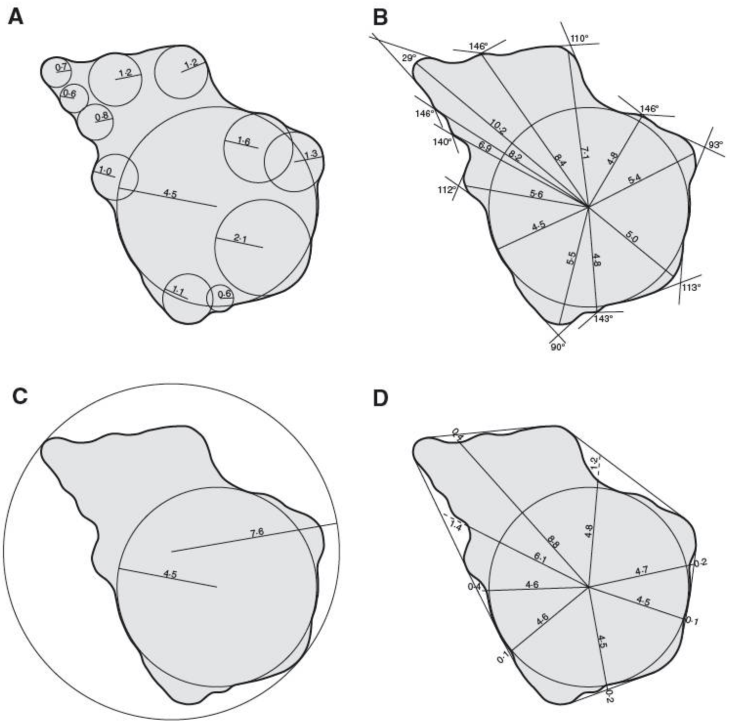

FIGURE 2.22: *A*, depicts Wadell (1935) method of measuring a particles roundness; *B* a measure of angularity proposed by citeLees1964; *C* the method of Riley (1941) to measure circularity; and *D* depicts Blott and Pye (2008) method of measuring a particles irregularity. The figure is taken from Blott and Pye (2008).

2.4 Studies on the motion of complex shapes

The main features of rockfalls are a series of ballistic trajectories in the air that are punctuated by ground contacts which can be momentary percussions, or longer sliding and rolling phases. Such behaviour is common to almost all sporting activities involving a ball or projectile. Similarly studies of bomb and missile ballistics draws parrallels, but generally without multiple ground contacts. The following section illustrates research from these areas investigating the dynamics of objects in flight and at impact, making comparison literature in rockfall and discussing the implications of this research for rockfalls. This highlights some of the emerging techniques in the measurement of a body's dynamics, and finally focuses on studies in rockfall which have specifically dealt with a rock's dynamics.

2.4.1 Ballistics

In missile and bomb design, ballistics plays a key role in assessing a projectile's trajectory, especially for re-entry ballistic bodies. Mostly design deals with stabilising a body and concerns problems in aerodynamics, rotational motions and roll effects (Platus, 1970, Garber, 1959, Glover, 1965). One case, however, has provided interesting insights into spinning bodies during impacts, and is probably the only case of a bomb involving multiple surface impacts before detonation, akin to rockfall. Wallis (1942b) was the inventor of the 'bouncing bomb' designed to attack large hydroelectric dams in Germany at the end of the war in 1943. The bomb design involved releasing a bomb from an aircraft that could bounce and skip over the water's surface to its target (Figure. 2.24).

The biggest challenge that Wallis (1942b) faced was achieving sufficient range of the bomb whilst bouncing over the water. Many scaled experiments were conducted in the laboratory over a tank of water, and later at full scale from a Wellington bomber onto reservoirs. Wallis (1943b, 1942a) investigated the coefficients of angular and velocity restitution for spheres and cylinders on water, finding that an angle less than 7° is required to produce a ricochet on water.

FIGURE 2.23: Upkeep bouncing bomb designs held at the Imperial War Museum Duxford. On the *left* is the spherical bomb design, and the *right* is the cylindrical bomb first designed by Sir Barnes Wallis in April 1942, they were manufactured by Vickers-Armstrongs and produced in February 1943.

Different bomb shapes were tested including a sphere and a cylinder (Figure. 2.23). It was observed that the ability of the bomb to bounce on water was improved if a rotation was imparted to the body prior to release. This created a laminar layer of air on the bomb surface which acted as a boundary between the water assisting the rebound during impact. It was found that the bomb range was independent of angular velocity, however, the angular momentum had to be sufficient to maintain rebound properties over the required range to the target. This lead to the selection of a cylindrical bomb shape (Figure. 2.23) as it had a greater angular inertia compared to the sphere and could better maintain the rotational speed required, in addition to being more stable over choppy water (Wallis, 1944, 1943a). A backwards spin was selected because this helped to keep the bomb behind the aircraft after release, preventing dangerous back-splash from hitting aircraft, in addition to preventing it from moving away from the target wall as it sank. The experimentation enabled the correct air speed (220 mph, 354 $km \cdot h^{-1}$), rotational velocity and release height (60 ft, 18.2 m) of the bomb to be selected for the desired range (425 yds, 389 m). The project lead to the successful bombing of the Möhne and the Eder dams, two key hydroelectric facilities in Germany, in May 1943.

Another challenge faced by Wallis was in capturing the projectile velocities before and after impact on water without the use of video cameras. Wallis' method calculated velocities based on the parabolic trajectory taken between impacts, measuring their geometry by placing aluminium power on the water's surface to capture the bounce distances. The bounce heights were measured by an observer reading off a gridded background. This eliminated the requirement for costly photography.

Wallis' experiments in the development of the bouncing bomb illustrate an important point about rotational stability of bodies during impacts related to their shape and mass distribution. He demonstrated that the angular momentum of a body plays an important role for continued stability after an impact. For rockfalls it implies that if rock bodies with large moments of inertia are able to gain sufficient angular momentum, then rotation and runout could continue over long distances without being perturbed by terrain irregularities.

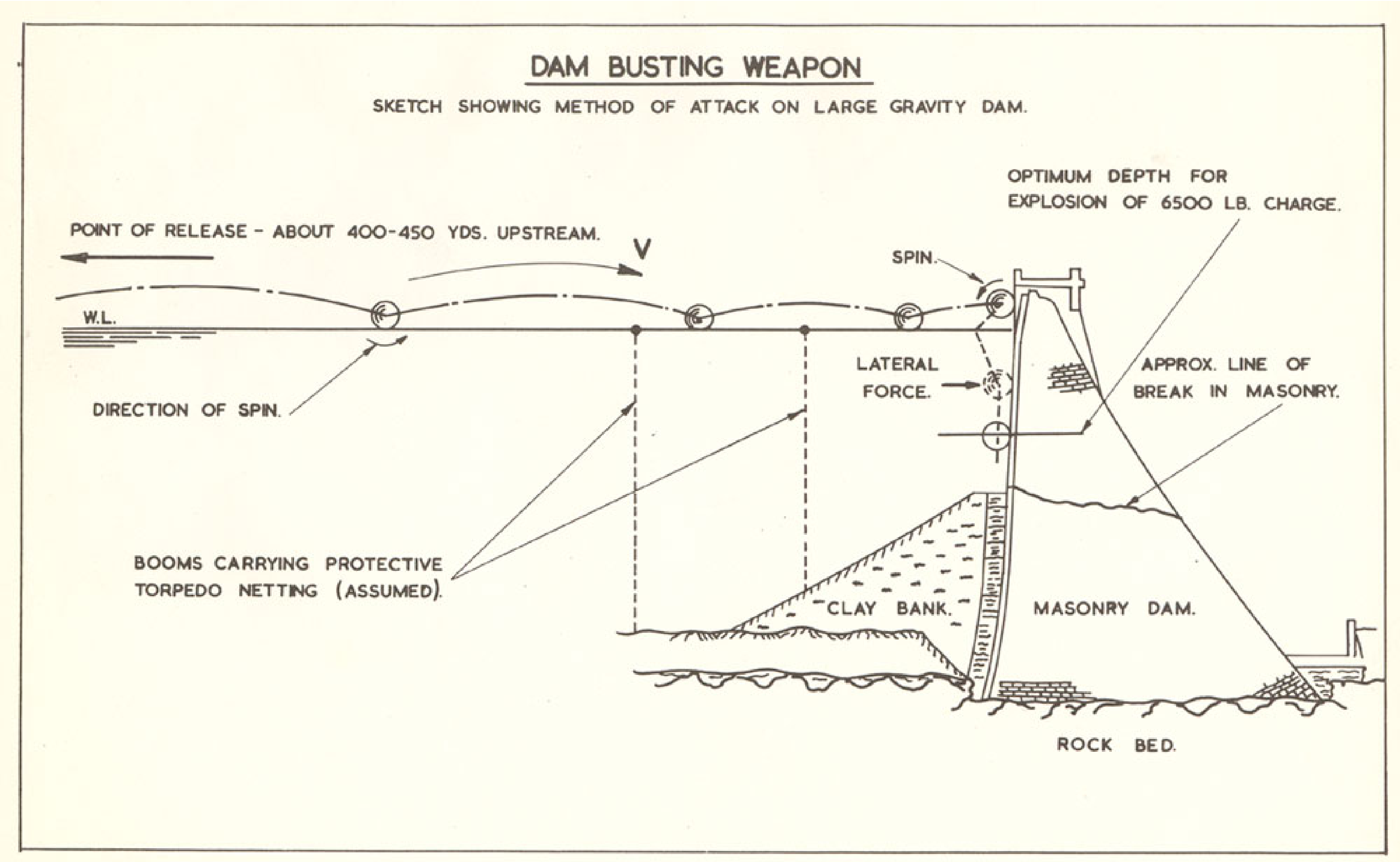

Figure 2.24: Diagram showing the proposed method of attacking the German dams using the bouncing bomb, copied with the permission of British Library.

2.4.2 Sporting balls

In sport, studies of motion and impact are closely related to rockfalls. Research can be separated into ballistic trajectories and impacts.

The trajectory phase in sport is used to deceive the opponent by creating an unpredictable movement in the air. This concerns the aerodynamic properties of the body, whereby a common effect exploited by sports players is the Magnus effect (Magnus, 1852) in which air flow that develops either side of a ball cause it to deviate or swing in flight. Rayleigh (1877) documented the effect in tennis generated due to the ball spin; also in football, players induce a high spin rate to the ball (up to 240 rad·s $^{-1}$) causing it to swerve and confuse the goalkeeper (Craig et al., 2006). In cricket the air turbulence to induce a swing on the ball is generated by the seam of the ball. The spin placed on the cricket ball is simply used to set the pitch angle of the seam in flight. Mehta (2005) finds that a seam angle of 20° produces the most swing on the cricket ball, and Lock et al. (2010) documents the dynamics of a reverse swing.

For rockfall, the mass, shape and nominal rotational velocities of between 15 rad·s^{-1} and 52 rad·s^{-1} (Spadari et al., 2012) render the aerodynamic effects such as Magnus forces negligible. Often a rock's rotational component during flight phases is generalised, assuming it to remain constant (Giani, 1992). The idea of rotational stability as was investigated by Wallis (1944), in addition to the decay of angular velocity during the trajectory phase of a rockfall. The latter was investigated for sports balls by James and Haake (2008) using high speed video analysis, suggesting that the decay of a ball's spin is attributed to the aerodynamic drag related to material on a ball's surface, and mostly due to the inertial affects of different balls. Fuss et al. (2012) measured the effects of spin decay using an instrumented cricket ball, with 3-D gyroscopes measuring up to ± 350 rad·s^{-1} at 500 Hz. Releasing cricket balls between 60 rad·s^{-1} and 120 rad·s^{-1} they were able to record rates of spin decay between 0.013 rad·s^{-2} and 3.670 rad·s^{-2}. It is noted that this was for a cricket balls sized sphere and it is to be expected that such spin decay has a greater effect than for bodies of greater mass such as rockfall.

Fuss et al. (2012) observed a tendency for a cricket ball to move from rotations about the axis perpendicular to the ball's seam towards the rotational axis that lies parallel to the seam. Another example of this is the classic boiled egg experiment in which if an egg is spun on its side with sufficient rotational speed it will stand up to spin vertically, in doing so raising its centre of mass (Moffatt and Shimomura, 2002). This effect occurs due to the interplay of gyroscopic and frictional forces. In rockfall the transition between axes of rotation becomes important during flight as this would consume energy due to the imbalance of rotations. Moreover, the rotation of a rock body about a given axis can tend towards another because it is unstable, leading to a complex impact configuration that compounds this perturbation. For example, Pfeiffer and Bowen (1989) suggest that it is the transitions between modes of motion that lead to the dispersive nature of rockfalls and divergent trajectories. Although there is little quantitative evidence of this in rockfall literature, it is suggested that this transition occurs due to the rotational decay of a rock-body as it slows to a halt, and can often explain the 'curved hook-shaped' trajectories at the very end of a rockfall runout path. This feature of rockfall is investigated in the laboratory experiments in Chapter 4.

2.4.3 Measurement techniques

Fuss et al. (2012) highlighted the emergent trend of embedded micro-sensor technology for the study of particle dynamics. Similar micro-sensor technology was applied by King. et al. (2011) studying bowling ball dynamics, and McGinnis and Perkins (2012) in the study of the release characteristics of a base ball. In both cases micro 3-D gyroscopes and accelerometers imbedded in the balls were used to resolve the ball's velocity vector and rotations. In this study similar technology has been employed to study the dynamics of rockfalls.

Before this technology was readily available, the motions of objects were recorded with high speed video cameras and motion tracking algorithms, both in sport (Cross, 2002, James and Haake, 2008), and in rockfall (Bourrier et al., 2012, Dewez et al., 2011). Video analysis has the advantage of being able to resolve the two-dimensional and, in some cases (Dewez et al., 2011), the three-dimensional translational velocities of objects, and at frame rates over 1000 frames per second, highly detailed insights into the process can be gained. It is also possible to resolve an object's 3-D velocity vector using accelerometers and integrating the accelerations (McGinnis and Perkins, 2012). However, this method is renowned to accumulate an "integration" drift, especially when handling the complex motions of an impact (Volkwein et al., 2006). McGinnis and Perkins (2012) compared their results from 3-D acceleration sensors to advanced motion tracking technology and find their results are within 3% error of the video analysis, which in its self is subject to error. In fact the error of plotting an objects centre of mass is a common problem for video motion tracking, which is then compounded if differentiated to resolve velocity. Most researchers address this by decomposing the horizontal and vertical components of a trajectory and fit a quadratic curve to the data to account for gravity (Bourrier et al., 2012, Cross, 2002, Dewez et al., 2011). The time and effort involved in video analysis is enormous, as although there are tracking algorithms to plot a body's centre of mass this often has to be corrected by hand (Cross, 2002). Carré et al. (1999) address the issue of large data sets and the processing time by using stroboscopic photography to capture the entire motions of a ball impact in a single image. Each method has advantages and disadvantages, and with a combination of methods in physical experiments it is now possible to capture most of the dynamics of a process. With the limitations and effort involved it is clear to understand how the addition of numerical modelling can assist in gaining insights into the full three-dimensional dynamics of rockfall.

2.4.4 Ball impacts

Impacts are of primary interest for sporting games. Rebounds are also approximated by means of restitution coefficients (see Chapter 1). Many studies have placed effort into characterising restitution coefficients of objects in sport (Carré et al., 2006, Cross, 2002, 1999, 2010, Haron and Ismail, 2012) and in rockfall. In sport there are even standard restitution coefficients stipulated for ball manufacture, for example, tennis balls must exhibit a normal restitution coefficient of 0.74 ± 2.3% when dropped from 2.54 m (Cross, 1999). What is readily recognised in sporting literature is the dependency of restitution coefficients on not only different terrain surfaces (Carré et al., 2006), but in addition to the dynamics of an impact and its configuration. These are the parameters which sports persons can influence. It is commonly known that balls show a reduction in the normal restitution coefficient with increasing velocity of impact (Haron and Ismail, 2012).

Cross (1999) and Carré et al. (2004) considered the impact force evolution and respective ball deformation that occurs during impact, plotting force deformation hysteresis curves. Cross (1999) investigated a range of balls finding that tennis balls have a stiffer initial force at contact that softens during the impact and that rebound occurs still with a compressed ball. They go on to suggest that the major energy loss occurs during the compression of the ball rather than the rebound. In fact to increase the rebound speed of a tennis ball from the racket, a lower tension should be selected as this prevents over compression of the tennis ball which dissipates greater energy (Cross, 2000). In similar tests on a cricket ball Carré et al. (2004) find a disparity in the dynamic force displacement curves in accordance with the orientation of the cricket ball at impact, where impacts on the seam result in more ball deformation and consequently dissipate more energy. This is related to the orientation of the internal ball structure with respect to the impact force. This disparity has implications for rebound angle, velocity and spin of the cricket ball.

As in rockfall, the interaction of a body and ground is recognised as significant but complex. Sporting literature offers an insight into this behaviour, because the influence is more evident and of greater importance for the outcome of a game. In a study by Carré et al. (1999) different sports surfaces were investigated on the outcome of cricket ball impacts. Using stroboscopic imagery different types of soil and grass combinations of cricket pitches were tested. The non-linear deformation behaviour of both the ball and the soil were non-intuitive characteristics of the impacts. Given similar initial impact conditions, the authors find that both hard and soft ground surfaces produce high rebounds. This is explained with the hard and dry pitch having a high restitution coefficient, while the damp soft pitch is much more compliant during impact and the deformation creates a crater geometry which provides a ramp for the ball generating a similarly high rebound as the hard pitch. The rebound speeds are, however, faster for the hard pitch and slower for the soft.

A similar effect is suggested by Cross (2002) investigating the rebound properties of a tennis ball and an extreemly bouncy toy ball known as a super-ball. Cross (2002) examines inclined 20° inclined impacts of balls both with top and back spin, and without spin. Cross (2002) notes that in tennis ball ground impacts that commonly occur under 20° will involve sliding through the impact before obtaining grip and rebounding. Where top spin is imparted to the ball, this aids rolling and improves grip through the impact respectively increasing the restitution coefficient causing the ball to bounce even higher. This is exploited by tennis players to deliver a service with a high bounce. The difference is noticed between the average service velocity at Wimbledon (185 $km \cdot h^{-1}$) and the French open (160 $km \cdot h^{-1}$), played on a grippy grass court and a soft slippy clay court respectively (Cross, 2002). This is because of the lower friction clay surface at the

French open, players sacrifice service speed to apply a top spin to the ball which aids grip and generates a higher bounce. Additionally on the clay courts, there is a noticeable ploughing of material in front of the ball generating a small ramp adding to rebound height as is also observed by Carré et al. (1999). In rockfall this effect is even more evident with the impact scars that plough into the surface terrain (Figure. 2.7), and has been discussed in (Section. 2.2).

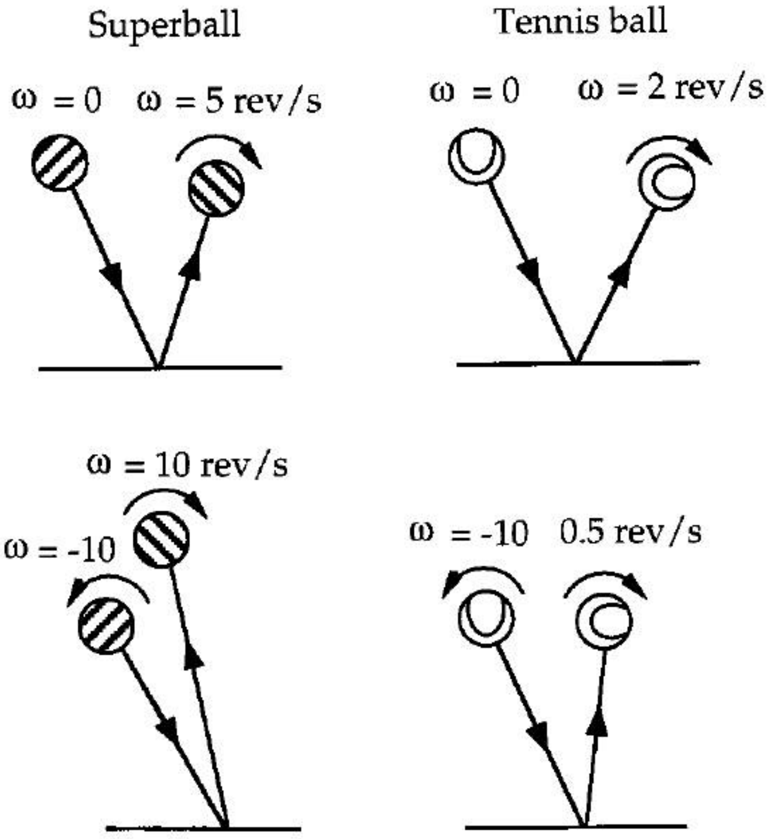

FIGURE 2.25: Sketched image of ball impacts in which the direction of rotation is reversed, from Cross (2002).

Not only is the deformation behaviour of the ground important during an impact, the rotational dynamics at impact are also fundamental to the outcome of an impact. The influence of a balls spin on a rebound is well known in sport and a desired property to impart to a ball. Cross (2000) note that with increasing friction, greater spin can be generated on a ball. Nicolaides et al. (2013) study the effects of stringing pattern on a tennis racket's ability to impart spin to the ball, finding that by decreasing the number of cross strings, top spin could be dramatically increased from 117 - 170 rad·s^{-1}. For rockfalls the concept of available friction comes in the form of the roughness that a rock will encounter during runout, mainly due to terrain roughness (Bourrier, 2008), but also related to a rocks angularity.

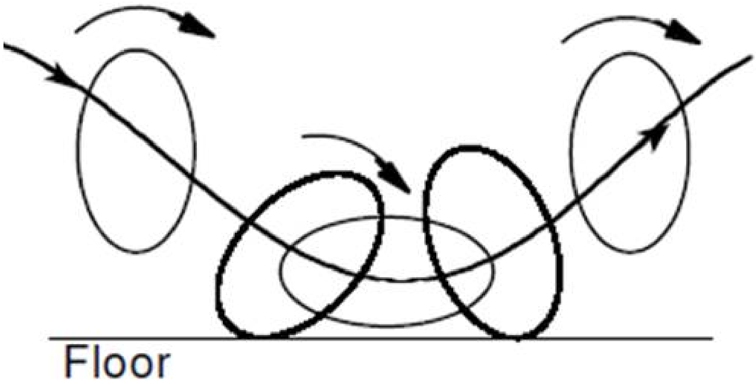

Figure 2.26: Sketched sequence image of an oval shaped ball impacting a flat surface, from Cross (2010).

Some important effects of spin are observed by Cross (2002) who document that a ball impacting a surface at 20° without spin will rebound with forward spin. The same impact with backspin on the ball will cause the ball to bounce backwards but will reverse the direction of the initial spin (Figure. 2.25). Cross (2010) took this further in one of the only studies investigating the bounce behaviour of oval shaped balls, such as a rugby ball. He demonstrates how the bounce of an oval ball is less predictable because the normal reaction force can act ahead or behind the centre of the ball (Figure. 2.26). Cross (2010) finds that the ball bounces backwards if the impact occurs without spin and if the top end of the ball points backwards on impact. If impact occurs mostly with top spin, the oval ball bounces forwards and often with a bounce height higher than normal. This is also reflected in a measured restitution coefficient that is greater than unity, as is also reported in the rockfall literature (Bourrier et al., 2012, Buzzi et al., 2012). Additionally it could be observed that the horizontal speed of the ball could also be larger than before the bounce; as reflected in a reversal of the friction force, captured by a force plate, due to the spin direction. With respect to rockfalls, these observations of the behaviour of sporting balls with spin and impact configuration provide strong evidence that different rock shapes in combination with spin can have varied rebound characteristics.

2.5 Modelling rockfalls

The task of modelling rockfall has the ultimate goal of generating rockfall susceptibility and hazard intensity maps (Baillifard et al., 2003, Chau et al., 2003, Frattini et al., 2008, Santi et al., 2009), and are strongly based on trajectory modelling (Dorren, 2003). The quality, reliability and detail of the information available on such models are greatly dependant on the type of model and indeed the complexity with which the rockfall runout process is modelled.

2.5.1 Numerical modelling of rockfalls

In recent years with the advancement of rockfall protection design and a lower acceptance of risk among people visiting rockfall affected areas (Rheinberger, 2011), there is an increasing demand for three-dimensional rockfall simulations that deliver probabilistic data including complete information on a rock's dynamics. The range of rockfall models span a board spectrum, including:

i) how rockfall is modelled spatially,

ii) how the rock is represented in the simulation domain and numerically modelled,

iii) how the contact is modelled.

These models can be divided into categories of how rockfall is modelled spatially. These are *horizontal* two-dimensional (2-D), a *vertical* two-dimensional (2-D) approach, a combination of the latter two methods forms a 2.5D approach, and 3-D simulations.

2.5.2 2-D rockfall models

The simplest approach in rockfall modelling is the *horizontal* 2-D approach in which the potential rockfall inundation area is estimated by assuming a uniform friction for the hazard zone, and is performed in one of two ways. One method is to assume that the rock only slides. This involves performing a regional topographic-hydrological analysis of an area assuming a sliding friction. This uses nearest neighbour analysis performed using geographical information systems GIS (Van Dijke and van Westen, 1990). This approach finds the path of steepest decent over terrain from the source zone. The second approach is the rockfall energy line method, known as either the *Fahrböushung* (travel angle) (Heim, 1932), which the methodology was further adapted in the *shadow angle* method (Evans and Hungr, 1993). These methods project a line from the rockfall source zone to the farthest deposits (Figure. 2.1). The Fahrböushung takes the start point from the top of a rockfall source zone, while the shadow angle method projects the line from the base, and takes into account the assumption that rockfalls lose 75-85% of their energy during the first impact with the slope. The angle of the line is taken with respect to horizontal and is most commonly selected based on documented boulder runout lengths at the site (Hungr and Evans, 1988, Holm and Jakob, 2009). Additional information about the expected kinetic energy across the shadow angle area can also be predicted by using the potential height between the topography and the energy line (Erismann and Abele, 2001) (Figure. 2.1). The *horizontal* 2-D methods have the advantage of being able to make a broad scale and quick assessment of rockfall hazards, and is easily implemented using GIS. There are also models which offer this as a separate software (i.e. ConeFall (Jaboyedoff and Labiouse, 2011)).

The second approach is to perform rockfall simulation along a 2-D *vertical* topographic profile (Spang and Sönser, 1995), commonly selected as the path of steepest decent (Van Dijke and van Westen, 1990) or a user defined slope profile, on which a series of ground impacts and their flight phases are modelled. There are a number of rockfall models adopting the *vertical* 2-D approach which are listed in Table 2.1. The differences between them are reflected in their approach to modelling the rock-ground impact. This approach is limited in predicting the lateral spread of rockfalls. However runout distances, jump heights, translational velocities and in some cases angular velocity and contact forces can be computed for a 2-D profile.

2.5.3 2.5-D rockfall models

The 2.5-D approach is essentially the combination of the *horizontal* and *vertical* 2-D modelling methods. Firstly *horizontal* 2-D modelling is performed to define the path of steepest decent generating the 2-D vertical profiles for the trajectory modelling; an example of this is Rocky3 (Dorren and Seijmonsbergen, 2003). These approaches all provide some information of a rock's kinematics across the spreading area. They do not however account for the potential of a rock to deviate from its course due to terrain morphology or rock-shape, and as such do not account for lateral spreading.

2.5.4 3-D rockfall models

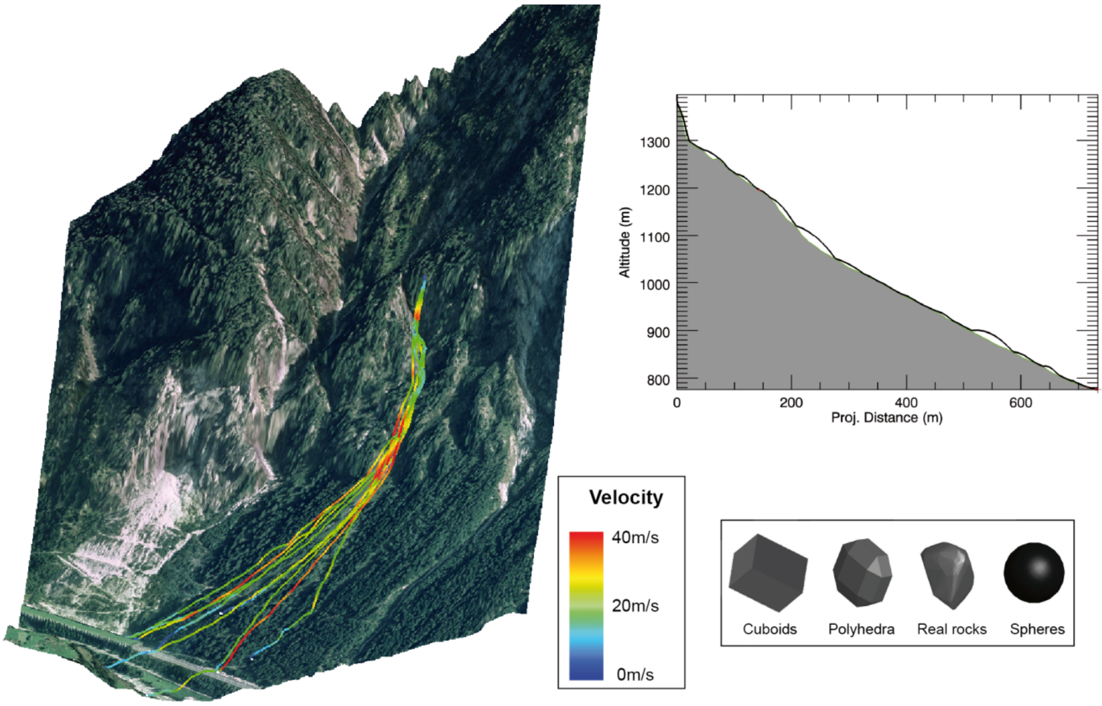

FIGURE 2.27: Three-Dimensional rockfall model. RAMMS::Rockfall, Leine et al. (2014).

Three-dimensional (3-D) rockfall models compute the rock position vector in three dimensions with varying degrees of detail. The main advantage over 2-D approaches is that 3-D models are able (to a greater or lesser degree) to account for the effects of terrain morphology and can compute trajectory deviations. A full list of rockfall models and their capabilities, updated from Volkwein et al. (2011), is given in Table 2.1. The main differences in both 2-D and 3-D approaches can be noted in how the rock is modelled (Figure. 2.27).

1. Point-mass models consider the entire rock-body as a point-like particle. These models neglect the rock geometry and the energy interchange between angular and translational velocity. The kinematic information computed include position and translational velocity vectors.

2. Sphere models consider a rock block as a rigid sphere with a set radius. This permits the blocks mass and moment of inertia to be computed along with position, translational

and angular velocity vector. A problem with using spheres is that they will roll on all inclined surfaces, and as such often over predict runout and must therefore be stopped with threshold values.

3. Rigid-body models allow a geometry to be given to the rock, this can be a simple rectangular block, ellipsoids or arbitrary polyhedra. The body is given a mass for which the centre of mass is tracked in relation to the body and its inertia tensor. This method allows the position vector of the modelled rock to be resolved along with its orientation, which is commonly described with a quaternion, Thus a position, translational and angular velocity vectors are given. This approach permits full gyroscopic forces to be considered and enables the forces to be calculated at explicit contact points on the rock-body. This enables the study of the influence of rock geometry on runout characteristics. The rock is considered rigid and indestructible. Therefore, the effects of fragmentation and the body's deformation due to the applied forces are not accounted for. However, the approach is more numerically efficient than discrete element methods, and along with the advance of personal computers, calculation times can be under 1 second per trajectory.

4. Discrete element methods, model a rock-body as a collection of small spheres or mass-points which are connected by elastic elements. In this way deformations of the body can be predicted, providing criterion to break and fragment.

Table 2.1: Summary of rockfall models available to perform rockfall trajectory analysis. The models are classified according to their approach to modelling the impact and the rock along with the dimensions with which they simulate rockfall.

Rockfall model	Reference	Rock model	Impact model	Probabalistic	Forest
3-D	**(x,y,z)**				
RockFall Analyst	Lan et al. (2007)	Lumped-mass	Rebound (ε_N, ε_T)	partly	no
STONE	Guzzetti et al. (2002)	Lumped-mass	Rebound (ε_N, ε_T)	yes	no
3-D-GEOTEST-Zinggeler	Zinggeler and Pfeifer (2009)	Hybrid	Rebound (ε_N, ε_T)	yes	yes
HY-STONE	Crosta et al. (2004)	Hybrid	Rebound (ε_N, ε_T)	yes	yes
RockyFor3-D	Dorren (2010)	Hybrid	Rebound (ε_N, ε_T)	yes	yes
EBOUL-LMR	Descoeudres and Zimmermann (1987)	Rigid-body (simple shapes)	Hard contact	no	no
STAR 3-D	Dimnet (2002)	Rigid-body (simple shapes)	Hard contact	no	yes
Trajec3D	Basson (2012)	Rigid-body (simple shapes)	Hard contact	yes	yes
CRSP-3D	Andrew et al. (2012)	Discrete Element Method	Visco-elastic	yes	yes
RAMMS:Rockfall	Leine et al. (2014)	Rigid-body (arbitrary polyhedra)	Hard contact	yes	yes
2.5-D	**(x.y coupled slope profile)**				
Rocky3	Dorren and Seijmonsbergen (2003)	Hybrid	Rebound (ε_N, ε_T)	yes	yes
2-D	**(slope profile)**				
PROPAG/CETE Lyon	Rochet (1987)	Lumped-mass	Rebound (ε_N, ε_T)	no	no
ROCKSIM	Wu (1985)	Lumped-mass	Rebound (ε_N, ε_T)	yes	no
Rocfall	Stevens (1998)	Lumped-mass	Rebound (ε_N, ε_T)	yes	no
CADMA	Azzoni et al. (1995)	Hybrid	Rebound (ε_N, ε_T)	yes	no
SASS	Bozzolo and Pamini (1986)	Hybrid	Hard contact	yes	no
Rockfall (Dr. Spang)	Spang and Sönser (1995)	Rigid-body (simple 2-D shapes)	Hard contact	yes	yes
Discrete Element Method	Cundall (1971)	Rigid-body (simple 2-D shapes)	Hard contact	no	no

2.6 Rockfall protection structures

Rockfall protection structures are an essential tool to mitigate rockfall hazard. Since some of the early works on the processes of rockfall and protection structure design (Ritchie, 1963), attempts have been made to provide engineers with rock slope specific design guidelines for protection measures. The variety in rockfall protection solutions available are typically designed with the purpose of halting or deflecting rockfall from its path, and to withstand the expected or modelled impact energy (ASTRA, 1998) derived from rockfall modelling (Figure. 2.28).

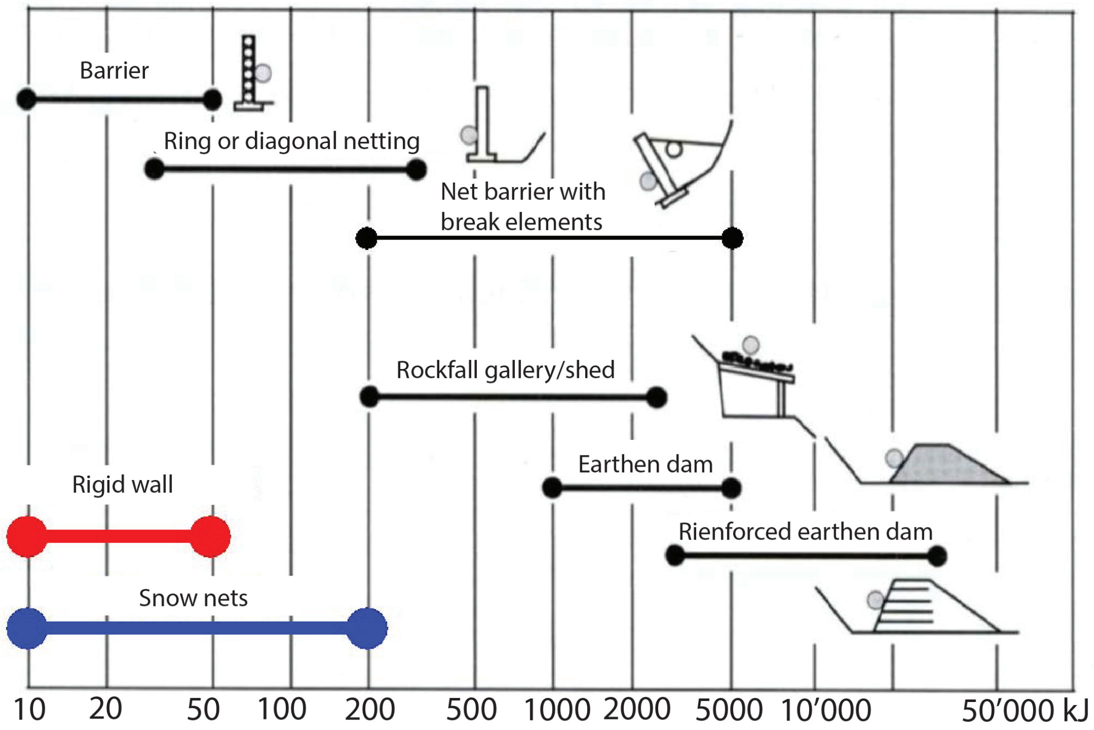

Figure 2.28: Rockfall barrier systems and their energy rating (ASTRA, 1998).

2.6.1 Rockfall barriers

Rockfall barriers are structures made of steel wire netting supported by posts and foundations. Nets are suspended with guide ropes which contain brake elements which plastically deform under load along with the netting. Through this process the impulsive forces of rockfall can be spread over time and reduce the loads in the retaining structure. Such approaches are widely applied as standard rockfall mitigation measures.

FIGURE 2.29: Flexible rockfall barrier system made of high tensile steel wire netting being impacted by a rock. Photo: Gerber, 1996.

Rockfall netting design is supported by rigorous testing procedures and guidelines for their construction (EOTA, 2008, Gerber, 2001). While the testing of rockfall barrier systems is restricted to a standardised rock-shape (Figure. 2.13), this standardisation omits the possibility to observe the effects of angular sharp rocks which would deliver a much greater punctual loading that has yet to be fully investigated.

2.6.2 Rockfall attenuator systems

A growing market in a rockfall protection solution is known as rockfall 'attenuators', that utilise flexible steel wire nets draped over the slope with a top-opening designed to intercept, guide, and attenuate the kinetic motion of rockfall (Glover et al., 2012), (see Figure 2.30). These systems are an attractive solution to mitigating rockfalls because they guide rocks to the base of a rock slope allowing rockfall to be collected at the road side with out the requirement for rebuilding.

During full-scale testing of these systems Glover et al. (2010) found that the rock-shape plays a critical role in the attenuating effect of these systems. Sharp angular rocks are shown to become caught in the meshing structure and can lead to tangling of the rocks in the netting. For larger rocks with high angular velocity, this can lead to sever lacerations to the netting structure. Thus, both the shape and the dynamics of a rock at impact are of crucial importance to mitigation design (Glover et al., 2012).

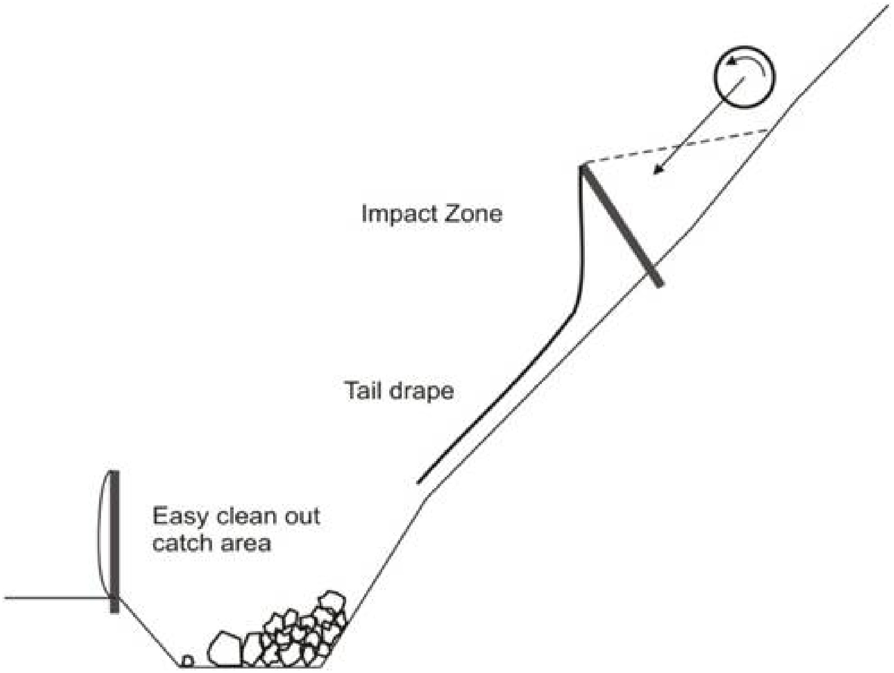

Figure 2.30: Sketch drawing of a rockfall attenuator system showing the impacting rock that is caught in the net opening. The rock's dynamics are then attenuated by the draped netting that lies on the slope, guiding the rock into an easy clean out ditch.

2.6.3 Rockfall embankments

Rockfall embankments are categorised into structures which are comprised of piled up earth and those which are reinforced. These systems are designed to absorb rockfall impacts through the plastic deformation of the construction materials and impounding. Lambert and Bourrier (2013) provide an overview of their design and testing procedures. Again, an issue with the testing approach of rockfall embankments is that the loading involved single punctual impacts with regular shaped bodies, which have often been accelerated on a pendulum or zip-line to the point of impact with the embankment. This approach has neglected the effects of sharp angular rocks and the rotational dynamics. The rotational behaviour is of importance because it gives the rocks the potential to roll up and over the embankment (Lambert et al., 2013).

The role of rock-shape in the design of rockfall protection structure is of key importance. Rock-shape is important as it defines the distribution of forces of impacts into rockfall protection structures. While the rotational dynamics are of importance in defining the interaction behaviour for embankments which can lead to rock-rolling over the structures, or in rockfall systems using nets rocks can become tangled. An understanding of the runout dynamics of rockfalls according to shape can therefore assist with the task of improving rockfall mitigation structure design.

2.7 Summary

The central theme of rock-shape exists throughout the rockfall process, starting with the geological release characteristics, through the detailed runout dynamics to the deposit zones. This has implications for the prediction and assessment of rock mass failure, the modelling and hazard assessment of rockfall runout paths, and the influence on deposit patterns and the design of rockfall mitigation measures. The following key points have been highlighted:

- Rock-shape is rooted in the characteristics of a rock mass, where the shape, size and failure mechanisms and release orientation of detachable rocks are predetermined by discontinuities (Jaboyedoff, 2011, Lambert and Nicot, 2011) which reflect characteristic geological settings (Fityus et al., 2013).

- Rock-shape classifiers, form, angularity, and sphericity is important to distinguish the features of possible rock shapes. Combining the rock form classifier of Sneed and Folk (1958) with a measure if the equivalent inertial ellipsoid (Wang et al., 2007) allows an inclusion of the properties important for dynamics into shape classification. Changes in form have the potential to influence the inertial properties of a rock and consequently rotational behaviour (e.g. Pettit, 2009). In particular shape has the potential to store angular momentum to maintain stability (e.g. Wallis, 1944).

- The measurement of particle motion with the use of videogrammetry, while possible to capture three-dimensional trajectories (e.g. Dewez et al., 2011), is thwart with practical difficulties (Cross, 2002), even more so when attempting to capture the rotations of a body. A new emerging micro technology (e.g. King. et al., 2011) offers the potential for high-resolution data of dynamic impacts and rotation behaviour.

- Rebound behaviour of rock-ground impacts has been documented to produce *extreme* values of restitution (Buzzi et al., 2012). The number of spatial variables that influence rock-ground rebounds (Volkwein et al., 2011) are a potential source for such *extremes*. When considering the definition of restitution coefficients are measured from the rock body's centre of mass, the effects of rock-shape are lost.

- During the runout of rocks over terrain it is suggested that the transition states between modes of motion are responsible for the dispersive nature of rockfalls (Pfeiffer and Bowen, 1989).
- Numerical models employing a rebound model with restitution coefficients (e.g. Spang and Sönser, 1995) are limited in their approach to capture full dynamics of rockfall runout behaviour and have to rely on threshold values to define transitions between modes of rockfall motion (e.g. Crosta et al., 2004) and treat impact condition stochastically (Bourrier et al., 2009b). Rigid-body dynamics offers a method to simulate the full dynamics of a rock body during ballistic trajectory and impact (Leine et al., 2014).

The following chapter presents the methods and experimental design applied to address the research aims highlighted in this literature review and set out in Chapter 1.

Chapter 3

Methods

Rockfall occurs with sufficient frequency and magnitude to pose a threat to buildings and infrastructure the world over. However, the natural occurrence of rockfall is a highly variable process that within the time scale of this research is sporadic, and renders the live study of rockfall purely a qualitative task if attempting to generate sufficient data to quantify rockfall runout behaviour according to shape. The following methods described in this chapter were applied to address the research goals set out in chapter 1 in which qualitative observations of live rockfalls have guided the experimental design to quantify rockfall runout with sufficient detail to characterise its behaviour according to rock-shape.

3.1 Experimental design

The experimental design of this research was to isolate the role of rock-shape in rockfall runout dynamics from the large number of additional influencing parameters (e.g. terrain morphology and material properties). To move beyond sporadic observations of rockfall and quantify the role of rock-shape in rockfall runout, the experimental approach had to be repeatable. For large natural rockfalls ($> 0.01m^3$) this is impractical. Thus, an approach which used physical experiments with small sized rocks in combination with numerical modelling of rockfalls that was informed from observations of large natural rockfalls was applied. This approach facilitated repeatability and the quantification of rockfall dynamics with sufficient resolution to be examined statistically and characterise the behaviour of rock-shape during runout.

Three empirical experimental campaigns were conducted in this research which complement each other: i) the first of which was rock rolling experiments using real rocks of large size (500 - 2000 kg), these were limited to 14 rock rolls, and were largely qualitative; ii) the second were physical experiments using three end-member rock shapes of smaller size conducted under controlled conditions. The experiments with the smaller rocks permitted sufficient repeatable experiments to quantify the role of rock-shape in runout dynamics statistically; iii) the final component to this research was numerical modelling of rockfalls using the rigid-body rockfall model ‘RAMMS::Rockfall‘. The rockfall model provides the bridge between the experiments with small and large rocks and allows the behaviour of rockfalls to be studied in real terrain using a case study of a real rockfall event in New Zealand. Detailed descriptions of the experimental design of the physical experiments and numerical experiments are provided in chapters 4 and 5.

This chapter explains the application of techniques in video tracking, ballistics, and embedded micro sensors technology used to extract rockfall velocities jump heights and rotational velocities from both post event field observations as well as live rockfall events and experiments. It describes how the data are processed, exploring some of the limitations and possible areas of error in data capture and processing. It explains the theories behind how the data are further processed into comparable metrics (apparent restitution coefficients, rotational order and disorder) of rockfall behaviour with which the deposition patterns and dynamics of different rock shapes could be examined. The chapter closes with a description of the RAMMS::Rockfall model, explaining the model parameters and how the rigid-body approach to rockfall modelling is applicable to the study of the role of rock-shape in rockfall runout dynamics.

3.2 Physical experiments with small rocks

A planar slope was selected for the physical experiments as it removes the influence of terrain morphology and roughness. This allows an exclusive investigation of the influence of rock-shape on the runout trajectory and dynamics. The use of a planar slope is intended to be analogous to the modern rock-cut slopes used for the construction of roads and railways, where modern controlled blasting techniques (presplit and cushion blasting) produce smooth rock slopes with little roughness and fewer potential launching features (Pierson et al., 2001). While it is known that terrain roughness also has a strong influence on the runout behaviour of rockfalls (Crosta and Agliardi, 2004), the effects of rock-shape are commonly bundled together with roughness and are as such neglected. Therefore, the rational for a planar slope is to explicitly target and quantify the effects of rock-shape excluding all other possible influencing factors on runout behaviour. Indeed it would be an interesting research question to study the coupled effects of roughness and rock-shape. In an initial step, this approach serves to deliver a dataset of rockfall runout behaviour exclusively influenced by rock-shape and offers a comparative benchmark with which to study the coupled effects of roughness and rock-shape in future research.

3.2.1 Laboratory apparatus

The planar slope was 1.50 m wide and 2.20 m long and constructed of wood, onto which the test bodies could be dropped at five set slope angles (20°, 27°, 37°, 42° and 55°) (Figure. 3.1). The five slope angles were selected to be within the range of slope angles with which Ritchie (1963) defined the different modes of rockfall motion, and also allows a comparative analysis of the findings of Ritchie (1963). The slope was covered in a carpet material which provided a small amount of damping for the impact. A 10 cm grid (Figure. 3.2) was painted on to the surface to allow quick reference when reading coordinates of the deposit locations and in the video analysis. The runout zone was carpeted 3.0 m beyond the toe of the slope after which the surface was bare concrete. The test rock release mechanism consisted of a large adjustable clamp (Figure. 3.3) which permitted accurate gripping of the test rocks' centres. This offered a system releasing the test bodies into free-fall without additional dynamics prior to the first contact with the slope. The release position was set above the central axis of the planar slope and fixed at a height of 1.70 m to make the potential energy constant for each experiment. With the changes in slope angle and release orientation the initial free fall distance was altered for each combination of rock, slope angle and release orientation. The initial free fall distances and respective impact velocities are given in Tables 3.1 and 3.2.

TABLE 3.1: Release heights according to slope angle set for the experiments to ensure constant potential energy.

Slope angle		20°	27°	37°	42°	55°
		Release height (cm)				
Equant	*A*	98.9	75.6	44.8	30.8	11.8
	B	97.9	74.6	43.8	29.8	10.8
	C	97.9	74.6	43.8	29.8	10.8
Platy	*A*	97.6	74.3	43.5	29.5	10.5
	B	100.7	77.4	46.7	32.7	13.7
	C	97.6	74.3	43.5	29.5	10.5
Elongate	*A*	96.0	72.7	41.9	27.9	8.9
	B	99.9	76.6	45.9	31.9	12.8
	C	99.9	76.6	45.9	31.9	12.8

TABLE 3.2: Release velocities according to slope angle set for the experiments to ensure constant potential energy.

Slope angle		20°	27°	37°	42°	55°
		Velocity (ms^{-1})				
Equant	*A*	4.4	3.9	3.0	2.5	1.5
	B	4.4	3.8	2.9	2.4	1.5
	C	4.4	3.8	2.9	2.4	1.5
Platy	*A*	4.4	3.8	2.9	2.4	1.4
	B	4.4	3.9	3.0	2.5	1.6
	C	4.4	3.8	2.9	2.4	1.4
Elongate	*A*	4.3	3.8	2.9	2.3	1.3
	B	4.4	3.9	3.0	2.5	1.6
	C	4.4	3.9	3.0	2.5	1.6

3.2.2 Rock-shapes

The test rocks (Figure. 3.2) are based on the geometry used in the Swiss standard for testing rockfall barriers (Gerber, 2001). Shape was varied by changing the aspect ratios of the principal geometric axes, so to achieve three end-member shapes according to

---

FIGURE 3.1 *(following page)*: A 2.20 m planar test slope with adjustable slope angles θ from 20 - 55°. The release position was set at a fixed location about the central fall line with a potential height of 1.70 m. Two cameras recorded events from side and a front view; a laptop serves as the interface with the StoneNode motion sensor module.

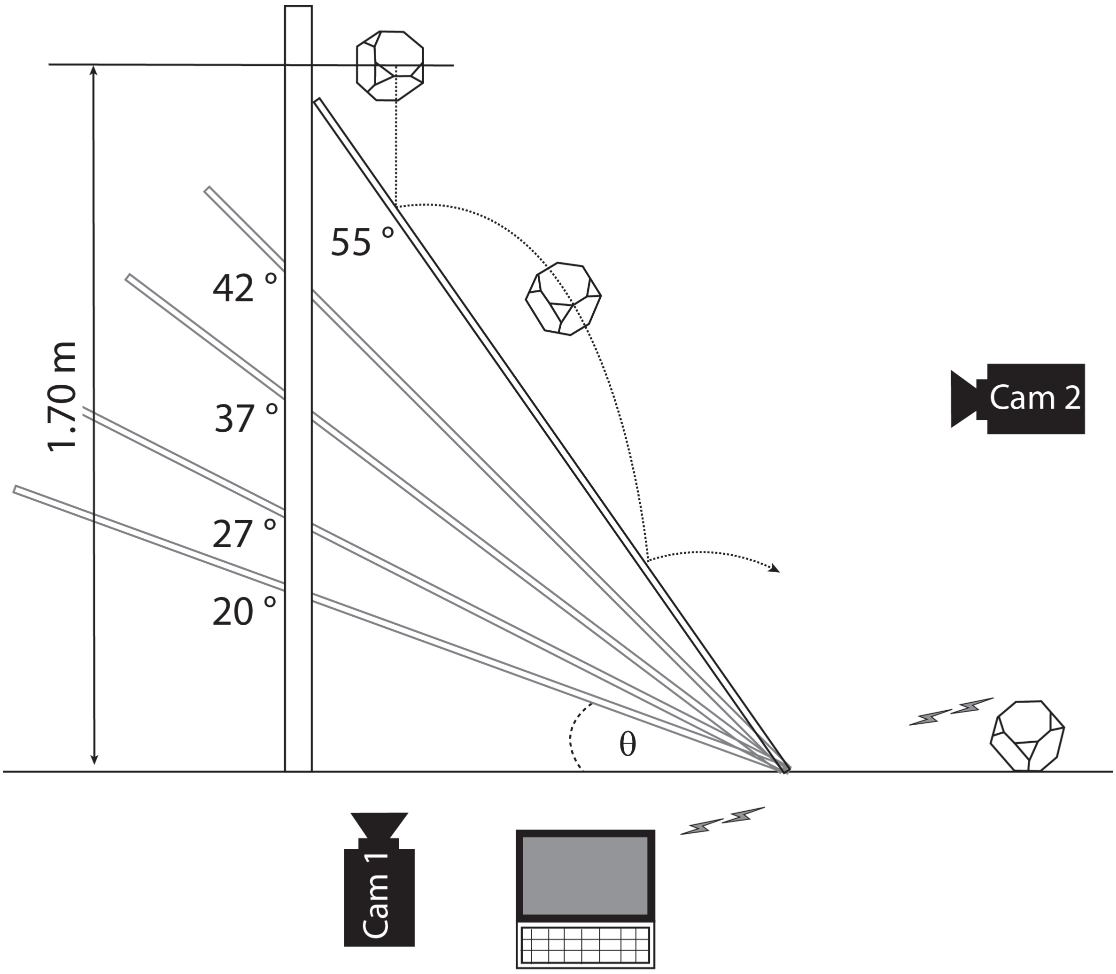
1.70 m
55 °
42 °
37 °
27 °
20 °
θ
Cam 2
Cam 1

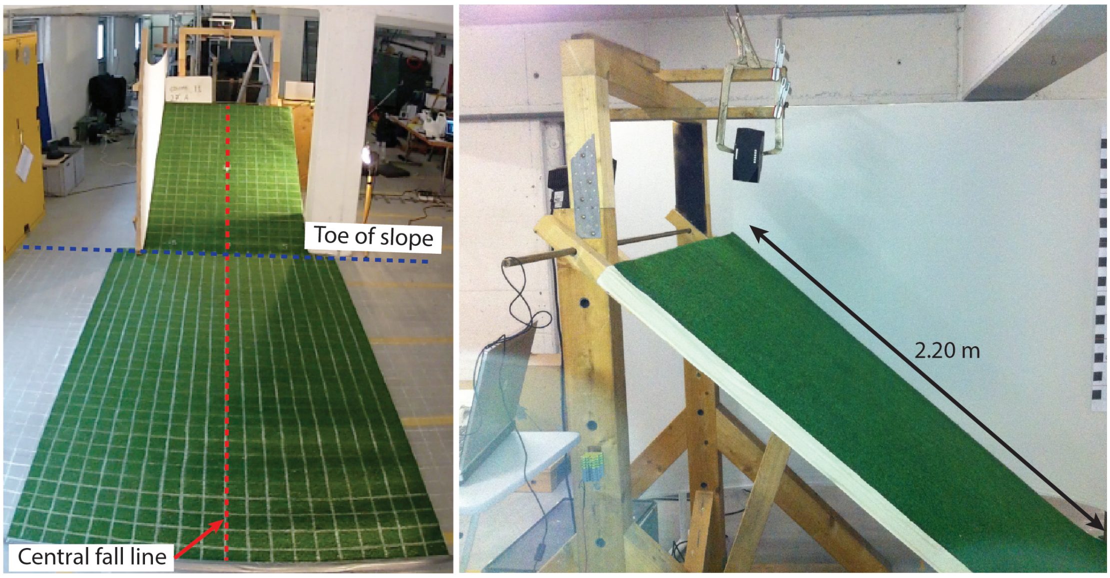
Toe of slope
Central fall line
2.20 m

those proposed by Sneed and Folk (1958). The shapes are symmetrical and devoid of additional irregularities or uneven mass distributions that are found in natural rocks. These aspects of rock-shape where not included in the physical modelling for the simple reason that this would have multiplied the iterations of the experimental campaign beyond what was realistically achievable in the time available. Irregularities in mass distribution and angularity are treated in the numerical modelling component of this work.

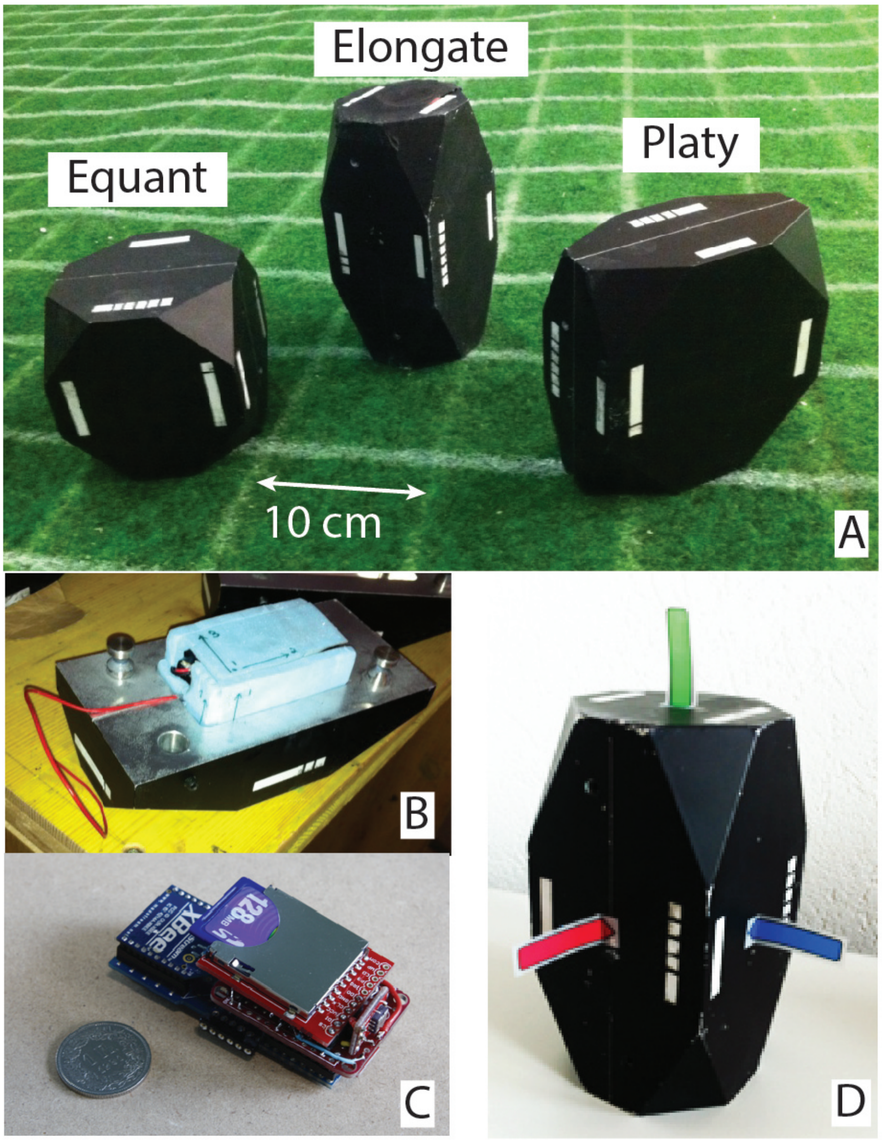

FIGURE 3.2: A: The three end-member shapes used for the test bodies *equant*, *elongate* and *platy* (A). The housing can be separated to reveal a void space (B) in which the StoneNode motion sensor module measuring the bodies three-dimensional rotations and accelerations (C). The motion sensor module is aligned with the test rock's principal inertial axes; illustrated on the *platy* test body (D), the green axis holds the smallest principal moment of inertia, the red and the blue axis are equal and the largest principal inertial moment.

The investigations consisted of a pilot study in which smaller test rocks were used but of the same design. The final test series, of which the main part of the analysis is based, involved larger test rocks which had a void space cut into their centre to house the motion sensor described in section 3.5. The test rocks are constructed of milled aluminium which was selected for its machinability and density (2700 kg m^{-3}), which is approximately equivalent to the average for continental lithospheric rocks. Details of the physical properties of each of the test bodies are listed in Table 3.3.

3.2.3 Release orientation

There were three main release positions selected for each shape, as listed in Figure 3.3. These were selected to investigate how the initial impact configuration influenced runout. This was intended to include a sample of the possible release orientations that are preset by the discontinuities of a given rock-mass (see Chapt. 2, Sect. 2.3). Care was taken to ensure that the clamp held the test bodies about their centre, however, slight deviation ($\pm 5°$) from this position was permitted. This served to capture the natural variation governing the release position that would be expected during rockfall.

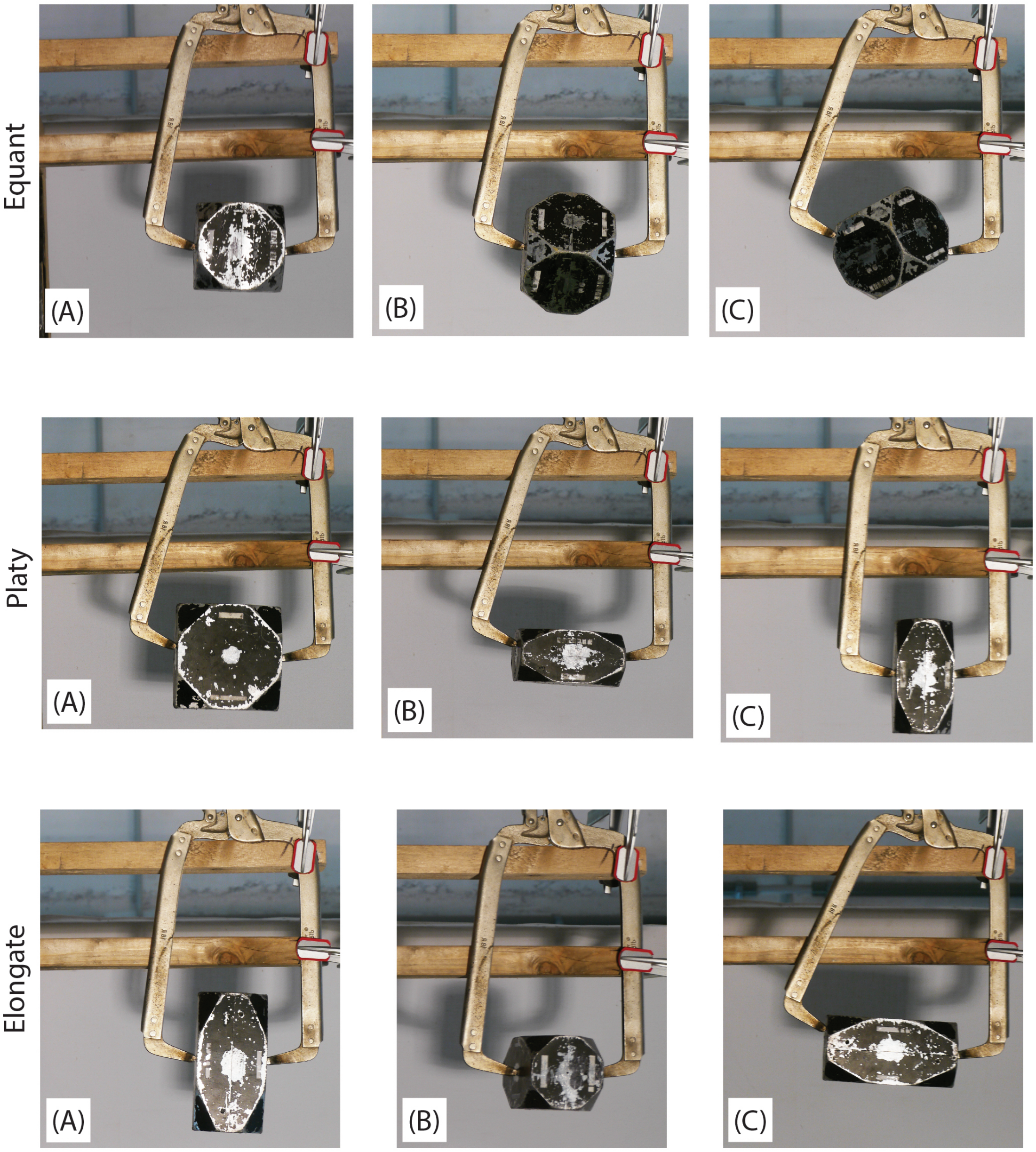

FIGURE 3.3: Release orientations A, B & C for each shape. Orientations A and C of the *elongate* form, and A of the *platy* form align the largest moment of inertia parallel with the central fall line. The *elongate* form's B orientation aligns its smallest moment of inertia with the fall line, similar to how a barrel would roll. The *platy* form's B and C orientations align its smallest moment of inertia with the fall line. The *equant* form has equal principal inertial axes, release orientation change in this case ensures different edges and facets impact the slope first.

Table 3.3: Test rock dimensions and key properties. Note: the density of the aluminium used to create the rocks is 2700 kg m^{-3}. However, to accommodate the sensor the rocks lose mass to create the void space, giving an effective density of the test rocks is 2490 kg m^{-3}.

Test Rock	Prin. length axes			Vol.	Mass	Prin. I moments			Equiv. Ellip. semi-axes		
	L (cm)	I (cm)	S (cm)	(cm^3)	(kg)	I_1 ($kg{\cdot}m^2$)	I_2 ($kg{\cdot}m^2$)	I_3 ($kg{\cdot}m^2$)	E_{2a} (cm)	E_{2b} (cm)	E_{2c} (cm)
Equant (Sensor Rock)	10.00	10.00	10.00	940.0	2.34	0.0037	0.0037	0.0037	6.25	6.25	6.25
Platy (Sensor Rock)	12.60	12.60	6.30	940.0	2.34	0.0058	0.0036	0.0036	7.88	7.88	3.94
Elongate (Sensor Rock)	15.88	7.94	7.94	940.0	2.34	0.0058	0.0058	0.0023	9.95	4.94	4.94

3.2.4 Test series

The experimental campaign using the larger instrumented test bodies was conducted on five different slope angles (20°, 27°, 37°, 42° and 55°). Each rock-shape on each slope angle was released $n = 100$ times, and within the 100 releases $n = 33$ (± 1) made up each of the 3 release orientations (Figure. 3.3).

The experiments were filmed from 2D side and front views, and the accelerations and angular velocities captured with the motion sensors (Figure. 3.1). The frontal video served to capture the test bodies' dispersion angle at the base of the slope. The enormous effort involved in processing video data (Cross, 2002) and processing the sensor data meant that side-view high-speed video recording and dynamic data were only taken for 10 experiments of each possible combination. The data set consisted of $n = 1500$ iterations of which $n = 450$ yielded high speed video and motion data. The data produced during these testing series are available for further study. Should you be interesting in using any of these data, please make contact with the author.

3.2.5 Patterns of single rockfall runout paths

The geometry of the rockfall affected area was measured using the ratio (W/L) of the distance (L) to the furthest run-out deposits and the furthest lateral distance W. The dispersion measure was used to quantify both the rockfall dispersion of the entire rockfall affected area (e.g. Figure, 2.12), and for single runout events. The extension of the dispersion ratio (W/L) to single runout paths within this work permits a comparison between individual runout paths.

3.3 Video tracking

In order to obtain a more accurate measure of rockfall velocities and motion, video tracking methods were employed. This section describes the apparatus and installation considerations required to use video to track the motion of an object in 2D to accurately derive its translational velocity and measure distances and angles within the field of view.

3.3.1 Video camera setup

Video tracking of rockfall motion was performed using an AOS high speed video camera, the specifications for which are listed in Table 3.4. Most experiments were captured using frame rates between 120 and 250 fps. The image raster provides a coordinate system to track the position the object of interest. Distances are measured by setting a scale in the camera's field of view and converting from the pixel to metric coordinate system. Due to perspective distortion, objects that are in the foreground of an image appear larger than objects in the back ground. Therefore, the image plane must correspond to the object trajectory plane for accurate measurements to be made. The conversion between planes is illustrated in Figure 3.4A.

TABLE 3.4: High speed camera, technical data.

Item	Description
Image Sensor	Progressive CMOS, 800 x 600 pixels, mono or colour
Sensor size (@ full resolution)	11.2 x 8.4 mm, 14 μm pixel size
Light sensitivity	ISO 3200 (monochrome), ISO 1600 (colour)
Dynamic range	8 bit
Frame rate at full resolution	1000 fps @ 800 x 600 pixels
Typical fps/resolution settings	800 x 600 @ up to 1000 fps
Max. frame rate	1000 fps
Shutter type	Global electronic shutter
Shutter exposure times	4 μsec to 1/frame rate
Image memory	Built-in DRAM, circular buffer
Sequence length (typical)	2.7 sec @ 800 x 600 / 1000fps (1.3 GB memory)

The optimum camera direction for 2D video tracking is perpendicular to the object trajectory (Figure. 3.4)A. In this way minimal scaling corrections are required to adjust the scaled plane to the image object plane. In the case that an object passes diagonally through the image, each frame must be scaled accordingly. This can be measured using a second camera that films the relative distance of the tracked object to the side view camera (Figure. 3.4)B.

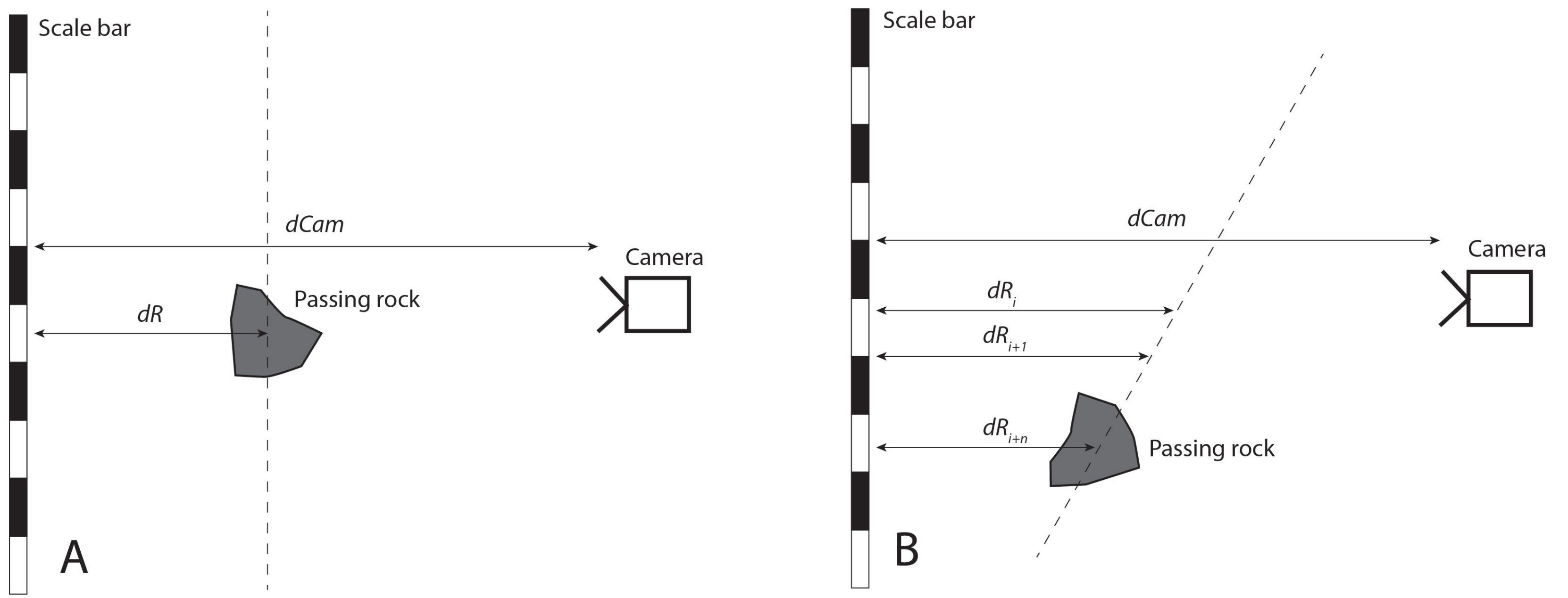

FIGURE 3.4: A)Sketch of scaling the camera view to the plane of the moving object. The distance dR between the rock and the scale bar, and the distance $dCam$ between the video camera and the scale bare are required. B) Sketch of scaling the camera view to the plane of an object moving diagonally through the image. The distances dR_i between the rock and the scale bar over the image sequence, and the distance $dCam$ between the video camera and the scale bare are required.

Accurately following an object requires sharp images that contrast the background. Depth of focus, exposure (lighting and shutter speed), and object background colour are the parameters that can be altered to ensure a crisp image. The object-background contrast is optimised by painting the objects in contrasting colours. The best combination was black objects on a white background. Best focus is achieved by focusing at the object trajectory plane depth of field.

3.3.2 Exposure

The exposure of the image controls how sharp or blurred an object will appear, and is influenced by the lighting, shutter speed and the speed of the object passing through the image. Sharp images are achieved if the object's relative velocity at the camera's sensor Sv is no less than two pixels Ab during periods when the camera shutter is open (Figure. 3.5). The shutter speed or *Exposure* setting is independent of frame rate and is selected by estimating the objects velocity at the sensor scale Sv. The *Exposure* is found by taking the observed velocity of the object Ov moving in the field of view FoV across the sensor plane Ss having the pixel dimensions Sd. An example of calculating the correct shutter speed is given in (Figure. 3.6).

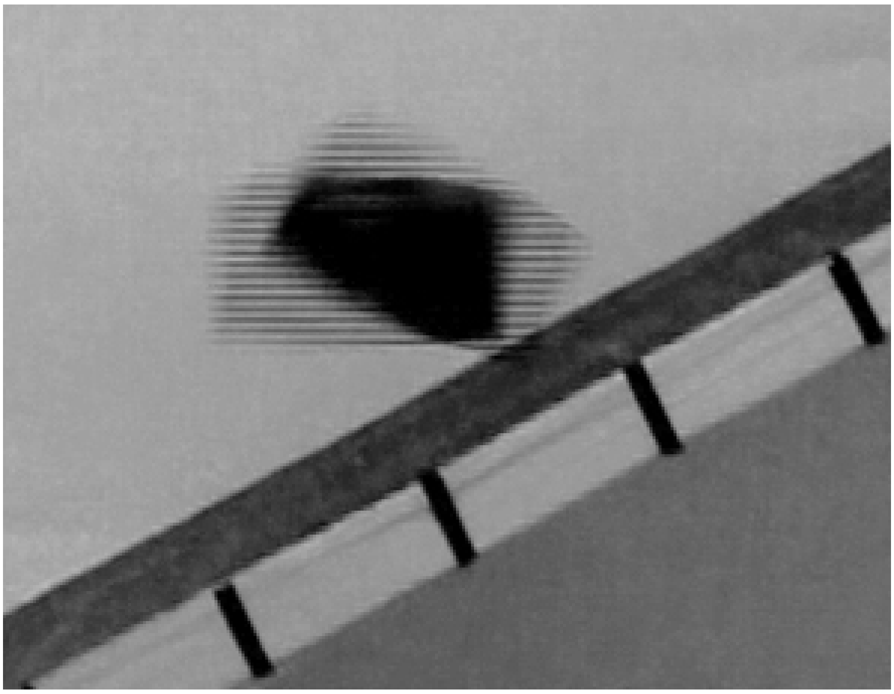

FIGURE 3.5: Blurred image due to false shutter speed.

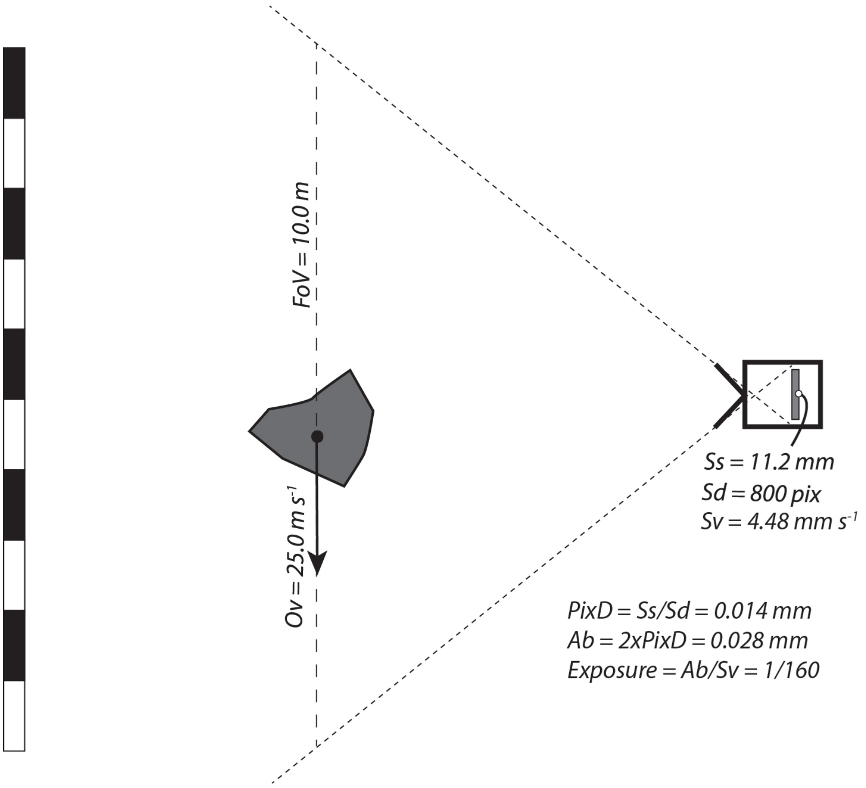

FIGURE 3.6: Sketch drawing showing the calculations required to select the correct camera *Exposure*.

With increasing frame rate, increasingly higher intensity lighting is required. In controlled conditions of the small scaled experiments (Chapter. 4) 2×500 watt lamps were used, while for large-scale rock rolling experiments natural light must be relied upon. This is made more challenging because of changing lighting conditions and the camera direction in relation to the sunlight over the course of a day.

3.3.3 Object tracking

Sharp images assist video tracking algorithms to position a target over a series of images. In this work the video tracking software Kinovea was used. The tracking algorithms in this software uses a cross correlation coefficient between a candidate search window and a feature window of the previous image (Figure. 3.7). This tracking algorithm works best with a strong contrast between the tracked object and the background. However, rotating bodies cause problems and often require manual correction to relocate the centre of mass.

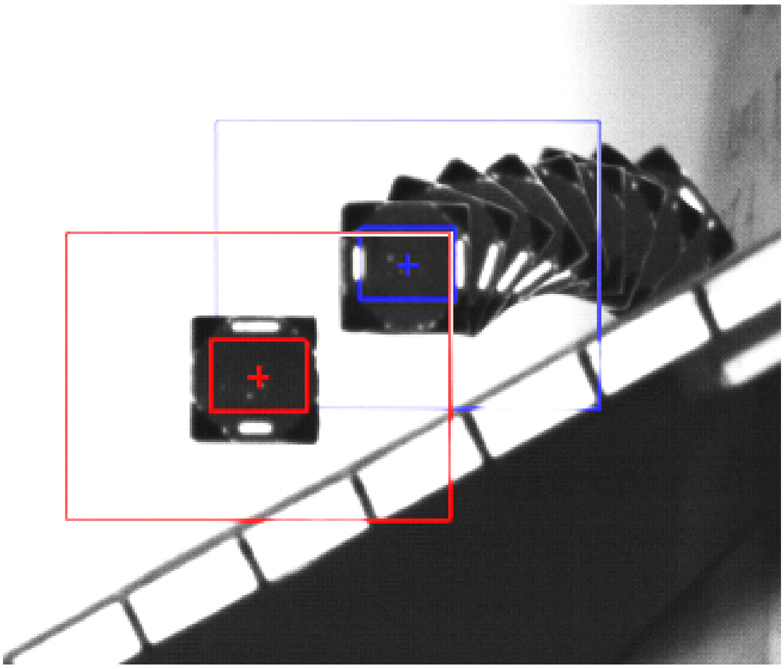

FIGURE 3.7: Video tracking search window used to follow the rock centre of mass over an image sequence.

3.3.4 Lateral deviations and depth of field correction

The lateral deviation of a rockfall is measured using a second video camera with the rock travelling towards the camera (Figure. 3.8). This measurement serves two purposes; First, this ensures that correct scaling (Section. 3.3) is set for each frame by providing a measure of the object's depth-in the field of view (Figure. 3.4)B; and the second, quantifies the deviation angle between the pre- and post-impact trajectories (Figure. 3.8).

3.3.5 Positional error

Naturally there are user and computer errors involved in positioning the centre of mass of an object. This is assessed with a trajectory of known geometry and time. With the time and distance between impacts, the theoretical trajectory can be plotted where air resistance is assumed negligible Eqs.(2.8) & (2.9). The objects position for the same trajectory is then plotted using the video tracking technique. Comparing the two results the small positional errors are evident. However, the maximum and standard deviation of difference between the plotted and theoretical trajectory for its position are up to a maximum of 1.0 cm, which is within acceptable limits (Figure. 3.9)B to describe the trajectory's geometry. The positional error does however become unacceptable when the

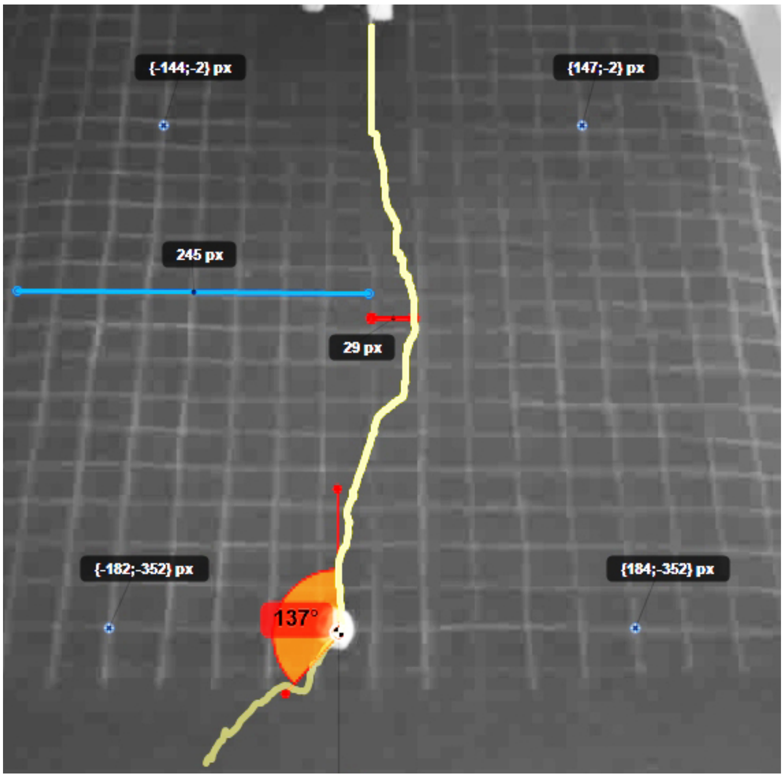

FIGURE 3.8: Image from the frontal view camera tracking the lateral deviation of the rock by recording its relative position to the side of the image, and the angle of deviation following an impact.

positions are differentiated over time to obtain a velocity; this error becomes amplified with increasing frame rate and can result in up to 4.5 ms^{-1}.

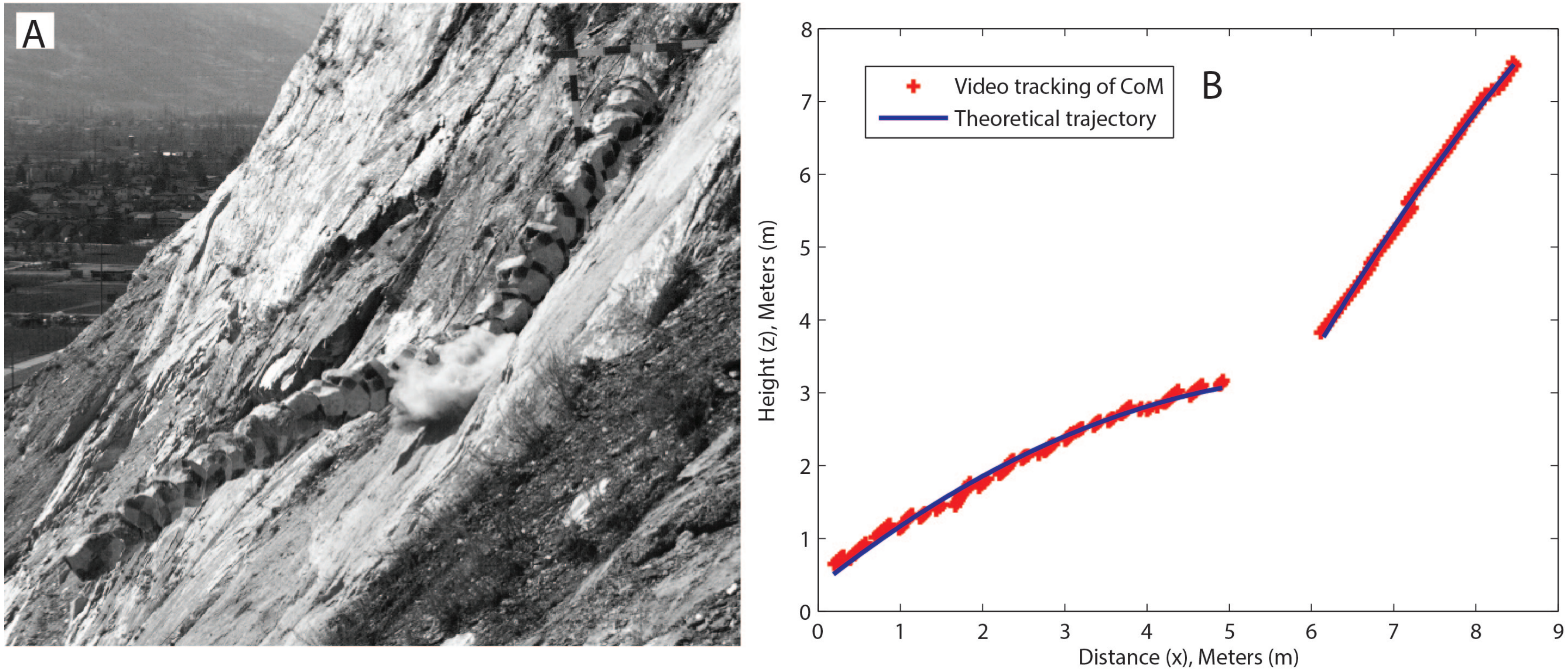

FIGURE 3.9: A)Sequence image of a rock impacting the St Léonard rock cut slope. The rocks centre of mass is tracked by plotting its position in each frame using the object tracking algorithms. Often this requires manual correction. B)Position tracking compared to fitted ballistic parabola. The results of the position tracking from (A) are plotted in red crosses with the parabola (the blue line) of the fitted ballistic trajectory.

3.4 Video data processing

In this section the methods used to extract velocities from video data are described, and are then converted into measures of apparent restitution coefficients of the impacts for analysis. Furthermore an explanation of the method used to quantify the angle of the impact configuration in terms of geometric orientation and orientation of the impacting velocity vector are given.

3.4.1 Velocity

There are two techniques that can be applied to analyse the video data to extract the velocity of the rock's centre of mass: i) The first relies on plotting the position of the centre of mass through the image sequence. The instantaneous velocity between plotted positions can be obtained (e.g. Figure, 3.7), while this is prone to large error, especially if the sequence is of high frequency. Thus, in most cases a best-fit parabola is applied to obtain the velocity (Figure. 3.9), full details of this method and the errors are given in Glover et al. (2012); ii) The second is to extract the position and time of slope impacts and fit a ballistic parabola between the known impact points. This is much more accurate if the contact positions can be well-constrained.

In full-scale rockfall experiments this is complex and in most cases the first method (i) is preferred. However, the physical experiments in chapter 4 the planar slope with constant angle facilitates locating each impact point in space and time and is therefore the chosen method for this analysis. Both methods require sharp, high quality, video images with good object-background contrast that are correctly scaled so that distances can be accurately measured in the observation plane (see methods section 3.3).

Method (ii) using impact positions is performed by measuring S and f from the scaled video (Figure. 3.10) and the time t of each impact. The x and z components of S must be found which is trivial for a planar surface of known slope. x and z are given from the slope ϑ of S in the following equations:

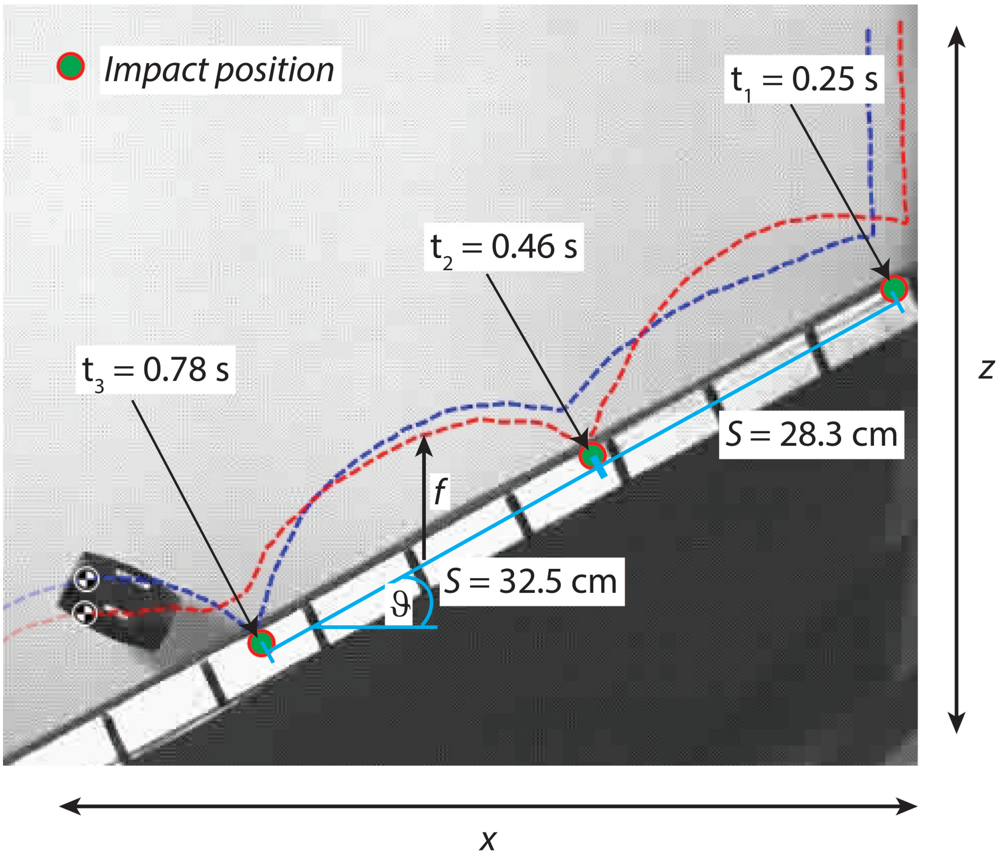

FIGURE 3.10: Method to extract velocity from video analysis of the physical experiments locating impact points. The green dots indicate the terrain impacts on the planar slope which divide up the inter-impact ballistic trajectories. The times of the impacts are measured from video, along with distanced f and S which prescribe the form of the ballistic parabola. The red and blue tracking lines are the trace of two tracked points on the rock body as it rotates through the field of view.

$$x = S\cos\vartheta,$$

and

$$z = S\sin\vartheta. \tag{3.1}$$

The rebound velocity in the horizontal V_x^r and the vertical V_z^r components are found using the jump height f using the following equations:

$$V_x^r = -x/\delta t,$$

and

$$V_z^r = 4f - z\sqrt{\frac{g}{8f}}. \tag{3.2}$$

Similarly the incident velocity in the horizontal V_x^i and vertical V_z^i components are given in the following:

$$V_x^i = V_x^r,$$

and

$$V_z^i = V_z^r - g\delta t. \tag{3.3}$$

The absolute velocity for the incident V_i and rebound V_r are given using the respective horizontal and vertical velocity components in the following equations:

$$V_i = \sqrt{V_x^{i2} + V_z^{i2}},$$

and

$$V_r = \sqrt{V_x^{r2} + V_z^{r2}}. \tag{3.4}$$

This method has proved effective in rapidly extracting velocities from the video data, and avoids the aforementioned errors inherent to video motion tracking. The time t of impacts was either extracted from the video time stamp or in some cases the signal of the embedded accelerometer (presented in the following sections) was used to identify rock-slope contact.

3.4.2 Apparent restitution coefficients

The limitations of using apparent restitution coefficients to model the impacts of rockfalls are clear (Chapters. 1 & 2). However, apparent restitution coefficients provide a useful metric to compare rock-ground impacts between real rockfall events, physical experiments and numerical simulation results generated with a rigid-body rockfall code. In this work, apparent restitution coefficients R^{App} are measured using incident V^i and rebound V^r impact velocities (Eq. 3.5) of the rock body's centre of mass (Figure. 2.4)).

$$R^{App} = \frac{V^r}{V^i} \tag{3.5}$$

Further decomposing the absolute apparent restitution coefficients into normal R_n^{App} and tangential R_t^{App} components, with respects to the angle θ of the common tangent plane of the coincident contact point p, provides a more detailed measure of an impact's characteristics. Velocities are measure in a horizontal and vertical coordinate frame. Therefore, normal V_n and tangential V_t velocity vectors are obtained for pre- and post-impact events applying the rotation matrix $[Rm]$ with respect to the angle θ of the common tangent plane (Eqs.(3.6), (3.8), and (3.7)).

$$Rm = \begin{bmatrix} cos\theta & -sin\theta \\ sin\theta & cos\theta \end{bmatrix} \tag{3.6}$$

$$\begin{pmatrix} V_n^i \\ V_t^i \end{pmatrix} \equiv [Rm] \begin{pmatrix} V_x^i \\ V_z^i \end{pmatrix} \tag{3.7}$$

$$\begin{pmatrix} V_n^r \\ V_t^r \end{pmatrix} \equiv [Rm] \begin{pmatrix} V_x^r \\ V_z^r \end{pmatrix} \tag{3.8}$$

Here, θ is the orientation of the common tangent plane (the slope at point of contact) (Figure. 2.4). The normal and tangential apparent restitution coefficients for the centre of mass can then be calculated using equations (3.9) & (3.10). In all cases, comparisons with literature are made where the same method has been used (Chau et al., 2002, Guzzetti et al., 2002, Dorren, 2003, Labiouse and Heidenreich, 2009).

$$R_t^{App} = \frac{V_t^r}{V_t^i} \tag{3.9}$$

$$R_n^{App} = \frac{V_n^r}{V_n^i} \tag{3.10}$$

Often an impact will involve a series of contacts before the rock body leaves the ground. The pre- and post-impact velocities in all instances are defined as the period between the final time step before the first contact is detected and the time step after impact following which no further contacts are detected.

3.4.3 Impact configuration

The purpose of investigating the impact configuration was to quantify its effect on rebound. In particular it was designed to draw out how impact rebound is affected by the physical differences in the equivalent inertial ellipsoid of the test rock which is brought about by changes in rock-shape.

Investigation of the impact configuration considers the full dynamics of an impact in which edge and corner points become lodged into the terrain and set up a moment arm between the contact point and the rock's centre of mass. The lodged corner or edge contact acts as a fulcrum about which the rock's centre of mass is then rotated. In some cases this means the mass must be lifted and in other the rock body is already in a toppling state.

The length of the position vector r_i between the rock's centre of mass S and ground contact point p along with the rock's mass distribution sets the magnitude of the moment arm. The moment arm magnitude coupled with the distance that must be travelled to enter a toppling state then sets the amount of work that must be done to overcome the contact point lodged in the terrain. This is very much dependant on the orientation angle α of the rock contact position vector r_i in relation to the slope at the time of first contact. The measurement of angle α is depicted in Figure 3.11.

The success of an impact overcoming the lodged contact point is dependent on the kinematics of impulsive forces involved in the impact; i.e. the orientation and magnitude of the translational velocity vector $\overrightarrow{U}$ of the impact point p in relation to the slope and the rock's angular speed Ω. The orientation of $\overrightarrow{U}$ is measured as the angle γ between $\overrightarrow{U}$ and the terrain surface (see Figure, 3.11).

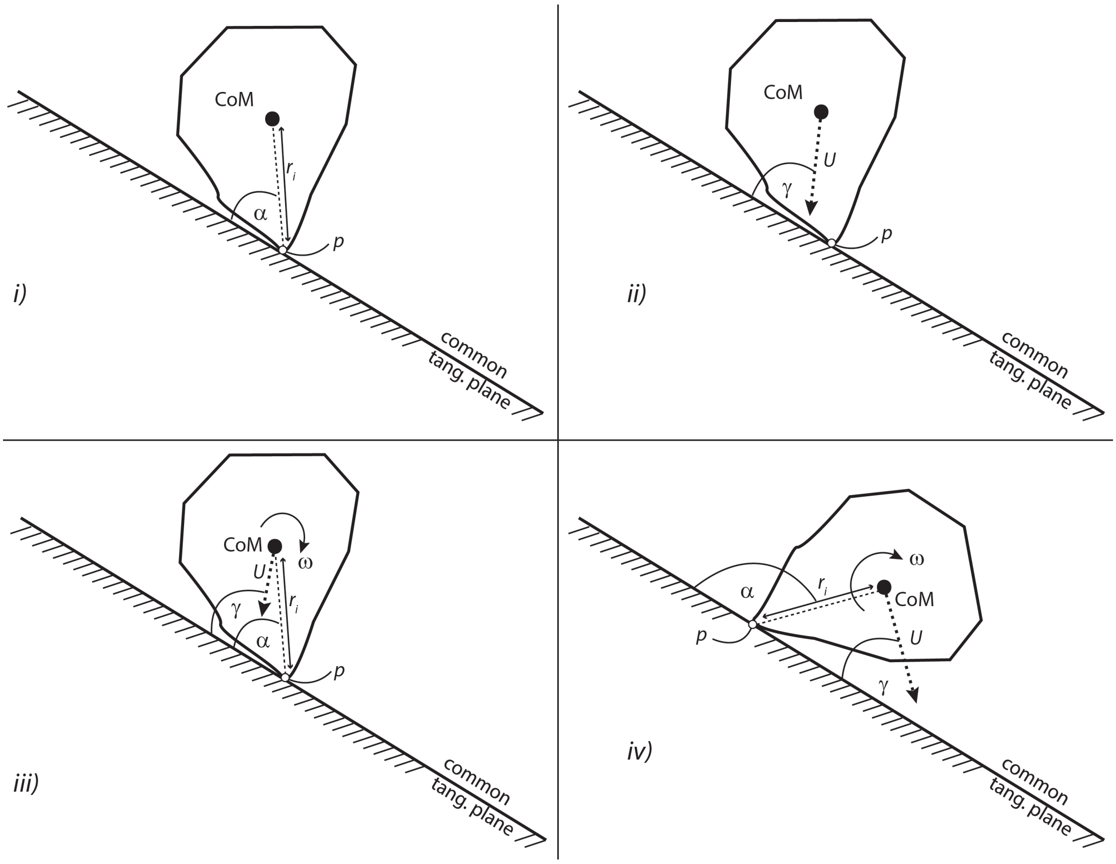

FIGURE 3.11: Two dimensional sketch diagrams illustrating the components of the impact configuration measured during the experiments. i) Illustrates the impact orientation at the point of first contact. The angle between the position vector r_i and the common tangent plane is the angle α. r_i is the position vector of contact point p in relation to the centre of mass CoM. ii) Shows the angle γ of the translational velocity vector U in relation to the local slope angle; Note this is not always coincident with the location of p. Illustration iii) is an example which includes the angular velocity vector ω in a case where the impact orientation α is acute, while the orientation γ of the velocity vector is a large acute angle which approaches a normal impact with the slope. iv) Illustrates a second example in which the impact orientation α is obtuse, while the orientation of the velocity vector γ is acute. The angular velocity vector ω in each case is also different. With the latter two illustrations iii) and iv), an impression can be gained of how the differences in the impact configuration can affect the outcome of rebound. Moreover, an idea of the potential for variability in rebounds is obtained.

Impact configuration is measured in this work using video analysis. Using the angle measurement tool of the Kinovea video analysis software, the impact configuration orientation is measured. Figure 3.12 illustrates the ideal case of a 2D image in controlled laboratory experiments. The impact configuration angle is obtained by measuring the angle between the planar surface and the line that intersects the coincident contact point and the rock centre of mass. In the case of large rockfall experiments this task proves more challenging because locally to the contact the orientation of the slope angle can be highly variable due to surface roughness. Where video analysis to obtain impact configuration of large rockfall experiments has been used, the impact configuration has been measured with respect to the horizontal plane. The orientation has then been corrected with respect to the slope angle of the contact point obtained from a detailed laser scan of the terrain.

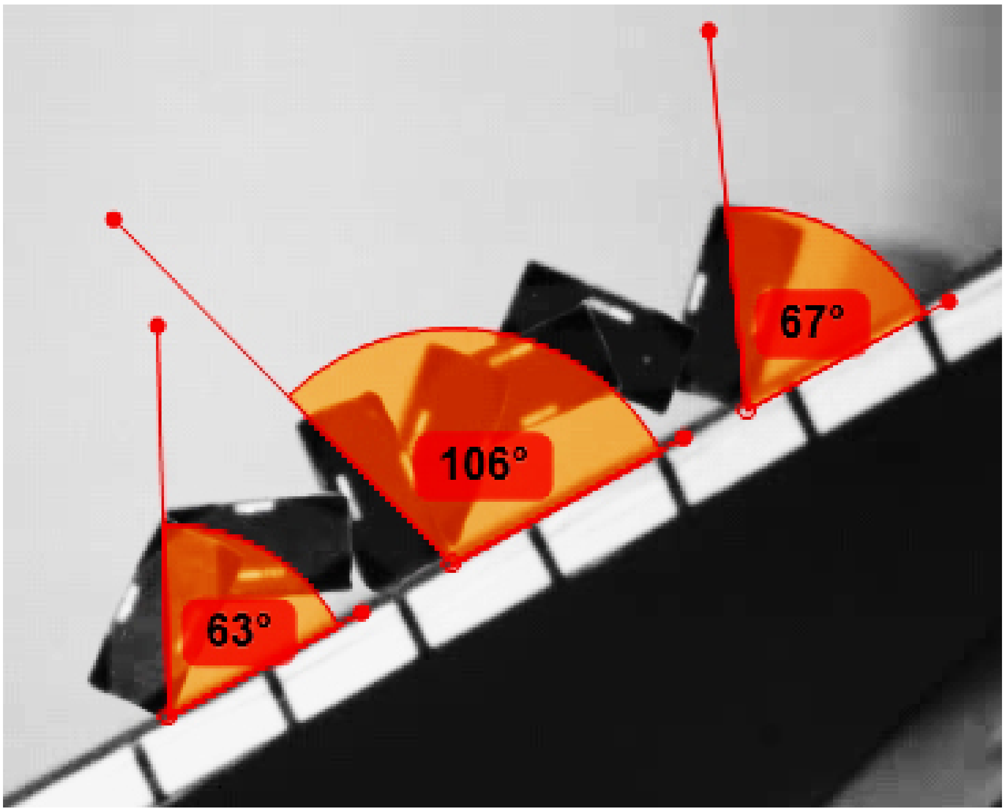

FIGURE 3.12: Impact configuration measured with video analysis program Kinovea: Angle α between common tangent plane and the position vector r_i between the centre of mass (CoM) and the coincident contact point p.

3.5 StoneNode: Embedded acceleration and rotation sensors

To address the limitations of 2D measurements of rockfall dynamics and the additional processing challenges of 3D video tracking, a sensor module was designed to take direct measurements of acceleration and angular velocity about the three principal inertial axes of a rigid-body. The custom construction of the sensor module with software programming was completed by Embeddedlab (`http://www.embeddedlab.ch`). The senor module, which is referred to as StoneNode, was tested and calibrated within the bounds of this project. This section covers the component parts of the StoneNode, its calibration, along with data capture and processing techniques. The StoneNode was used in this project to investigate the kinetics of different shapes by inserting it into custom built rigid bodies in a series of physical experiments (Chapter. 4). Ultimately it is intended that the StoneNode will be used in large scale rock rolling experiments where it is placed into the centre of mass of natural rocks via drilling.

3.5.1 Components and construction

Table 3.5: StoneNode component parts.

Item	Description	
Logging rate		600 Hz
Gyroscope ITG-3200	3- Axis	2000° s^{-1} ; 35 rad·s^{-1}
Acceleration sensor ADXL 193	1-Axis	± 250 g
Barometric Pressure sensor BMP 085		300-1000 hpa
Microcontroller Arduino FIO		
Max. frame rate		1000 fps
SD card		128 MB
Wireless Communication XBEE		
Rechargeable LiPo battery		3.3V; 1100 mA

3.5.2 Interface & data

The StoneNode is communicated to via an xBee wireless connection and controlled using a custom made interface software, with the function to *idle*, *record*, *upload* or *reset*. During record mode the StoneNode samples at a rate of 600 Hz. The micro controller has 2 kB of random-access memory RAM to store data. Once the RAM is full there is a pause in recording while data is saved to the internal SD card. The breaks in recording can reduce the average sampling rate to around 500 Hz. The upload intervals are dependent on the amount of activity registered by all micro sensors. As a result, data have irregular time intervals. Following an event the module is set to idle and data are transferred to a computer via the wireless connection which are saved in *.cvs format (Table. 3.6). Gyroscope data deliver a measurement of angular change at each sample in degrees, signalling the direction with ± sign. Accelerations are given in $m\ s^{-2}$, also with the sign indicating the direction.

Table 3.6: StoneNode *.cvs data format.

millis	angle0	angle1	angle2	acc0	acc1	acc2	temperature	barometric
9720	-0.01	0.003	0.007	-0.01	0.244	0.244	26.7	838.1
9720	-0.01	0.003	0.007	-0.01	0.244	0.244	26.7	838.1
9720	-0.01	0.003	0.007	-0.01	0.244	0.244	26.7	838.1

3.6 Data processing (gyroscope)

3.6.1 Angular velocity

During rockfall angular velocity can be imparted to a rock body if the impact configuration with the ground is eccentric. In such collisions a tangential force due to friction acts to form a pivot point at the rock's contact with the ground about which a torque can act. The rocks translational collision velocity is in part converted to an angular velocity. The primary output of the gyroscope sensor is an angular value θ reflecting the angular change relative to the previous sample. The angular velocity obtained from the derivative of θ over time.

$$\frac{\delta\theta}{\delta t} = \omega \tag{3.11}$$

The SI unit for angular velocity is rad·s^{-1}, thus values in angular degrees are converted to radians. Angular velocity is given for each axis ω_i, thus absolute angular velocity Ω is defined by:

$$\Omega = \sqrt{\omega_1^2 + \omega_2^2 + \omega_3^2} \tag{3.12}$$

3.6.2 Impact orientation (α) error

There are two possible sources of error in the measurements of the angle α the first lies in the assumption that the contact forces operational during impact work around the position vector r_i between the contact point and the mass centre. Given that this was measured from a video this could only be measured in two-dimensions, therefore trajectories that fall out of the *2-D* plane cannot be accounted for using this method. For this reason the analysis was only conducted on experiments that were released in position A (see, Figure 3.3). In these experiments, rotations were in most cases simple and about a single rotation axis, which simplified the analysis.

The second source of error was with the test body's rotational speed and the video camera frame rate (Hz). The maximum angular change between images is given by the angular speed between two images. Footage of the experiments was filmed at 120 and 250 Hz, and the absolute maximum rotational speed recorded for all experiments measured was 60.2 rad·s^{-1}. The potential error in the impact orientation between video images is defined by:

$$\pm\alpha = \frac{\omega}{Hz} \tag{3.13}$$

However, the additional impact dynamics should also be considered. The following sections assess the dynamics during the period of the impact, initially the impact velocity vector, and the rotational speed at the point of impact.

3.6.3 Angular kinetic energy

Angular kinetic energy T is important as it can form a large portion of a rock's total impact energy. Moreover, during a rockfall impact with the ground a large amount of the translational energy is converted to rotational energy. The relationship between rock-shape angular kinetic energy and impact velocity has remained an unexplored field in rockfall mechanics. The StoneNode has provided an opportunity to explore this dynamic. Angular kinetic energy is a function of an objects angular velocity Ω and its moment of inertia I, as defined by:

$$T = \frac{1}{2} I \Omega^2 \tag{3.14}$$

This can be decomposed into the three principle inertial axes (I_1, I_2 and I_3) of a given body and the respective rotations (ω_x, ω_y and ω_z) about them.

$$T = (\frac{1}{2} I_1 \omega_x^2 + \frac{1}{2} I_2 \omega_y^2 + \frac{1}{2} I_3 \omega_z^2) \tag{3.15}$$

3.6.4 Total rotations

The preferred axis of rotation is observed in two ways. The first is resolved by summing the total angular change over time (Figure. 3.13). This allows the overall dominance of a particular axis in the rockfall motion to be observed, in addition to viewing if reverse rotations have been registered.

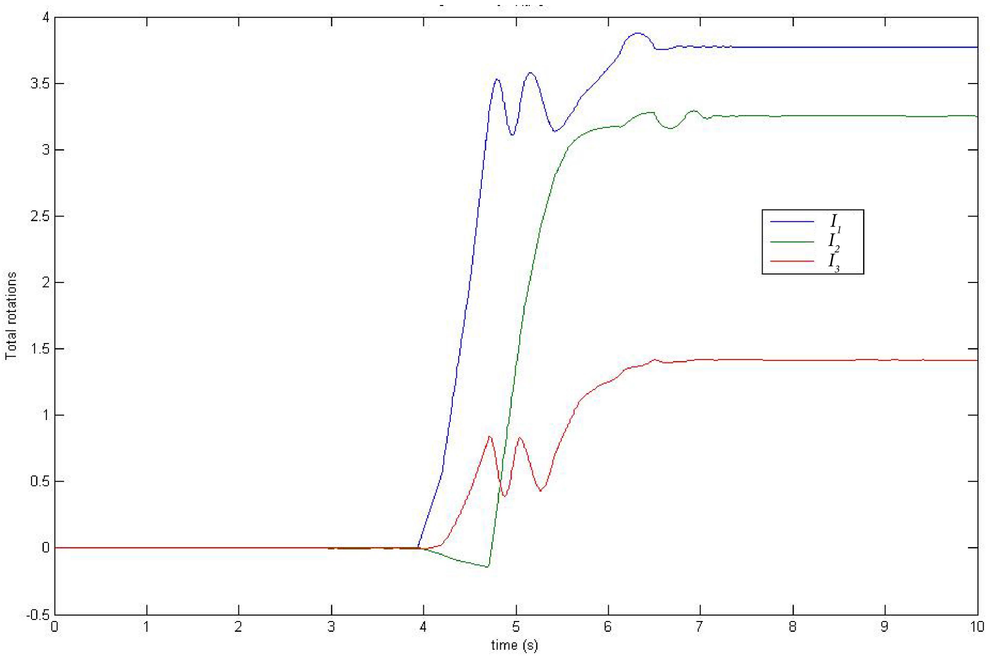

FIGURE 3.13: Total rotations about each principal axis of inertia summed over time. Rotations are recorded in both directions about a given axis and are recorded as a positive or negative signal. Summing the signal over time will show how there is forwards and backwards rotations about an axis by causing an oscillation in the signal as is observed in the figure.

The instantaneous preferred rotational axis can be obtained by normalising the angular kinetic energy of each principal inertial axis over the total angular kinetic energy (Figure. 3.16), as defined by:

$$\begin{aligned} Er_1 &= \frac{\omega_1}{\Omega} \\ Er_2 &= \frac{\omega_2}{\Omega} \\ Er_3 &= \frac{\omega_3}{\Omega} \end{aligned} \tag{3.16}$$

$$Er_{tot} = Er_1 + Er_2 + Er_3 = 1 \tag{3.17}$$

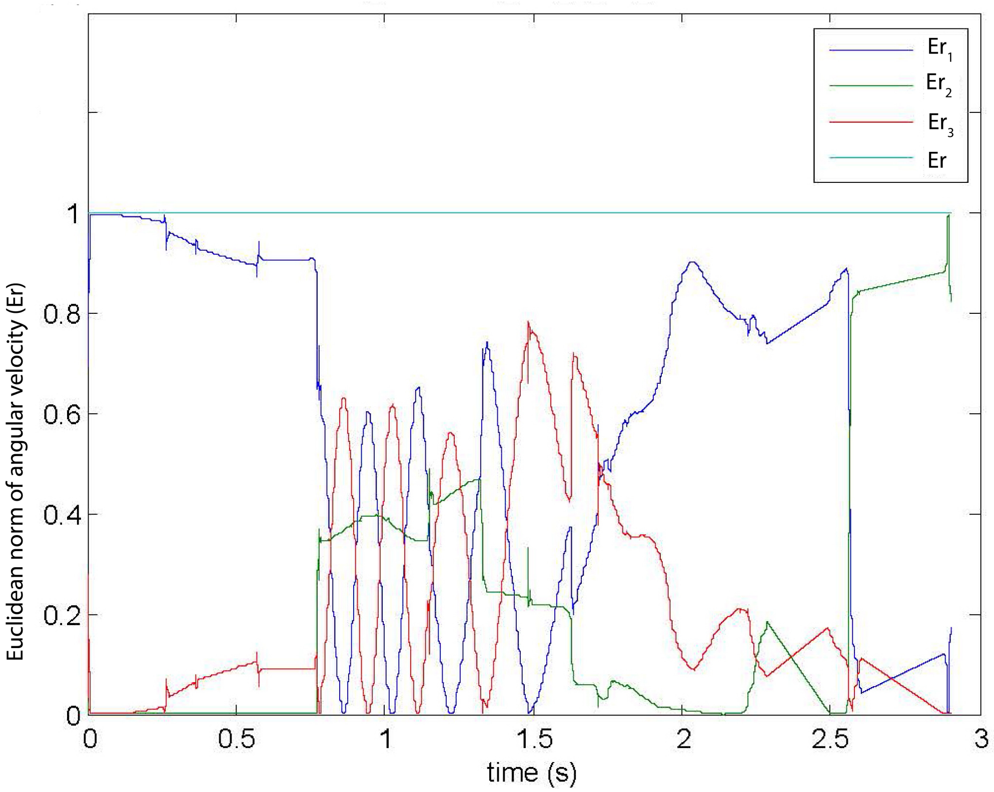

FIGURE 3.14: Euclidean norm of angular velocity for each principal axis of inertia.

3.7 RAMMS::Rockfall rigid-body rockfall model

The rockfall model applied in this work is based on a code developed by Schweizer (2008), Schweizer et al. (2011) for hard contact detection between rigid-bodies. This provided the foundation for the rigid-body rockfall model (Leine et al., 2014) which has been integrated into the RAMMS natural hazards software which includes an advanced graphical user interface (Christen et al., 2012). The name for the software is

"RAMMS::Rockfall", which is a command input method taken from the IDL (Interactive Data Language) with which the RAMMS user interface is programmed. Within this section a summary of the model features, parameters and mechanics that are applied to perform rockfall simulations is provided. For a complete explanation see Schweizer (2008), Schweizer et al. (2011), Leine et al. (2014).

RAMMS::Rockfall models complex mountain terrain using a high-resolution digital elevation model, and the rock-body is modelled as a convex hull polyhedron that is indestructible. The shape of rock body's are user defined by providing a point cloud of the geometry. Shapes can be simple geometric forms or models of real rocks. Compared to rebound models that employ apparent restitution coefficients to model entire impacts, the rigid-body approach applies forces to the rock edges and corner points, and a special ground contact friction and drag model which simulates the effects of impact scaring and soil deformation. Modelling the rock-ground contacts in this manner permits the entire mechanics of an impact to be simulated deterministically. The moment arms and torques responsible for how different rock-shapes convert translational movement into angular momentum and influence rebound heights are computed, allowing an accurate model of rolling, skipping, sliding and jumping.

With this deterministic approach, the influence of rock-shape on the dynamics of runout can be simulated. This is important because the model is highly sensitive to rock-shape, which for rebound approaches, has previously had to be treated with stochastic methods (Bourrier et al., 2009a). The role of rock-shape in runout dynamics is crucial in determining rotational and rebound behaviour. For specific rock-shapes, distinctive runout behaviour such as extreme jump heights and runout distances are observed. Dynamics of this kind are decisive for hazard mapping and rockfall protection structures, and with full three-dimensional data of rock position, velocities, rotations, energies and impact forces, rockfall management and the design of protection structures can be optimised.

The application of rigid-body theory to rockfall modelling has advanced the capacity to include detailed and hazard-specific information on rock-shape and size. This allows the inclusion of lithology and geological setting to establish realistic initial conditions. With RAMMS::Rockfall predefining the shape, size and release orientation of detachable rocks is an essential part of the analysis. The observation that different geological settings produce characteristic rock shapes has been well-documented by Fityus et al.

TABLE 3.7: RAMMS::Rockfall dynamic data of each rockfall trajectory that is available to the user.

Data symbol	Description	Units
t	time	s
x	X coordinate CoM (CoM = Centre of mass)	m
y	Y coordinate CoM	m
z	Z coordinate CoM	m
$p0$	Quaternion	
$p1$	Quaternion	
$p2$	Quaternion	
$p3$	Quaternion	
v_x	Velocity (X) CoM	ms^{-1}
v_y	Velocity (Y) CoM	ms^{-1}
v_z	Velocity (Z) CoM	ms^{-1}
w_x	Angular velocity about inertial axis (X)	$rad \cdot s^{-1}$
w_y	Angular velocity about inertial axis (Y)	$rad \cdot s^{-1}$
w_z	Angular velocity about inertial axis (Z)	$rad \cdot s^{-1}$
E_{tot}	Total energy including potential energy with respects to the lowest point in simulation domain	kJ
E_{kin}	Total Kinetic energy	kJ
$E_{kintrans}$	Translational Kinetic Energy	kJ
E_{kinrot}	Angular kinetic energy	kJ
zt	Height position of lowest point on rock body's surface	m
F_n	Normal contact force	N
F_t	Tangential contact force	N
$Slippage$	Slippage distance	m
μs	Coulomb friction value	$\mu = tan\theta$
v_{res}	Absolute velocity	ms^{-1}
w_{res}	Absolute angular velocity	$rad \cdot s^{-1}$
$jumpH$	Jump height, vertical distance of CoM to the terrain surface	m
$projDist$	Projected distance traced over ground from release point	m
Jc	Distance to the centre of SD	m
JH_{Jc}	Distance between SD at Jc to CoM	m
SD	Distance between two impacts	m

(2013) among others. RAMMS::Rockfall includes a rock library with which common rock forms with user defined that volumes can be generated and used directly for a tailored rockfall simulation.

3.7.1 Terrain model

The RAMMS rockfall model simulates the trajectories of falling rocks over a three-dimensional terrain defined using a high-resolution digital elevation model. The terrain coordinate system is taken as the simulation frame O. Terrain elevation Z_m is specified for each coordinate pair (X_m, Y_m), for which four coordinate pairs define the vertices of planes constructing the tessellated terrain surface (Figure. 3.15). The planes are flat, while their orientation is different because the Z_m- elevation of each coordinate pair can differ. The distance between coordinates (X_m, Y_m) defines the model terrain resolution and therefore the detail with which the terrain morphology is represented. Typically, a resolution between 1.0 m and 10.0 m is employed for simulations as this accurately models potentially important terrain features such as gullies and cliffs. It is important to note that the resolution of the digital terrain model will affect the outcome of modelling results, because terrain features can be missed or modelled as completely rigid bodies when in fact they are unconsolidated sediment such as talus. Details of these effects are discussed in Bühler et al. (2014). The properties of each plane can be varied to take into account variable surface properties, such as hardness and roughness. Forests for example are defined to be planes with enhanced drag.

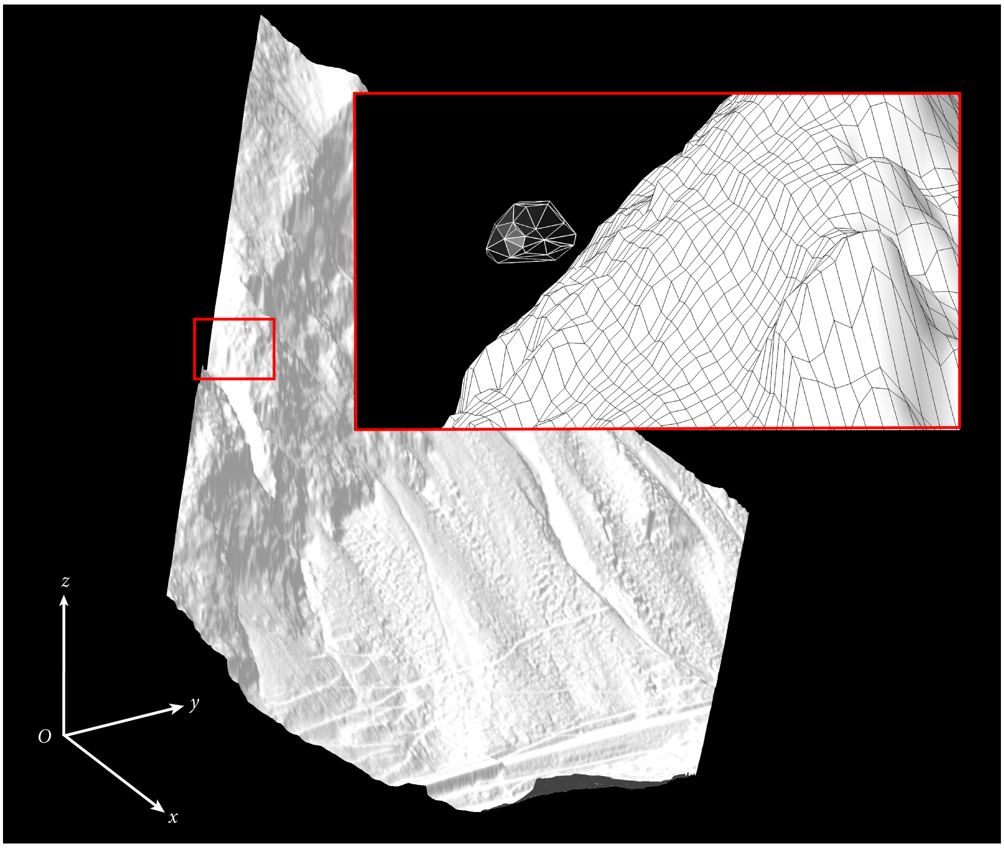

FIGURE 3.15: High resolution three dimensional terrain model, forms simulation frame O in which the four sided planes form the tessellated terrain surface with which the rock-body can come into contact with.

3.7.2 Rock model

Rock bodies are introduced into the simulation domain coordinate frame as a cloud of points based in a coordinate system of their own with origin (K). The coordinate frame (K) serves to map the rotations of the rock-body. Points are given in x, y, z format as $^*.pts$ files, and can be artificially generated or gathered from rock deposits directly (Figure. 3.17). A convex hull of the rock-body's point cloud is created, and in doing so an entirely convex body is created, whereby concavities are closed. The next step is to calculate the centre of mass of the body, for which the density is assumed to be homogeneous. Finally, the inertial tensor of the body is calculated finding the three principal moments of inertia, where the origin is the rock's centre of mass (S). The translations of the rock-body in the simulation domain are mapped using the coordinate frame K in relation to O (Figure. 3.16).

The rock's mass m is derived from its volume calculated from the convex-hull of the point cloud and density ρ which is user defined (typically 2700 $kg\ m^{-3}$). The rock has three translational (linear momentum) and three rotational degrees of freedom (spin) to describe the rocks mass centre position q^T=(X,Y,Z) any time t in the terrain coordinate frame O. Rotational motions capture the orientation of the rock's external geometry in space. At time t=0 the rock is released from position (X_0,Y_0,Z_0), which is located at some distance above the terrain, $Z_0 > Z_m$, and thus the release height h_0 is h_0=$Z_0 - Z_M$.

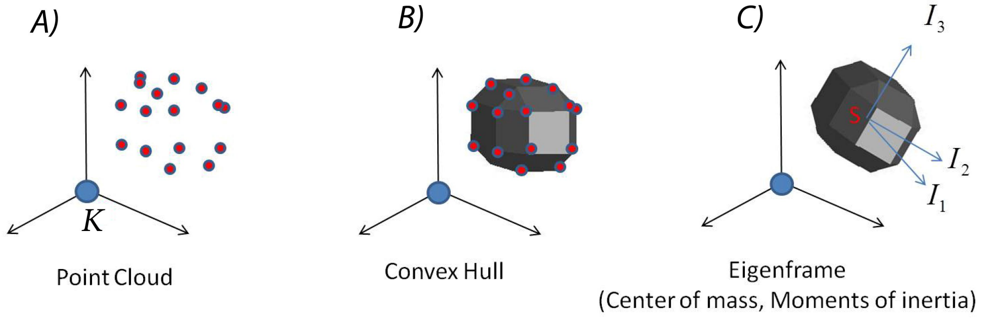

FIGURE 3.16: Depiction of how RAMMS::Rockfall generates rigid-body rocks from a point cloud of its geometry. A) The rocks geometry is described with a set of point in the rock coordinate system K its Eigen frame. B) A convex-hull of the points is made, this is essentially like draping a cloth over all the points and pulling it tight. C) Within the Eigen frame the centre of mass and moments of inertia are computed.

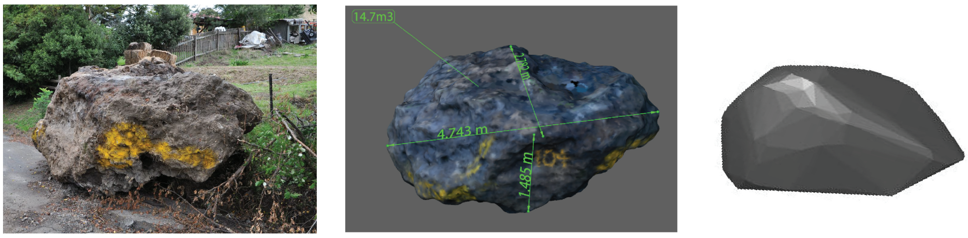

FIGURE 3.17: Laser scans of real rocks are captured in the field converted into rigid-body rocks for RAMMS::Rockfall simulation. The point cloud representing the rock geometry is then used to model a convex-hull polyhedron representative of the rock-body to be used in the rockfall model. Image (*left* Louise Vick, Canterbury University New Zealand. Image (*middle*) Garth Archibald, GNS sciences, New Zealand.

3.7.3 Motion and contact-impact

In free flight, the governing equation of motion is defined by (see Leine et al. (2014)):

$$M\dot{u} - h(q, u) = 0 \tag{3.18}$$

where M is the constant and diagonal mass matrix containing the mass m and three moments of inertia I. The vector u contains the rocks three translational and three rotational velocities. The rock motion is governed by a number of forces which can determine the trajectory. Gravitational force (F_g) acts globally; a drag force (D) is implemented to represent the effects of trees, undergrowth and soil deformation, along with gyroscopic forces G which can cause rocks of irregular shape to become upright and rotate about a rolling axis. All force terms h are functions of the rock's position q and velocity u forming the force vector h:

$$h(q, u) = \left\{ \begin{array}{c} F_g + D \\ G \end{array} \right\} \tag{3.19}$$

During contact between the rock and the terrain, contact forces λ and frictional contact forces (F_c) act about the point of contact. These forces can be considered as external forces that change the direction of the falling rock.

The contact of the rigid rock is detected by continually measuring the vertical gap length g_N between the rock body's corner points (P) and the terrain projections (Q) for every time step (Fig. 3.18). The gap length is defined as

$$g_N(X, Y, Z) = Z - Z_m(X_m, Y_m) \tag{3.20}$$

When $g_N > 0$ there is no contact, but when $g_N \leq 0$ there is contact and the contact forces λ, acting at the contact point P, are computed. The contact forces are denoted using the Greek letter lambda because the contact forces are lagrangian multipliers that enforce the non-penetration constraint. Minimal penetration with the terrain is permitted to allow the assessment of the contact condition (3.20). This is a non-physical penetration and purely for numerical purposes.

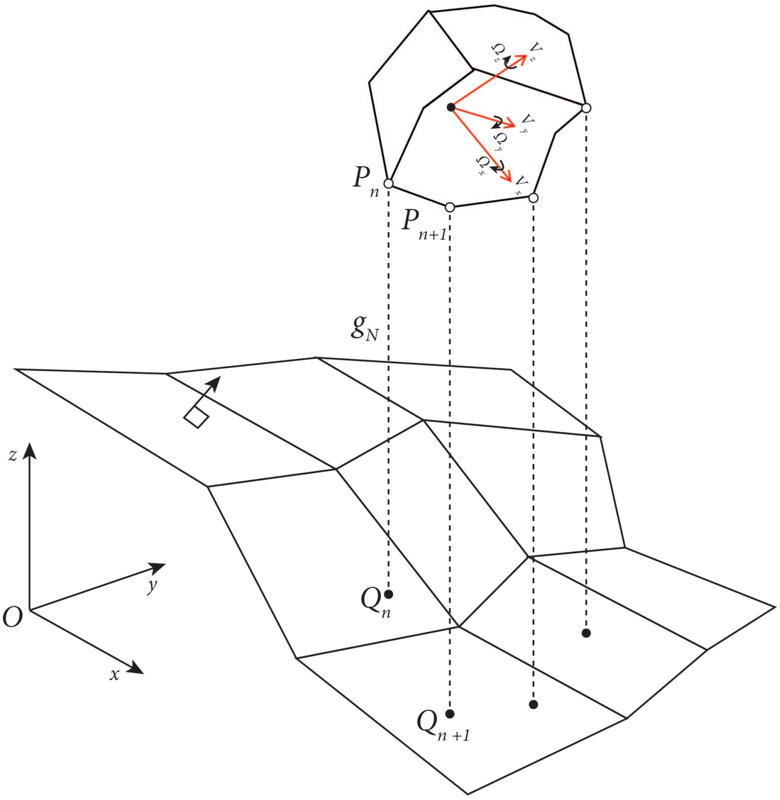

FIGURE 3.18: RAMMS::Rockfall contact detection.

3.7.4 Contact forces

During contact, the governing equations of motion are defined as:

$$\mathbf{M}\dot{u} - h(q, u) = W(q)\lambda, \tag{3.21}$$

where the direction of the contact forces is given by $W(q)$. There can be a number of active contact forces depending on the rock's configuration at the point of contact. Ultimately it is the combination of these forces λ (and force directions $W(q)$) that allows the complex rotations and trajectory deviations to be simulated.

The advantage of this hard-contact rigid-body approach is that the contact forces are applied directly about the contact points, respecting the configuration (orientation and kinetics) of the impact. This is achieved by considering the contact pair (Q, P) within the contact frame $C = ({}_O n, {}_O t_1, {}_O t_2)$ which is attached to the terrain surface at contact point Q (Fig. 3.19).

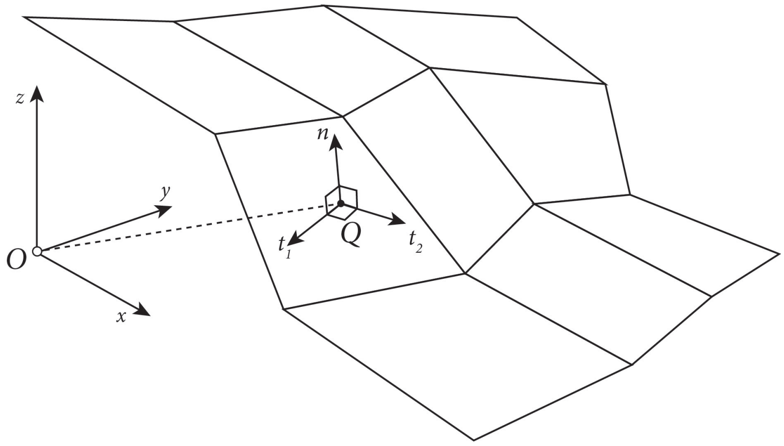

FIGURE 3.19: Contact frame C at point Q detected with the gap function g_N.

The contact frame C has a normal contact force component λ_N and two tangential components $\lambda_{T1}, \lambda_{T2}$. The contact force λ_N guarantees the unilaterality of the contact, i.e. the non-penetration constraint. The tangential force components are due to Coulomb friction and are governed by the contact laws.

3.7.5 Friction forces

The normal force component λ_N is resolved with a contact cone differential inclusion in which the transient normal force vector over the finite contact period can be computed. During the contact period this is a set-valued normal force considering all periods of contact identified with the gap function g_N. The tangential force component λ_T is assumed to obey Coulomb's friction law. Stiction of the contact occurs $\gamma_T = 0$ as long as the magnitude of the tangential force $\|\lambda_T\|$ is less than $\mu\lambda_N$ in which λ_N is the applied normal force and μ the friction coefficient. The direction is also resolved with a normal cone inclusion projecting a friction disc on to the surface (Fig. 3.20). This formulation covers both sticking and sliding cases during impacts.

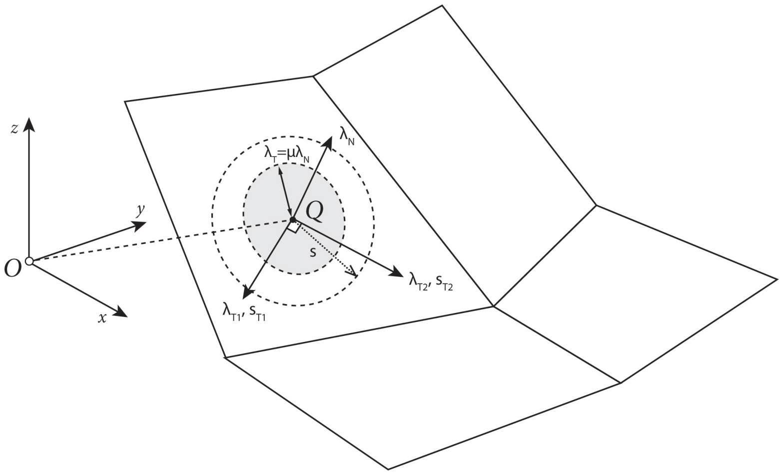

FIGURE 3.20: RAMMS::Rockfall model friction frame. The rock contact point at Q is allowed to slip s within the friction cone composed of two tangential frictions (λ_{T1} and λ_{T2}) and λ_N which govern the direction of s.

3.7.6 Impulsive forces

Impulsive contact forces occur when ever the gap function detects contact with negative velocity $\gamma_N^- < 0$: that is to say that the point would theoretically move through the terrain surface if not treated with the impulsive contact force. This requires a velocity jump such that the post-impact normal velocity is non-negative $\gamma_N^+ < 0$. This impact law is based on a Newtonian impact law in which the relative normal velocities of the contact pair before and after impact are governed by ε_N the normal restitution coefficient. $\varepsilon_N = 1$ corresponds to complete restitution of normal velocity while a smaller ε_N dissipates energy. Generally speaking this value is set very low. Newton's law is fulfilled if (3.22):

$$\gamma_N^+ + \varepsilon_N \gamma_N^- = 0. \tag{3.22}$$

Impulsive normal forces also induce impulsive tangential forces. While this is mainly seen in the elastic impacts of super-balls (Cross, 1999), in the rockfall model ε_T is set at $\varepsilon_T = 0$ since these effects are absent.

To determine the resultant force direction acting on the rock-body the configuration of the impact must be computed. This requires finding the relative velocity between the contact points P and the terrain Q. Importantly, the velocity of contact point P is composed of the translational velocity with respect to the body's centre of mass v_S and its angular velocity ${}_K\Omega$ in the fixed body frame (K), for which P also has a fixed position vector relative to the centre of mass S. The contact algorithm in the rigid-body approach considers the rotational speed of the rock at contact. Because the forces are then applied at points away from the centre of mass, and with a direction respecting the impact configuration, to a body with three degrees of translational and rotational freedom, torques and moment arms can act generating rotations and rebounds that represent the true mechanics of an impact.

3.7.7 Contact Friction and drag

Two physically different forces oppose the motion of a falling rock: *sliding friction* and *drag*. Sliding friction acts at points of the rock's surface that are in contact with the ground. Sliding friction is a Coulomb-type friction associated with the distance the rock slides on the ground. When the rock is no longer in contact with the ground, this friction no longer acts. However, because this friction acts on a point on the rock's surface, it will generate torque that initiates rotational movement. The parameterisation of the friction force is of great importance because it controls when the rock slides, rolls or jumps. Drag, on the other hand, acts at the rock's centre of mass and therefore creates no additional rotational moment. Drag acts in the direction opposite to the rocks movement (velocity). There are two drag forces parameterized in the RAMMS::Rockfall model. The first accounts for vegetation drag; the second accounts for the viscoplastic drag due to terrain deformation during ground contact. Full details of how the drag forces are implemented and typical ranges of values are explained later in this chapter (Section. **??**).

3.7.8 Coulomb Friction and Slippage

The mechanical contact law considers hard contacts between the rigid-body and the terrain. In principle, this is only representative of extremely hard rock-on-rock contacts. In reality rock-ground interaction occurs between a range of different materials with differing deformation properties. In an extreme case, the rock contact can be with soft soils that easily deform under contact. In such contacts there is a compliance of the soft soil terrain and a degree of penetration and sliding of the rock-body as it ploughs into the soil cover accumulating material behind, it leaving distinctive impact scars (Figure. 3.21).

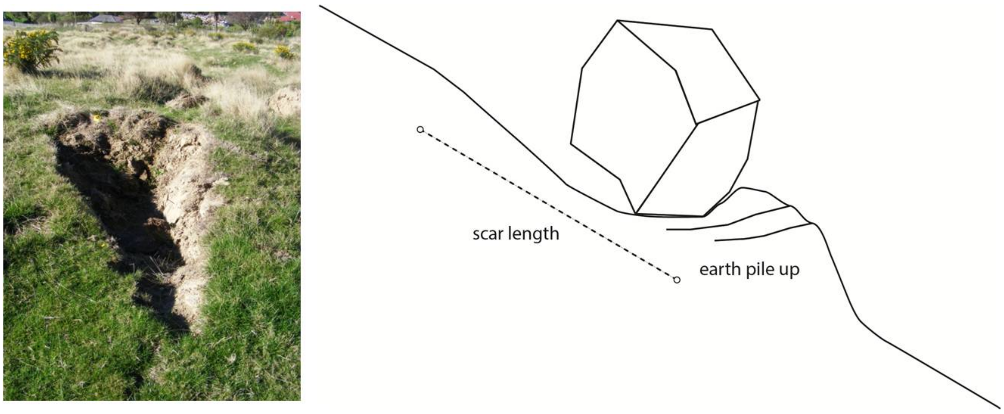

FIGURE 3.21: Rock impact scar on soft soil; the scar morphology is tapered widening towards the accumulation of earth at the scar end were an earth ramp structure is formed. This is modelled as a climbing friction from the beginning of the scar $s = 0$ at first contact which tends towards high friction at the end of the scar.

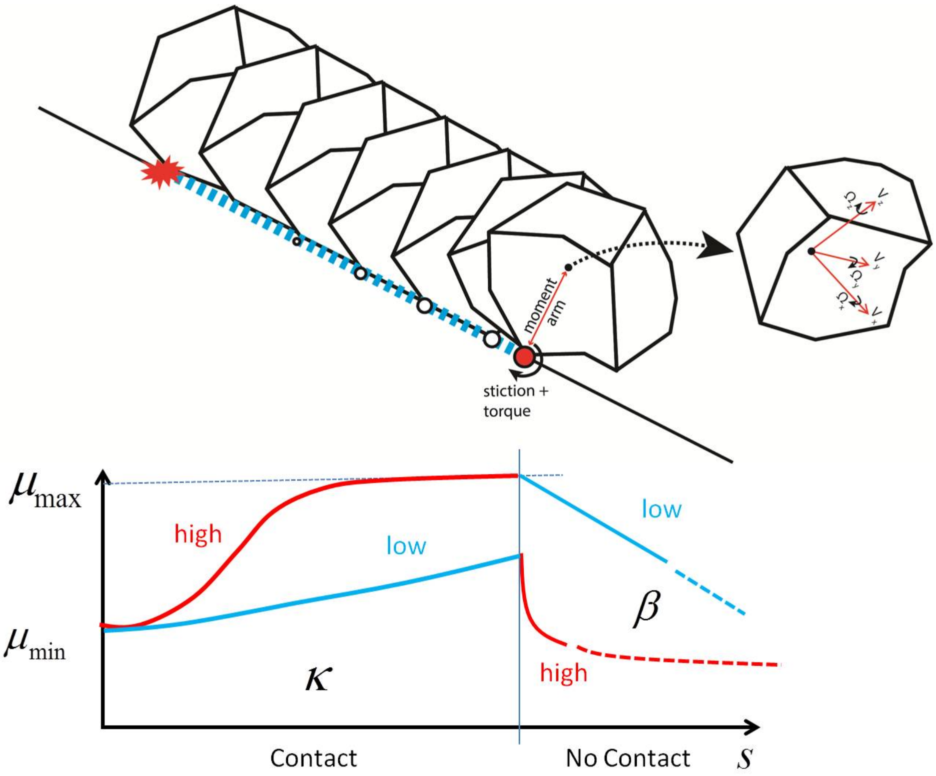

FIGURE 3.22: A schematic depiction of the slippage model where rock contact and slips during the contact period. At the moment of contact friction μ_{min} climbs to μ_{max} as a function of κ creating torque resulting in non-contact and the decay of friction as a function of β.

To simulate ground deformation within the framework of a hard contact model requires the introducing of a slip (s) dependant friction that acts during sliding and accounts for the increase in friction due to material accumulation behind the rock as it slides during the impact. The slip dependant friction is an extension of the Coulomb friction model in which the friction value μ is made dependant on the slip distance (s) travelled by the centre of mass $\mu(s)$ (Figure. 3.22). In this instance,

$$\lambda_T = \mu(s)\lambda_N. \tag{3.23}$$

The force λ_N enforces a non-penetrability constraint. The force λ_T acts tangentially on the terrain surface (see Fig. 3.20). The dependence of the friction coefficient on the slip distance (s) is:

$$\mu_{(s)} = \mu_{begin} + \frac{2}{\pi}(\mu_{end} - \mu_{begin})\arctan(\kappa s) \tag{3.24}$$

Where μ_{begin}, μ_{end} and κ are parameters of the friction model. The initial friction encountered at the contact where $s = 0$ is μ_{begin}. Over the slip period, μ tends toward μ_{end} for large slip values (see Figure, 3.22). The parameter κ controls how quickly the friction increases from μ_{begin}, to μ_{end}. Typically $\mu_{begin} < \mu_{end}$ meaning that the friction increases the longer the rock is in contact with the ground. It is entirely possible that there are brittle ground materials where the opposite behaviour ($\mu_{begin} > \mu_{end}$) is encountered. The slip distance (s) is a transition state variable having a time evolution which is defined as the following:

$$\dot{S} = \begin{cases} \|v_S\| & \text{if contact with terrain} \\ -\beta_S & \text{else} \end{cases} \tag{3.25}$$

The parameter β controls how quickly the friction is released as the rock departs the ground scar. If β is large, friction is immediately removed as the rock moves away from the ground. Conversely, when β is small, sliding friction can act, even after the rock is no longer in contact with the ground. The parameter β is linked to the penetration depth of the rock into the ground. Larger penetration depths (softer materials) are associated with smaller β values.

3.8 Drag forces

3.8.1 Viscoplastic Ground Drag

An additional slip dependant drag force is introduced to account for the viscoplastic deformation that occurs in soft soils under rock impact. Large viscoplastic deformations are also encountered in harder substrate materials such as scree, where rubbing between scree granules dissipates energy. Viscoplastic ground drag is given by:

$$D_v = -C_v \frac{m}{2} V_s^2 \qquad C_v = \begin{cases} \hat{C}_v(X,Y) & \text{if } g_n < 0, s > 0 \\ 0 & \text{if } g_N \geq 0 \end{cases} \tag{3.26}$$

Ground drag acts when the rock is in contact with the ground ($g_N < 0$) as the rock is sliding on the terrain surface ($s > 0$). The drag force F_v is proportional to the square of the rock velocity V_s^2 as well as the mass of the rock m. That is, heavier and faster moving rocks will experience more drag than smaller, slower moving rocks, as they penetrate the ground surface. The drag force is proportional to the rock total kinetic energy. The drag coefficient $\hat{C}_v$ varies between 0 (hard) and 1.0 (soft).

3.8.2 Forest-Vegetation Drag

Forest drag is given by (Fig. 3.23):

$$F_f = -C_f V_s \qquad C_f = \begin{cases} \hat{C}_f(X,Y) & \text{if} Z < Z_h \\ 0 & \end{cases} \tag{3.27}$$

The idea behind forest drag is that a resisting force acts on the rock centre of mass when it is located below the drag layer height Z_h. This force is linearly proportional to the rock velocity V_s. The forest is parameterized by the effective height of the vegetation layer Z_h as well as the drag coefficient $\hat{C}_f$. The effective height Z_h roughly corresponds to the height of the forest but in some cases, for example in old forests, the drag force in the tree crowns might be negligible and therefore the effective height could be smaller than the actual tree height. The model does not account for a Z-dependency in forest structure as it assumes a homogeneous layer with mean drag properties. Typical values for Z_h are between 1 m and 10 m; typical values for $\hat{C}_f$ range between 1000 $kg\ s^1$ and 10,000 $kg\ s^1$. It is acknowledged that the solution of a homogeneous drag layer to represent forested areas in a generalised assumption and by no means models the true effects of a forest stand. The implementation of an effective and physically correct forest model remains future work.

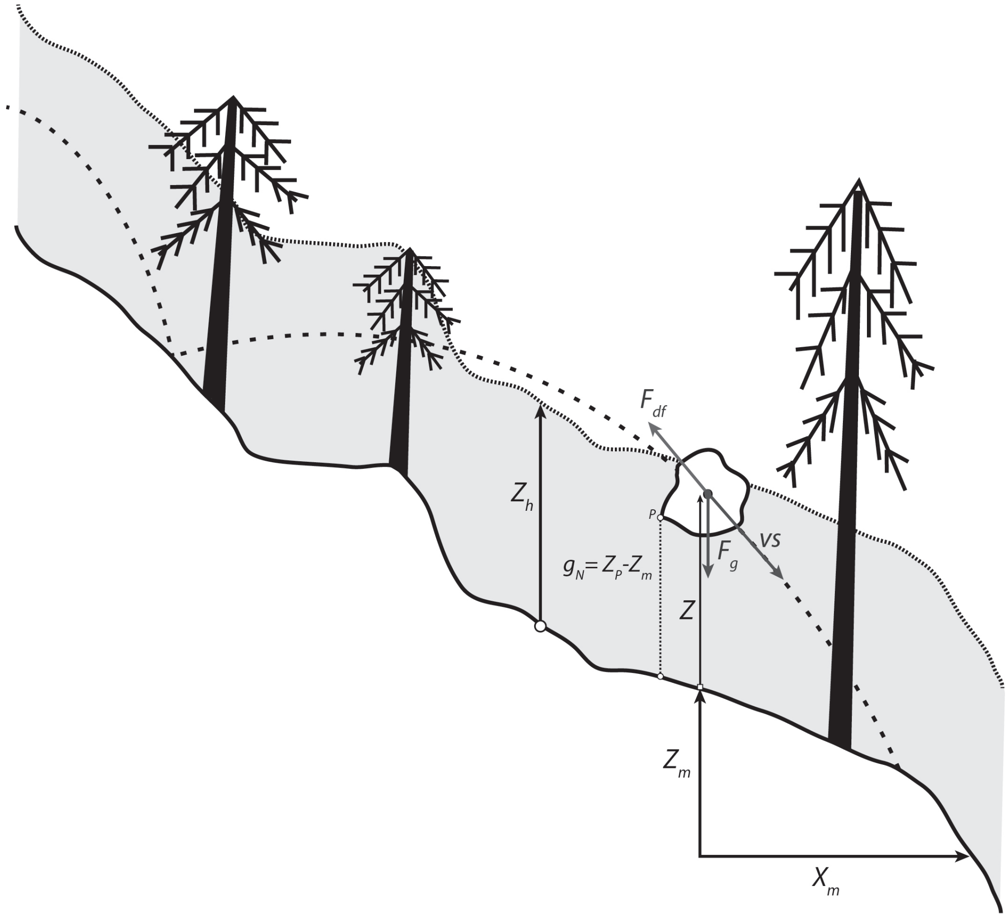

FIGURE 3.23: Forest drag is implemented to act on the centre of gravity of the rock body at height zh.

3.9 Model parameter selection

Applying the rockfall model to investigate the additional aspect of shape, a body's angularity; first required a degree of model calibration and validation based on the physical experiment results. Two model input parameters, the normal coefficient of restitution and the static friction angle, could be selected based on two simple physical tests. The ϵ value, which is a true restitution coefficient, was measured with a simple drop test onto the ramp surface involving a perfect sphere made of the aluminium used to fashion the test rocks (Figure. 3.24).

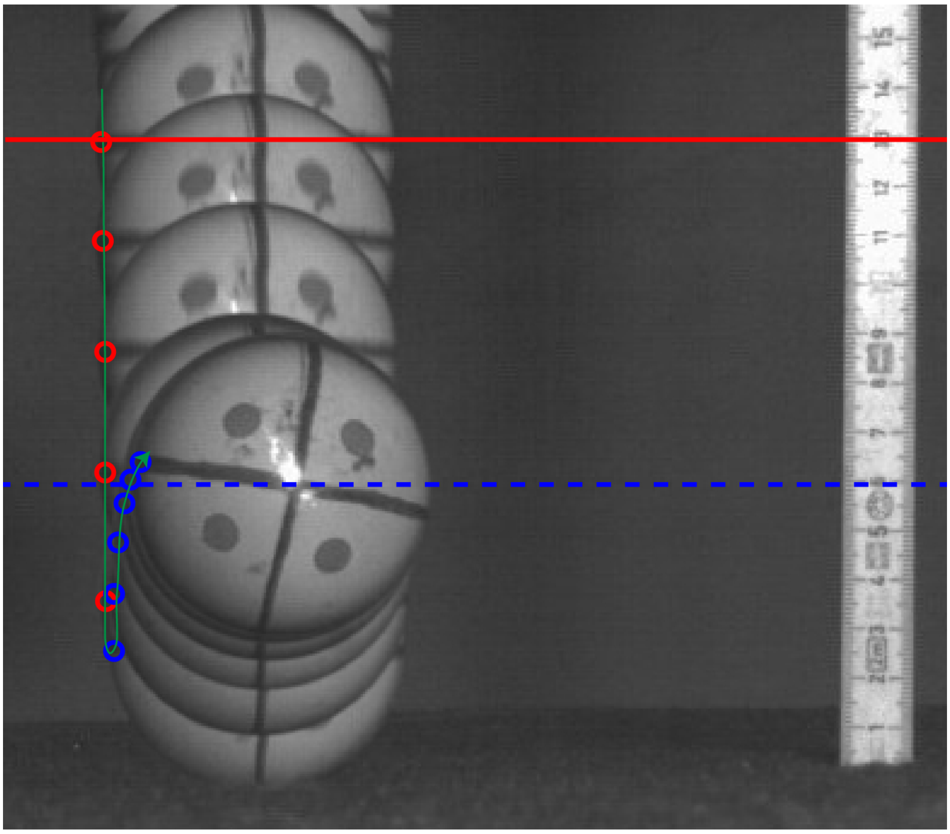

FIGURE 3.24: Sequence image of a drop test to determine ϵ the slope normal coefficient of restitution between the terrain surface of the physical experiments and the aluminium material used to fashion the test rocks.

In these small series of drop tests it can also be seen that the ϵ value (equivalent to R_n) also responds with a negative correlation to increasing impact velocity. For the purposes of the numerical experiments, an average of the ϵ values was taken, which was $\epsilon = 0.48$. The high ϵ value in this case reflects the inherent bounciness of the wood used in the construction of the planar slope, which also partly explains the high R_n values observed during the physical experiments with the test rock forms (Section. 4.5).

The static friction angle was measured by placing the test blocks on the experimental test slope and gradually increasing the slope inclination until sliding occurred. From these experiments a $\mu_{max} = 0.6$ was selected, this is the equivalent to a friction angle of 30°. An issue with this measure of friction is that it only represents the friction value for a rock-ground contact involving sliding. During the impact process, and in cases when a rock body meets a degree of surface roughness, the effective friction can be significantly higher than static friction. It is during these impulsive high friction events that the high contact forces are generated which cause the rock to jump and rotate on rebound. Therefore, setting the frictional parameter space, of the contact-impact slippage model, that suitably modelled the range of potential contact conditions, was one of the main tasks of the model validation exercise.

The main model parameters steering the slippage friction model are μ_{min}, μ_{max}, κ and β. Full details of these model parameters are provided earlier in this chapter. In summary, μ_{min} and μ_{max} set the model friction space, i.e. μ_{min} is the first friction value that a rock-ground contact will be exposed to. During the contact period the friction then climbs towards the μ_{max} as a function of κ. Once contact is lost, friction returns to μ_{min} via the function β.

3.10 Summary of methods

- The methodology which uses numerical rockfall modelling to provide the link between full scale rockfall experimentation and observations of live rockfall events with physical experiments with small rocks is explained.

- Details are given of how 2D videogrammetry is complimented with a novel 3D motion sensor, the StoneNode, which includes 3-D accelerometers and gyroscopes to provide measurements of the full three-dimensional motions of rocks during runout.

- An explanation of how apparent restitution coefficients are computed from velocity measurements made from video observations is outlined. The methodology allows a comparison of the values measured with those of current literature. Moreover, a measure of the impact configuration α of rocks as they impact the slope is provided.

- The model description of the RAMMS::Rockfall software is supplied with detailed graphical additions to assist the explanation. This is a simplified summary of a more complete and detailed explanation provided by Leine et al. (2014) in which the time stepping methods are also explained. While it is possible with the rigid-body approach to model multi-body interaction of many particles, and it would be possible to include a fragmentation law in the model, these features are not yet implemented in the model and remain areas for further development.

Chapter 4

Physical experiments on rock-shape

4.1 Introduction and experimental design of the physical experiments

The physical rockfall experiments were conducted using small rocks embedded with micro-sensor technology 3.2.2. The size of the laboratory apparatus assisted in overcoming the requirement for repeatable tests with sufficient iterations to examine the results in a statistical manner providing a quantification of characteristic rockfall behaviour according to rock-shape. Data of this resolution and volume required to quantify characteristic rockfall behaviour would not have been possible if larger rocks in natural terrain were used due to the impracticalities of experimentation at such large scale.

The decision to use small rocks allowed an accurate control over their size (940.0 cm^3) and shape. Moreover, the dimensions of the experimental apparatus and rocks ensured that the dimensions of the physical experiments could be well constrained for the numerical model in which these experiments are back-analysed (Chapter. 5). The physical experiments were designed to focus on the influence of changes in rock form on runout behaviour, thus, three end-member rock forms *equant*, *elongate* and *platy* were selected. The additional variables that were included in the experimental design were: i) slope angle; and ii) release orientation.

The planar slope could be adjusted to five different slope angles (20°, 27°, 37°, 42° and 55°). This was performed to examine if the classical modes of rockfall motion according to slope angle, as identified by Ritchie (1963), also hold when different rock-shapes are involved.

The final variable, rock release orientation, had the purpose of investigating whether the initial impact and acceleration phases of rockfall are influential in determining the runout dynamics and deposition patterns of each rock-shape. The reason behind investigating release orientation is rooted in the contrasts in the magnitudes of the principal moments of inertia inherent to changes in rock-shape. This was designed to observe how different alignments of the principal inertial axes with respect to the slope fall line affect the runout dynamics and deposition patterns. This is important because, in rockfall producing rock-masses, the discontinuities that predefine rock-shape and size also predefine their release orientation. Therefore, rock-mass characteristics have the potential to predetermine the rockfall behaviour of a particular geological and geomorphological setting.

4.1.1 Chapter overview

This chapter presents the results of these physical experiments in which a total of 1500 experiments were conducted. The data are examined in a systematic way building up from the runout deposit patterns in the first section. This is designed to identify if specific rock shapes generate characteristic runout. In addition to characteristic trajectories to see if they also hold characteristic runout zone geometry. The data produced during these testing series are available for further study. Should you be interesting in using any of these data, please make contact with the author.

Following analysis of the deposition patterns, the dynamic data captured from rockfall in motion are examined to quantify the translational and rotational motions of the different shapes; in addition to investigating relationships between the test rock dynamics and deposit patterns this includes an assessment of rock velocity, jump height and rotational behaviour.

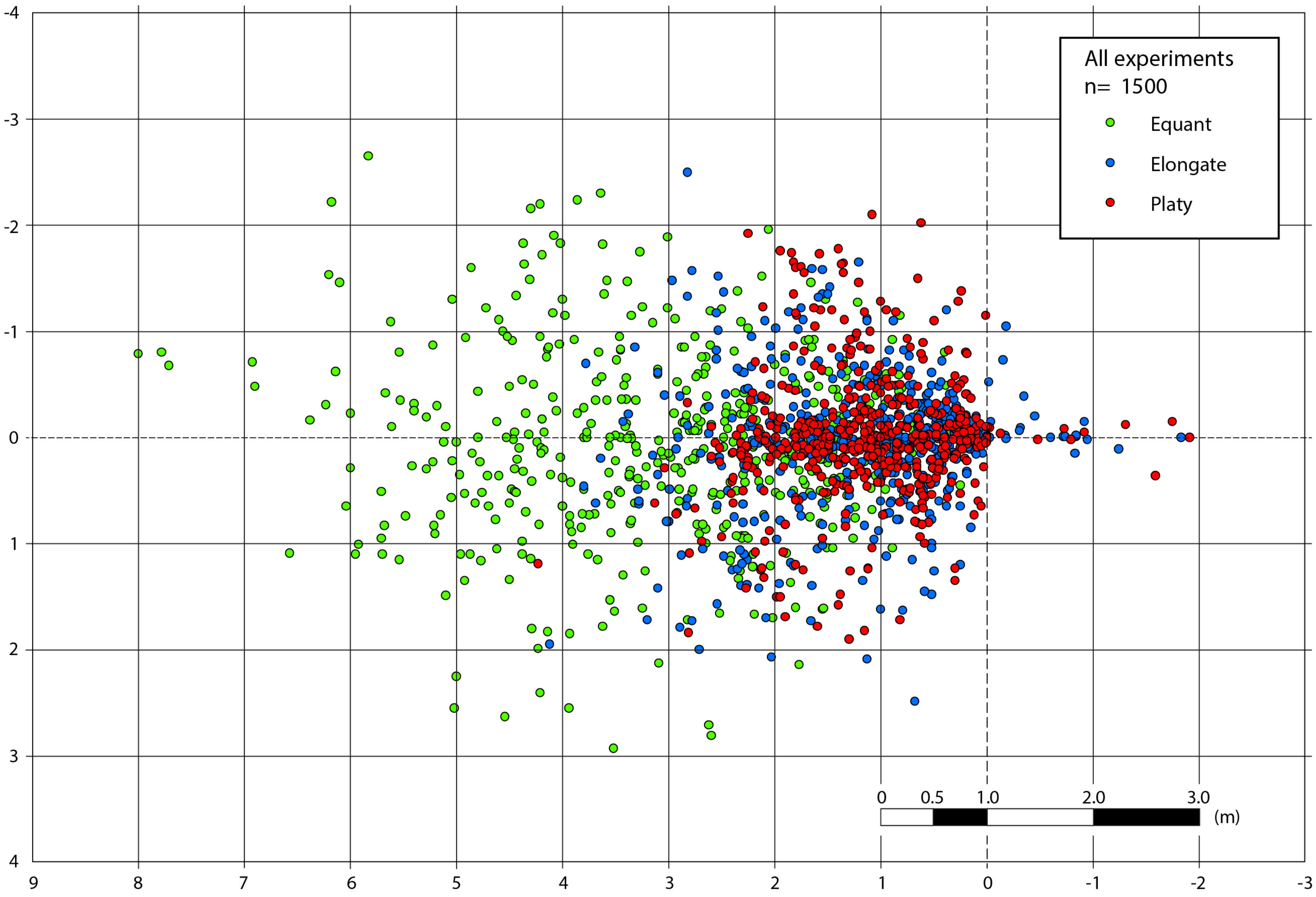

Figure 4.1: On the map the experiment was run from right to left and the toe of the slope is marked with the dashed line. Points which lie to the left of the zero line reflect test bodies which became stuck on the slope, which only occurred for non-equant rocks. Mapped deposition data from laboratory experiments is plotted for every slope angle in which the entire $n = 1500$ data set presented. The three end-member shapes the *equant* (green), *elongate* (blue) and *platy* (red) are differentiated by their colour.

In order that the findings can be compared with current research on rockfall rebound, apparent restitution coefficients of impacts during the experiments (Section. 3.4.2) are considered. This section draws together the findings of measured dynamics to investigate how the rock-ground impact configuration controlled by shape affects the nature of the rebound behaviour and rotational dynamics of rockfalls which lead to the observed deposition patterns recorded.

4.2 Runout zones

Here the effect of different rock-shape on runout behaviour is quantified. The mapped deposition data are presented in Figure 4.1, and are presented as individual shape classes in Figure 4.2, to observe the influence from rock-shape on delineating the deposit zone, of which the geometric properties (length, width, and area) are extracted.

The first general observation that can be made from the runout deposition patterns (Figure. 4.1) is that the *equant* rock shows greater runout distance than non-equant rocks. However, there are many underlying variables that complete the entire data map that render any further interpretation of Figure 4.1 unreasonable without disaggregating each data set.

Figure 4.2 separates each map by rock-shape, and includes data from each slope angle. The runout-zone's area was measured by calculating the convex hull around the deposit end points from the toe of the slope. Any points further than one standard deviation away from neighbouring points in both x and y directions were considered outliers and excluded from this analysis. The areas are 29.86 m^3, 15.36 m^3 and 10.14 m^3 for the *equant*, *elongate* and *platy* rocks, respectively. This shows that the *equant* rock is most mobile running out over the greatest area, while the *platy* rock is the least mobile with comparatively a third the area of the *equant* rock.

The shape of the runout-zone area is characterised by the ratio of maximum width to maximum runout length W/L (see Sect. 3.2.5) normal to and parallel to the slope, termed the dispersion factor. Values towards 0 reflect long and narrow inundation;

FIGURE 4.2 *(following page)*: Maps only showing each data set from the three end-member shapes the *equant* (green), *elongate* (blue) and *platy* (red), each data set contains 500 experiments.

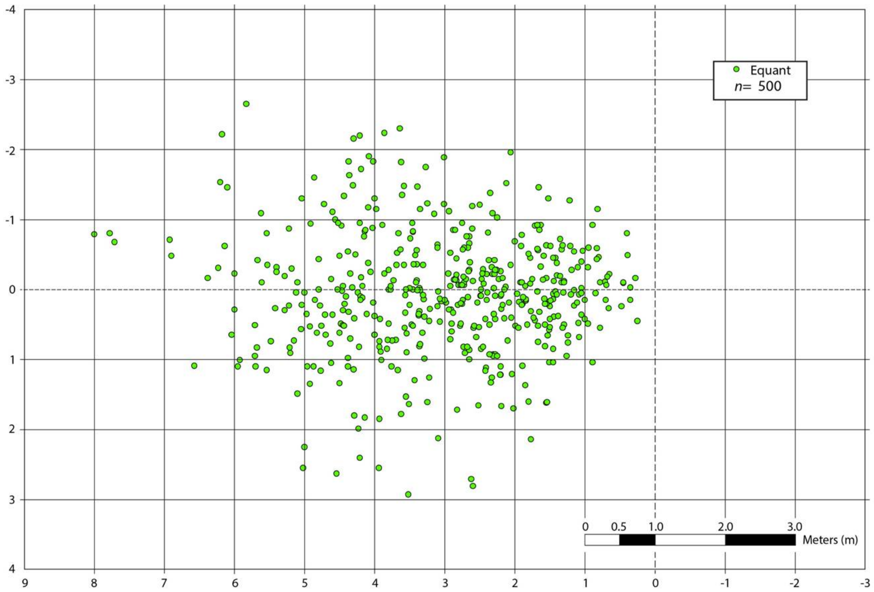
Equant
n= 500
-4
-3
-2
-1
0
1
2
3
4
9
8
7
6
5
4
3
2
1
0
-1
-2
-3
0 0.5 1.0 2.0 3.0
Meters (m)

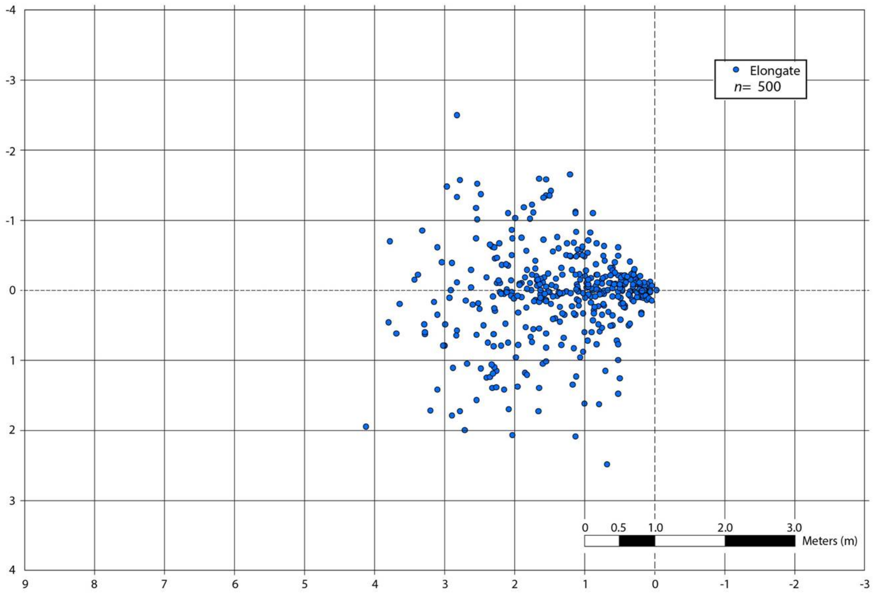
Elongate
n= 500
-4
-3
-2
-1
0
1
2
3
4
9
8
7
6
5
4
3
2
1
0
-1
-2
-3
0 0.5 1.0 2.0 3.0
Meters (m)

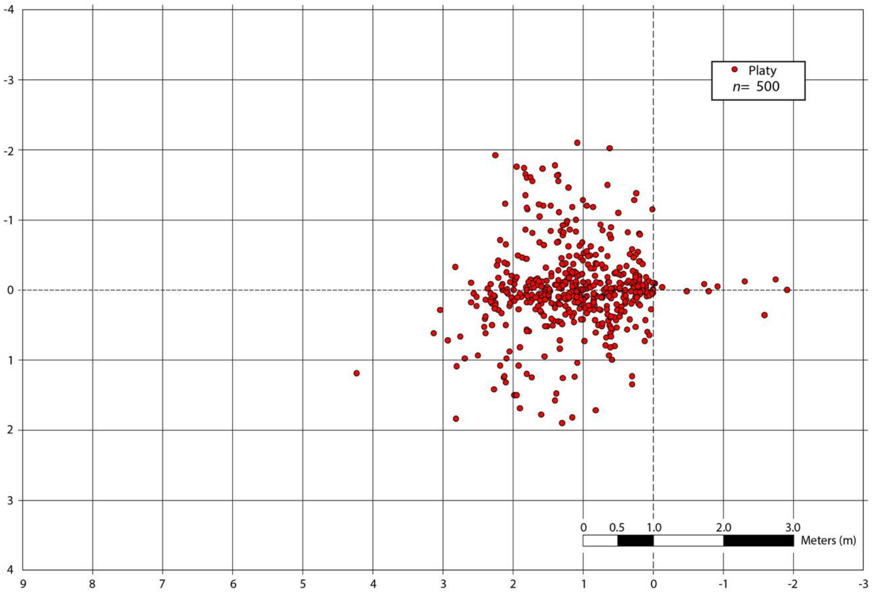
Platy
n= 500
-4
-3
-2
-1
0
1
2
3
4
9
8
7
6
5
4
3
2
1
0
-1
-2
-3
0 0.5 1.0 2.0 3.0
Meters (m)

while values approaching 1 reflects dispersive runout patterns. The dispersion factors for the inundated areas were 0.56, 0.83, and 0.81 for the *equant elongate* and *platy* rocks respectively. Thus, while the *equant* rock shows a greater inundated area, *elongate* and *platy* rocks are more dispersive.

4.2.1 Deposit characteristics according to slope angle and rock-shape

In the following section the runout data are separated according to slope angle and then release orientation i.e. Figure 3.3. The separation of the data sets into slope angle and release orientation is important to investigate the following hypothesises:

i) Changes in slope angle effect the dynamic motion of rocks during runout, as loosely observed by (Ritchie, 1963); and respectively, the potential runout distance and dispersion.

ii) The initial release orientation can pre-set the dynamics of the rock during runout.

Maps of single runout positions have been sorted according to slope angle and the data for each rock-shape plotted in Figures 4.3 and Figures 4.4, the three end-member shapes the *equant* (green), *elongate* (blue) and *platy* (red) are differentiated by their colour.

These plots provide an overview of which slope angles were the best at producing the farthest runouts. The maps show that runout increases with increasing slope angle, where on the 37° slope the greatest runouts are attained, following this runout decreases with increasing slope angle. This can be attributed to the sever slope transition at the toe of the slope leading onto the flat runout area as the slope angle increases. With low slope angles the transition from the slope to the flat runout area is mellow which assists in preserving the momentum of the rocks as they runout onto the slope. At higher slope angles the transition is sever and thus the rocks experience larger impacts when reaching the base of the slope.

FIGURE 4.3 *(following page)*: Maps of the runout deposit locations of all three end-member rock shapes (*equant*, *elongate* and *platy*) for the 20°, 27°, and 37° slopes. On the map the experiment was run from right to left and the toe of the slope is marked with the dashed line. Points which lie to the left of the zero line reflect test bodies which became stuck on the slope, which only occurred for non-equant rocks. The three end-member shapes the *equant* (green), *elongate* (blue) and *platy* (red) are differentiated by their colour.

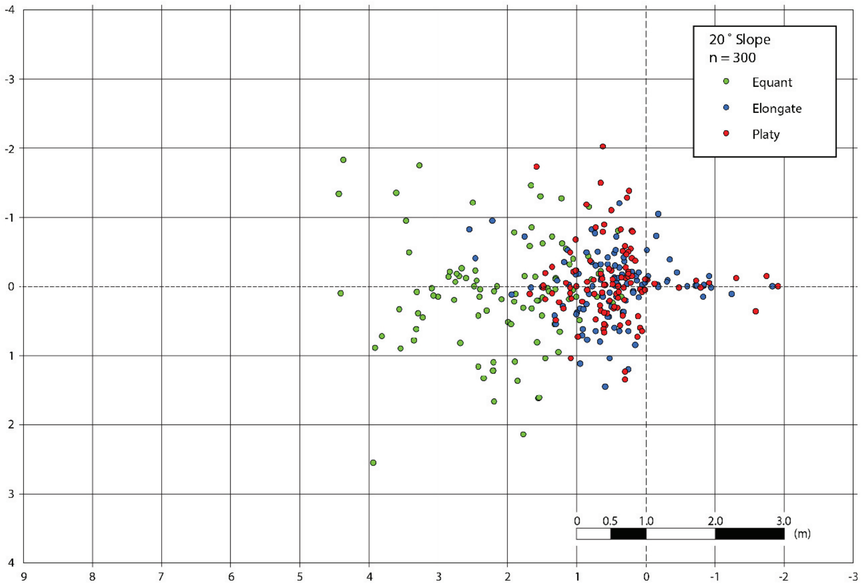
20 ° Slope
n = 300
Equant
Elongate
Platy
0 0.5 1.0 2.0 3.0
(m)
-4
-3
-2
-1
0
1
2
3
4
9
8
7
6
5
4
3
2
1
0
-1
-2
-3

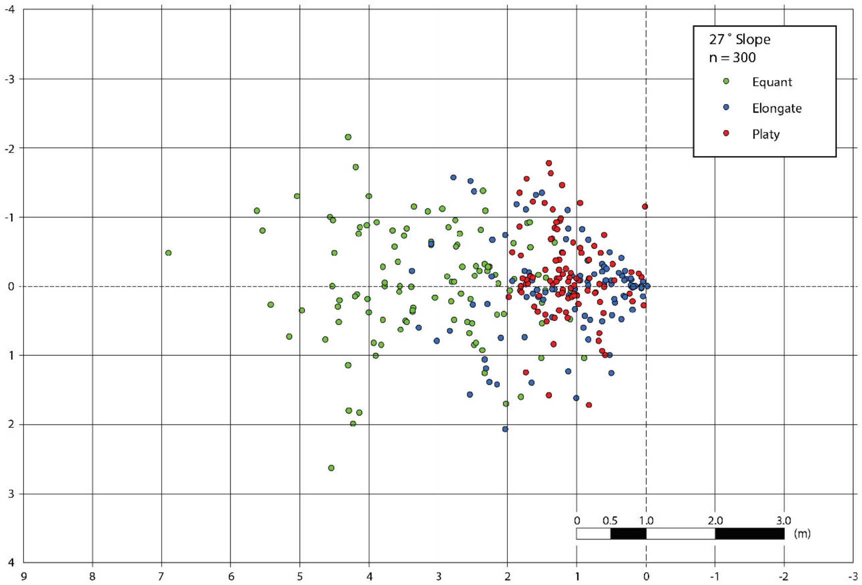
27 ° Slope
n = 300
Equant
Elongate
Platy
0 0.5 1.0 2.0 3.0
(m)
-4
-3
-2
-1
0
1
2
3
4
9
8
7
6
5
4
3
2
1
0
-1
-2
-3

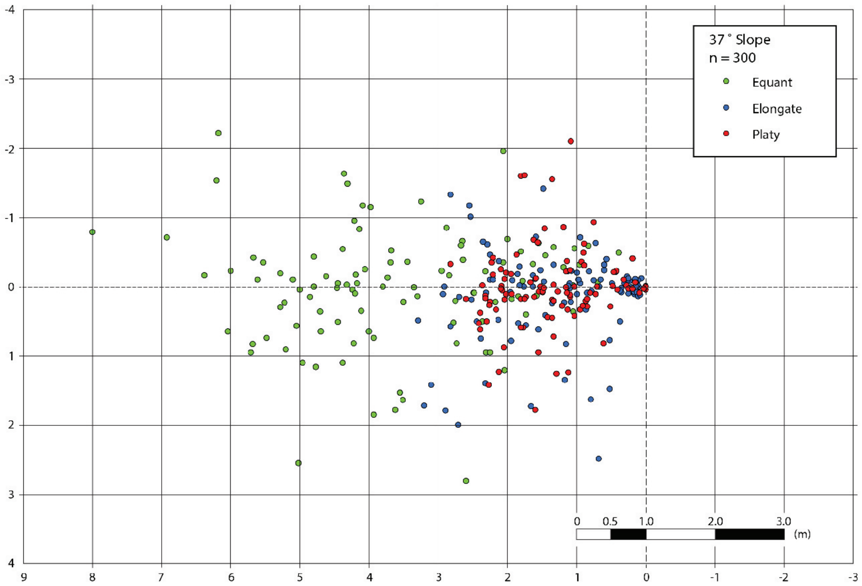
37 ° Slope
n = 300
Equant
Elongate
Platy
0 0.5 1.0 2.0 3.0
(m)
-4
-3
-2
-1
0
1
2
3
4
9
8
7
6
5
4
3
2
1
0
-1
-2
-3

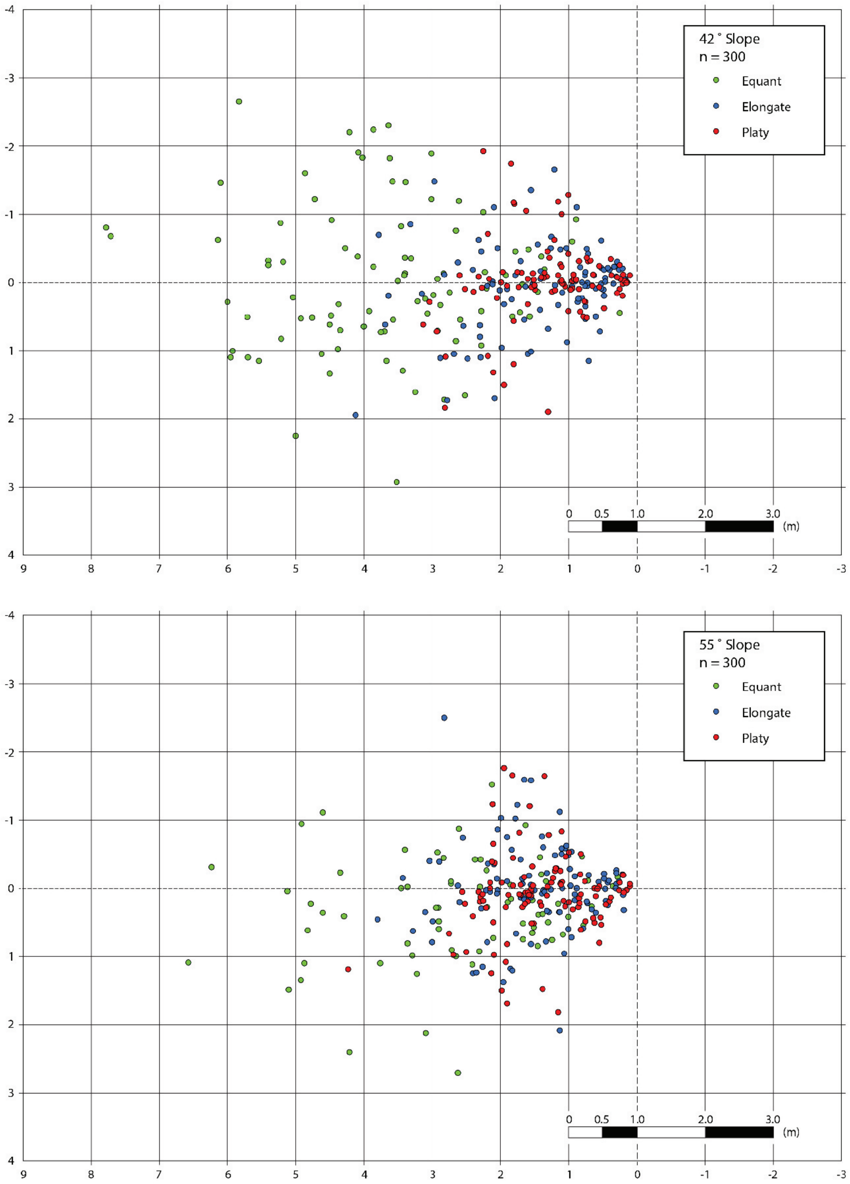

Figure 4.4: Maps of the runout deposit locations of all three end-member rock shapes (*equant*, *elongate* and *platy*) for the 42° and 55° slopes. On the map the experiment was run from right to left and the toe of the slope is marked with the dashed line. Points which lie to the left of the zero line reflect test bodies which became stuck on the slope, which only occurred for non-equant rocks. The three end-member shapes the *equant* (green), *elongate* (blue) and *platy* (red) are differentiated by their colour.

There appears a focusing of where the rocks come to a rest about the central fall line with increasing slope angle, which is reflected with a higher density of point about this location. Rocks that disperse away from the central fall line are still evident and ultimately define the total runout area, while they appear to be less frequent. However, this trend is difficult to observe if considering the data in map form.

Grouping each single runout trajectory in this manner gives an impression of the entire inundated area, while gives no insight on the likelihood of a single event reaching the extremes of the runout area. Therefore, the following analysis also looks at the dispersion of each single event that composes the entire runout area, and thus the likelihood of the extreme events can be considered.

4.2.2 Runout distance and lateral dispersion

By looking at the longitudinal and lateral runout distances, the influence of rock-shape and slope angle on runout can be observed. Although the potential energy was constant, both the initial impact as the rock made contact with the slope and the transition from runout slope to stopping changed according to slope angle. For shallow slope angles the initial impact with the slope has greater velocity, while the angle between the slope and the flat runout zone at the toe of the slope is smoother. On the other hand steeper slopes in this experimental set up generate initial impacts of slower velocities while the transition from runout to stopping zone is more severe.

FIGURE 4.5 *(following page)*: Data of runout distance and lateral dispersion are displayed in cumulative distribution plots, and the dispersion data are presented as probability density curves. The data are sorted vertically according to the slope angle. The columns A to E (left hand column) show runout distance L from the toe of the slope measured in cm in a straight line traced over the planar slope and onto the flat runout zone. The central column, F to J, shows lateral runout distance from the central line W measured in (cm), here the absolute values have been plotted. The far right column, K to O, shows probability density function of dispersion values (W/L) for each individual trajectory are presented. The runout data from laboratory experiments compares the three end-member shapes are indicated as the *equant* (green) square, *elongate* (blue) circle and *platy* (red) triangle, and for each slope angle, starting top with 55° down to 20°.

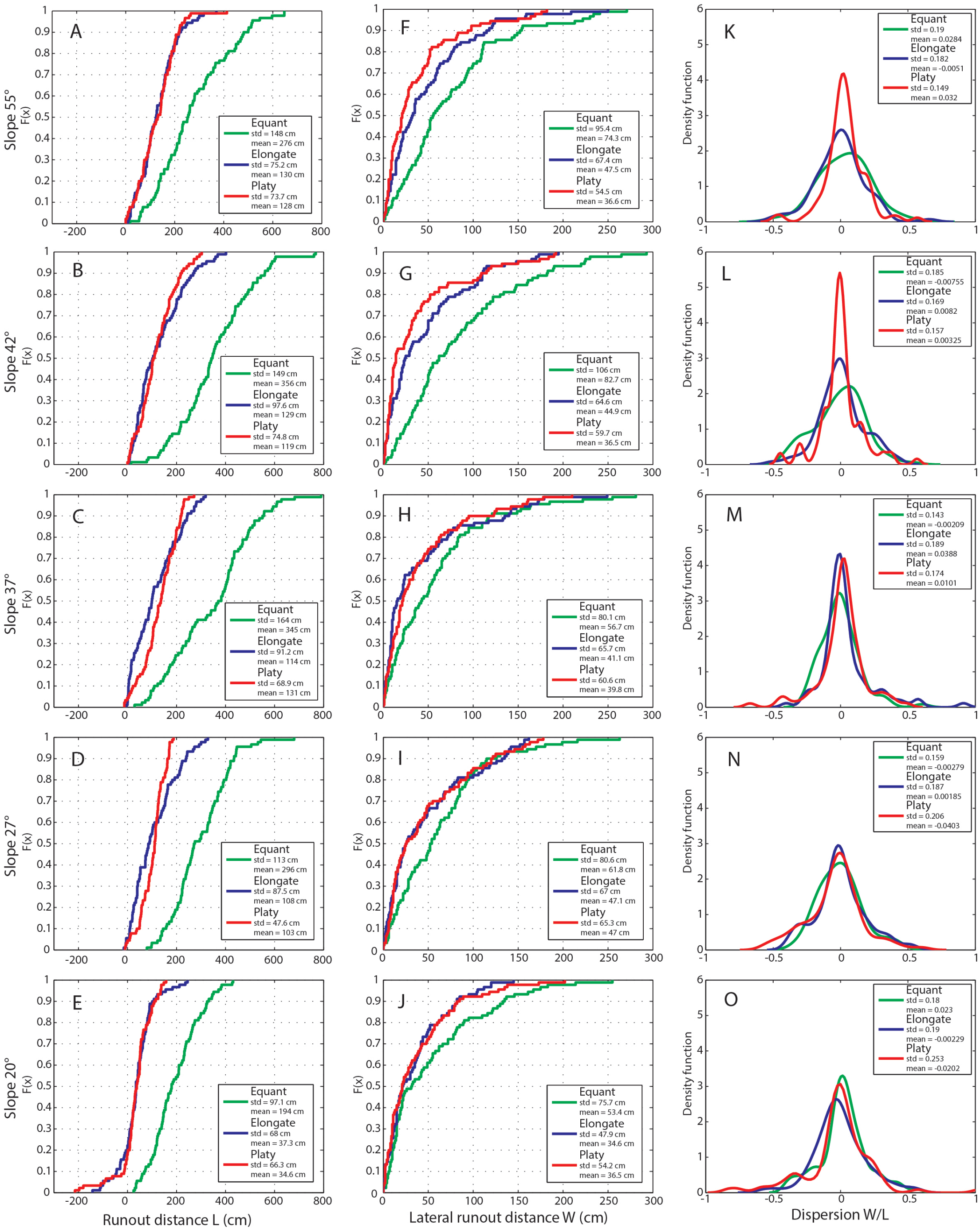
Slope 55°
Slope 42°
Slope 37°
Slope 27°
Slope 20°
F(x)
Density function
A
Equant
std = 148 cm
mean = 276 cm
Elongate
std = 75.2 cm
mean = 130 cm
Platy
std = 73.7 cm
mean = 128 cm
F
Equant
std = 95.4 cm
mean = 74.3 cm
Elongate
std = 67.4 cm
mean = 47.5 cm
Platy
std = 54.5 cm
mean = 36.6 cm
K
Equant
std = 0.19
mean = 0.0284
Elongate
std = 0.182
mean = -0.0051
Platy
std = 0.149
mean = 0.032
B
Equant
std = 149 cm
mean = 356 cm
Elongate
std = 97.6 cm
mean = 129 cm
Platy
std = 74.8 cm
mean = 119 cm
G
Equant
std = 106 cm
mean = 82.7 cm
Elongate
std = 64.6 cm
mean = 44.9 cm
Platy
std = 59.7 cm
mean = 36.5 cm
L
Equant
std = 0.185
mean = -0.00755
Elongate
std = 0.169
mean = 0.0082
Platy
std = 0.157
mean = 0.00325
C
Equant
std = 164 cm
mean = 345 cm
Elongate
std = 91.2 cm
mean = 114 cm
Platy
std = 68.9 cm
mean = 131 cm
H
Equant
std = 80.1 cm
mean = 56.7 cm
Elongate
std = 65.7 cm
mean = 41.1 cm
Platy
std = 60.6 cm
mean = 39.8 cm
M
Equant
std = 0.143
mean = -0.00209
Elongate
std = 0.189
mean = 0.0388
Platy
std = 0.174
mean = 0.0101
D
Equant
std = 113 cm
mean = 296 cm
Elongate
std = 87.5 cm
mean = 108 cm
Platy
std = 47.6 cm
mean = 103 cm
I
Equant
std = 80.6 cm
mean = 61.8 cm
Elongate
std = 67 cm
mean = 47.1 cm
Platy
std = 65.3 cm
mean = 47 cm
N
Equant
std = 0.159
mean = -0.00279
Elongate
std = 0.187
mean = 0.00185
Platy
std = 0.206
mean = -0.0403
E
Equant
std = 97.1 cm
mean = 194 cm
Elongate
std = 68 cm
mean = 37.3 cm
Platy
std = 66.3 cm
mean = 34.6 cm
J
Equant
std = 75.7 cm
mean = 53.4 cm
Elongate
std = 47.9 cm
mean = 34.6 cm
Platy
std = 54.2 cm
mean = 36.5 cm
O
Equant
std = 0.18
mean = 0.023
Elongate
std = 0.19
mean = -0.00229
Platy
std = 0.253
mean = -0.0202
0
0.1
0.2
0.3
0.4
0.5
0.6
0.7
0.8
0.9
1
-200
0
200
400
600
800
50
100
150
200
250
300
1
2
3
4
5
6
-1
-0.5
0.5
Runout distance L (cm)
Lateral runout distance W (cm)
Dispersion W/L

4.2.3 Runout distance

Plots of runout distance (Fig. 4.5a) show that overall the *equant* rock has the greatest runout distance with the absolute maximum of just less than 8.0 m. The *elongate* and the *platy* rocks show considerably shorter runout distances with overall maximums up to 4.0 m, half of the *equant* rock (Figure. 4.6). Mean and standard deviations of each population are reported on the Figures 4.5 and an overview given in Figure 4.6. The general trend follows where the mean runout distance increases with increasing slope angle. The *equant* rock shows a reduction in runout for the steepest slope angle 55°. The *platy* rock shows a spike in the mean runout distance at 37° exceeding that on the 55° slope mean by 2 cm. At slope angles 37° the *equant* rock runs out double the distance of the non-equant rocks, while at lower slope angles the difference increases to $\sim$ 80% and $\sim$ 64% for the 20° and 27° slopes respectively.

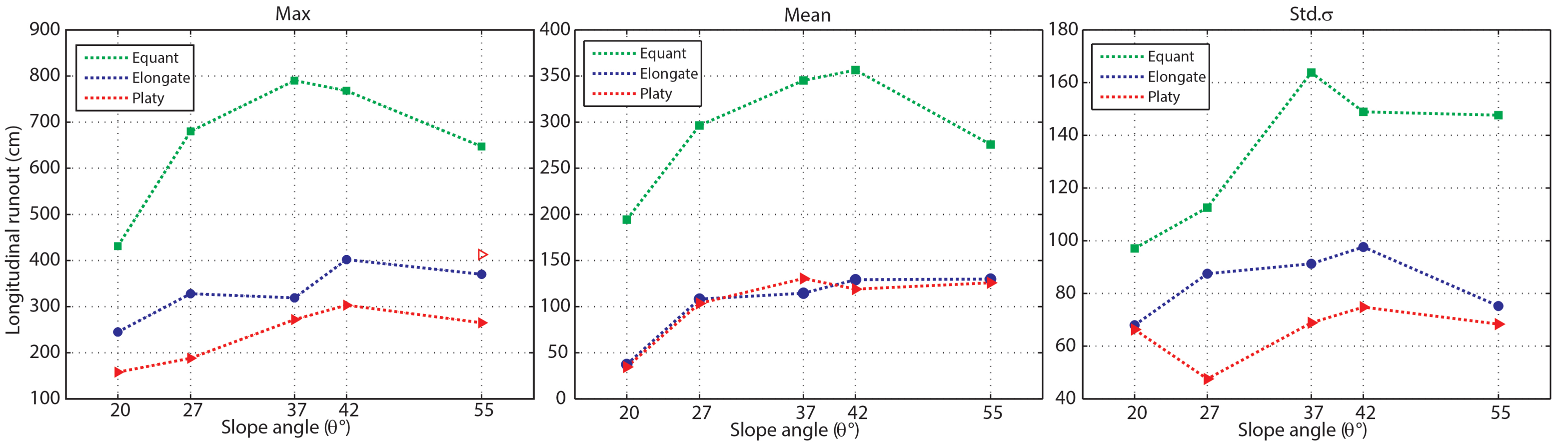

FIGURE 4.6: Summary statistics of the runout distances; A (left) are the max runout distances for each slope angle and shape; B (middle) are the mean values; and C (right) are the standard deviations. The three end-member shapes are indicated as the *equant* (green) square, *elongate* (blue) circle and *platy* (red) triangle.

4.2.4 Lateral runout

The central fall line of the experiment is the path of steepest descent, and in the case of these experiments on a planar slope it can be drawn through the centre of the experimental slope from the first contact point. On the maps, this is indicated by the dashed zero line that runs horizontally. The lateral runout distance is measured perpendicular to this line from the stopping point of the test rock for each experiment. Positive values indicate test rocks which deviated to the left facing down slope, and negative values those which travelled to the right. It is important to consider the lateral runout distances because not only are they responsible for defining the extent of the rockfall runout zone, but it is often assumed (Section. 2.5) that a rock will follow the path of steepest descent over any terrain. This assumption has lead to many popular 2-D rockfall modelling approaches that are performed on terrain profiles taken from the topographic fall line or steepest path (e.g. Dorren and Seijmonsbergen, 2003). By quantifying the lateral runout, the tendency for a particular rock to follow the fall line, or deviate from it, can be investigated. A measure of the assumption that rock will follow the fall line can be made, along with identifying the specific features of rock that may be responsible for a rock holding a steepest path trajectory. The central column of Figure 4.5b displays the absolute values of lateral runout distance in empirical cumulative frequency distribution plots. From the plots of lateral runout distance, it can be seen that the *elongate* and the *platy* rocks seem to follow a similar trend for slope angles 20 - 37° with only the absolute maximum values showing the greatest difference in lateral movement. For slopes of 42 - 55° the *elongate* rock shows increased lateral runout for mid-cumulative density values between 0.3 and 0.9. The *elongate* and the *platy* rocks then converge and following a very similar trend for cumulative densities above 0.9.

The *equant* rock for all cases has a distribution encompassing larger lateral runout distances for a greater portion of the data set. Only at the 20° slope angle for the first 50% of the dataset does the *equant* rock mirror the trend of the *elongate* and *platy* rocks, after which behaviour diverges again. For the 27° and the 37° the *equant* rock converges with the trend of the *elongate* and *platy* rocks for the upper 20% of the dataset; while still in all cases the *equant* rock produces the greatest runout distances.

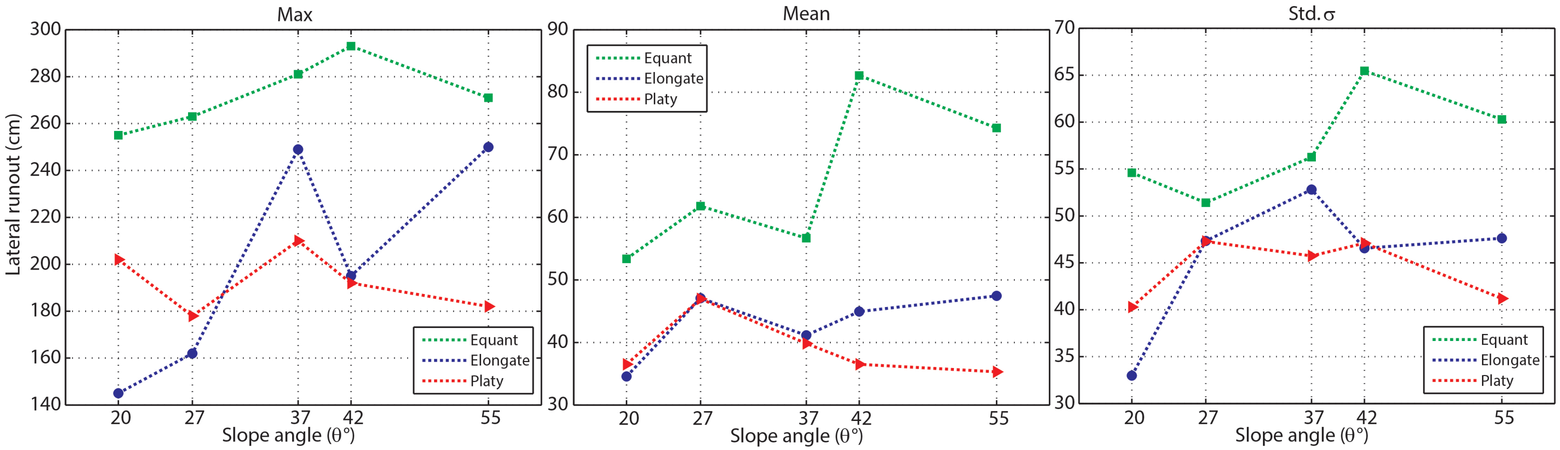

FIGURE 4.7: Summary statistics of the lateral runout distances; A (left) are the max lateral runout distances for each slope angle and shape; B (middle) are the mean values; and C (right) are the standard deviations. The three end-member shapes are indicated as the *equant* (green) square, *elongate* (blue) circle and *platy* (red) triangle.

Figures 4.7 plot B provides the summary statistics for the lateral runout distance. The plot shows that the average lateral runout of the *equant* rock is around 20 cm greater than non-equant rocks for lower slope angles 20-37°. There is an initial peak in lateral runout distance for 27° after which the non-equant rocks on average decrease in lateral runout. While the *equant* rock shows a second increase in lateral runout to over 80 cm for the 42° slope, it again drops off for the slope at 55°. In general there is no discernible trend within the statistics of lateral runout distance. However, in all cases the slope-normal and slope-parallel runout distances for the *equant* rock are greater than non equant rocks. This result may be influenced by the change in transition angle at the base of the slope. The relationship between the runout distance and lateral deviation from the fall line gives a better indication of how rock-shape influences runout.

4.2.5 Dispersion W/L

The dispersion ratio of each single trajectory is calculated (see Chapt. 3, Sect. 3.2.5), to give an indication of the extent of lateral relative to longitudinal runout. In the case of single trajectories the runout distance is measured from the point of release, so includes runout over the inclined slope itself. In doing so the proportion of the experiments that travelled to the right or left of the central fall line can be assessed.

For the data a kernel density estimation (KDE) is used to calculate the probability density function of given dispersion values (Fig. 4.5c). KDE bandwidth (bw) is selected using a Gaussian model where the standard deviation σ and the number of samples n of the population is used (Eq. 4.1):

$$bw = (\frac{4\sigma^5}{3n})^{1/5} \approx 1.06\sigma n^{-1/5} \tag{4.1}$$

Peaks in the plots around 0 indicate that a nominally straight path was taken following the central fall line, while values greater or less than zero indicate an increasing proportion of lateral deviation. The most striking observation is that the *platy* rock shows a peak focused around the central fall line with board shoulders, ranging between 1.1 and -1.0, indicating high dispersion. The density of the shoulders is more pronounced at lower slope angles, and the density concentration of dispersion values around the central fall line increases with increasing slope angle. Inflections in the distribution also become more pronounced with increasing slope angle which reflects a lower occurrence of large lateral deviations. The *elongate* rock initially follows a similar trend as the *platy* rock up to the slope angle of 37°, following this with increasing slope angle the lateral dispersion for the *elongate* rock is greater in comparison to the *platy* rock. The *equant* rock shows for slope angles 20 - 37° low levels of lateral dispersion compared to the non-equant rocks, after which the *equant* form flattens, centred on the central fall line indicating increasing lateral dispersion.

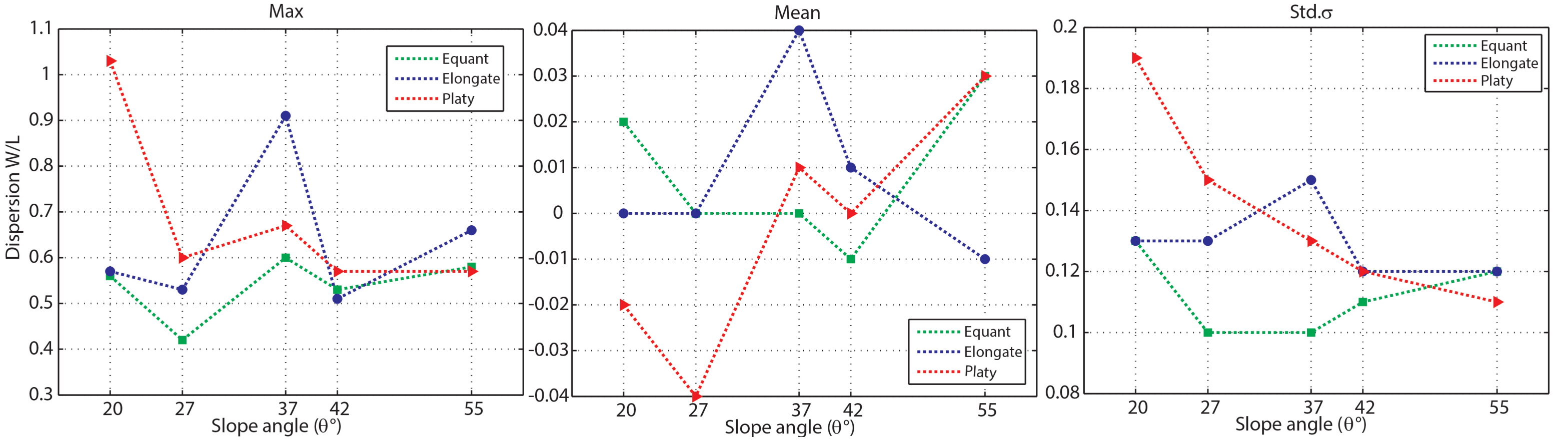

FIGURE 4.8: Summary statistics of the dispersion values W/L; A (left) are the max dispersion values W/L for each slope angle and shape; B (middle) are the mean values; and C (right) are the standard deviations. The three end-member shapes are indicated as the *equant* (green) square, *elongate* (blue) circle and *platy* (red) triangle.

The tendency for lateral dispersion is summarised by plotting the standard deviation of dispersion values against slope angle (Figure. 4.8). This illustrates how, for shallow slope angles 20 - 37°, the non-equant rocks tend to be dispersive while lateral dispersion decreases with increasing slope angle. The *platy* rock shows this trend best, indicating that with increasing slope angle there is a tendency for the rocks to follow the fall line more closely. The *equant* rock also follows this trend up a slope of 37°, after which lateral dispersion increases, attaining greater standard deviations than the non-equant rocks. However, again it is difficult to draw a definitive trend from the summary statistics of W/L in this case. It appears that the largest runouts which were recorded for the 37 ° are dominant in the observed trends and are responsible for the spike in W/L for this slope angle. This finding substantiates that geometry of the transition between the slope and the flat runout terrain could be of key influence here. It suggests that the 37 ° slope is the optimum combination of accelerating the rock and providing a mellow enough transition at the toe of the slope to prevent large losses in momentum through the collision with the flat portion of the experimental setup.

4.2.6 Release orientation

The three principal release orientations for the test rocks were designed to include a sample of the possible preset orientations that are induced on detachable rock blocks by the geometry of the rock-mass discontinuities (see Chapt. 2, Sect. 2.3). The purpose was to investigate if the rock's initial impact orientation with the slope holds an influence on runout. Of the $n = 100$ experiments performed for each shape on each slope angle, $n = 33$ (± 1) were assigned to one of three release orientations (Figure. 3.3).

Orientation A orients the largest moment of inertia of the *elongate* and *platy* rocks such that it lies parallel with the fall line; position C of the *elongate* rock is also oriented in this manner but with a larger facet impacting the slope first. Orientations B and C of the *platy* rock and B of the *elongate* rock are orientated such that the axis of smallest inertia lie parallel to the fall line (Figure. 4.9).

Whilst the *equant* rock's principal inertial axes were all equal, changes in rock release orientation result in different edges and facets impacting the slope first: Position A is oriented with the largest facet facing the slope; orientation B is such that an edge faces the slope; and, in C the smallest facet faces the slope. Figure 4.9 provides a sketch

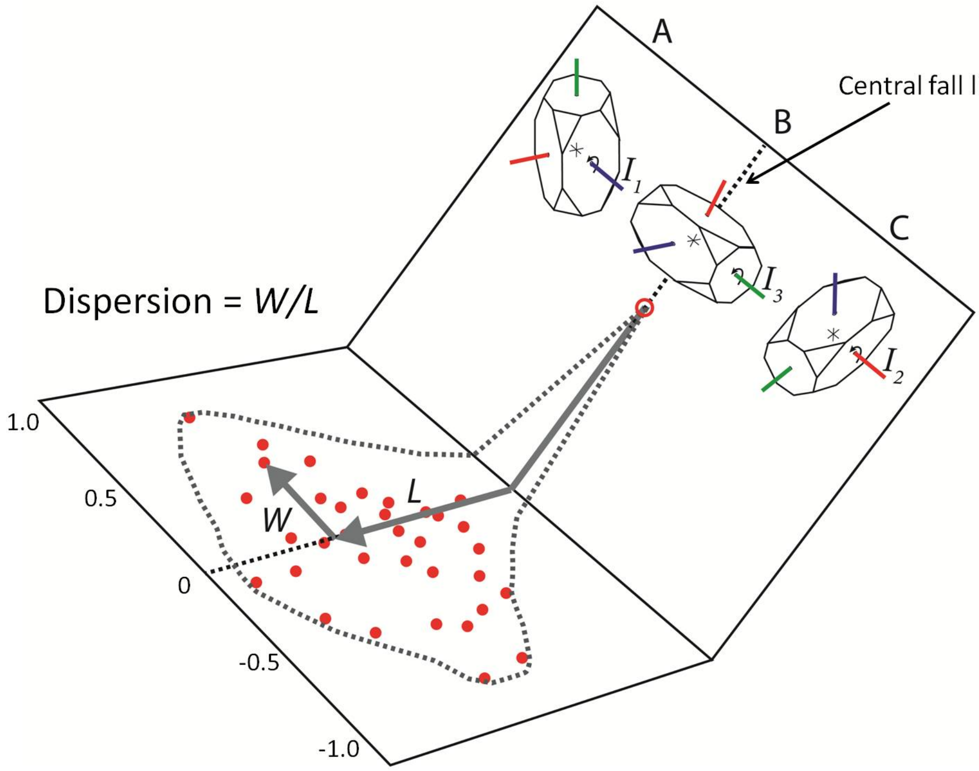

Figure 4.9: Sketch diagram to show the three principal release orientations chosen for each experiment series conducted on each slope angle. The example shown is of the *elongate* form. The test rocks were each released on to the same location on the ramp. Orientation A for the *elongate* form aligns the largest moment of inertia I_1 perpendicular to the central fall line of the slope, and has the block standing upright. Orientation B orients I_3, the smallest of the principal inertial axes, perpendicular to the fall line. While orientation C aligns the I_2 perpendicular to the central fall line, which has the same magnitude at I_1 in the case of the *elongate* form.

example of how the *elongate* rock from aligned the principal inertial axes to the slope fall line with the respective orientation letter A, B and C.

Maps of the runout point sorted according to the release orientation are shown in Figure 4.10. There is a clear difference in the runout results if the rock bodies are released in different orientations. For release orientation A in each case the largest moment or inertia is aligned parallel to the fall line of the slope, it can be seen that there is a concentration of the runout locations about the central fall line and a large degree of bunching increasing the density of the results. Release orientations B and C show more disperse results. For the elongate rock form the release orientation C shows less dispersion than B and is more similar to release orientation A as it also shows high density of results around the central fall line. This is partly because for the *elongate* rock aligned its largest moment of inertia with the slope fall line for both release orientations A and C.

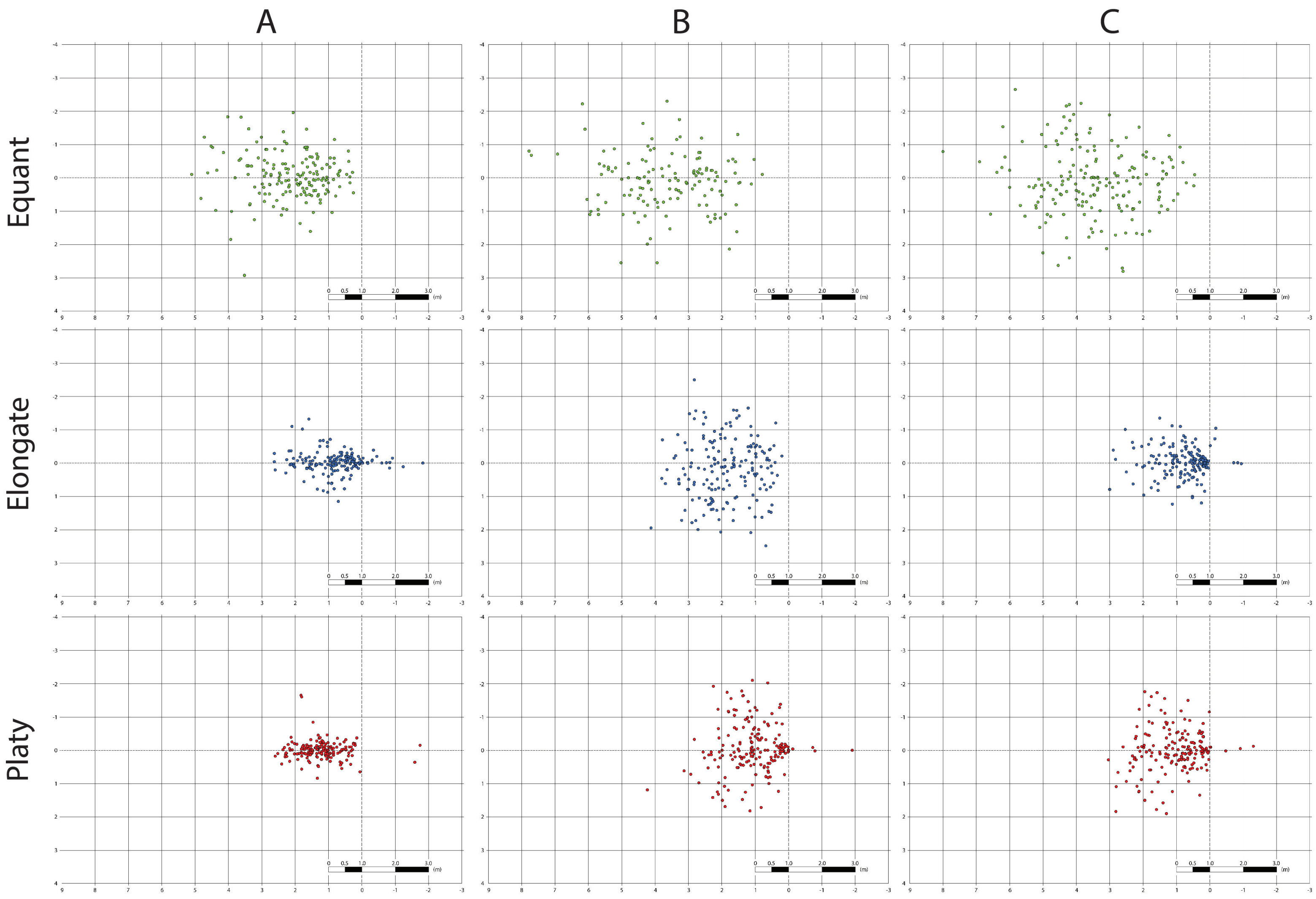

FIGURE 4.10: Maps of the runout point of single rockfalls sorted according to release orientations A, B, and C for each of the three end-member rock shapes (*equant*, *elongate* and *platy*). On the map the experiment was run from right to left and the toe of the slope is marked with the dashed line. Points which lie to the left of the zero line reflect test bodies which became stuck on the slope, which only occurred for non-equant rocks. The three end-member shapes the *equant* (green), *elongate* (blue) and *platy* (red) are differentiated by their colour. Each map contains all the data from every slope angle.

To further assess the details of this data, they are explored with the dispersion measure W/L as this includes a measure of both the longitudinal and lateral runout distances. Separate plots (Figure. 4.11) of the release orientations are made for each shape and slope angle combination. These plots show clear focusing of runout on the fall line (low dispersion) for the A orientation of both the *elongate* and the *platy* rocks. For the *platy* rock the density of dispersion values around the central fall line increases with slope angle. The *platy* rock's highest dispersion is found at lower slope angles 20 - 27° for orientations B and C. Orientations where the test rock entered the slope with the smallest axes of inertia aligned parallel to the fall line. This trend shows a reduction in dispersion with increasing slope angle.

For the *elongate* rock, prominent probability density peaks focus around low dispersion values for orientation A. For the slope angles 37° and 42°, the *elongate* rock's orientation C also produces a similar distribution to orientation A. Both orientations A and C of the *elongate* rock align the greatest moment of inertia parallel to the fall line. The *elongate* rock's orientation B shows high dispersion for all slope angles. At 42°, this setup shows significant skew in the data towards positively dispersed runout.

Skew in the probability density functions of the *equant* rock is also apparent, in particular for slope angles 27° and 55°. There appears no clear trend in the skew of the *equant* rock's probability density functions; however, values are both towards negative and positive skew in dispersion values. Overall, the *equant* rock shows a trend of increasing dispersion with increasing slope angle, a trend that cannot be attributed to a specific release orientation. Non-equant rocks have higher dispersion values than the *equant* rock for release orientations that align the smallest axis of inertia with the fall line of the test slope.

FIGURE 4.11 *(following page)*: Probability density functions of the dispersion data (W/L) are displayed for each release orientation under each test rock-shape. Release orientation A is given as a solid line, B is given as a medium dashed line, and C a fine dashed line. The different shapes are assigned the colours according to the previous plots, additionally to the dashed lines the hue of the shapes colour corresponds to a given release orientation. Plots A to E are the *equant* rock in descending order of slope angle starting top with 55° down to 20°. F to J are for the *elongate*, and K to O are for the *platy* rock. Each distribution contains 33 ±1 data points.

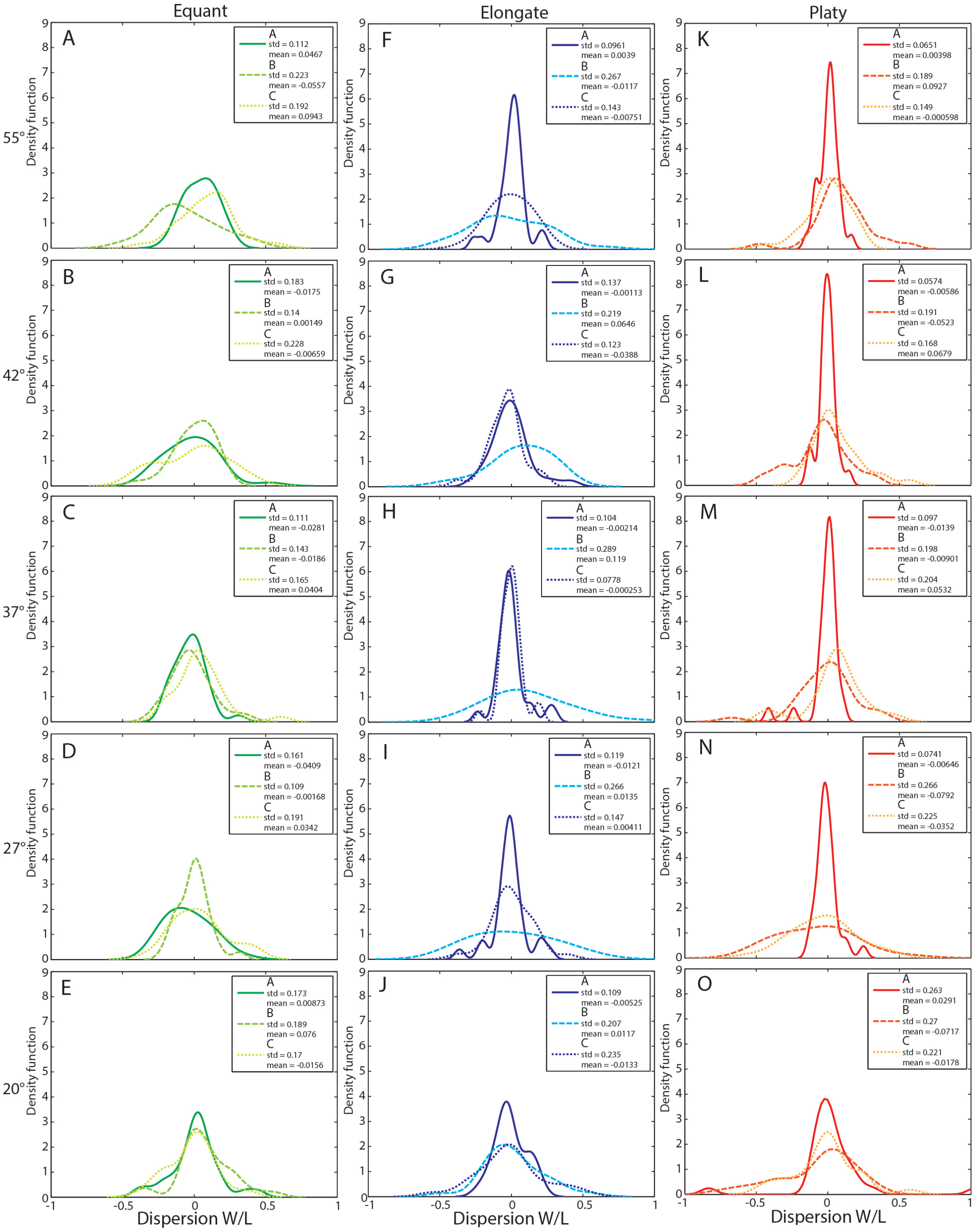
Equant
Elongate
Platy
55°
42°
37°
27°
20°
Density function
0 1 2 3 4 5 6 7 8 9
-1 -0.5 0 0.5 1
Dispersion W/L
A
A
std = 0.112
mean = 0.0467
B
std = 0.223
mean = -0.0557
C
std = 0.192
mean = 0.0943
B
A
std = 0.183
mean = -0.0175
B
std = 0.14
mean = 0.00149
C
std = 0.228
mean = -0.00659
C
A
std = 0.111
mean = -0.0281
B
std = 0.143
mean = -0.0186
C
std = 0.165
mean = 0.0404
D
A
std = 0.161
mean = -0.0409
B
std = 0.109
mean = -0.00168
C
std = 0.191
mean = 0.0342
E
A
std = 0.173
mean = 0.00873
B
std = 0.189
mean = 0.076
C
std = 0.17
mean = -0.0156
F
A
std = 0.0961
mean = 0.0039
B
std = 0.267
mean = -0.0117
C
std = 0.143
mean = -0.00751
G
A
std = 0.137
mean = -0.00113
B
std = 0.219
mean = 0.0646
C
std = 0.123
mean = -0.0388
H
A
std = 0.104
mean = -0.00214
B
std = 0.289
mean = 0.119
C
std = 0.0778
mean = -0.000253
I
A
std = 0.119
mean = -0.0121
B
std = 0.266
mean = 0.0135
C
std = 0.147
mean = 0.00411
J
A
std = 0.109
mean = -0.00525
B
std = 0.207
mean = 0.0117
C
std = 0.235
mean = -0.0133
K
A
std = 0.0651
mean = 0.00398
B
std = 0.189
mean = 0.0927
C
std = 0.149
mean = -0.000598
L
A
std = 0.0574
mean = -0.00586
B
std = 0.191
mean = -0.0523
C
std = 0.168
mean = 0.0679
M
A
std = 0.097
mean = -0.0139
B
std = 0.198
mean = -0.00901
C
std = 0.204
mean = 0.0532
N
A
std = 0.0741
mean = -0.00646
B
std = 0.266
mean = -0.0792
C
std = 0.225
mean = -0.0352
O
A
std = 0.263
mean = 0.0291
B
std = 0.27
mean = -0.0717
C
std = 0.221
mean = -0.0178

4.2.7 Summary of runout zones

In summary the results of the runout patterns show that the *equant* rock runs out the furthest both longitudinally and the lateral distance to the central fall line, hence encompassing the greatest possible runout areas. However, the dispersion ratio W/L of the deposits and individual trajectories indicate that non-equant rocks produce greater dispersion of the deposits relative to the longitudinal runout distance. It has also been shown that although the non-equant rocks generate high lateral dispersion, their release orientation is responsible for low lateral dispersion. Low dispersion (*elongate* and *platy* rocks) is identified for release orientations which aligned the rock's largest moment of inertia parallel to the fall line of the slope.

These data identify the significance of slope angle, rock-shape and release orientation on runout pattern. The motion dynamics that are responsible for the deposition patterns are explored in the following sections which look at the velocities and rotational behaviour of each rock-shape during runout.

4.3 Runout velocity

During rockfall the greatest acceleration is during free fall. The kinetic energy (Eq. 4.2), gives an indication of the damage capacity and hazard intensity, as defined by;

$$KE = (\frac{1}{2})mv^2 \tag{4.2}$$

In these experiments free fall from the height available (1.70 m) would attain 5.78 ms^{-1}. Slope impacts and frictional sliding act to slow velocity during runout (Figure. 4.12). Thus, the average velocity of each rock-shape over a fixed distance reflects how efficiently a rock travels over terrain.

4.3.1 Average velocities

Of the experiments that were filmed, the rock's average velocity was measured from the first slope impact to a fixed distance of 1.0 m measured parallel to the planar test slope

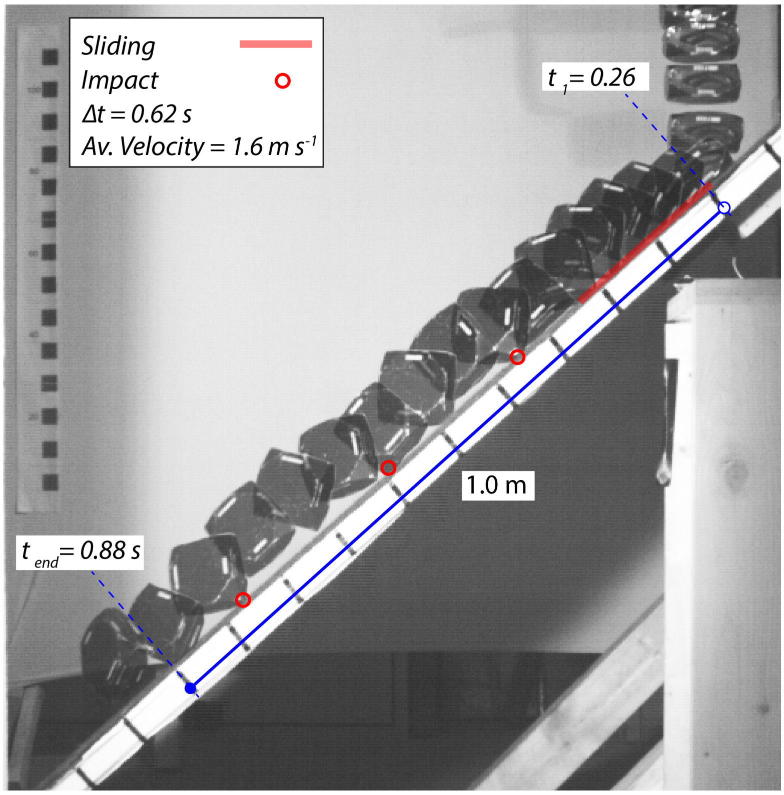

FIGURE 4.12: Sequence image of a runout of the *platy* rock depicting the method applied to capture the average velocity of the test rocks over a fixed distance of 1.0 m parallel to the slope. The blue line indicates the slope parallel distance between which the time the centre of mass of the test rock passes the start point (blue circle) and exits the end point (solid blue dot) is measured. The activity can be a combination of sliding (red line) or impacts (red circle).

(Figure. 4.12). This measure includes deceleration due to slope impacts and frictional sliding. The box plots in Figures 4.13 summarise the average velocities measured using this method for each shape and all slope angles. The average velocities (Fig. 4.13, (left)) indicate the *equant* rock is the fastest, followed by the *elongate* and the *platy* rocks respectively. Velocity measurements of zero (Table. 4.1) correspond to test rocks which came to a stop within the 1.0 m measurement distance. The average velocities show a clear shape dependency, while the release orientation also holds some influence.

Figure 4.13 presents the data for all experiments separated by release orientation (Figure. 3.3). It can be seen that for orientations A and C the *equant* rock is the fastest followed by the *platy* rock, and then the *elongate* rock is the slowest. For orientation B, however, the *elongate* rock is the fastest overall. It should be noted that the *elongate* rock's B orientation enters the slope with rotation about an axis where the two moments of inertia are equal in magnitude, as in the case of the *platy* rock. If the mean velocities are compared between release orientations (Table. 4.1), release orientation A

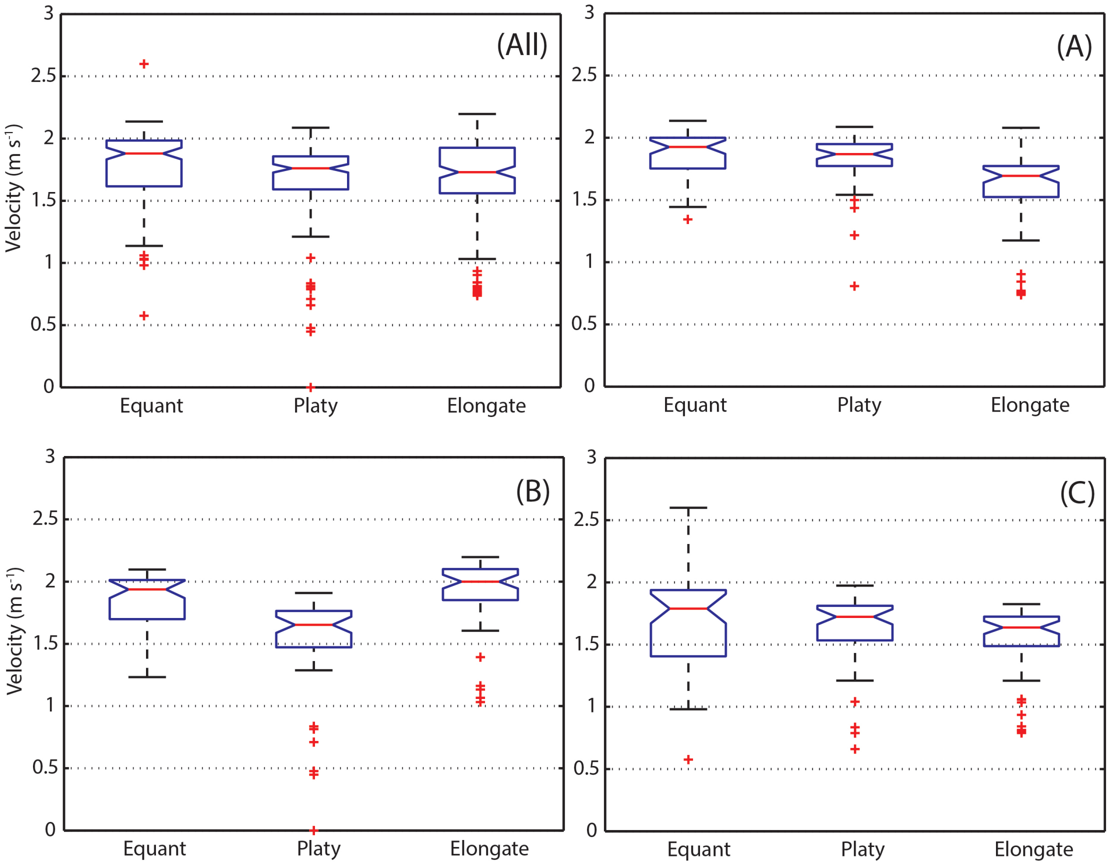

FIGURE 4.13: Boxplots displaying the average velocities of the experiments for each different test rock. The red lines central to the boxplots indicate the median value of the data, the upper and lower blue notched boxes indicate the upper and lower quartiles of the data respectively. The quivers on either end of the blue boxes indicate the maximum and minimum values respectively. While points marked as red crosses are the outliers in the data set. Upper left (All) displays all the data together. The remaining plots separate the data into the A, B and C release orientations.

generates the fastest rockfall which also enters the slope with rotation about an axis where the two inertial moments are equal in magnitude. The velocities of the *elongate* rock in orientation B and the *platy* rock in orientation A also have the lowest standard deviation compared to their additional release orientations. This observation generates questions about how the stability of rotation may influence velocity.

The *equant* rock generates similar rockfall velocities for each release orientation, while mean velocity for orientation C is the slowest and respectively generates the highest standard deviation (Table. 4.1). The highest standard deviation of velocities overall was observed for the *platy* rock released in orientation B. In this orientation the *platy* rock's smallest principal axis of inertia aligns with the fall line of the slope.

To summarise, the average velocities show a rock-shape and release orientation dependency. With release orientations aligned with two equal moments of inertia parallel to the fall line, the fastest velocities for the given shape are observed.

However, this measurement generalises the different modes of motion that occur during runout. Additionally for these experiments having been conducted on a small sized slope with small rocks, the magnitude of the velocity differences are small and therefore difficult to discern how important the differences in shape are for average velocity. Important for rockfall hazard analysis are the velocities of individual parabolic trajectories between impacts. With this information the mechanics of individual rock-ground impacts are studied. Moreover, trajectory velocities are by definition higher than the average velocity and therefore of more use in the design of rockfall protection structures where impact forces need to be known. In the following, single parabolic trajectories are analysed.

Table 4.1: Summary statistics of the average velocities. The maximum, minimum, mean, median, standard deviation $Std.\sigma$ and inter quartile range IQR are given for each test rock. The data are separated according to release orientation.

Orientation	Shape	*Max*	*Min*	*Mean*	*Median*	*Std.* σ	*IQR*
All)	*Equant*	2.60	0.58	1.78	1.88	0.29	0.37
	Platy	2.09	0.00	1.66	1.76	0.34	0.27
	Elongate	2.20	0.74	1.67	1.73	0.35	0.37
A)	*Equant*	2.14	1.34	1.85	1.93	0.19	0.25
	Platy	2.09	0.81	1.83	1.87	0.23	0.18
	Elongate	2.08	0.74	1.57	1.69	0.34	0.25
B)	*Equant*	2.10	1.23	1.84	1.94	0.22	0.31
	Platy	1.91	0.00	1.53	1.65	0.41	0.29
	Elongate	2.20	1.03	1.90	2.00	0.29	0.25
C)	*Equant*	2.60	0.58	1.66	1.79	0.38	0.53
	Platy	1.97	0.66	1.63	1.72	0.29	0.28
	Elongate	1.82	0.79	1.53	1.64	0.30	0.24

4.3.2 Single trajectory velocities

The translational velocities before and after each impact were measured using slope impact points observed in the video. The method (see Chapt. 3, Sect. 3.4.1) gives the absolute velocity of the rock's centre of mass. Each measurement requires a closed impact pair, i.e. the velocity can only be calculated for a trajectory between two known impact points. If a trajectory exits the video field of view before impacting the slope it cannot be included.

Figure 4.14 presents boxplots of the velocities measured from single trajectories as the test rocks travelled down the slope. The analysis was only conducted for orientation A of each shape. This was because in the other orientations it was common that complex rotations occurred making an accurate measurement of the test bodies mass centre and impact configuration (Figure. 3.12) difficult. In the video data from release orientation A there were a number of experiments in which the test rocks entered into immediate sliding, these are not included in the results presented. The number of trajectories (n) that could be successfully measured are indicated above each boxplot (Figure. 4.14).

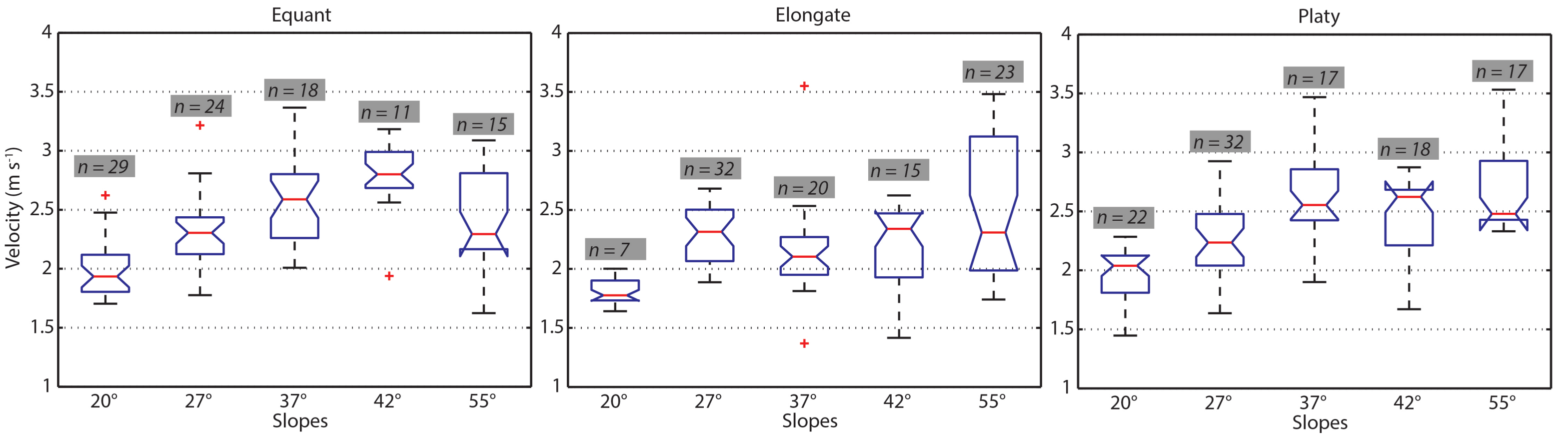

FIGURE 4.14: Boxplots displaying the velocities of single (inter-impact) trajectories. The data are separated according to the test rock; from left *equant*, middle *elongate*, and right *platy*. On each figure the distribution of the velocities is displayed according to the slope angle, from left 20° slope to right 55° slope. The central red lines on the boxplots indicate the median value of the data, the upper and lower blue notched boxes indicate the upper and lower quartiles of the data. The quivers on either end of the blue boxes indicate the maximum and minimum values.

Generally all shapes show increasing velocity with slope increasing angle, from the minimum just under 1.5 ms^{-1} recorded on the 20° slope for the *elongate* rock, to the maximum around 3.5 ms^{-1} on the 55 ° slope for the *platy* rock. There are, however, a couple of cases where this trend does not hold. The *equant* rock on the 55° slope shows a drop in velocity compared to lower slope angles. It should be noted that there is also a drop in the number n of measurable trajectories at higher slope angles. In many cases the test bodies at higher slope angles jumped out of the measurable field of view, particularly for the *equant* rock, limiting the number observable cases.

The *elongate* rock (Fig. 4.14 (middle)) shows a reduction in velocity between 27° and 37° slopes after which velocity continues to increase with increasing slope angle. What is also apparent for the *elongate* rock is that the range of values increases with increasing slope angle. For the 20° slope the *elongate* rock has a very low number of measurable trajectories, and shows that a high proportion of the experiments resulted in sliding.

Similar to the *elongate* rock's behaviour, the *platy* rock shows a reduction in velocities, but here between 37° and 42° slopes. Again data for the *platy* rock suffers from undersampling at higher slope angles. The *platy* rock consistently shows velocities between 1 - 1.5 ms^{-1}, a range more broad compared to the other shapes considered.

4.3.3 Summary of runout velocity

The velocities measured for single trajectories show a trend of increasing velocity with increasing slope angle, but differences according to shape are apparent. Specifically the *elongate* rock shows an increasing range of velocity with increasing slope angle, and the *platy* rock consistently shows a broader range of velocities as compared to other shapes. These observations cannot simply be attributed to the variables of shape and slope angle as the impact configuration (Section. 3.4.3) also contributes to the velocity during the parabolic trajectory between ground impacts. Given the main source of velocity gain is time spent in free fall, the jump heights and geometry of the trajectories are decisive in the velocity of rocks during runout.

4.4 Jump height and trajectory ratio *f/s*

The jump height and trajectory ratio f/s (see Chapter 2, Section 2.2.5) is important in rockfall because they can have a bearing on a rock's runout potential. In a sequence of rebounds, the history that precedes a rock-ground impact determines the impact configuration (velocity, impact angle, etc). Because rock-ground impacts involve a series of contacts in which edge and corner points become pinned generating torques, levering motions and rotations in the rock body, the magnitudes of a rock bodies principal inertial moments become important in determining the outcome of a rock-ground impact, and there for rock-shape. The purpose of documenting jump heights and trajectory ratios here was to investigate how the magnitudes of the principal inertial moments in each rock-shape affect the jump characteristics following rebounds.

Jump heights and trajectory ratios are measured using the method detailed in Chapter 2, Section 2.2.5. The results recorded according to each rock-shape for all slope angles are presented in box plots in Figure 4.15 and the summary statistics in Table 4.2.

4.4.1 Jump characteristics and rock-shape

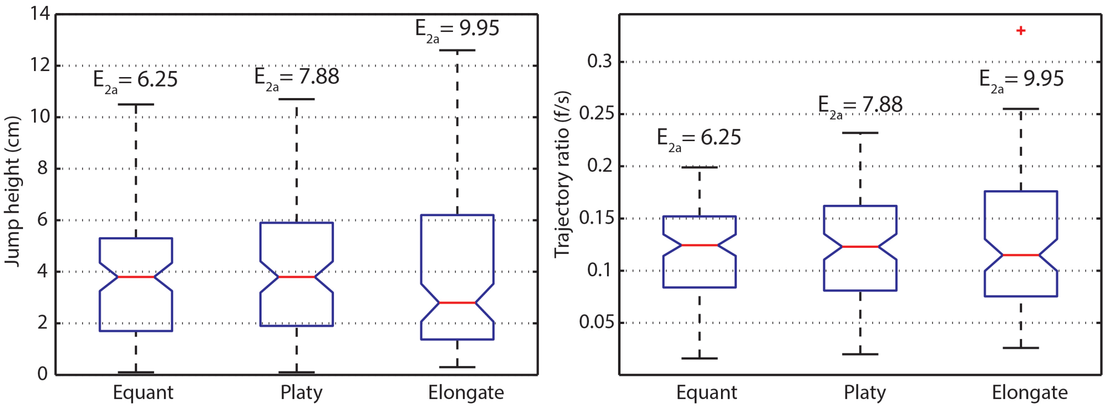

FIGURE 4.15: Boxplots presenting the jump heights recorded from all experiments according to rock-shape (left), and the trajectory ratio f/s (right). The number of measurements n is given above each box plot. The boxplots arrange the different shapes ranking them smallest to largest dimension (E_{2a}) of their equivalent inertial ellipsoid (Table. 3.3).

Cases where a rebound did not occur and the rock entered sliding are not presented in these data. The jump heights (Fig. 4.15 (left)) are between 0.1 and 13.0 cm. Jump height reflects the shape of the rock, and respectively the increase in size of the largest axis of the equivalent inertial ellipsoid. For the maximum jump heights and upper quartiles of jump height, the *equant* rock produces the lowest values, followed by the *platy* and the *elongate* rock which has the overall maximum (Figure. 4.15). However, median and mean jump heights show that, on average, the *elongate* rock produces lower jump heights than the *equant* and *platy* rock. This split in the result is reflected in the skew of the data for the *elongate* rock, in addition to a wide standard deviation (3.11 cm) is the highest compared to the other shapes. The jump height maxima (σ) and inter quartile range all show an increase with increasing length of the equivalent inertial ellipsoid's largest axis (in order of increasing size: *equant*, *platy* and *elongate*) (Table. 4.2).

Table 4.2: Summary statistics of the jump heights and trajectory ratios recorded of all slope angles for each shape.

	Jump height (cm)					
	Max	*Min*	*Mean*	*Median*	*Std.* σ	*IQR*
Equant	10.50	0.10	3.88	3.80	2.45	3.10
Platy	10.70	0.10	3.99	3.80	2.58	4.05
Elongate	12.60	0.30	3.78	2.75	3.11	5.25

	Trajectory ratio (f/s)					
	Max	*Min*	*Mean*	*Median*	*Std.* σ	*IQR*
Equant	0.199	0.016	0.119	0.131	0.048	0.069
Platy	0.232	0.020	0.119	0.118	0.052	0.081
Elongate	0.330	0.026	0.122	0.108	0.062	0.101

Trajectory ratios (f/s) give further information to the jump characteristics. It can be seen from the range of parabolic trajectories (Figure. 2.10), low values indicate their motion near-parallel to the slope and high values take a path that must initially work against gravity.

The trajectory ratios follow a similar trend to the jump heights (Figure. 4.15). The *equant* rock produces the flattest trajectories. The parabolic arch of trajectories increases for the *platy* to the *elongate* rock, shown also for the mean values (Table. 4.2). In all experiments, jump heights and trajectory ratios show a shape dependency which can be related to the length of the equivalent inertial ellipsoid's largest axis.

During a rock-ground impact the inertial axis of a rock acts as a moment arm or lever which must be overcome should an edge or corner point become pinned in the terrain surface. The characteristics of the jump depend on the amount of work that must be done to overcome the moment arm that is set up between contact point with the ground and the centre of mass. Because the slope angle of the terrain alters this condition, the results of jump heights and trajectory ratios have been further separated according to slope angle (Figure. 4.16), to observe how an increase in slope angle changes the jump characteristics.

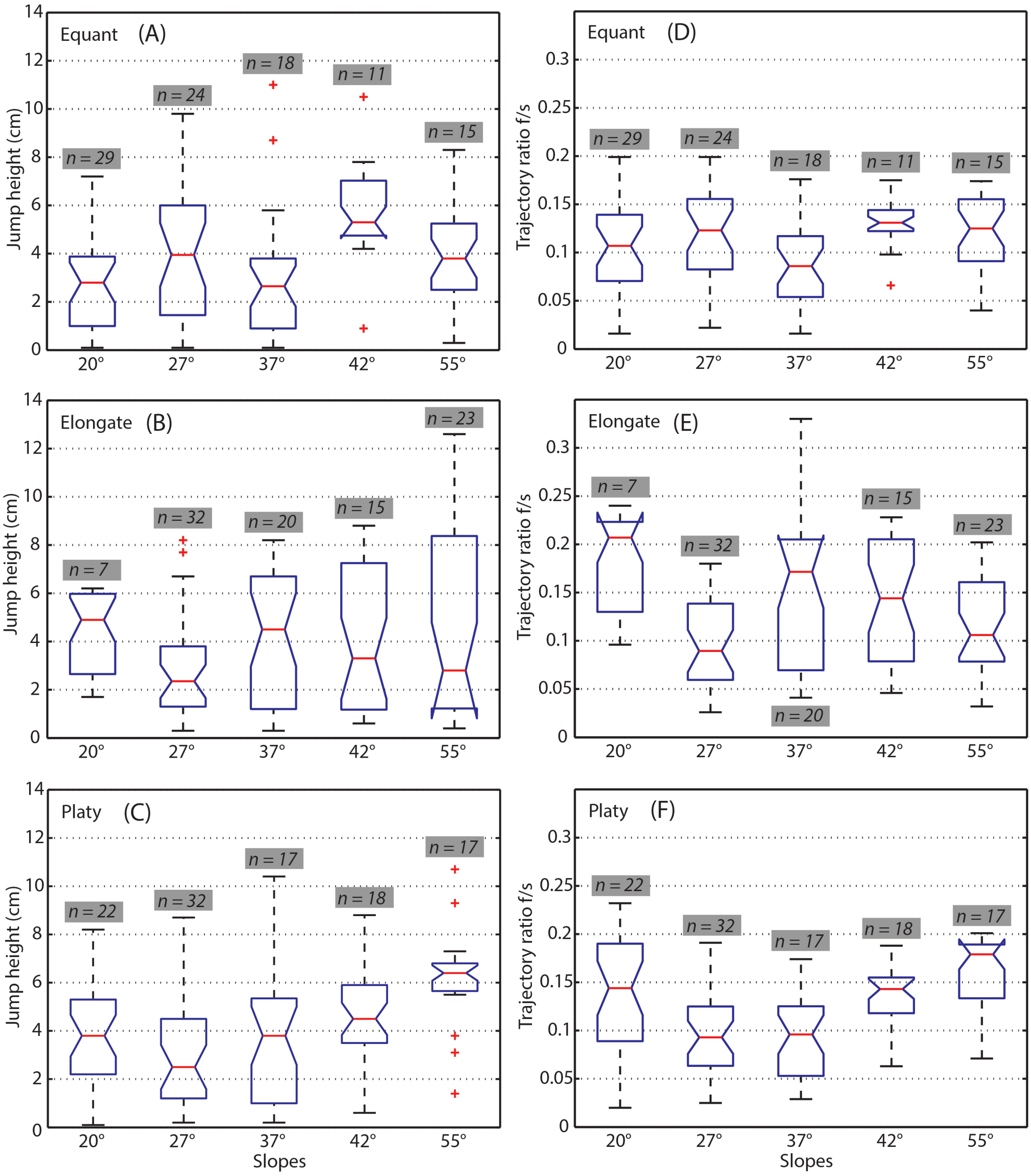

FIGURE 4.16: Left figures A, B and C present boxplots of the jump heights recorded for each slope angle and rock-shape. On the right figures D, E and F present the trajectory ratios f/s. The number of measurements n is given above each box plot.

4.4.2 Jump characteristics and slope angle

In nearly all cases jump height increases with increasing slope angle (Figure. 4.16). The *equant* rock suffers from under sampling at the highest slope angles due to the rock bouncing out of the camera view before the final impact could be measured (Section. 2.2.5). With the *elongate* rock jump height increases with increasing slope angle. Furthermore the range of jump heights also increases with slope angle. However, the median jump height decreases with increasing slope angle.

The trajectory ratios show a different trend to those expressed by the jump heights. The *equant* rock has consistently flat trajectories for all slope angles, with median values around $f/s = 0.1$ and the maximum values reach up to $f/s = 0.2$.

The *elongate* rock shows the greatest range in and highest values of f/s, which produce highly arced trajectory parabola. The *elongate* rock's maximum range in f/s values and maximum value of f/s occurs on the 37° slope, while there appears no clear trend that is dependent on slope angle.

The *platy* rock has its maximum value of and range of f/s for the 20° slope, which then falls reduces to the lowest values at 37°, after which f/s climbs again as slope angle increases. The *platy* rock's f/s values are generally higher than the *equant* but lower than for the *elongate* rock.

4.4.3 Summary: jump characteristics

To summarise the results of the jump characteristics recorded:

- In order of increasing jump heights; for maximum and upper quartiles of the full dataset, the *equant* rock generates the lowest, followed by the *platy*, and the *elongate* rock which achieves the highest jumps. This result correlates to the size of the largest axis of the equivalent inertial ellipsoid (E_{2a}) for each rock-shape.
- For an increase in the size of E_{2a} there is an increase in jump height.
- The *elongate* rock shows a clear variability in jump heights. While achieving the greatest overall jump heights, the same rock produces some of the lowest jump heights.

- Jump heights tend to increase with increasing slope angle.
- Trajectory ratios (f/s) do not mirror jump heights, but rather appear characteristic to each rock-shape.
- The *equant* rock produces the flattest trajectories, where trajectories travel closely parallel to the slope. The *elongate* rock produces the highest arced trajectories, but has the greatest variability in its data.
- No clear trend can be attributed to the trajectory ratio according changes in slope angle.

The jump characteristics between ground impacts shown above are a reflection of the rebound behaviour, where rebounds are a function of the rock impact configuration at the time of impact. The following two sections look at the apparent restitution coefficients (Section. 4.5) and impact configuration (Section. 4.6) in detail.

Apparent restitution coefficients are the popular method to quantify the kinetic losses of the rock to the ground during an impact, and therefore can provide a measure which relates rebounds to jump characteristics. The impact configuration on the other hand considers the position and kinetics of the rock at the initial rock-ground contact. Impact configuration includes the magnitude of the principal inertial axes, and the size of the principal axes of the equivalent inertial ellipsoid. The following section considers how impact configuration can determine the result of rebounds and respectively the jump characteristics.

4.5 Apparent restitution coefficients

Apparent restitution coefficients are the ratio between rebound and incident velocity vectors of the rock mass centre in slope tangential and slope normal directions (Eqs. 3.10 and 3.9). This approximation of rebound is a popular method to characterise rock-ground impacts in many modern rockfall models employing the 'lumped mass' rebound method (Section. 3.4.2). In most cases restitution coefficients are selected to represent the average rebound behaviour associated with a specific terrain material. The flaw in this method is that by only considering the velocity of the rock mass centre, rock-shape is neglected. The method cannot account for the differences in velocity that the rocks mass centre will experience compared to the outer contact point. This problem is accentuated as rock-shape departs from an *equant* ellipsoid (sphere), including changes due to angularity.

Specifically for slope normal velocities (R_n), one of the biggest difficulties is the case when the rebound velocity is greater than the incident velocity, $R_n > 1$. This implies the rock gains translational kinetic energy during the impact, which energetically must be incorrect if shape is ignored. Many authors now report R_n values that exceed 1 from field and laboratory experimentation (e.g. Bourrier et al., 2012, Buzzi et al., 2012, Spadari et al., 2012), while a full examination of the effects of rock-shape on restitution coefficients has been lacking.

The purpose of investigating restitution coefficients in these experiments was to illustrate how rock-shape and impact configuration affect the variability in restitution coefficients. Terrain parameters were constant throughout the experiments such that variance in the results can be attributed to a shape or impact configuration alone. This includes rock orientation, the impact velocity vector and the angular velocity. Slope normal R_n and tangential R_t restitution coefficients of single impacts were measured based on the velocity of the rock centre of mass as presented in previous sections.

There have been a number of experimental campaigns presented in literature that have investigated restitution coefficients. These can be divided into two main groups. i) Those involving single impacts that follow a period of free-fall in which the rock body is without rotational dynamics (Chau et al., 2002, Labiouse and Heidenreich, 2009), and ii) those which have been measured considering rotating rocks (Buzzi et al., 2012), and impacts during runout (Dorren et al., 2006).

Following the reasons above the restitution coefficients presented here are separated into these two groups. The first are those which result from first slope impacts after the free-fall release (Figs. 4.17 and 4.18). The second are those associated with the series of impacts during runout (Figs. 4.19 and 4.20).

4.5.1 First impacts

The scatter plot of first-impact R_t and R_n values (Figure. 4.17) shows that R_n has a negative correlation with R_t. The *elongate* rock shows the greatest range in behaviour, and even produces negative R_t values. This reflects an impact that causes a jump that is directed back up slope. Associated with the lowest R_t values the highest R_n values, are produced for experiments with the *elongate* rock. The mean values highlight the differences dependant on rock-shape. For first impacts, the *elongate* rock, on average, has low R_t but higher R_n values. The *platy* shape mirrors this characteristic having the lowest average R_n value, while the highest R_t value. The *equant* shape lies in the middle, but has higher R_t values.

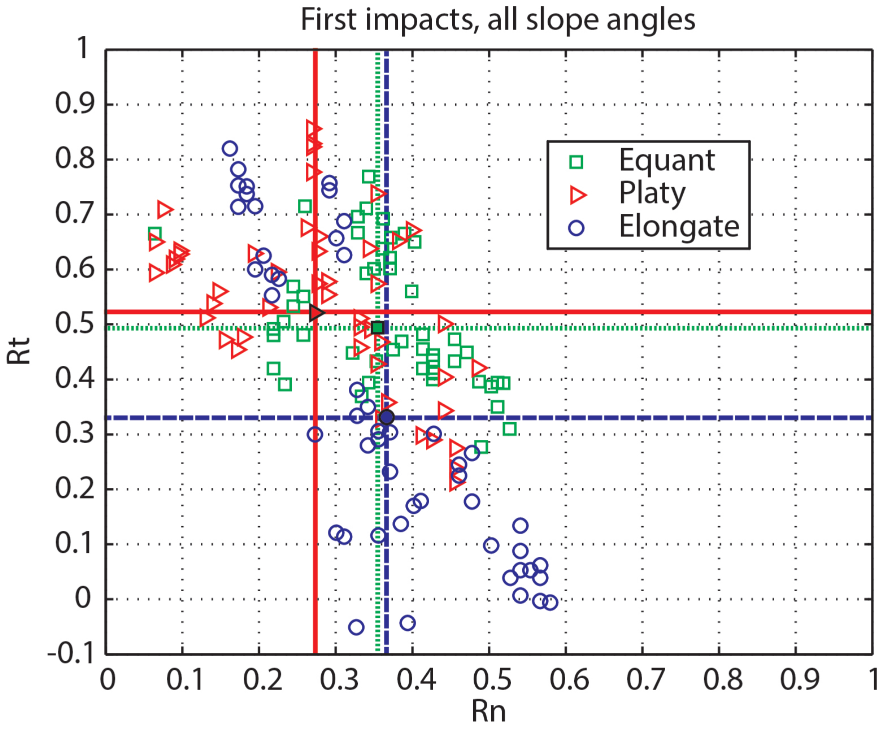

FIGURE 4.17: Tangential (R_t) and normal (R_n) restitution coefficients recorded from the fist impacts with the slope after release. Rock shapes are differentiated by the colour and shape of the symbol; *equant* (green, square), *platy* (red, Triangle) and *elongate* (blue circle). Mean values are indicated by the cross lines and markers that are filled in colour indicate.

The data from all slope angles are presented together to illustrate that single restitution coefficients cannot simply be associated to a single terrain property, in the case of these experiments a wooden board with a carpeted surface. The data from the first impacts shows great variability associated with the impact conditions relative to slope angle in this case. As potential energy was constant for experiments with all slope angles, the free-fall height before release reduces with increasing slope angle (Table. 3.1). This leads to faster first impact velocities at lower slope angles.

Figure 4.18 separate the data according to slope angle. For R_n values a positive correlation with slope angle is observed, which implies a negative correlation of R_n with impact velocity. The negative correlation of R_n with velocity is also observed in sports ball trajectories (Haron and Ismail, 2012). Here the *equant* and the *elongate* rocks capture this trend most clearly.

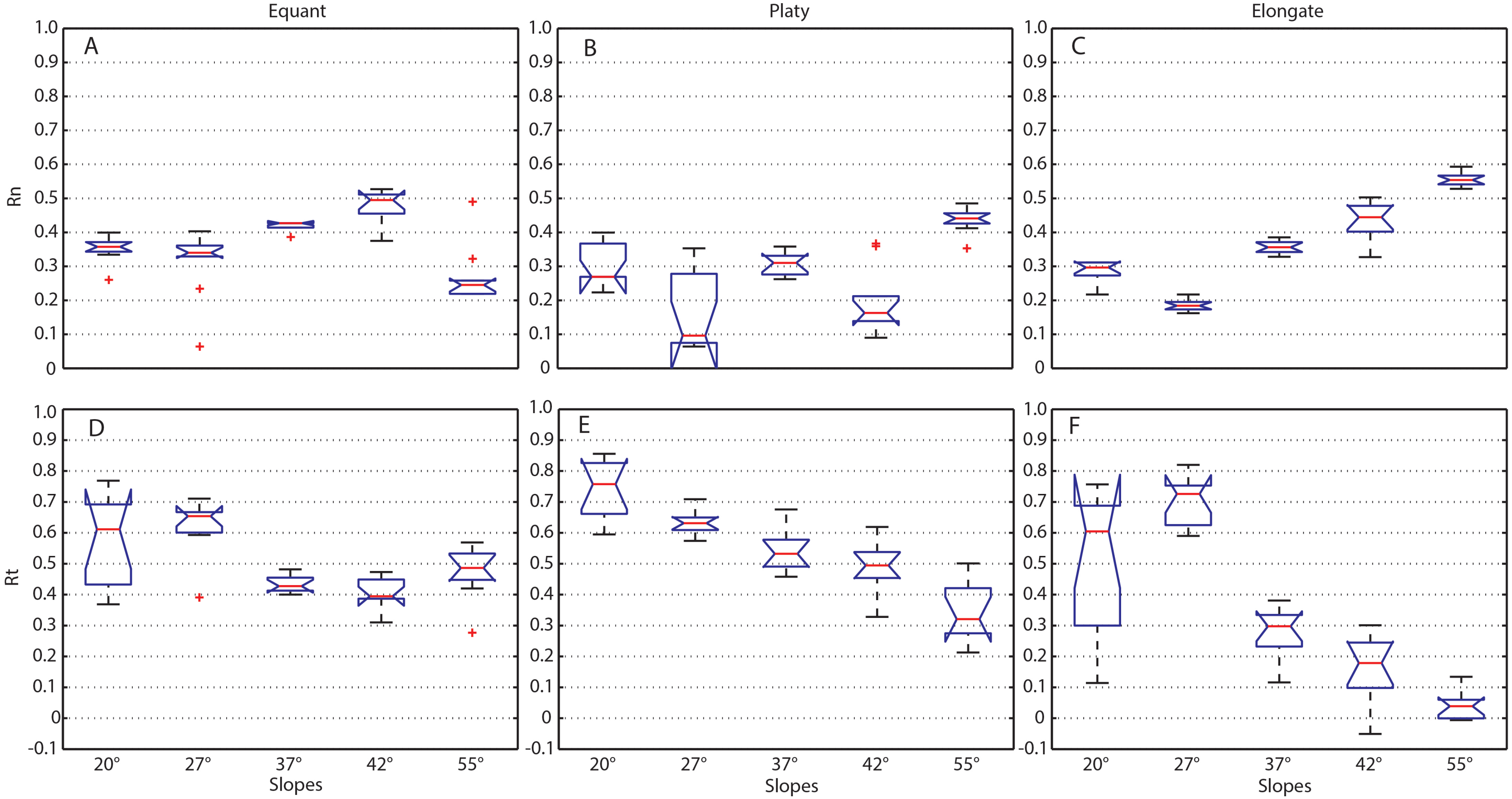

FIGURE 4.18: Box plots of measured normal R_n (A, B and C) and tangential R_t (D, E and F) restitution coefficients recorded for first impacts for each slope angle. The release orientation in all cases is A (Figure. 3.3).

R_t values show a negative correlation with increased slope angle, generating a positive correlation to impact velocity. Higher initial impact velocities produce greater values of R_t for first impacts. The effects of impact velocity influence the non-equant rocks more. *Elongate* and *platy* rocks have a greater range in both R_n and R_t values across all slope angles as compared to the *equant* rock. The most extreme is the *elongate* rock with R_t values ranging between -0.05 and 0.82. The *equant* rock on the other hand operates in a much smaller range. For example R_n values are between 0.2 and 0.5. All R_n and R_t values of first impacts are below unity, and in the range reported in similar experiments documented in literature (Chau et al., 2002, Labiouse and Heidenreich, 2009).

It is important to note that in first impacts the restitution coefficients of impacts occurred where the rock was without rotational motion, such that only the impact angle and translational velocity vector contributed to the impact configuration. As rotational motion will also have a bearing on the outcome of rebounds, restitution coefficients for impacts that occurred during runout of the test blocks are presented in the following section.

4.5.2 Impacts during runout

Figure 4.19 plots the restitution coefficients for rebounds that occurred during runout. The data show larger scatter than observed in first impacts, attributed to the addition of rotational behaviour. The range of R_t values is much smaller than compared to R_n. The boundary that indicates restitution equal to 1 (unity) is drawn into the figure as a dotted black line. These data show that R_n values greater than unity are common in these experiments. Yet a large portion of the experimental data still lies below $R_n = 1$. Mean values for all shapes all exceed 1. R_t values > 1 are also possible, although infrequently observed. R_t values show a negative but less apparent correlation to increases in R_n. As R_n values become more extreme this trend becomes less apparent. The max R_n values observed are just below 6 and are achieved in the *platy* rock experiments. For the extreme R_n values the corresponding R_t values are comparatively low for the *elongate* rock as compared to the *platy* and *equant* rocks.

The boxplots in Figure 4.20 present the restitution coefficient according to slope angle. R_n values for all shapes increase with increasing slope angle, in addition to increases in the range of values. This trend is best seen in the *platy* rock experiments (Fig. 4.20

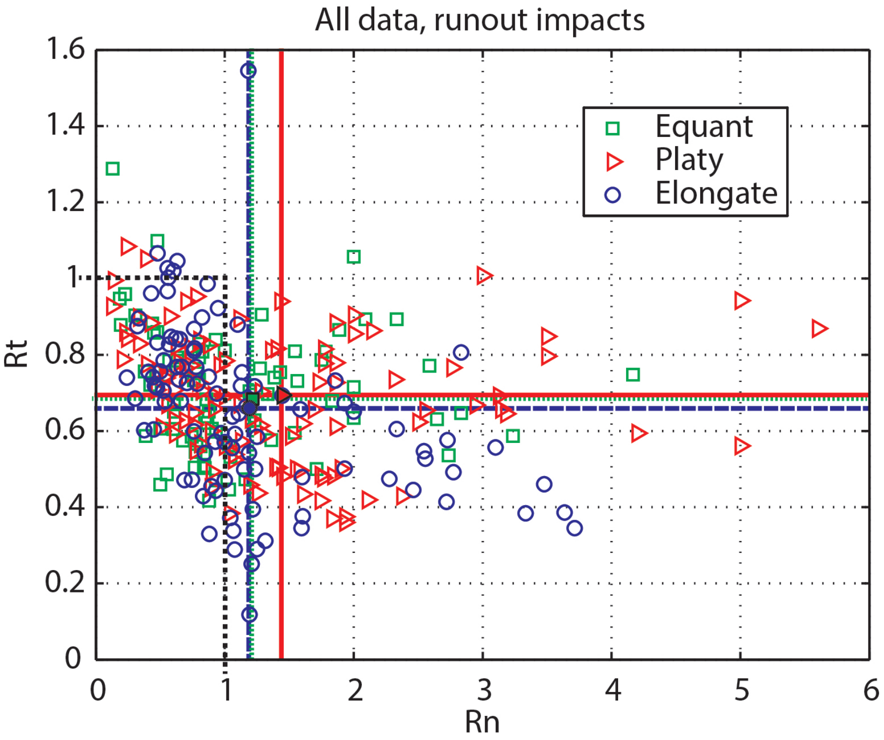

FIGURE 4.19: Tangential R_t and normal R_n restitution coefficients measured during runout over all slope angles. Note that the first impacts following the release of the test block are excluded from this data. Rock shapes *equant* (green, square), *platy* (red, Triangle) and *elongate* (blue circle). The markers that are filled in colour indicate the means of each shapes data set and are also located with the coloured cross-hairs.

(B)). In contrast to R_n values of first-impacts (Figure. 4.18) the *platy* rock experiments show the largest and greatest range in R_n during runout. It is evident that data for slope angles that are under sampled, the R_n and R_t values do not show this trend.

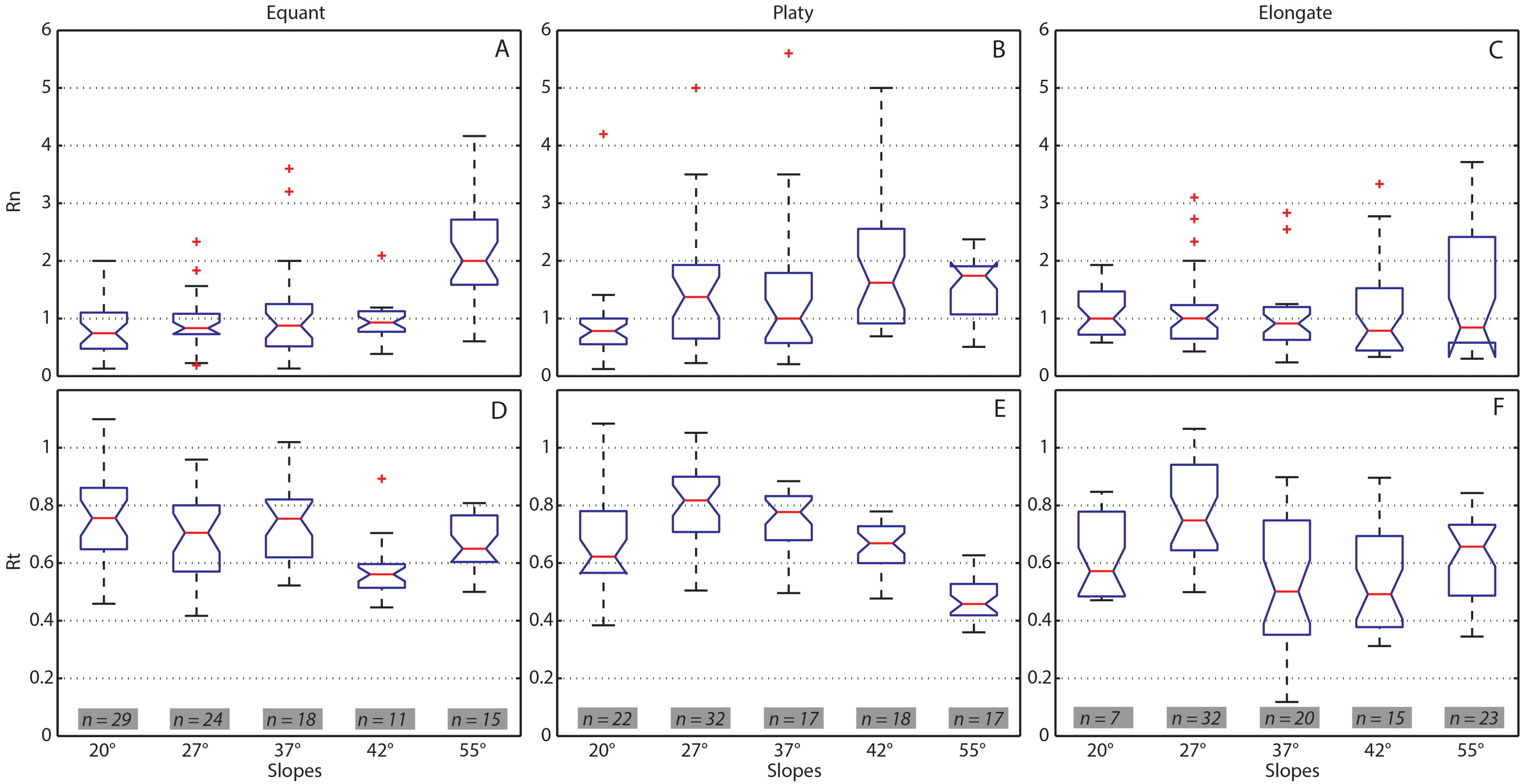

FIGURE 4.20: Box plots of measured normal R_n (A, B and C) and tangential R_t (D, E and F) restitution coefficients recorded *during runout* for each slope angle.

The tangential restitution coefficients (R_t) mirror R_n, as observed for first-impacts. This is best seen again for the *platy* rock, where R_t values decrease with increasing slope angle. This trend is more difficult to discern for the *elongate* and the *equant* rocks which both show a greater range in R_t values.

4.5.3 Summary of apparent restitution coefficients

Restitution coefficients presented here show a great range in values, which appears dependant on both shape and impact configuration. The following summarises these findings in detail:

- Two distinct patterns of restitution coefficients can be seen between first impacts following free-fall, and the impacts observed during runout. First-impact normal restitution coefficients all occur within the bounds of unity, while average R_n values during runout exceed unity for all rock shapes.
- For first-impacts the test bodies enter the slope without rotation. The R_n values for all shapes are negatively correlated to the initial impact velocity, while R_t values mirror this trend positively, correlating with impact velocity. It is anticipated that by adding rotation to the initial impact the R_n value might respond positively to increasing rotational velocity, while this is much dependant on the configuration of the initial impact.
- During runout maximum and upper quartile R_n values increase in value and variability with increasing slope angle.
- R_t values show a decrease with increasing slope angle, a trend most apparent for the *platy* rock.

It can be seen that by characterising rebounds using the method of apparent restitution coefficients shows great variability in behaviour. There appears a clear dependence in R_n and R_t on impact configuration. For first-impacts where the impact configuration was well-constrained (i.e. fixed velocity and rock orientation without rotation), the resultant restitution coefficients show clear dependence on velocity (Figs. 4.17 and 4.18). Moreover, the importance of shape is highlighted by the increase in the range of the data with increasing size of the principal inertial axis E_{2a} of the test rock. The *elongate* rock showed the greatest range in values of coefficients of restitution, while the *equant* rock has the smallest range in values.

The dependence of the rebound on the impact condition and shape is more difficult to discern from the data recorded during runout. The data show a far greater range in coefficients of restitution than those from first impacts above, and in many cases derive a large skew. For example, the greatest range of R_n values for the *elongate* rock are recorded for the 55° slope; here the upper quartile and max values are the largest observed while the median and minimum values are near the lowest compared across all slope angles.

To investigate further why more extreme restitution coefficients occur during runout and with a greater range in values, the configuration of the impacts was documented for each impact. This included the rock orientation during impact, its impact velocity vector and rotation speed.

4.6 Impact configuration

The following section presents the measurements of the initial impact configuration in respect to the outcome of each rebound (e.g. R_n values and trajectory ratio f/s). Indicators of impact configuration include rock orientation angle α, the angle γ and magnitude of $\overrightarrow{U^P}$, and the rocks angular speed Ω.

4.6.1 Rock impact orientation α

In order to investigate the mechanism of the moment arm that is set up by the orientation of the position vector r_i at the point of contact, its effect on R_n was first explored. R_n gives an indication of the proportion of the impact dynamics that are directed away from the slope into free space.

Figure 4.21 plots the impact orientation of the rock body α against the normal restitution coefficient R_n. The first observation is that with an increasingly acute impact orientation there is an increase in R_n. However there is a bi-modal distribution between 50- 60°, after which with more acute impact orientations R_n drops considerably.

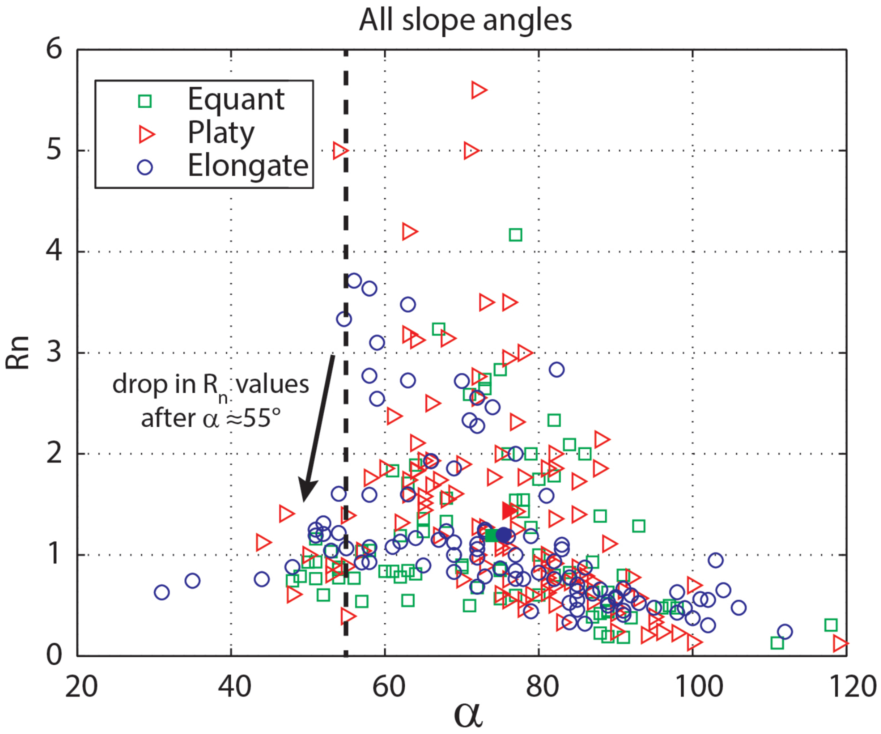

FIGURE 4.21: Normal (R_n) apparent restitution coefficient is plotted against impact orientation α. Results are plotted for each different shape and all slope angles. Average values are plotted as solid colour. The black sketched dotted line marks an apparent threshold in the data set after which the α angles are too acute and represents a drop in the R_n values.

Extreme $R_n(> 2)$ values occur between impact orientations of 55 - 80°. The *platy* rock experiments shows extreme R_n values produced larger angles from around 80°. In contrast, the *elongate* rock's extreme R_n values occur at more acute impact orientations starting at 70°.

With respect to impact orientations below 55° resulting in R_n values between 0.3 and 2, a higher proportion of these results can be attributed to the *elongate* and *platy* rock affect. At large α angles $> 80°$ R_n values are consistently lower, ranging between 0.05 and 1.0. Moreover, the range of R_n for larger α angles is much smaller than the highly acute impact orientations 23 - 55° which show greater spread in R_n. A summary sketch presents the three main regions which can be identified, is presented in Figure 4.22.

By studying the impact orientation angle α an insight of how the moment arm created by the position vector r_i can act as a lever during impact is provided. The notion that the lever sets the resultant trajectory geometry can be examined by plotting α against the trajectory ratio f/s.

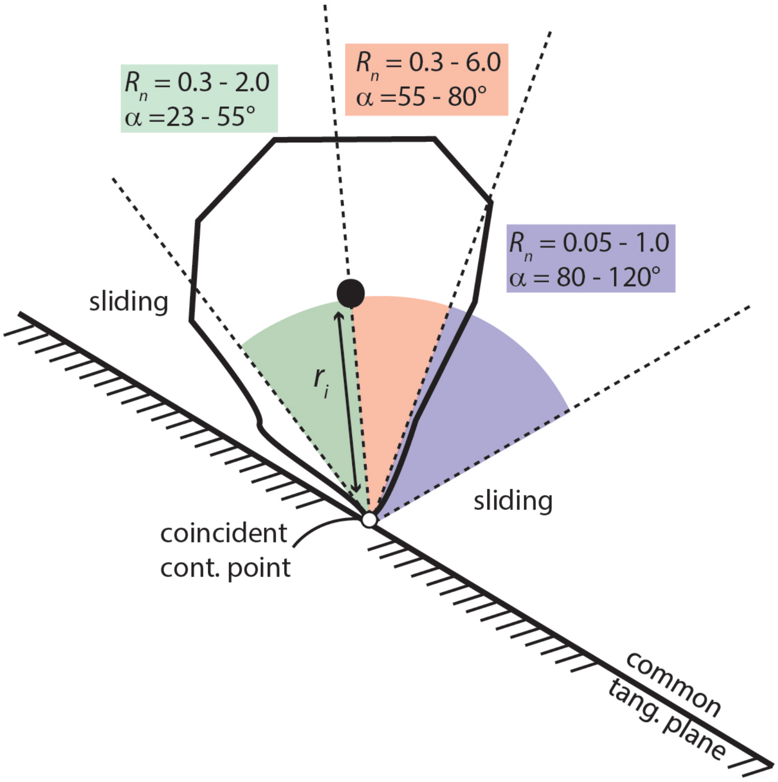

FIGURE 4.22: Sketch of the R_n values that result from the different impact orientations α. The red zone generates the most extreme R_n values. Impact orientations close to parallel with the slope commonly enter sliding.

Figure 4.23 shows that with increasingly larger impact angle α the trajectory ratio f/s decreases, reflecting flatter trajectories (see Figure 2.10). With increasingly acute α angles trajectories become increasingly arced. In this plot a linear relationship has been assumed and a regression analysis performed to summarise this relationship as controlled by shape. The regressions are performed excluding data $\alpha < 50°$, as data in this region sit close to the point where a rebound is not achieved and the test body enters sliding (Figure. 4.22).

The R^2 correlation coefficients give a moderately significant correlation. The *elongate* and the *platy* rocks correlate best with R^2 values of 0.72 and 0.77 respectively, while the *equant* rock does not correlate as well, with an R^2 of 0.61. Each linear trend shows a statistically significant relationship between the impact orientation α and the jump trajectory ratio f/s. With increasingly acute impact orientations the resultant rebound trajectory becomes increasingly arched (greater f/s values), and importantly the slope of this relationship is steeper for non-equant rocks.

Between rock shapes, the trend lines indicate different rebound characteristics. For example the *elongate* rock has a higher y- intercept than the *platy* rock. This shows that for equal impact orientations the *elongate* rock generates higher f/s ratios than the *platy* rock, reflecting higher arced trajectories. It is interesting to note that the increase in the gradient of the regression between the *equant* and non-equant rocks and the increase in the y- intercept between the *platy* and *elongate* rocks follows the increasing length of the longest principal axis of the equivalent inertial ellipsoid.

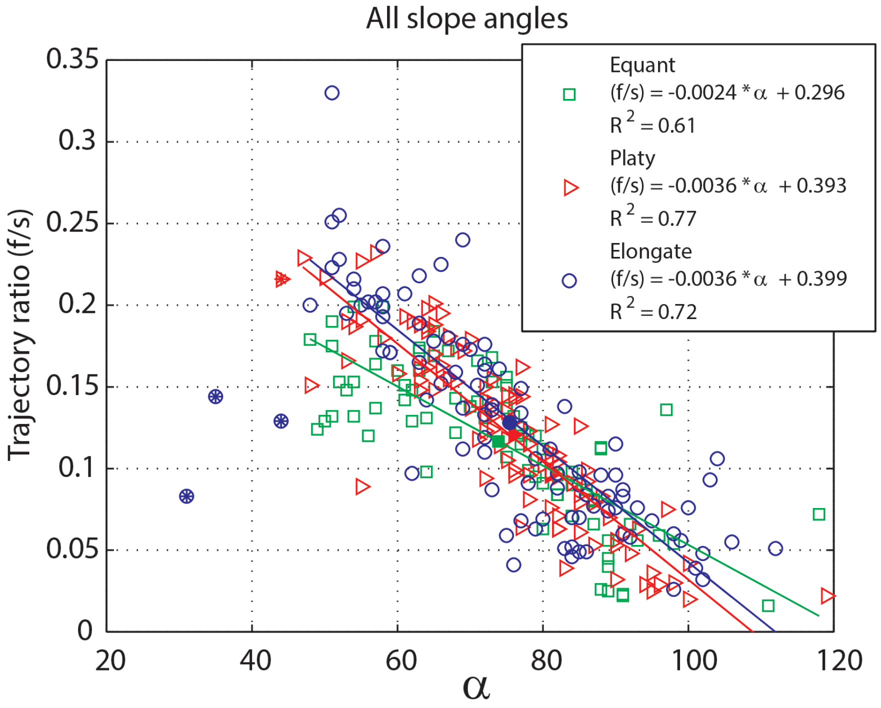

FIGURE 4.23: Trajectory ratio (f/s) plotted against impact orientation α. Results are plotted for each different shape and all slope angles. Average values are plotted as solid colour, standard deviations are given in the legend.

While the data show that impact orientation α and the trajectory ratio f/s are correlated, and impact orientation is a key component to the outcome of impacts, the standard error in the results and the R^2 values suggest this simple model misses important components of the dynamics that are involved in the impact mechanics. Moreover potential errors in the measurement have not been accounted for.

4.6.2 Orientation γ and magnitude of $\overrightarrow{U^P}$

During an impact, the angle γ between the slope surface and $\overrightarrow{U^P}$ was measured and compared to the resultant rebound. Figure 4.24 shows a positive non-linear response to $\overrightarrow{U^P}$. The second order linear fit has normally distributed residuals where the standard deviation of residuals is between $R_n = 0.5$ to 0.7. This demonstrates that as the impact approaches slope normal, R_n values increase.

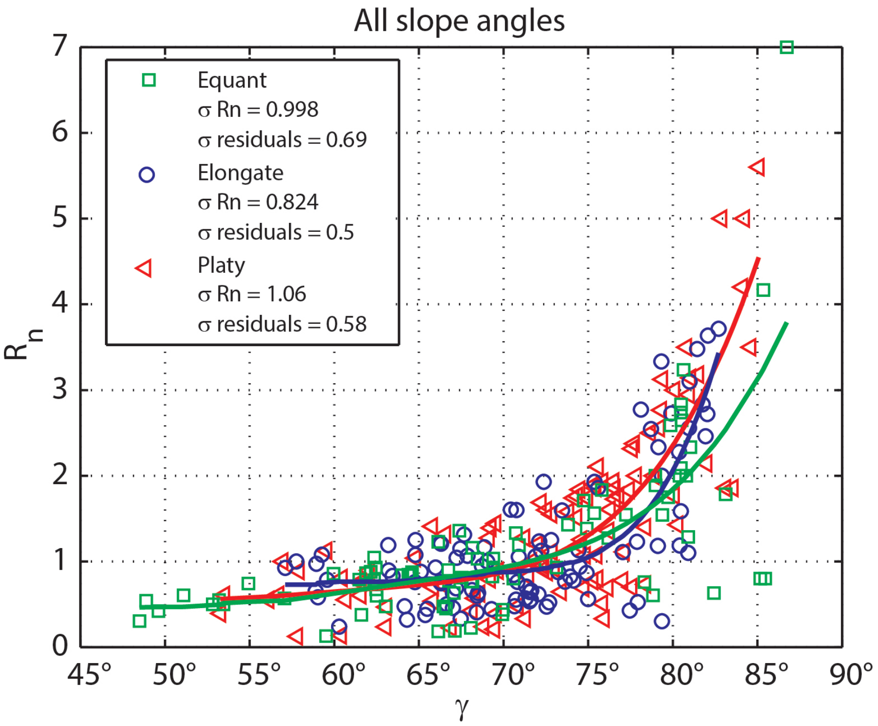

FIGURE 4.24: Normal (Rn) apparent restitution coefficient is plotted against the angle γ of the translational velocity vector with the slope. Results are plotted for each different shape and all slope angles. A second order trend line is fitted to each data set and represented as a solid line.

On the other hand, plotting γ against the trajectory ratio f/s and the jump height appears to have no discernible pattern (Figure. 4.25) and (Figure. 4.26), suggesting that the orientation of $\overrightarrow{U^P}$ is not essential in determining the shape of the rebound trajectory or the jump height.

4.6.3 Rock rotational speed Ω

The final dynamic component during an impact is the rotational speed Ω. Ω between impacts can be assumed to remain constant if rotational decay due to air resistance is neglected. The rotational speed between impacts was measured using the dynamic StoneNode. The segments of the signal were divided using the accelerations measured during impacts the method is given in Chapter 3 Section 3.5.

The rotational speeds of the test rocks can be observed by plotting the distribution of all the inter-impact angular velocities for each experiment. Figure 4.27 plots the

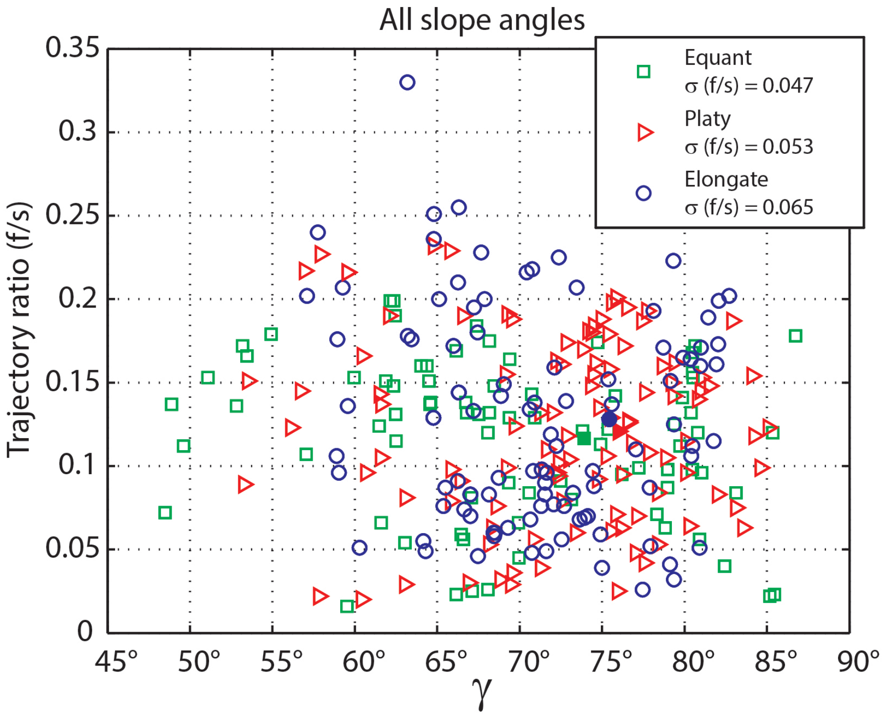

FIGURE 4.25: Trajectory ratio (f/s) plotted against the angle γ of the translational velocity vector with the slope. Results are plotted for each different shape and all slope angles. Average values are plotted as solid colour; standard deviations are given in the legend.

distributions of angular velocities according to each rock-shape. The figure groups all slope angles and release orientations into each data set, and gives the absolute rotational speed of the rock in rad·s^{-1}.

Figure 4.27 shows a bimodal distribution of rotational speeds, for each shape. The data range from 0 - 60 rad·s^{-1}.

Overall the results show the *platy* rock form to have the slowest rotational velocities while the *equant* rock form the fastest, each displaying a bimodal peak in rotational velocities. The first peak centres over the lower rotational velocities around 10 .0 rad·s^{-1}, while the second is centred over rotational velocities of around 40 rad·s^{-1}.

There is a convergence at a rotational speed of ∼28.0 rad·s^{-1}. The lowest median peaks lie between 9.0 - 10.0 rad·s^{-1}, and the maximum peaks are between 39.0 - 41.0 rad·s^{-1}, with maximums extending up to 60 rad·s^{-1}.

It is important to note the troughs before the peaks to the right which reflect the maximum rotational velocities. The troughs centre around 35.0 rad·s^{-1}, which is the limit sensitivity of the 3-D gyroscope sensors for each of the principal rotation axes.

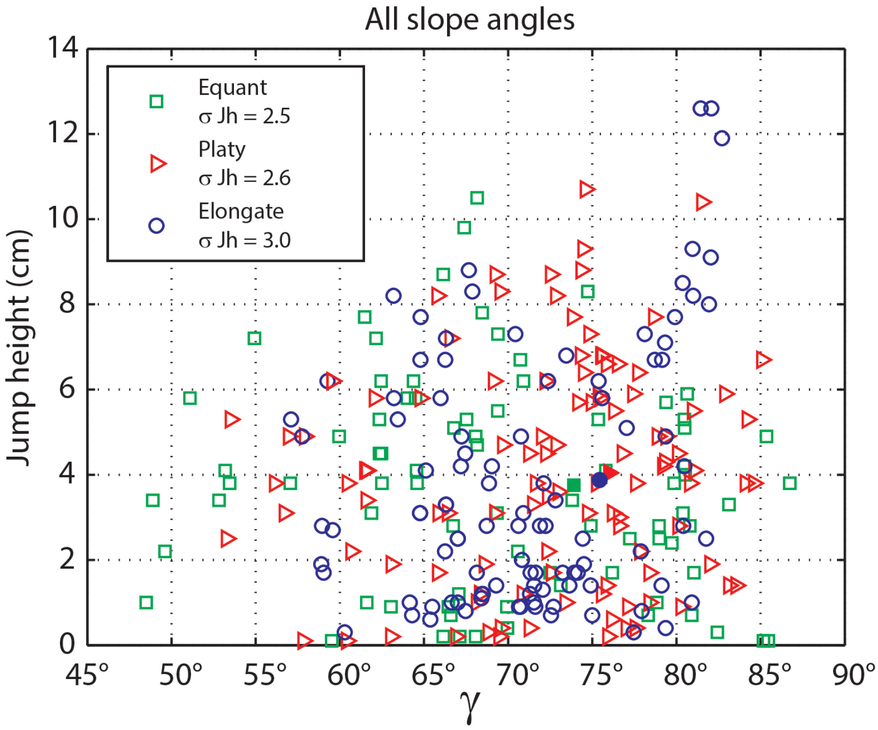

FIGURE 4.26: Jump heights (*cm*) plotted against the angle γ of the translational velocity vector with the slope. Results are plotted for each different shape and all slope angles. Average values are plotted as solid colour; standard deviations are given in the legend.

Given that the Euclidean norm of all contributing rotational axes is considered in this particular measure of angular velocity from these data, any angular velocities reported that exceed 35.0 rad·s^{-1} must reflect high velocity rotations about more than one of the principal rotation axes. With this, the maximum rotations capture the influence of rock-shape on the result. It suggests that the *equant* rock form, having principal inertial axes that are equal, can more easily engage multiple rotational axes and exchange rotations between rotational axes, while the non-equant rock forms do not experience this as much.

4.6.4 Angular speed, slope angle and release orientation

Slope angle and initial release orientation have an influence on rotational speed. The box plots on Figure 4.28 plot the distribution of inter-impact rotational velocities according to slope angle and release orientation. Similar to the work of (Ritchie, 1963) who identified characteristic rockfall runout behaviour (slide, roll, bounce and fall) according to slope angle, these figures illustrate that slope angle plays a key role in determining the

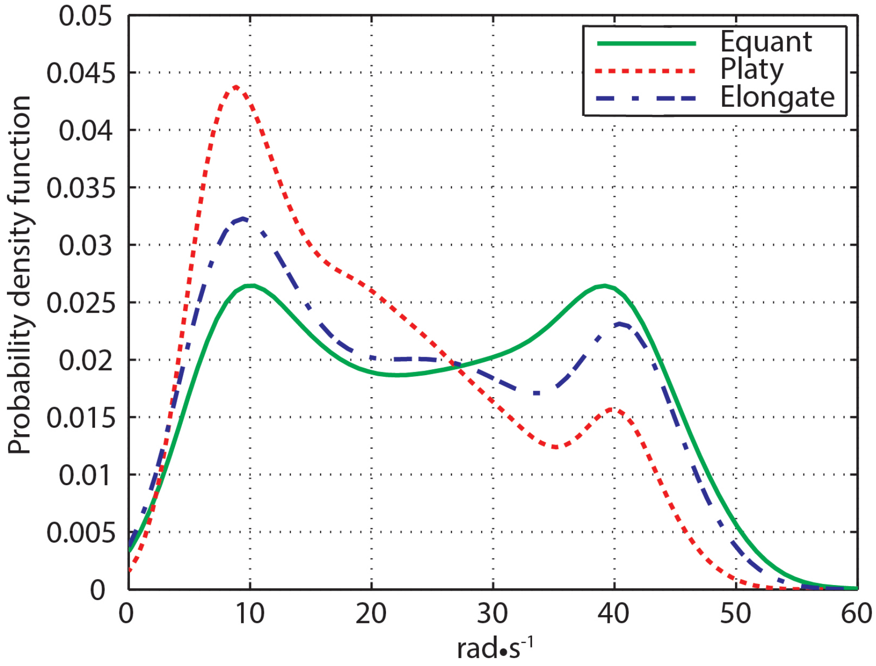

Figure 4.27: KDE showing distribution of rotational velocities according to each test rock-shape. The data are sampled from all experiments on all slope angles.

rotational velocity of the rock body. Moreover, the characteristics are pronounced to a greater or lesser degree as function of rock-shape.

The *equant* rock form shows the greatest response to slope angle in the rotational velocity showing two main trends. The maximum rotational velocity is lowest in experiments with the lowest slope angles (20°) reaching a maximum on slopes of 37°, after which velocities decrease again. For the median values of rotational velocity, the peak is at 27° after which it decreases strongly to slower velocities than those observed for the initial 20° slope. The *elongate* and the *platy* rock forms also show an increase and then a decrease according to slope angle with a peak around 37°. This trend is again more pronounced in the *elongate* rock form than the *platy*.

With respect to the initial release orientation, there are also differences albeit more subtle than according to slope angle. The *elongate* and the *platy* rock forms show an opposing trend in which release orientations that align the largest principal inertial axis perpendicular to the fall line of the slope produces the fastest rotational velocities for the *platy* rock form, while for the *elongate* rock form these velocities are comparatively slower. This trend is reversed for the release orientations with the smallest axis of inertia aligned perpendicular to the fall line of the slope.

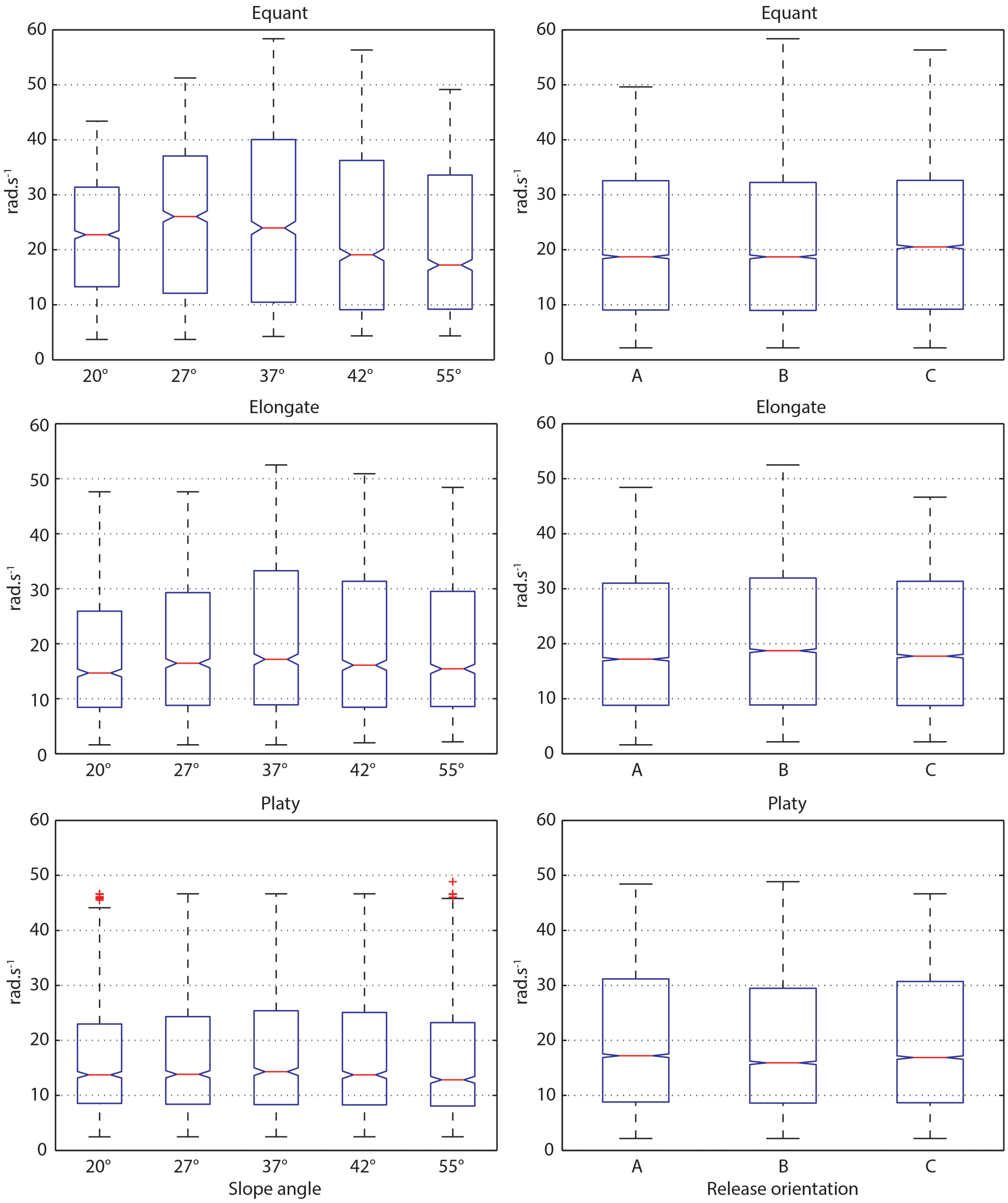

FIGURE 4.28: Box plots showing angular velocities of each rock-shape according to slope angle (*left column*, and according to release orientation (*right column*.

The *equant* rock form shows no clear trend that can be attributed to the inertial axes for the rock-shape as they are all equal. However, there are still some clear differences in the rotational speeds under different release orientations, suggesting that this behaviour can only be a function of the facets and edges that initially impact the test slope. This is an aspect of this work that could not be covered in the physical experiments because of the large number of experimental variations that would be generated if this additional aspect of shape was also included. However, with the utility of the numerical rockfall model, the multiple iterations required to investigate the additional aspect of rock-shape and angularity could be examined in the numerical modelling section (Chapter. 5).

The rotational velocity of rocks during rockfall is of importance because it can have a control on a rock's mobility over terrain. There are two features of rockfall motion that can be affected; Firstly the impact configuration, and secondly the rotational stability. Rotational stability in this sense is the tendency for a rock to maintain rotation about a single axis of principal inertia for a durated period of time.

4.6.5 Impact configuration and angular speed

The impact configuration and rotational velocity are of importance as these measures consider the common phenomena where rocks can gather translational velocity through rolling in an efficient manner, and then may suddenly catch an edge or corner which launches the rock particle into a ballistic trajectory exaggerating jumping behaviour. Rotational behaviour and impact configuration were investigated by looking at the coefficient of rotational restitution resulting from an impact with the ground.

4.6.6 Impact configuration summary

To summarise the results of the impact configuration the three key components impact orientation α, the angle γ of $\overrightarrow{U^P}$, and the angular velocity ω. These parameters cannot be considered in isolation: their composite influence defines the outcome of an individual impact.

4.7 Axes of rotation

Measuring the rotational dynamics of the test rocks had three main purposes: i) to consider the rotational dynamics before and after each impact and how this was related to the outcome of a rebound; ii) to identify if there was a preferred rotational axis between the three principal inertial axes according to the shape of the rock; iii) to associate the rotational behaviour to rockfall runout and deposition patterns. An attempt to quantify the characteristics of the rotations defining ordered and disordered rotational behaviour was made, which could then be compared to the lateral dispersion recorded during each runout.

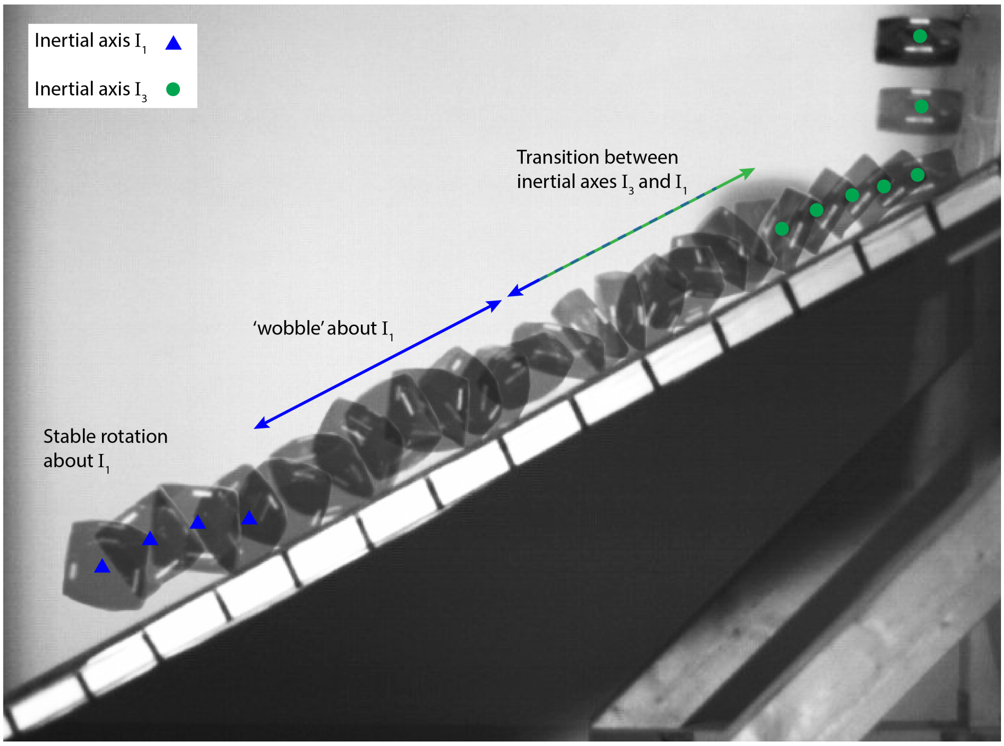

FIGURE 4.29: A sequence image of a typical runout experiment involving the *platy* rock. Images are sampled at 120 H_z with the high speed video camera, in this image an image is displayed every 25 H_z. The image depicts an experiment where the test rock enters the slope with its smallest axis of inertia I_3 (marked with a green dot) aligned perpendicular to the central fall line, i.e. looking into the image plane. There is a transition between rolling axes, from the smallest I_3 to the largest I_1 (marked with a blue triangle). During the period that the test rock stands up to rotate about the axis of greatest inertia I_1 there is a period of 'wobble' while the rock gathers momentum and stability. The video of this sequence is available online (`http://youtu.be/v5MlhyGFsfY`).

Figures 4.29 and 4.30 illustrate the concept of how transitions between principal rotation axes can lead to instabilities associated with higher degrees of dispersion in runout. The video footage of these examples can be viewed online (see Figures 4.29 and 4.30), and provides a better illustration of this behaviour. In the cases where instability in the rotations is observed, rotations occur about more than one of the principal rotation axes. This activity was recorded using the StoneNode motion sensor embedded in the test bodies, and permitted the following analysis.

Stable rotations are recognised as those which held a dominant rotational axis for the majority of the runout time, as shown in Figure 4.31. Again, the signal recorded of the angular velocity about each principal rotation axis is analysed to distinguish between

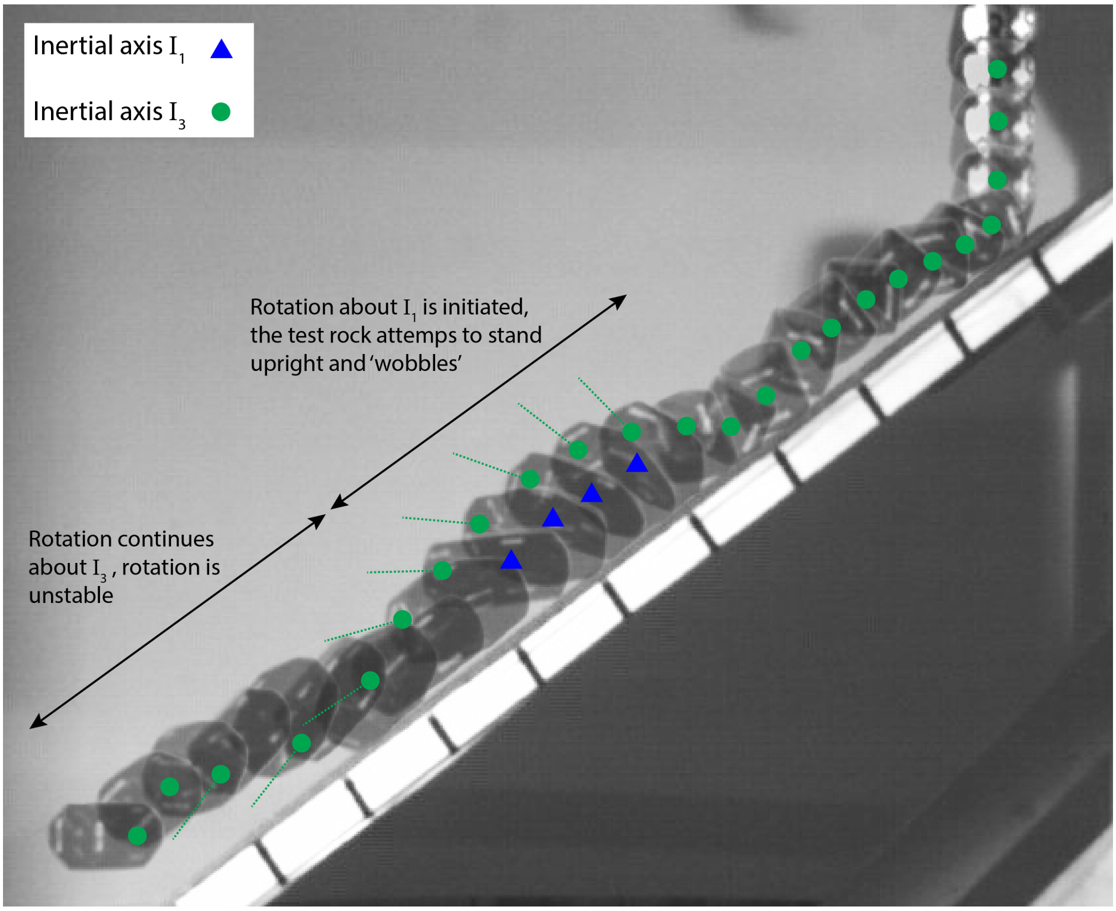

Figure 4.30: A sequence image of a runout experiment involving the *elongate* rock. Images are sampled at 120 H_z with the high speed video camera, in this image an image is displayed every 25 H_z. The image depicts an experiment where the test rock enters the slope with its smallest axis of inertia I_3 (marked with a green dot) aligned perpendicular to the central fall line, i.e. looking into the image plane. During the middle section the test rock has gained enough momentum to attempt to stand upright and rotate about the axis of largest inertia I_1 (marked with a blue triangle). The rock body doesn't achieve full rotations about I_1 and in the process delivers a 'wobble' instability into the rotations. The dominant axis of rotation remains I_3 following this event. The video of this sequence is available online (`http://youtu.be/h-IAnGH2jRk`).

disordered unstable rotational behaviour and ordered stable rotational behaviour. Additionally to the rotational stability, the relative dominance of the principal rotation axes was captured, and has allowed an investigation into the dynamics that lead to the unstable rotations which result in runout paths that deviate from the central fall line causing high lateral dispersion.

4.7.1 Preferred axes of rotation

The preferred axis of rotation during each experiment was identified by integrating the rotational activity about each axis over the period of the runout event, to establish the

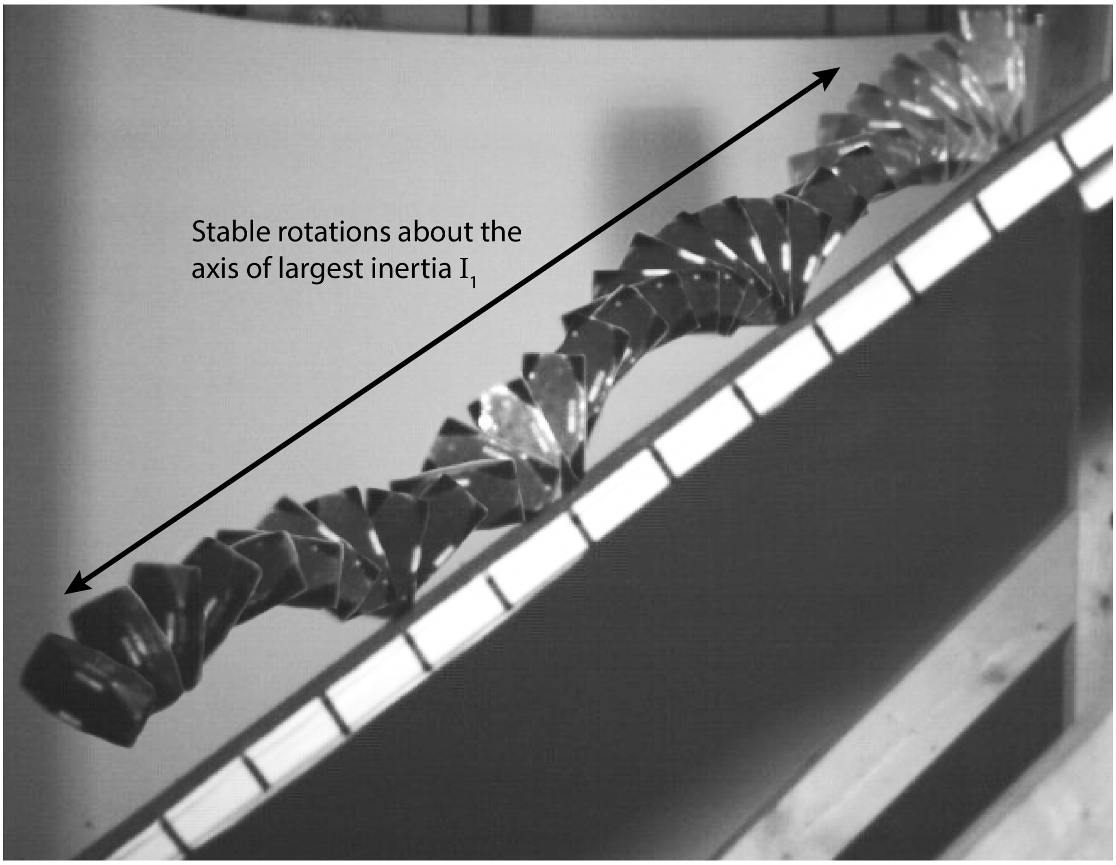

FIGURE 4.31: A sequence image of a runout experiment involving the *elongate* rock. Images are sampled at 120 H_z with the high speed video camera, in this image an image is displayed every 25 H_z. The image depicts an experiment where the test rock enters the slope with its largest axis of inertia I_1 aligned perpendicular to the central fall line, i.e. looking into the image plane. The rotation axis remains I_1 and is dominant throughout the runout event, the rotations are stable against the perturbations of the ground impacts. The video of this sequence is available online (`http://youtu.be/JxWiOt4jyFM`).

proportion of rotational its activity about a given axis relative to the others. Figure 4.32 identifies the dominant axis recorded for each experiment and the degree to which this axis was active relative to the others in the context of the final dispersion. As an example, a point that is illustrated as a blue star that lies on the 60% mark indicates that the I_1 axis was the dominant rotation axis during this event and commanded 60% of the total rotational activity which lead to an event with x dispersion.

TABLE 4.3: Table listing the overall percentage of rotational activity recorded about each principal rotation axis, and the degree of lateral dispersion in the runout patterns recorded for each rock.

	Orientation	I_1	I_2	I_3	$Max_{(W/L)}$	$Mean_{(W/L)}$	$\sigma_{(W/L)}$	$Max_{(Disorder)}$	$Mean_{(Disorder)}$	$\sigma_{(Disorder)}$
Equant	*A*	91.3%	2.2%	6.5%	0.53	0.11	0.10	3.68%	0.58%	0.69%
	B	24.5%	63.3%	12.2%	0.47	0.12	0.10	10.85%	1.11%	1.83%
	C	24.6%	66.7%	8.7%	0.59	0.16	0.13	2.82%	0.71%	0.55%
	All	44.7%	46.1%	9.2%	0.59	0.13	0.11	10.85%	0.80%	1.17%
Platy	*A*	95.8%	2.1%	2.1%	0.21	0.05	0.04	20.63%	1.87%	3.95%
	B	36.0%	4.0%	60.0%	0.44	0.16	0.12	51.10%	16.90%	12.69%
	C	30.6%	10.2%	59.2%	0.42	0.12	0.11	41.74%	14.17%	10.19%
	All	53.7%	5.5%	40.8%	0.44	0.11	0.11	51.05%	11.08%	11.66%
Elongate	*A*	60.9%	17.4%	21.7%	0.24	0.08	0.07	37.24%	9.34%	9.73%
	B	3.8%	0.0%	96.2%	0.67	0.19	0.15	51.40%	27.94%	10.76%
	C	8.5%	23.4%	68.1%	0.40	0.11	0.11	37.43%	14.80%	11.30%
	All	23.5%	13.1%	63.4%	0.67	0.13	0.13	51.40%	17.78%	13.20%

For the *equant* rock (top Figure 4.32) it is difficult to identify differences of behaviour between axes as they are all of the same length. Therefore, the data have been separated into release orientation mode. The distributions of the dominant rotation axes identify one clear trend; that when the *equant* rock was released in orientation C (onto a corner point), the highest values of dispersion were recorded. It should be noted that in this position none of the principal rotation axes are aligned perpendicular to the slope fall line. On the other hand, when the *equant* rock was released in position A, (which aligned a rotation axis perpendicular to the fall line); the lowest values of dispersion were recorded. This suggests that the angularity of the rock-shape could have a greater influence when the rock is equant.

For the *platy* rock there appears a clearer trend between the dominant rotation axes. With reference to Figure 4.32 B there are two peaks which differentiate between dominant rotations about the axis of largest inertia I_1 (represented in blue), and the axes of smallest inertia I_2 and I_3 (represented in the green and red dashed line). Because the principal axes of smallest inertia are in this case of the same magnitude for the *platy* rock, the results have been combined and displayed in a single distribution. It can be seen that there is a higher probability that for the *platy* rock rotations will occur about the axis of largest inertia. Of all experiments conducted, regardless of release orientation, the rotations about the largest axis of inertia dominated by 53.7% (Table. 4.3). This suggests that the largest inertial axis is generally preferred during runout of the *platy* rock. It can also be seen that when rotations are dominant about the axis of largest inertia and command a high proportion of the activity ($> 90\%$), the lateral deviations tend to be much lower, indicating that the rock has followed the central fall line. It is also possible when rotations are dominated by the largest axis of inertia that the lateral dispersion is high. However, it can be seen that in these cases the relative dominance over the additional axes tends to decrease when this occurs, as illustrated by the dotted line. With a decreasing relative dominance of a given rotational axis, approaching 33%, there is a dramatic increase in the lateral dispersion recorded for runout events.

The smallest axes of inertia for the *platy* rock is relatively less dominant as compared to the largest axis of inertia. Moreover, the peak in the events where the smallest axes of

---

FIGURE 4.32 *(following page)*: Dominant axes of rotation given in percent dominance over the other inertial axes. On the upper row they are plotted against lateral dispersion (W/L), and the lower row against the measured rotational disorder in percent.

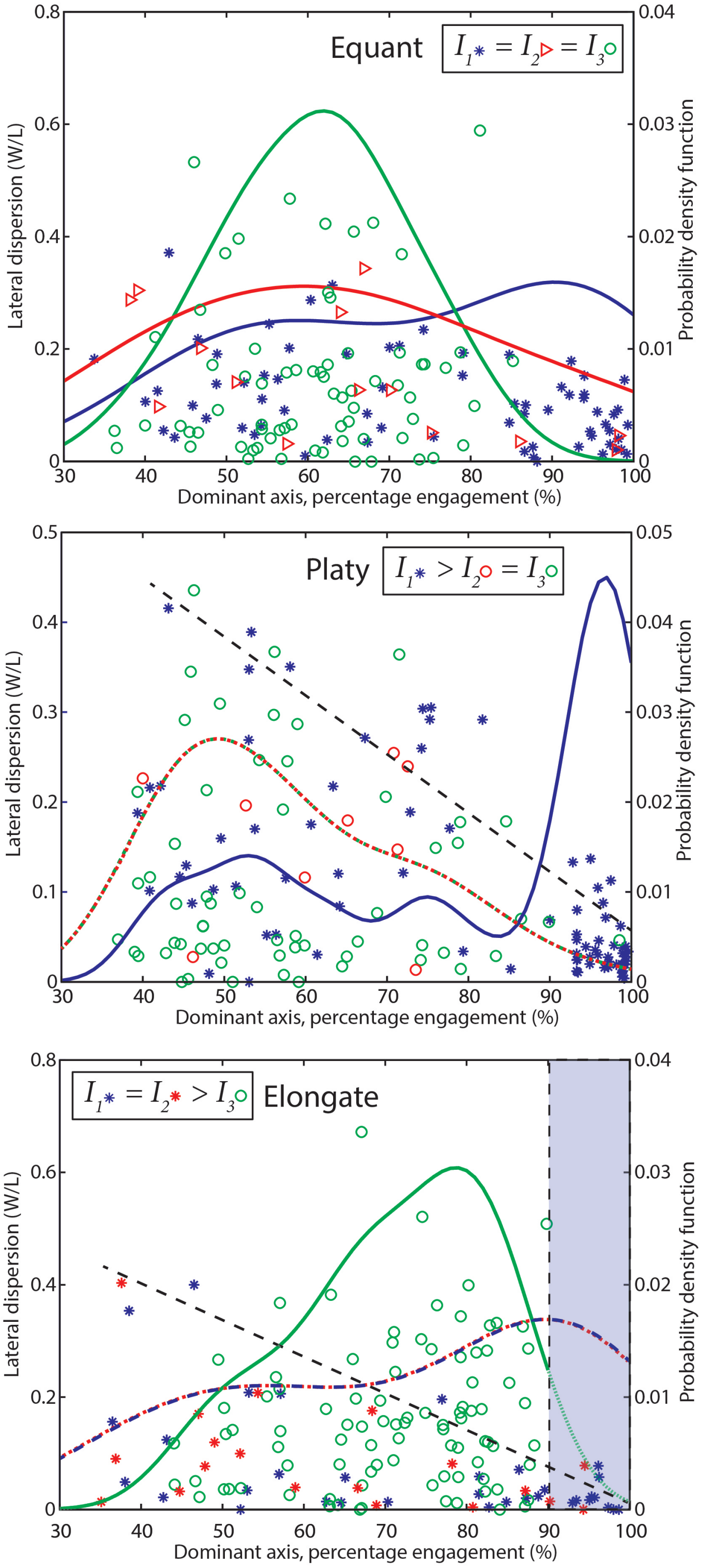
Equant
$I_1 * = I_2 \triangleright = I_3 \circ$
Lateral dispersion (W/L)
Probability density function
Dominant axis, percentage engagement (%)
0.8
0.6
0.4
0.2
0
0.04
0.03
0.02
0.01
0
30
40
50
60
70
80
90
100
Platy
$I_1 * > I_2 \circ = I_3 \circ$
Lateral dispersion (W/L)
Probability density function
Dominant axis, percentage engagement (%)
0.5
0.4
0.3
0.2
0.1
0
0.05
0.04
0.03
0.02
0.01
0
30
40
50
60
70
80
90
100
$I_1 * = I_2 * > I_3 \circ$
Elongate
Lateral dispersion (W/L)
Probability density function
Dominant axis, percentage engagement (%)
0.8
0.6
0.4
0.2
0
0.04
0.03
0.02
0.01
0
30
40
50
60
70
80
90
100

inertia was dominant involves events in which the dominant axis commanded only 50% of the rotational activity. It can also be seen that this coincides with events in which the highest lateral dispersions were recorded for the *platy* rock (Fig. 4.32 B).

The rotational behaviour of the *elongate* rock shows a different trend (Figure 4.32C). Rotations are dominated by the smallest axis of inertia with 63.4% of the rotational activity occurring about this axis (Table. 4.3). The relative rotational activity during events where the smallest axis of inertia commanded a high proportion of the activity, never exceeded 90% of the activity (Figure. 4.32) (highlighted in the right hand blue zone). This means that all rotations about the smallest axis of inertia were always accompanied by activity from the additional and larger rotational axes. This behaviour can be seen in the video and image of Figure 4.30, where there is a considerable *wobble* in the nature of the rotations. It can be seen that for these events the highest lateral dispersions (W/L) were recorded. While there is a tendency for the *elongate* rock to rotate about its axis of smallest inertia, it is interesting to note that the distribution of events in which rotation was dominated by one of the largest axes of inertia (blue and red dashed line, bottom Figure 4.32), there is a peak in the number of events with a high dominance of rotations in this axis, i.e. $>$ 90% of the activity. Furthermore, these events are those that produce the lowest deviation from the fall line and respectively the lowest lateral dispersion.

Thus, it can be said that for the *elongate* rock favours rotations about the axis of smallest inertia rotations which are inherently unstable due to the activity of the additional rotation axes, leading to higher lateral dispersion. While if rotations about a rotation axis of largest inertia can be established, the dynamics tend to be stable and the rocks tend to follow a straight path along the fall line.

4.8 Summary of physical experiments

- The *equant* rock is shown to have the greatest mobility, in particular for longitudinal runout distance, and also produce some of the largest lateral runout distances (see Figures 4.1 and 4.2). On the other hand non-equant rocks when considered with respect to the W/L ratio do show some of the most extreme values.

- Slope angle is also shown to be of importance in runout distance. For the experimental set up this appeared to be controlled by the transition from the slope onto the flat runout zone, as beyond the 37° slope runout decreased with increasing slope angle. This is thought to be because the transition is more sever for steeper slope angles and thus the hard impacts cause greater loss of momentum than shallower slope angles.

- The runout locations focus around the central fall line with increasing slope angle. This trend also correlates with the release orientation of the rocks. For release orientations where the rock has its axis of largest inertia aligned parallel to the central fall line it was show that rocks tend to hold this path and focus about the central fall line.

- The fastest average velocities are recorded for rocks which are released into the slope with their axis of largest inertia aligned parallel to the central fall line of the slope.

- Rockfall velocity shows an increase with increasing slope angle. While shape controls the range of potential velocities, where non-equant rocks show a greater range, the *platy* rock shows the greatest variability of velocities.

- For jump heights the *equant* rocks tend to have the shallowest jump heights. Non-equant rocks produce greater variability in jump heights where the *elongate* rock produces the highest arched trajectories. There is a positive correlation of jump height to the size of the largest axis of the equivalent inertial ellipsoid (E_{2a}).

- Two distinct patterns of restitution coefficients can be seen between first impacts following free-fall, and the impacts observed during runout. First-impact normal restitution coefficients all occur within the bounds of unity, while average R_n values during runout exceed unity for all rock shapes. Departure from the *equant* rock form produces a greater range and variability of restitution values, this can also be related to the size of the E_{2a}.

- The rebound behaviour of rocks is dependent on the impact configuration of the rock with the ground. In particular the impact angle α is of importance. Low impact angles produce high arched rebound trajectories, while large impact angle produce low flat rebound trajectories (f/s). These effects are more accentuated for non-equant rocks.

Chapter 5

Numerical rockfall modelling

The experimental investigations and field observations in this work supported the development of a new fully 3-D rigid body rockfall model RAMMS::Rockfall which was developed in conjunction with the Swiss Federal Institute of Technology in Zurich, ETHZ and the Swiss Federal Institute for Forest, Snow and Landscape Research WSL, Birmensdorf. Many of the observations of the sliding and jumping behaviour of the test bodies in the experiments of Chapter 4, in addition to field observations of impact scaring (Figure. 2.7) and live rockfalls, led to the development of a conceptual slip dependant friction model that mathematically treats the process of rock-ground penetration and ploughing of terrain material which leaves scars following rock-ground contact. The conceptual model could be included in the rigid-body rockfall code, and has been the contribution of this thesis to the development of the RAMMS::Rockfall rockfall model.

This chapter presents the results of the numerical experiments conducted using the newly developed RAMMS::Rockfall rockfall modelling software. The first sections gives summaries of a parameter study and model validation using the data generated in the physical experiments (Chapter. 4). The purpose of performing the validation was to back validate the application of the rockfall model for further investigations of the influence of rock-shape on runout behaviour. The validation exercise has selected model input parameters based on the observations from the physical experiments.

The model is then used in a series of numerical experiments which investigate the effects of changes in the degree of a rock's sphericity. In these numerical experiments the simulations are conducted at full size on a planar slope which was designed to simulate the simple geometry of engineered rock cuts; and that of the small preliminary full scale rock rolling exercise conducted in St Léonard.

The final application is to rockfall in real terrain. The effects of terrain morphology and roughness have been explicitly removed such that the effects of rock-shape on runout behaviour can be quantified. Therefore, a small series of shape experiments conducted on the terrain of rockfall case studies from Switzerland and New Zealand are presented. This serves to demonstrate the applicability of the rockfall model to full-scale rockfall events.

5.1 Experimental design of numerical modelling

The numerical modelling of rockfalls presented in this chapter serves to bridge the gap between the observations of rockfall behaviour observed in the physical experiments with small rocks and the field experiments with larger rocks (0.5 - 1.0 m^3) representing the common rock size of rockfall faced by society. Furthermore, the utility of the rockfall model once validated to the physical experiments, offered an experimental platform with which to investigate further aspects of rock-shape that due to the constraints of time could not be investigated in the physical experiments, such as sphericity.

The rigid body approach to modelling rockfall runout behaviour was selected because it explicitly accounts for rock-shape. Details of how this is modelled are presented in (Chapter. 3). Furthermore, full 3-D dynamic data of the simulated rock motion are generated and can be sampled from the simulations at the same frequency as that of the motion sensor used in the physical experiments presented in (Chapter. 4). In this way a direct comparison between numerical and physical experiments can be made.

The rockfall model has been used to explore an additional component of rock-shape, *sphericity*, which could not be dealt with in the physical modelling due to the large number of additional experiments that would be required to explore this in a rigorous manner. From Chapter 4 it is apparent that rock-ground impact events are stochastic in nature. Therefore, use of numerical rockfall model deals with the sampling problem faced by the physical modelling and the complexity involved in performing live rockfall experiments. The numerical modelling assists to better define the trends of rockfall runout behaviour according to rock form that are identified in the physical modelling.

5.2 Parameter sensitivity study

Parameterisation of the rockfall model was performed based on simple laboratory experiments to determine the normal restitution coefficient of a contact point and the sliding friction μ, as discussed in Chapter 3, Section 3.9. The remaining model parameters that compose the slippage friction contact-impact model were selected using a best fit approach that validated the numerical to the physical modelling experiments of Chapter 4. To gain an understanding of how the slippage-friction contact-impact model affects the behaviour of simulated rockfalls a small parameter study was performed.

The effect of making variations to the slippage impact model parameters on runout distances and the dynamic behaviour of the simulated test rocks are presented in the following. Model simulations which explore the parameter space were performed for the *equant* test rock on the 37° slope at the scale of the physical laboratory experiments. Three main experiments were performed to explore the slippage-friction contact-impact model, i.e. how the friction $\mu(s,t)$ evolves during a contact phase and essentially allows a contact point to slip a distance s (m^{-1}) to a point of stiction, this is $\dot{s} = 0$.

1. The first experiment involved changing the friction potential μ over a contact period. This was achieved by fixing $\mu_{min} = 0.1$ and varying the μ_{max} value between $\mu_{max} = 0.2$ and $\mu_{max} = 3.5$. Parameters κ and β, which steer how the friction is applied, were held constant at $\kappa = 200.0\ m^{-1}$ and $\beta = 200.0\ s^{-1}$.

2. The second experiment investigated κ between $0.002\ m^{-1}$ and $200.0\ m^{-1}$, while holding $\mu_{min} = 0.1$ and $\mu_{max} = 2.0$, and $\beta = 200\ s^{-1}$. In this numerical experiment the effects of altering the scar or slip length s (m^{-1}), over which $\mu(s)$ acts on a contact point, can be observed.

3. The final experiment investigated β between $0.02\ s^{-1}$ and $2000.0\ s^{-1}$, while holding $\mu_{min} = 0.1$ and $\mu_{max} = 2.0$, and $\kappa = 200\ m^{-1}$. In this experiment we investigate the release dynamics of the rock as it departs from the ground contact.

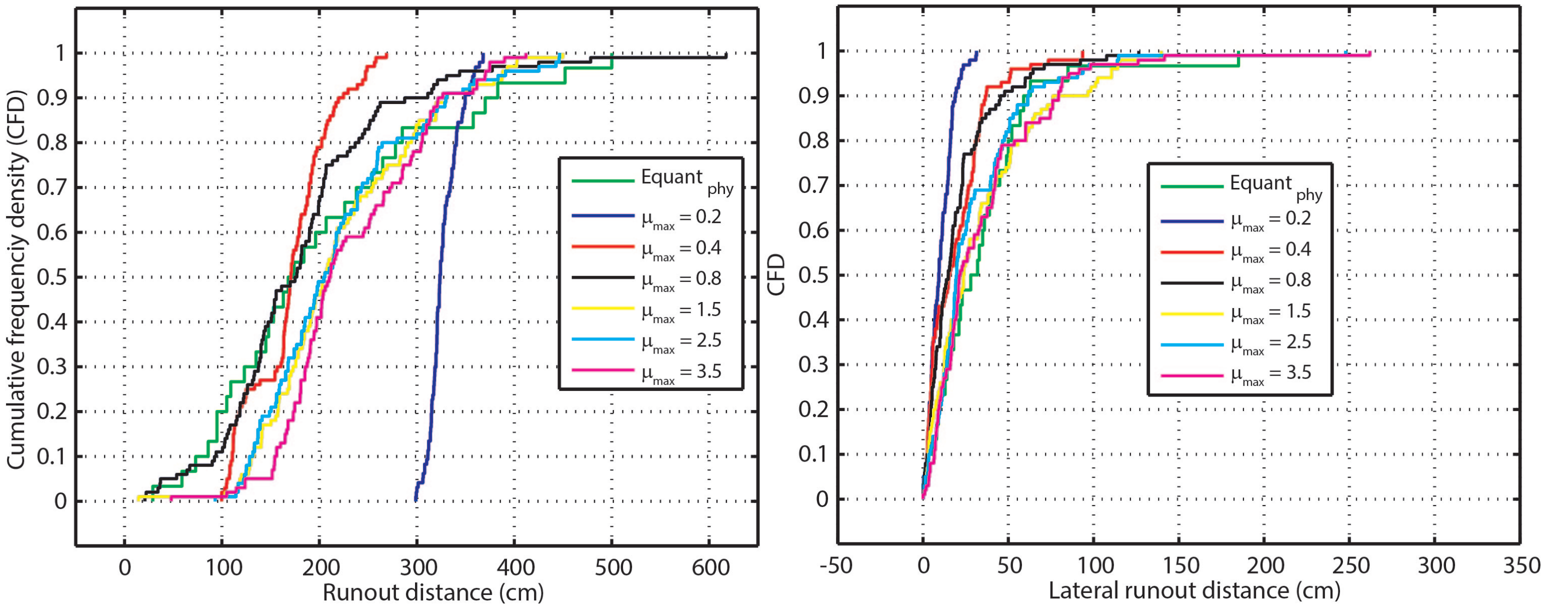

Figure 5.1: Cumulative frequency distributions of runout distances in (cm) for each simulation series with changing μ_{max}. The distance runout from the toe of the slope are plotted *left*, and lateral runout distances *right*. In each case the distribution of runout distances from the physical experiments is plotted in green.

5.2.1 Results runout and friction (μ_{max})

Figure 5.1 (*left*) illustrates how both low and high friction values can generate long runout distances. The low μ_{max} values $\mu_{max} = 0.2$ and $\mu_{max} = 0.4$ have both condensed runout distributions, and each start with an offset from the toe of the experimental test slope if compared to the results of the physical experiments. This suggests that mainly sliding occurred during these simulations as this has the potential for high mobility on flat terrain. The lowest friction value of $\mu_{max} = 0.2$ has the greatest overall mobility (the greatest number of rocks achieving long runout) although does not achieve the absolute maximum of all experiments. There is a large drop in runout distance as the friction is increased to $\mu_{max} = 0.4$, while friction increases beyond this show increases in runout distance. From visual comparison, the best fit to the results of the physical experiments lies between a friction value of $\mu_{max} = 0.8$ and $\mu_{max} = 2.5$.

A similar trend is observed for the lateral runout distance (Fig.5.1 *right*). While with the lowest μ_{max} value the smallest overall lateral runout distances are observed, the results show that lateral runout distance increases with increasing friction value. From the simulations of the selected friction values, the runout distribution for $\mu_{max} = 2.5$ best fit the results of the physical experiments (Fig.5.1 *right*). Summary statistics which present how the maximum, minimum, mean and standard deviation of both runout and lateral runout distances were affected by this parameter study are given in Figure 5.2. An additional observation is that the range of runout distances becomes more variable with increasing friction value, shown with the increase in the standard deviation (the error bars on the mean) with increasing friction.

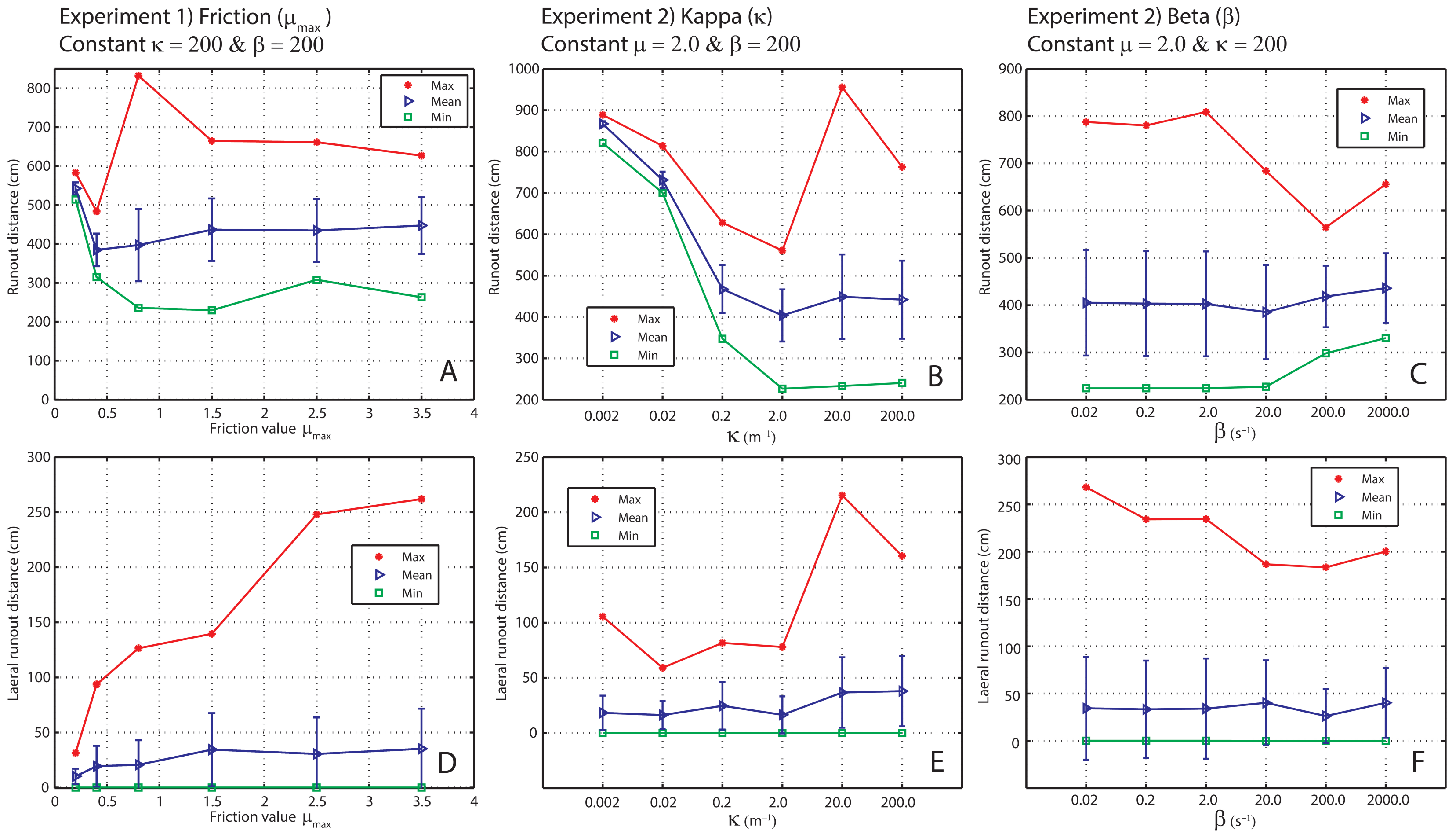

Figure 5.2: Summary runout statistics as a function of changes in maximum friction potential μ_{max} (plots A and D), the parameter $\kappa(m^{-1})$ steering the increase of friction from μ_{min} to μ_{max} over the scar distance s (plots B and E), and the decay of friction $\beta(s^{-1})$ (plots C and F). The results of the effects on runout distance are presented in plots A,B, and C; and those for lateral runout distance presented in plots D, E, and F. Each plot displays the statistics from $n = 100$ simulations, where max values are the red stars, the mean values are the blue triangles and the minimum are the green squares. Standard deviations are indicated as the blue error bars on mean values.

5.2.2 Experiments with κ (m^{-1}): The influence of scar length s on runout behaviour

Plots B and E of Figure 5.2 summarise the effects of altering κ on the runout distance. The parameter κ reflects the slip distance s over which μ_{min} requires to climb to μ_{max}, and controls how quickly the friction increases from μ_{begin}, to μ_{end}. With low κ values sliding is dominant, the contact is held with low friction for a relatively large contact distance. As a result limited torque can be applied to the contact point and there is a tendency for sliding. Figure 5.2 demonstrates this effect, where the highest runout distances are recorded for the lowest κ values. Here, lateral runout is small and there is on average small deviation from the central fall line. As κ increases the average runout decreases, while the standard deviation increases along with the range between minimum and maximum runout values. Lateral runout shows an increase in both the maximum and the standard deviation with increasing κ values. As increasing κ causes the friction $\mu(s,t)$ to act with greater magnitude over a smaller distance it creates a snatching effect which induces grip and torque, and is likely to cause the rock to deviate from a straight path (i.e. greater lateral dispersion) and generate large variability in runout distance.

5.2.3 Experiments with β (s^{-1}): The influence of contact release time on runout behaviour

Friction is effective after ground contact has been lost and is set by the parameter β which returns friction $\mu(s,t)$ back towards μ_{min}. Figures C and F of Figure 5.2 show a trend that mirrors κ. It can be seen that for low β (0.02 - 2.0 s^{-1}) the largest range and standard deviations are recorded for both runout and lateral runout distances. This is because low β high friction values are effective for longer periods following contact, this is similar to having a high κ deriving high friction values quicker. Increasing β has the effect of reducing runout distance and variance in runout.

The application of friction values in the rigid-body approach to rockfall modelling is counter-intuitive, in that runout distance increases with higher friction. This result underscores a salient feature of rockfall dynamics; rock mobility is more related with jumping and rotational dynamics as a result of the friction acting locally at the rock-ground contact point. It is of interest to observe how changing these parameters affect the nature of the runout behaviour.

5.2.4 Parameter study jump heights

The summary statistics in Figure 5.3 plot the effect of the parameter variations on the dynamics of runout behaviour. Jump height is shown to increase with increasing $\mu(s,t)$, for max, mean and standard deviations values. Standard deviations are very low for the lowest friction values ($\mu_{max} = 0.2$ and $\mu_{max} = 0.4$), and the max and mean values are the same for jump heights ($f = 14.0$ cm and $f = 11.0$ cm, respectively). This indicates that only a single rebound occurred following free fall, and the simulated rocks mostly entered sliding motion. As soon as high friction values are used there is a dramatic increase in jump heights, along with range and variability in runout which is also reflected in the increase in runout standard deviation.

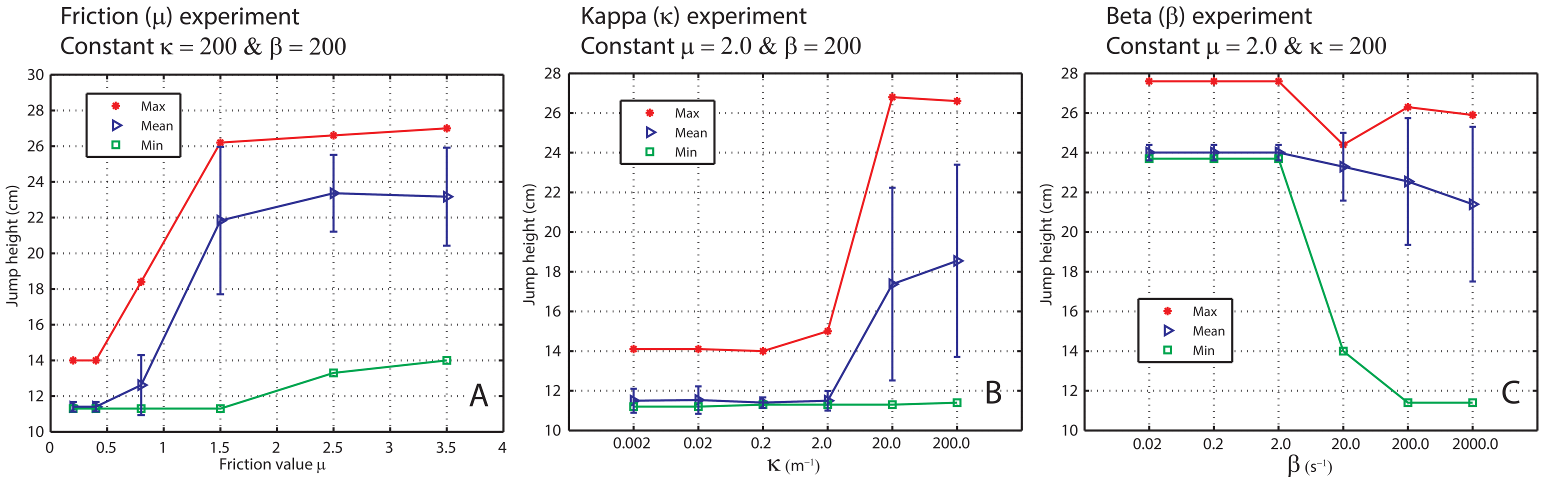

FIGURE 5.3: Summary statistics of how jump heights (f) are affected by changes in friction μ_{max} (plot A), the parameter $\kappa(m^{-1})$ in plot B, and the rate $\beta(s^{-1})$ of frictional decay (plot C). Each plot displays the statistics from $n = 100$ simulations, where max values are the red stars, the mean values are the blue triangles and the minimum are the green squares. Standard deviations are indicated as the blue error bars on mean values.

For small κ values there is limited effect on the jump height until $\sim \kappa = 2.0$ after which there is a large increase in the magnitude and range of jump heights produced. The low κ values between $\kappa = 2.0$ and $\kappa = 0.002$ would be the equivalent of allowing the rock to slide between $s = 0.5$ m and $s = 0.5$ m, respectively, before reaching μ_{max}.

The opposite trend is observed for the model parameter β. With slow acting β i.e. low values, jump heights are large but exhibit small standard deviations. The effect is as if to hold the high μ_{max} for a long period of time. As β increases the jump heights begin to decrease while the variance in jump height increases. By setting β to large values, the frictional effects of a contact are rapidly decreased.

5.2.5 Angular velocity(Ω)

The angular velocity Ω increases with increasing contact friction, as is illustrated in Figure 5.4A. Interestingly the greatest range in angular velocity is found for $\mu_{max} = 0.8$. Figure 5.4B shows that κ only appears effective above $\kappa = 2.0$; after this there is an increase in Ω along with standard deviation. Setting a fast acting β, (i.e. high β values), has the opposite effect and effectively reduces angular velocity (Figure 5.4C). This illustrates that once the high friction has pinned a contact point (s no longer increases) torque is generated which acts to create the rotations of the rock body. Hence, if β acts slowly, then the high friction of a contact is effective for longer periods and has more potential to transform translational motion into rotations.

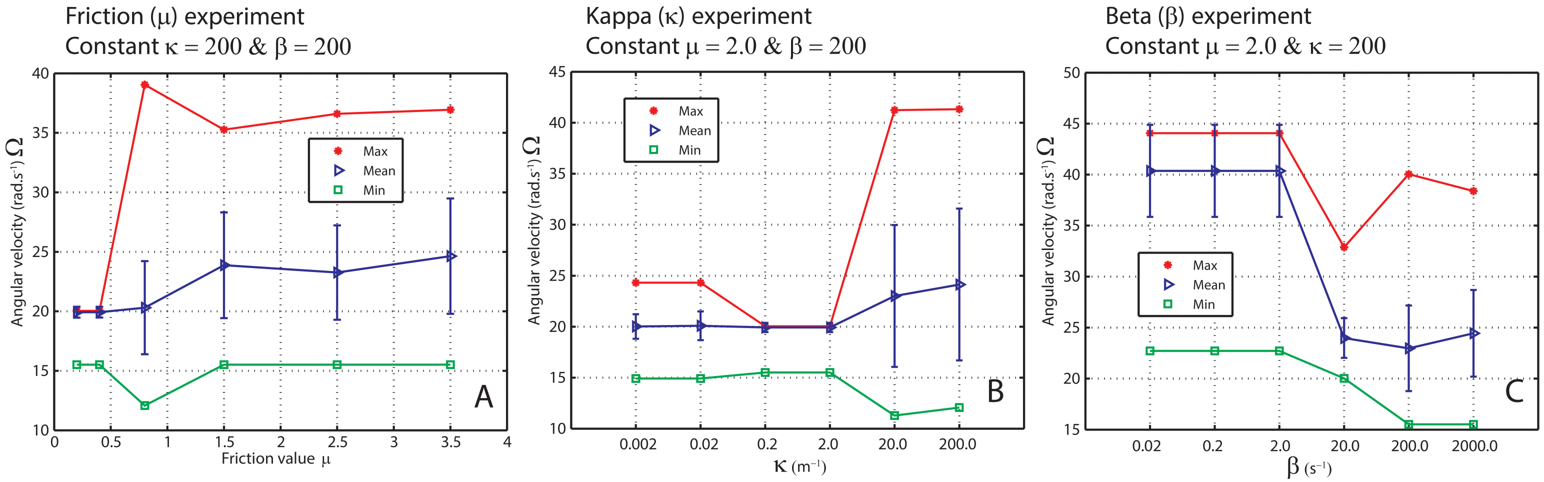

FIGURE 5.4: Summary statistics of how angular velocity Ω is affected by changes in friction μ_{max} (plot A), the parameter $\kappa(m^{-1})$ in plot B, and the rate $\beta(s^{-1})$ of frictional decay (plot C). Each plot displays the statistics from $n = 100$ simulations, where max values are the red stars, the mean values are the blue triangles and the minimum are the green squares. Standard deviations are indicated as the blue error bars on mean values.

5.2.6 Velocity (v)

The translational velocity v responds with an opposite trend to those observed for jump heights and angular velocities. Increasing the friction value from a low μ_{max} to a high μ_{max} value, reduces the simulated test rock velocity (Figure 5.5A). The maximum range between velocities is 0.5 - 0.7 m s^{-1}; a greater standard deviation of velocities is observed with increasing friction value. Another counter-intuitive feature of rockfall arises: runout distance does not necessarily correlate with high velocity, rather it appears that for high runout distances the angular velocity is of greater importance. Thus, if runout is thought of in terms of total kinetic energy then the drop in translational velocity reflects the increase in angular velocity which produces the greater runout distances. For an increasing κ velocity decreases, but increases the range and standard deviation of velocity. β, mirrors the trend of κ and causes an increase in velocity with increasing β value.

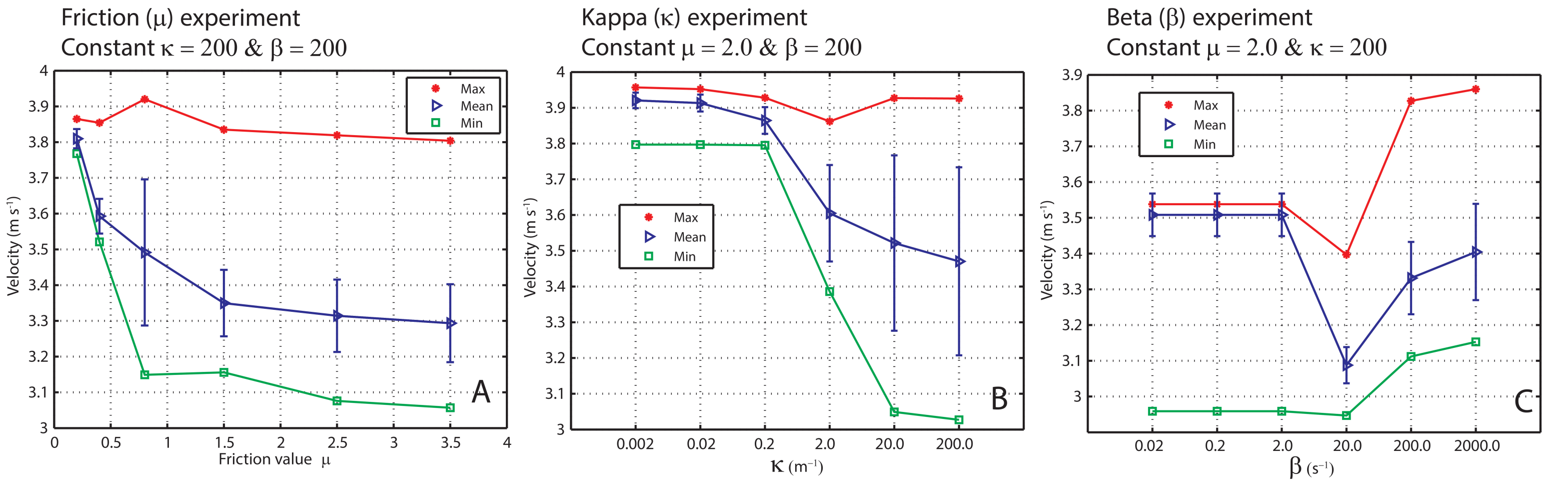

FIGURE 5.5: Summary statistics of how velocity (m s^{-1}) is affected by changes in friction μ_{max} (plot A), the parameter $\kappa(m^{-1})$ in plot B, and the rate $\beta(s^{-1})$ of frictional decay (plot C). Each plot displays the statistics from $n = 100$ simulations, where max values are the red stars, the mean values are the blue triangles and the minimum are the green squares. Standard deviations are indicated as the blue error bars on mean values.

5.2.7 Summary of RAMMS::Rockfall parameter study

To summarise the parameter study, its purpose was to illustrate how changes in the slippage friction model space affected the runout potential and dynamics of the rocks during runout. The following observations have been made:

- The slippage friction model space is composed of μ_{min}, μ_{max}. During contact, friction increases as a function of κ, and once contact is lost, decays as a function of β.
- Low μ_{max} (0.2 and $\mu_{max} = 0.4$) results in sliding and long runout distances. Increasing μ_{max} initially reduces runout distance, while with high $\mu_{max} = 3.5$ the greatest runout distances with the greatest standard deviations are observed.
- Application of friction laws in rigid-body rockfall modelling is counter-intuitive, in that runout distance increases with higher friction. This result underscores a salient feature of rockfall dynamics. The mobility of rocks has more to do with the jumping and rotational dynamics a result of the friction acting locally at the rock-ground contact point.
- Lateral runout distance is low for small μ_{max} and increases with increasing μ.
- Jump heights f and angular velocity Ω increase with increasing friction.
- Velocity reduces with increasing friction. However, increasing friction also induces an increase in angular velocity and therefore runout distances are longer in general.
- Runout distance does not correlate with high velocity. It appears that for high runout distances the angular velocity is of greater importance.
- The slip distance required for μ_{min} to climb to μ_{max} is governed by κ. Holding κ low promotes sliding of the block, while high κ values allow the high μ values to be reached quicker, creating a snatching effect on the rock body. This leads to higher jump heights f and angular velocity Ω.
- The β parameter determines the decay of the maximum friction once contact with the ground is lost. If β is held low then it allows high friction values to be effective for longer and thus promotes higher jump heights and angular velocities. With

increasing β the frictional effects of a contact are disabled more rapidly, resulting in reduced jump heights and angular velocities.

This parameter study has illustrated the effects of the slippage-friction contact-impact model on the runout potential and dynamics of rigid-body rockfall simulations. It has provided a guide of how the parameter space will affect the behaviour of simulated rock bodies during rockfall simulations. It can be seen how the model parameters can be applied to model the effects of different terrain types and morphologies (i.e. surface roughness). It has not been the purpose of this task to provide a precise model calibration and validation, but it has assisted in selecting a best-fitting parameter set for the validation of the model through the back calculation of a data set taken from the physical experiments (Chapter. 3).

5.3 Back-calculation of laboratory experiments

With the first parameter study as a guide, parameters could be found which best fit the entire data set for the 37° slope for each test rock-shape (*equant, platy* and *elongate*). All permutations of the physical experiments were back-calculated according to three release orientations (Figure. 3.3). The release conditions were also matched to the physical experiments. During the physical experiments it was possible to conduct n = 33 ±1 releases of each test rock-shape and release orientation; in the numerical experiments n = 1000 were performed for each possible release combination.

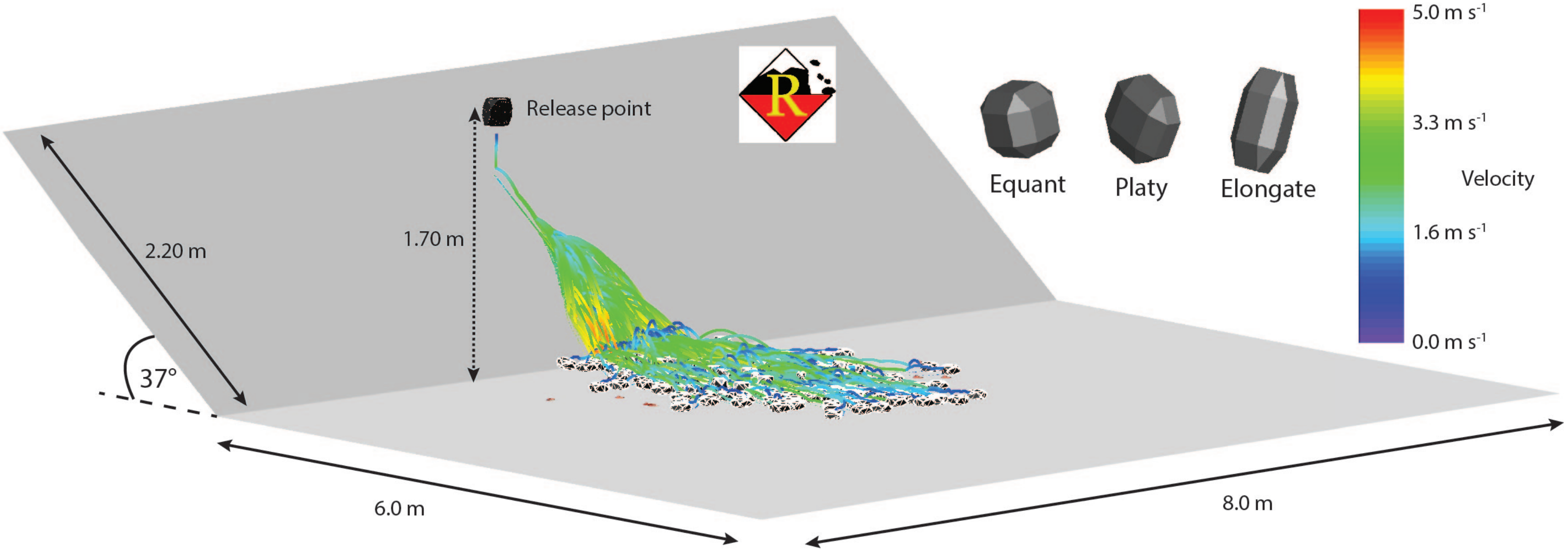

FIGURE 5.6: Rockfall simulation of the physical laboratory experiments using the RAMMS::Rockfall model. The terrain model is dimensioned to the size of the physical experiments, in addition to scaling the dimensions of the test rocks to the exact size of the physical experiments. The example presented is the point release of the *platy* rock from the fixed release height. The simulated trajectories are coloured according to the velocity they attain indicated on the scale bar. Examples of all the rock shapes (*equant*, *elongate*, and *platy*) used for the numerical modelling series are also shown.

A list of the selected model parameters is given in Table 5.1. ϵ_n which is the restitution of a contact point, was set to a value of the drop test and the friction parameter space was set so as to span the measured static sliding friction observed (Section. 3.9). A high μ_{max} was used to simulate the impulsive impacts of corner points and edges during runout. The application (κ) and decay (β) of the friction over an impact period had to act relatively quickly as there was limited sliding due to the hard nature of the wooden carpeted surface. Initially the surface properties of the simulated physical experiments were assumed equal over the entire terrain. This assumption excluded the transition from the planar slope to the concrete floor of the experimental laboratory, especially after $L = 3.0$ m where the carpeted runout area ceased and the test rocks could runout onto concrete alone. This assumption generated problems for the *equant* rock which frequently ran out over the concrete floor. An additional series of numerical experiments were performed to include the spatially different impact conditions of the carpeted and concreted runout zones.

TABLE 5.1: Best fit parameters selected for the back-calculation of the physical experiments with the rigid-body rockfall model.

Parameter set	Slippage-friction				Contact-impact		Drag
	μ_{min}	μ_{max}	$\kappa(m^{-1})$	$\beta(s^{-1})$	ϵ_t	ϵ_n	F
1	0.10	2.00	500.00	200.00	0.00	0.48	0.00

5.3.1 Validation of numerical model from physical experiment runout patterns

The initial goal in searching for the best-fitting parameters was to find the best match between the numerical and physical experiment results. First results are presented from the model that assumed uniform impact parameters over the entire simulation domain. Figures 5.8, show that the simulated results of the *platy* and the *elongate* rocks fit well to the inundation areas of the physical experiments. However, the *equant* form under-predicts the total runout distance as shown in Figure 5.7. This shows that in reality the *equant* rock is more mobile, which is likely to be because the final concrete section of the physical experimental setup was not included into the spatial impact model, because in the RAMMS::Rockfall model version used to perform these simulations the ability to apply spatially variable contact laws was not possible at the time.

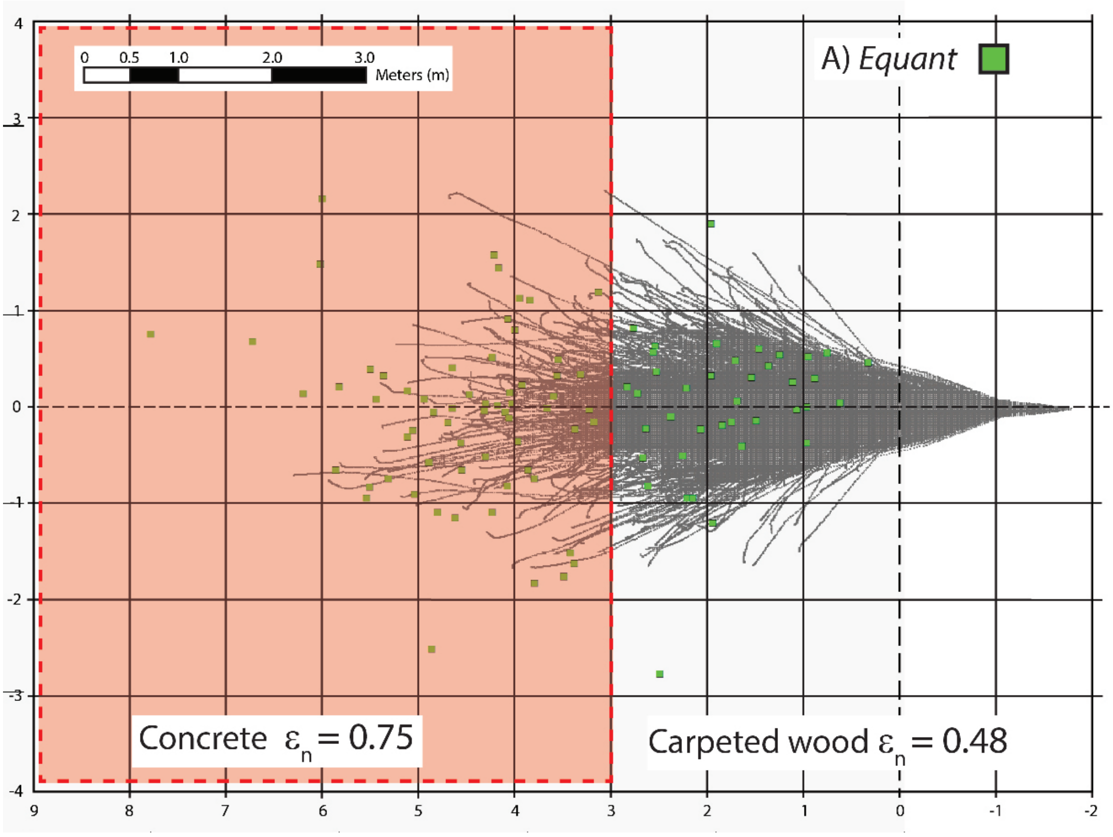

FIGURE 5.7: Comparison between physical and simulated deposit patterns for A) *equant* rock. The transition from the slope to the flat runout area is found along the large dashed line running vertically up from the zero mark. The carpeted zone of the experimental setup only ran until $L = 3.0$ m, beyond this point the material was concrete. The concrete zone is marked in red.

To gain a more detailed impression of differences in runout, the cumulative distributions of physical and simulated runout distances are plotted together (Figure. 5.9). The non-equant rocks show a good correlation between the distributions of run out and the overall runout distance. Another positive result is that, the *equant* rock shows that after 2.0 m runout, the numerical results under predict the runout distance bay around 1.5 m. This is likely the effect of the change of ground surface at 3.0 m runout distance from carpeted wood to concrete.

A total of $n = 1000$ numerical simulations were performed for each release combination. The distributions of the runout distances are compared using quantile-quantile plots (Q-Q plots). The Q-Q plots of Figure 5.10 show that in all cases that the mid range quantiles of the runout distances are similarly distributed. However, the tails of the distributions reveal that the upper qantile of the numerical simulations predict a greater number of longer runout events are more likely to occur than was shown in the physical experiments.

For the lower quantiles, it is shown that the *equant* and the *platy* rocks the lower runout distances are over predicted, whilst the *elongate* rock fits well at lower runout distances. Overall the gradients of the trend lines indicate if the runout distances are under- or over-predicted. The relationship between the modelled and experimental *equant* rock has a steep gradient indicating that the numerical experiments are under-predicting runout distance.

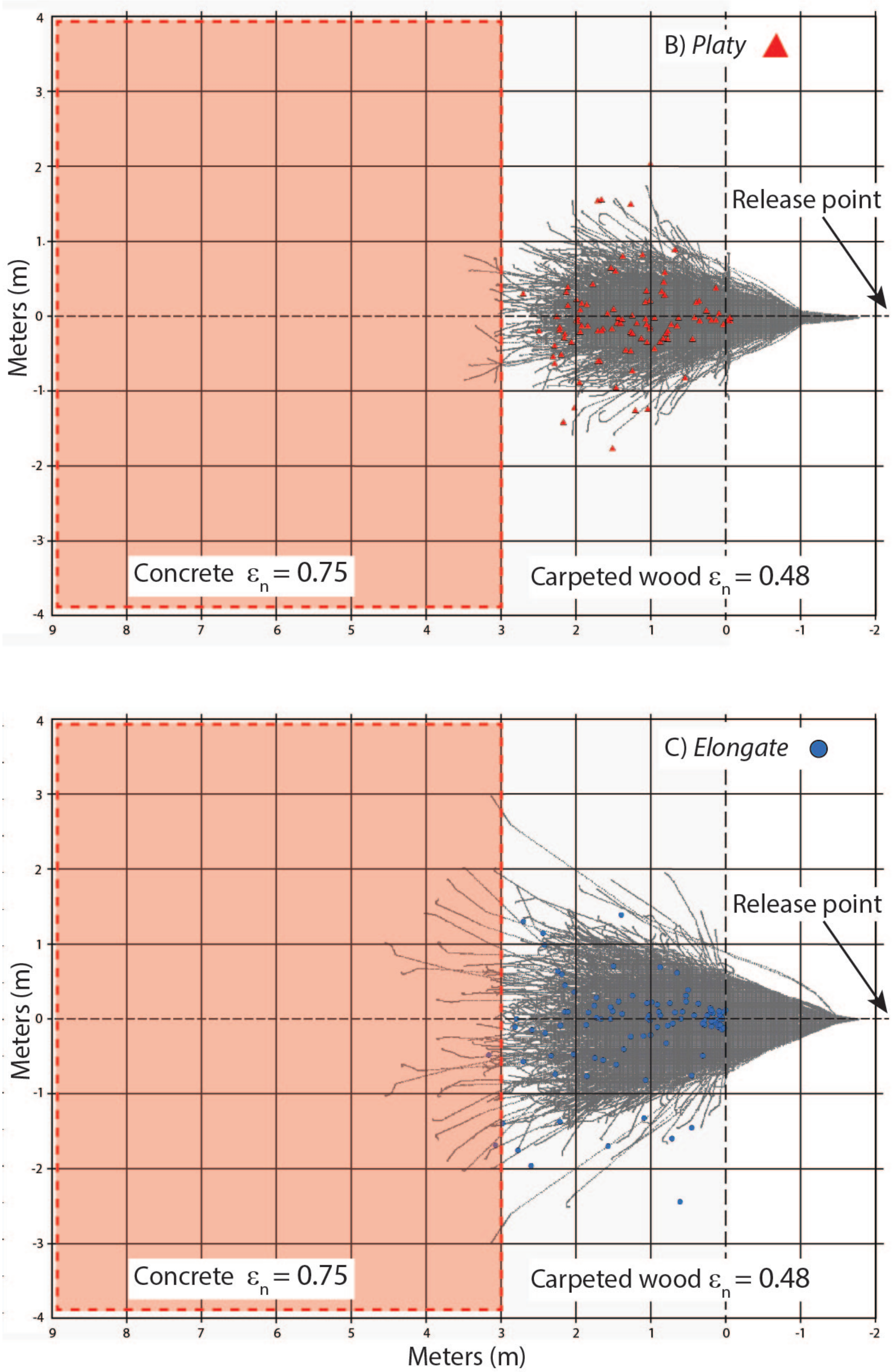

FIGURE 5.8: Comparison between physical and simulated deposit patterns for the B)*platy* and C) *elongate* rocks. The transition from the slope to the flat runout area is found along the large dashed line running vertically up from the zero mark. The carpeted zone of the experimental setup only ran until $L = 3.0$ m, beyond this point the material was concrete. The concrete zone is marked in red.

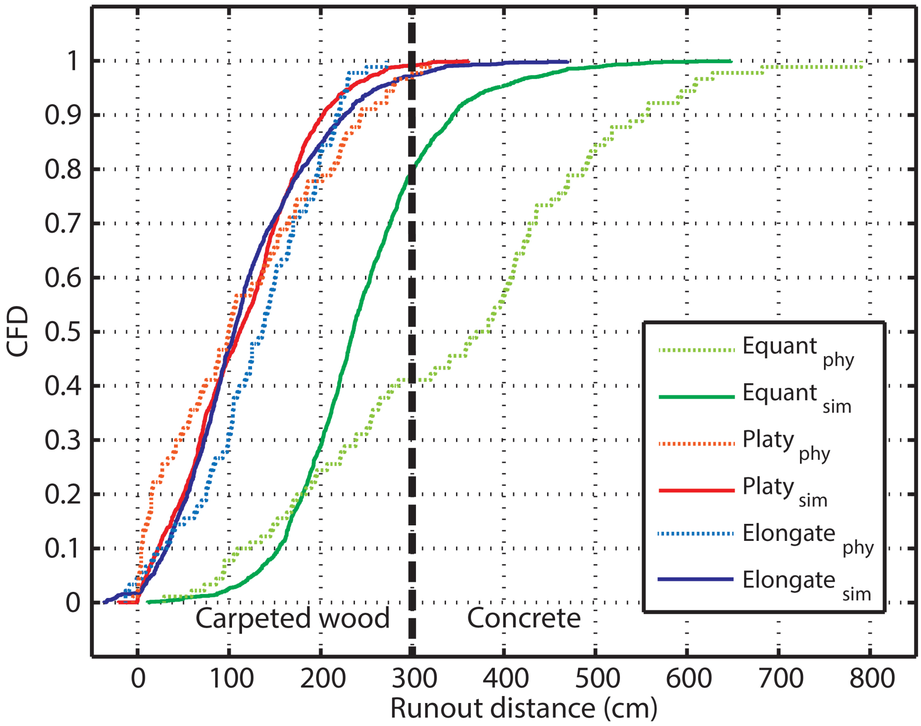

FIGURE 5.9: Cumulative frequency density (CFD) plot of maximum runout distances from both the physical and simulated experiments for each rock-shape. The physical experiments are indicated by the coloured dashed line and simulated runout distances are given with the solid line. The *equant, platy* and *elongate* rocks are differentiated by *green, red* and *blue* colour respectively. The transition from carpeted wood to concrete terrain material is indicated with the thick vertical dashed line.

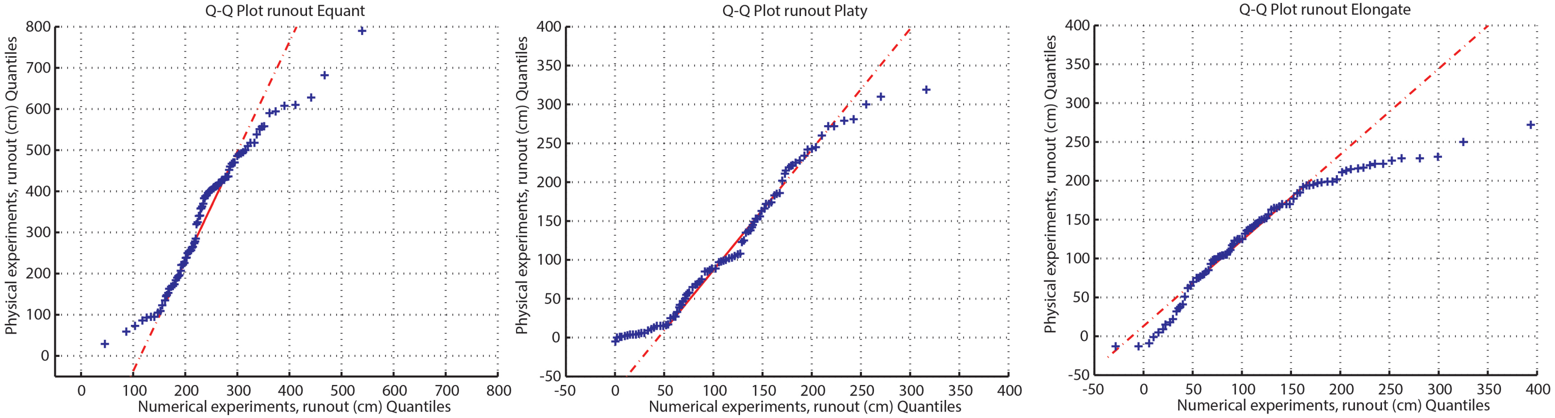

FIGURE 5.10: Quantile-Quantile plots compare the runout distributions between the simulated runout distances (horizontal axis), and the runout distances of the physical experiments (vertical axis). The blue crosses plot the quantile values from the distributions of runout distances from simulated and physical experiments. Should the points follow a straight line, this indicates that the results are from the same distribution. The red line joins first and third quartiles of each distribution, and is extrapolated to the ends of the samples.

Figure 5.11 presents the cumulative frequency density for lateral runout distances, which show the distributions are a better fit than runout distance. The Q-Q plots illustrate that for the *equant* and *elongate* rocks the distributions of lateral runout distances between numerical and physical experiments are similar. The *platy* rock demonstrated the greatest misfit of the distributions from one another. This is the case for the physical experiment results that ran out to the right (positive values, see Figure 5.11). The 45 ° gradient line for each slope of the non-equant forms reveals that for the physical and the numerical results, similar lateral runout is achieved. However, the *equant* form has a steeper trend line in the Q-Q plot and again shows that the numerical simulations slightly under-predict the lateral runout distances seen in the physical experiments.

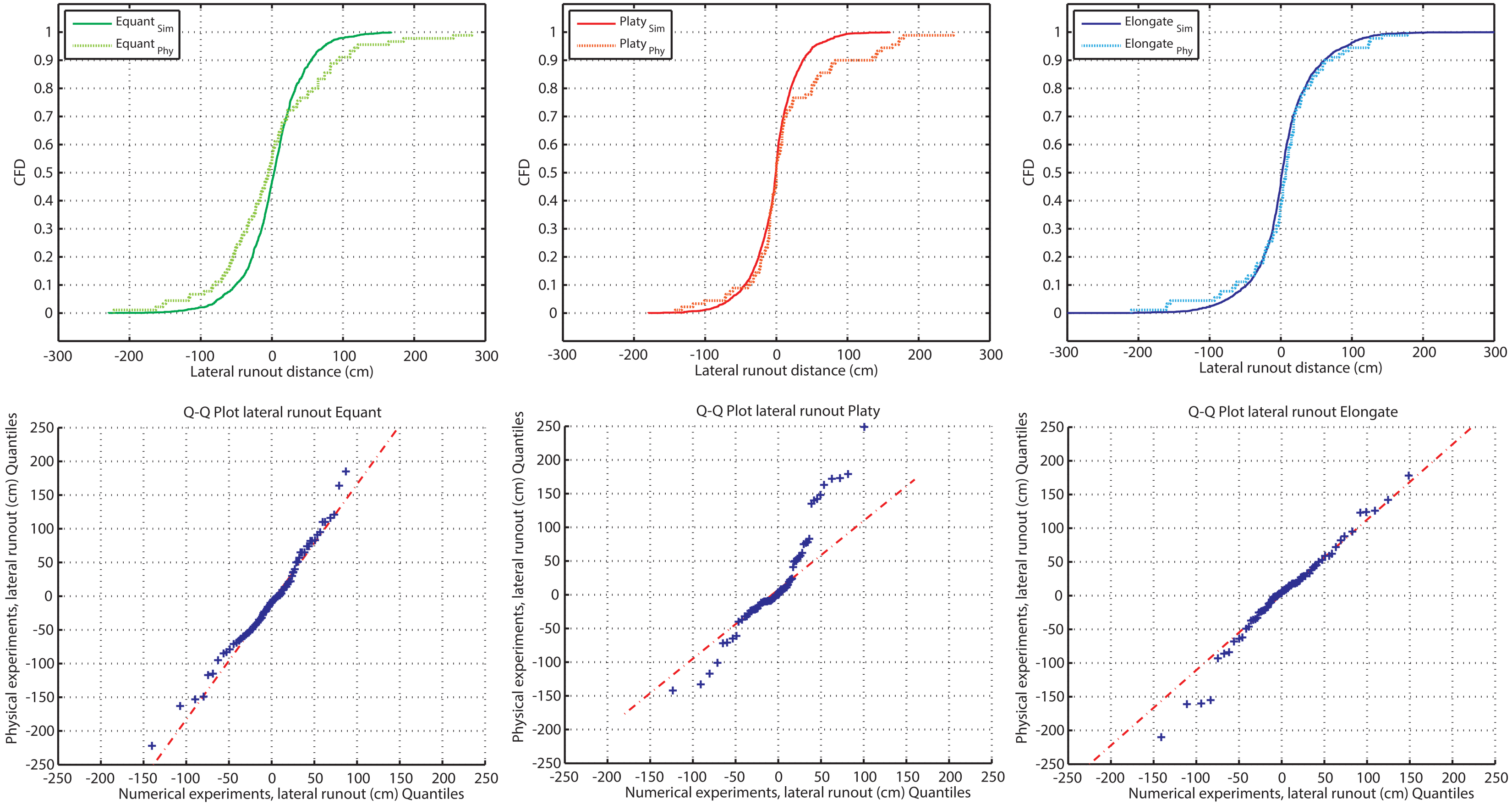

FIGURE 5.11: Plots A, B and C present cumulative frequency density plot of maximum lateral runout distances from both the physical and simulated experiments for the *equant, platy* and *elongate* rocks respectively. The physical experiments are indicated by the dashed line and simulated runout distances are given with the solid line. The *equant, platy* and *elongate* rocks are differentiated by *green, red* and *blue* colour respectively. Beneath each cumulative frequency plot is a Q-Q plot comparing each of the distributions.

The comparison between inundation zones and runout distances illustrates that in most cases the numerical model does well at predicting the runout distances of the physical experiments. Some discrepancies in the distributions of runout results between numerical and physical datasets can be attributed to spatial impact parameter selection. For example, for the *equant* rock the numerical simulations under predict the runout distances of the physical experiments. This is likely to be due to the carpet-concrete transition zone at $L = 3.0$ m. While other features, such as the *platy* rock (Figure. 5.11), show that the numerical experiments apparently under predict lateral runout distance to the right of the runout zone, could be attributed to sampling issues. If this is the case it brings into question which data set best reflects the reality, could it be that this feature of the *platy* rock is in fact a case where insufficient physical experiments could be conducted to obtain an even spread over the terrain? This is important statistical problem because it has a bearing on the number of numerical simulations that must be performed to be considered representative of the true hazard intensity.

5.3.2 Numerical model validation of the rockfall dynamics

In the preceding section, a comparison was made between the experimentally observed and calculated runout distances and lateral dispersion. In this section, the observed and calculated velocities, jump heights and rotations are compared. The experimental data has been presented in Chapter 4 for the three different rock shapes.

5.3.3 Velocity (v) measured from numerical model

In the experimental analysis a distinction was made between the average velocity and the pre-impact velocity. The average velocity is found by timing the rock over a fixed slope distance (Figure. 4.12), while the pre-impact velocity is the velocity sampled from singular impacts. For the comparison between experimental and back-calculated data the pre-impact velocities are used.

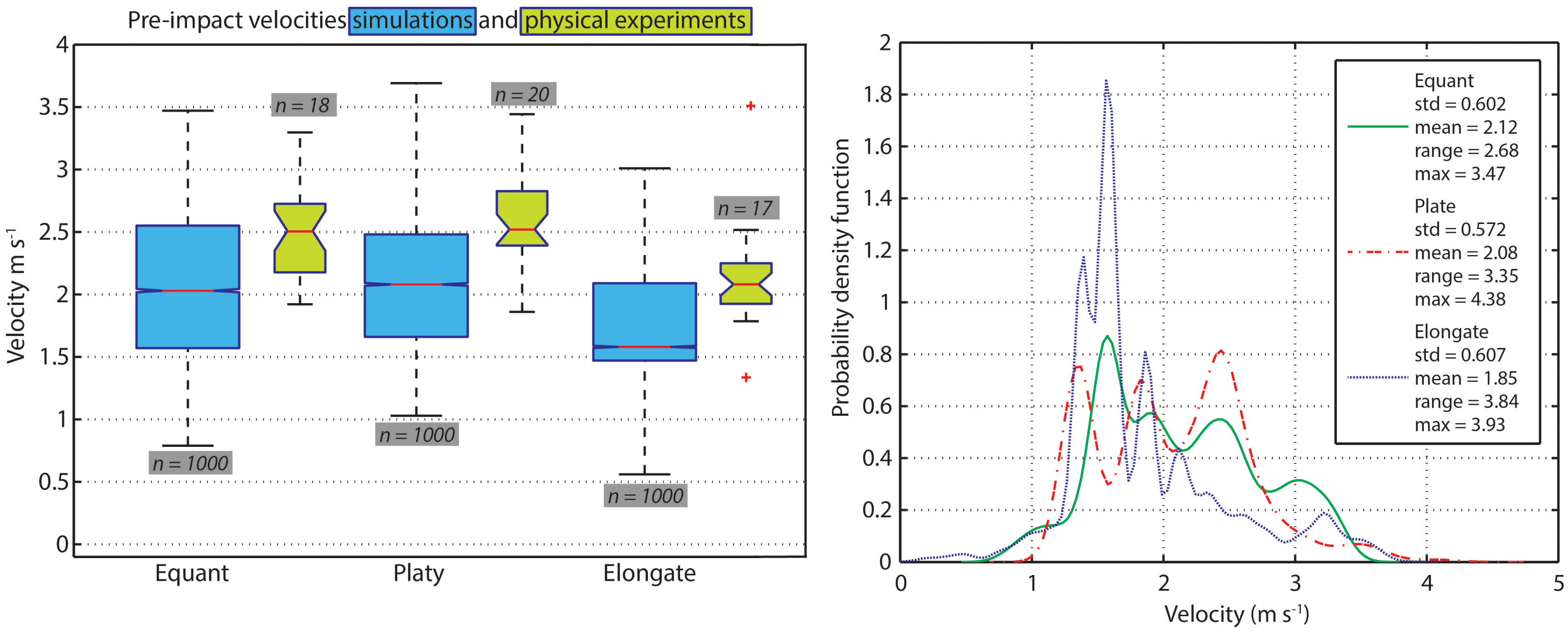

FIGURE 5.12: Boxplot (*left*) indicating the distribution of pre-impact velocities for impacts along the simulated 37° planar slope which occurred within the same viewing pane of the physical experiments are shown in blue. The equivalent results for the physical experiments are shown in yellow the boxplots. The same pre-impact velocities are presented in the form of a probability density functions plot on the (*right*). Velocities are given in m s^{-1}.

Figure 5.12 displays the velocity comparison for *equant*, *platy* and *elongated* rocks on a 37° slope. The range of experimentally and calculated velocities for all three rocks is in good agreement. However, the median velocities in the calculations are somewhat ($\sim$0.5 ms^{-1}) smaller than the experimentally observed median velocities. It should be pointed out that the median of the calculations is constructed with n=1000 simulations, whereas the experimental data was determined from relatively low sample size $n < 20$. The simulations reproduced the experimental trend according to the rock form. For example, *platy* forms in both experiment and simulation had the largest maximum in-slope velocities. In addition, the *elongated* rock had the lowest median velocity in both.

An alternative representation of Figure 5.12 (*left*) is the depiction of the probability distribution of the three rocks (Figure. 5.12) (*right*). This plot reveals that the velocity of the *elongated* form averages 1.5 ms^{-1}. This behaviour is not visible in the distribution of the *equant* and *platy* rocks. The result demonstrates that the *elongated* rock has a singular and preferred mode of motion, induced after the first impact. The multi-modal probability density functions of the simulations of the *equant* and *platy* rock indicate that these exhibit more than one preferred mode of motion. The preferred mode is also likely to be determined by the initial impact orientation.

In the laboratory experiments there was a limitation on the region where the velocities could be sampled (Section. 4.3). The terminal velocity was often reached at the end of the slope which was outside the camera's field of view. The numerical experiments have permitted the sampling of the terminal velocity. The probability distributions of calculated terminal velocities are presented in Figure 5.13. This plot reveals that the *equant* rock is on average the fastest, but with the smallest range and standard deviation in velocities. The distribution for this rock form is bi-modal. The *elongate* rock is on average the slowest while exhibiting a larger range and standard deviation of velocities compared to the *equant* form. The *platy* form has a similar mean velocity as the *equant* rock, while its range and standard deviation of velocity is much larger. Moreover, the non-equant forms are more variable and have a greater likelihood of unusual events.

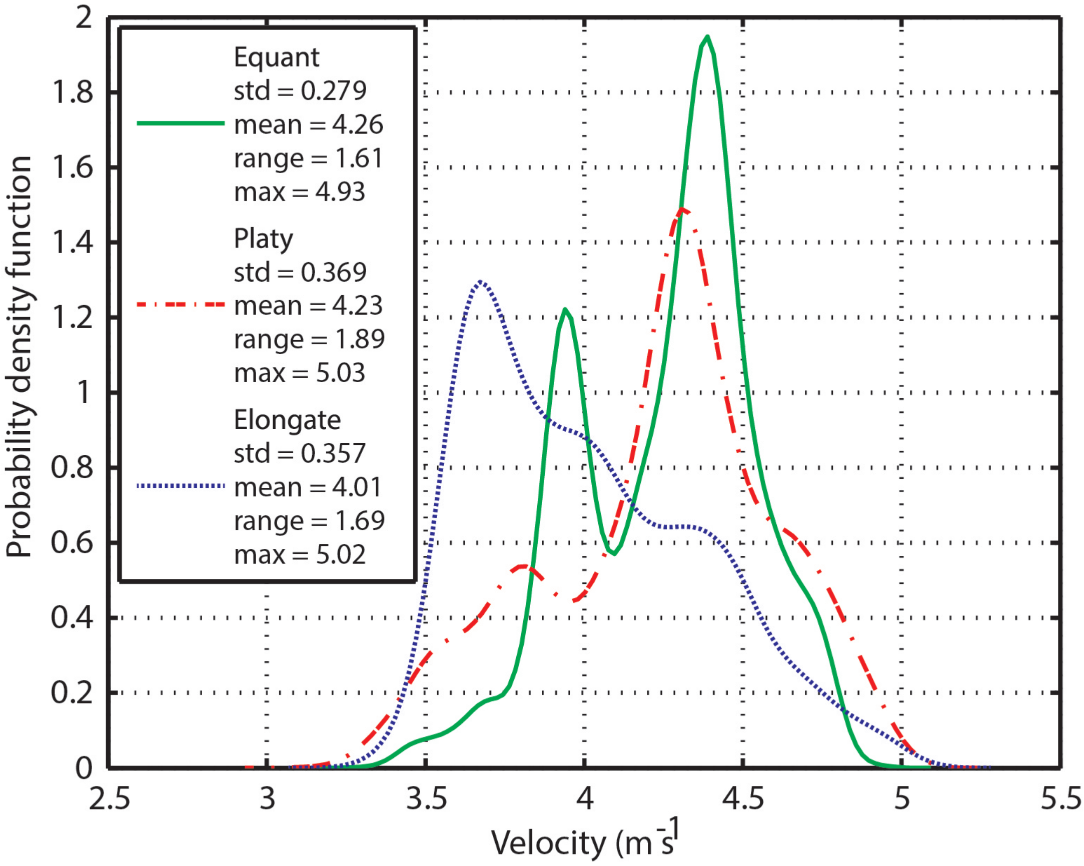

FIGURE 5.13: Probability density function of terminal or maximum velocities attained during simulations, these are sampled from the entire simulation beyond the restricted sampling window of the previous plots. Max, mean, range and standard deviations for each rock-shape are given in the plot legend.

5.3.4 Modelling apparent restitution coefficients of laboratory experiments

A comparison between the experimental and simulated apparent restitution coefficients is valuable, but is hampered by the definition of the contact. In the numerical simulations, contact is defined when the contact force is non-zero. Because of the rock geometry, non-zero contact forces can be applied at different points and different durations as the rock is bouncing, sliding or rolling on the surface. The problem when determining the apparent reinstitution coefficients is to define the beginning and end of a rock-ground contact, particularly in contacts involving multiple mechanisms. The beginning and end defines the pre- and post-impact velocities required to determine the restitution coefficients. Essentially the numerical algorithm provides discrete contact values that must be grouped into periods of contact and non-contact. A second problem with the definition of the apparent restitution coefficients is that it operates in tangential and normal directions. It does not account for the rotation of the rock and the fact that the rock is impacting the ground at exterior points. This can lead to situations where the slope-normal pre-impact velocities are close to zero and the post-impact normal velocities are large, resulting in extreme apparent restitution coefficients. This effect has already been observed in the laboratory experiments and it is amplified in the numerical back-calculations due to the discrete time stepping.

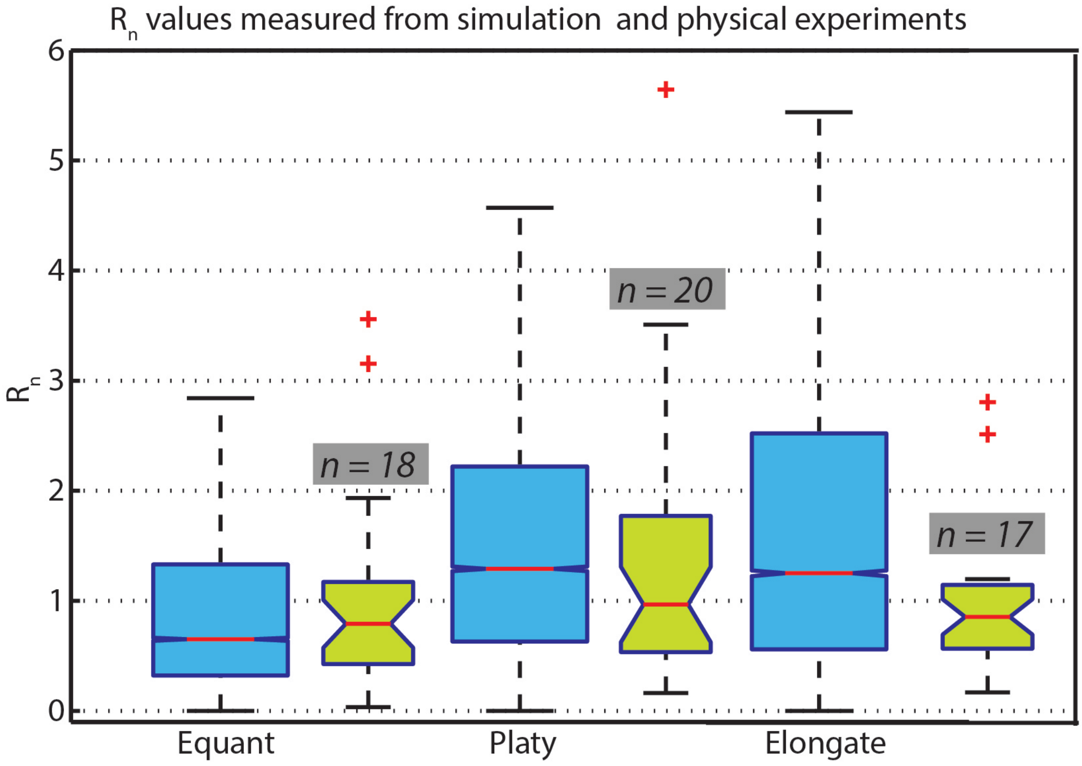

FIGURE 5.14: Boxplot (*blue*) showing restitution coefficients R_n, sampled from numerical simulations back calculating the physical experiments on the 37° planar slope. The R_n values measured in the physical experiments are presented in *yellow*, neighbouring the simulated results.

An example of this problem is shown in Figure 5.15, where normal restitution coefficients of over 600 are calculated. This result simply exemplifies the problems of using apparent restitution coefficients as a method to simulate rockfall contact. Nonetheless, the boxplot of the simulated results (Figure. 5.14) provides median values of R_n for the different rock forms. The simulated range is wide, producing values much larger than 1. In fact for the *elongate* rock, the most awkward shape, the distribution exhibits the most variable and ranging behaviour in the simulations.

Another problem with the simple definition of the apparent restitution coefficient in the tangential direction is that it does not account for the transfer of rotational energy

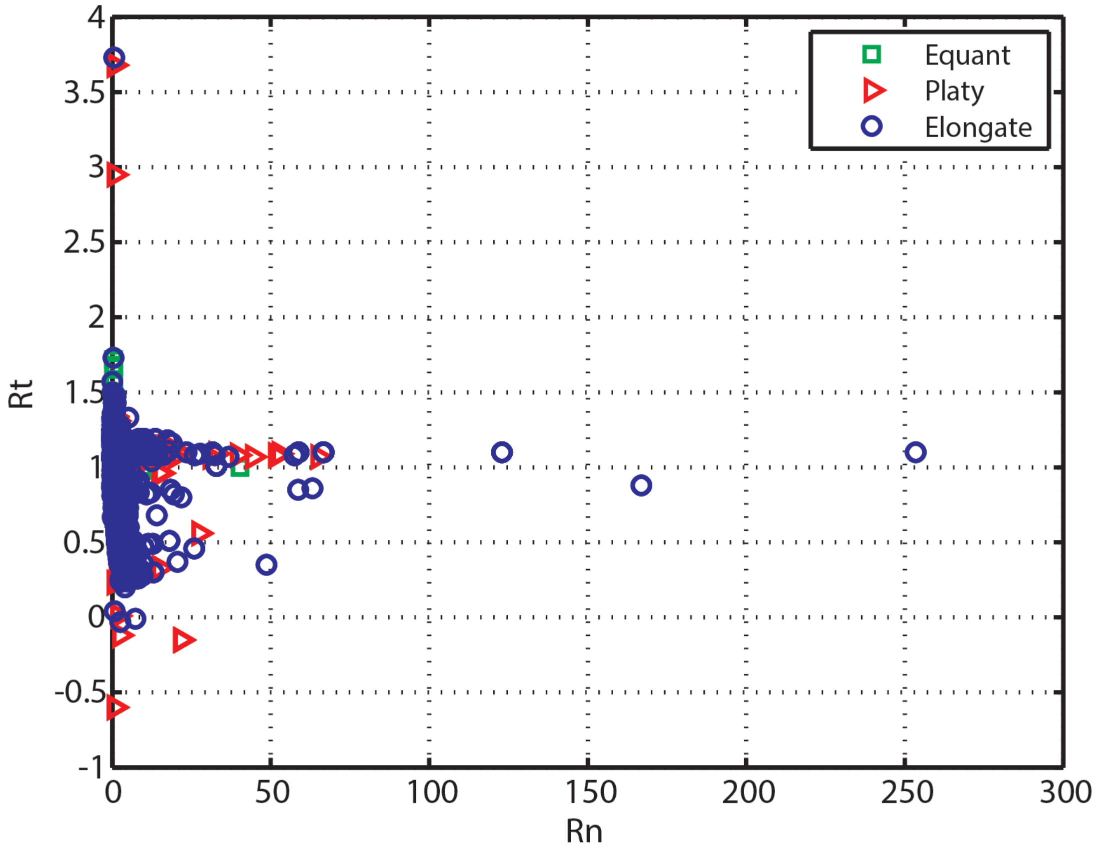

FIGURE 5.15: Scatter plot showing restitution coefficients R_n and R_t, sampled from numerical simulations of the physical experiments on the planar slope. Note that the extreme values plotted here are a function of the discrete time stepping of the numerical model.

into translational velocity on steep slopes. If the R_t values are plotted on flat slopes, where the slope parallel acceleration is zero, the median values decrease to less than 1, indicating deceleration. It is important to note that the contact algorithm correctly reproduces the observed translational and rotational velocities of the experiments. This implies that the contact forces are applied accurately on the rock's exterior surface. The high variability of the calculated restitution coefficients is an indication of the highly variable nature of rock-ground impact that is difficult, if not impossible, to summarize by an apparent restitution coefficient alone.

5.3.5 Angular velocity Ω of the numerical experiments

The simulated angular velocities are presented in Figure 5.16. Mean values indicate that the *equant* rock achieves, on average, the greatest angular velocity (38.0 rad·s^{-1}). This is then followed by the *platy* rock (34.0 rad·s^{-1}), and the *elongate* rock (33.0 rad·s^{-1}).

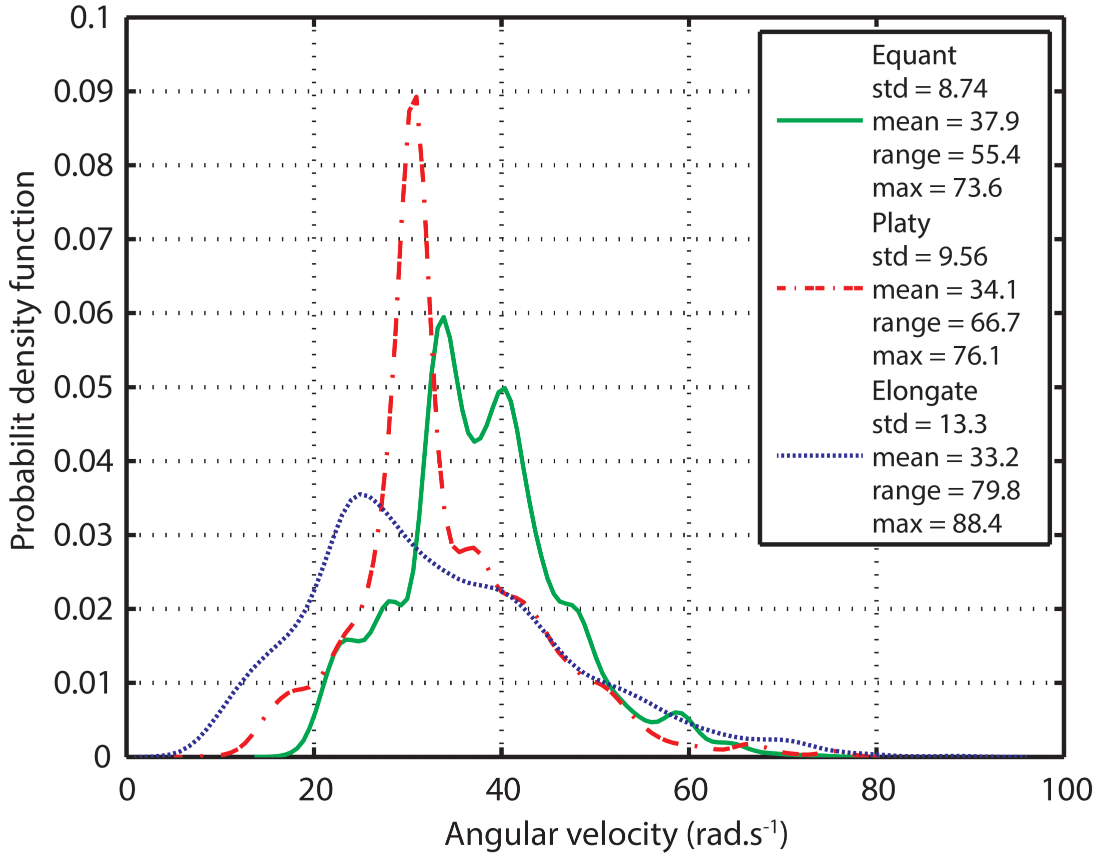

FIGURE 5.16: Probability density function showing the distribution of angular velocities sampled from the numerical experiments back calculating the physical experiments on the planar slope.

However, for extreme events the *equant* rock does not rotate the fastest. The non-equant rocks in each case present a greater range, standard deviation and maximum value of angular velocity. The *elongate* rock shows the greatest range and variability followed by the *platy* rock, while on average the *elongate* rock has the slowest mean angular velocity. Comparing the distributions with those of the physical experiments (Figure. 4.27), the mean values are similar to those recorded by the second peak in the distribution. The simulated results (Figure. 5.16) do not capture the low angular velocity peak about 10.0 rad$\cdot$s^{-1} recorded in the physical experiments. There are number of peaks in the distributions of the *equant* and the *platy* rocks, while less so for the *elongate* rock. The peaks are likely to reflect the different release positions and the respective runout modes.

5.3.6 Summary of numerical model validation

It has been demonstrated that a back calculation of the physical experiments is possible using the best fit parameters to constrain the model (Table. 5.1). It has also been shown that the model is sensitive to terrain changes such as the contrasting transition from carpet to concrete as in the physical experiments.

5.4 Sphericity Ψ

It could be seen in the physical modelling that a rock's form has a strong bearing on the runout potential and dynamics (Chapter. 4), while it was additionally noted that the sphericity Ψ (2.15) of the particles also plays an important role. This was particularly evident for the *equant* test rock which demonstrated characteristic differences in the results when comparing between release orientations even though all inertial axes were the same. In order to investigate the effects of sphericity further a series of numerical experiments using the rockfall model were conducted. The numerical experiments were conducted on a larger rock slope with bigger rocks ($1.0m^3$), with the purpose of bridging the gap between the physical experiments with small rocks and the larger rock sizes expected during rockfall.

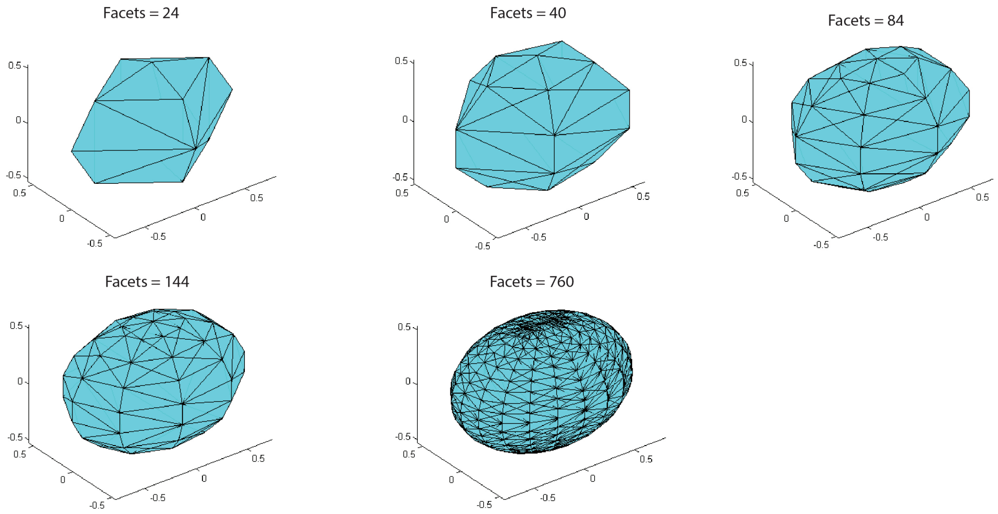

FIGURE 5.17: Ellipsoid which the axial dimensions have been held constant, while the angularity has be altered according to the number of facets that make up its shape.

The numerical experiments exploring sphericity were conducted using an elongate ellipsoidal form released onto a 50° planar slope. Rocks were released with a total height potential of 65.0 m of which 5.0 m was free fall before first slope impact. These initial conditions were selected as an example case because it is similar to what might be expected of some modern road cuts for traffic routes (Pierson et al., 2001). Changes in sphericity were induced by selecting the number of facets required to construct the ellipsoid (Figure. 5.17), respectively altering the sphericity of the particle (Table. 5.2). Adjustments were made to the lengths of the principal axes to ensure each ellipsoids was a constant volume of 1.0 m^3, while the ratio between principal axis lengths was held constant. With a constant density of 2700.0 kg m^{-3} this ensured a fixed mass and that the equivalent inertial ellipsoid of each rock was the same. Release positions were set such that the rock shapes were rotated 90° about each principal axis in a total of 10 steps of 9° for each axis. This ensured that the full range of release orientations were performed and in total n= 1000 numerical simulations for each different shape.

Table 5.2: Physical properties of the Ellipsoidal rocks used to investigate the effects of sphericity.

Ellipsoid	Prin. Axes length			Vol.	Mass	Surf. area	Facet area	Sphericity
	L	I	S					
Nr. Facets	(m)	(m)	(m)	(m^3)	(kg)	(m^2)	(m^2)	Ψ
24	0.94	0.71	0.67	1.00	2700.0	5.60	0.230	0.863
40	0.89	0.65	0.62	1.00	2700.0	5.28	0.130	0.917
84	0.84	0.61	0.57	1.00	2700.0	5.09	0.061	0.950
144	0.83	0.59	0.55	1.00	2700.0	5.06	0.035	0.956
760	0.81	0.57	0.54	1.00	2700.0	4.98	0.007	0.970

The terrain model had a smooth surface, therefor a parameter set was selected with a slow acting κ and β (Table. 5.3) to ensure a greater slope contact period during impacts and preventing the rocks from simply bouncing down the entire slope after the first rebound. Importantly the parameter set remaind constant for all model simulations which allowed the investigations to focus on the effects of changes in the rocks sphericity.

Table 5.3: Contact parameters applied globally to the numerical experiments exploring sphericity using an elongate ellipsoidal form released onto a 50° planar slope.

Parameter set	Slippage-friction				Contact-impact		Drag
	μ_{min}	μ_{max}	$\kappa(m^{-1})$	$\beta(s^{-1})$	ϵ_t	ϵ_n	F
1	0.65	2.00	5.00	3.0	0.00	0.00	0.40

5.4.1 Runout and dispersion

The cumulative frequency distributions of runout distance (Figure. 5.18) show that with increasing sphericity there is an increase in maximum runout distance. However, the distributions of the runout distances indicate that this is only the case for the upper 30% of the data. Below this the trend becomes more mixed and the rock-shape with 40 facets shows the greatest runout distances while the rock with 760 facets produces the lowest runout distances. The crossover of the trends occurs at around 50.0 m runout, at 70% of the data. Summary statistics of the data are given in Figure 5.21.

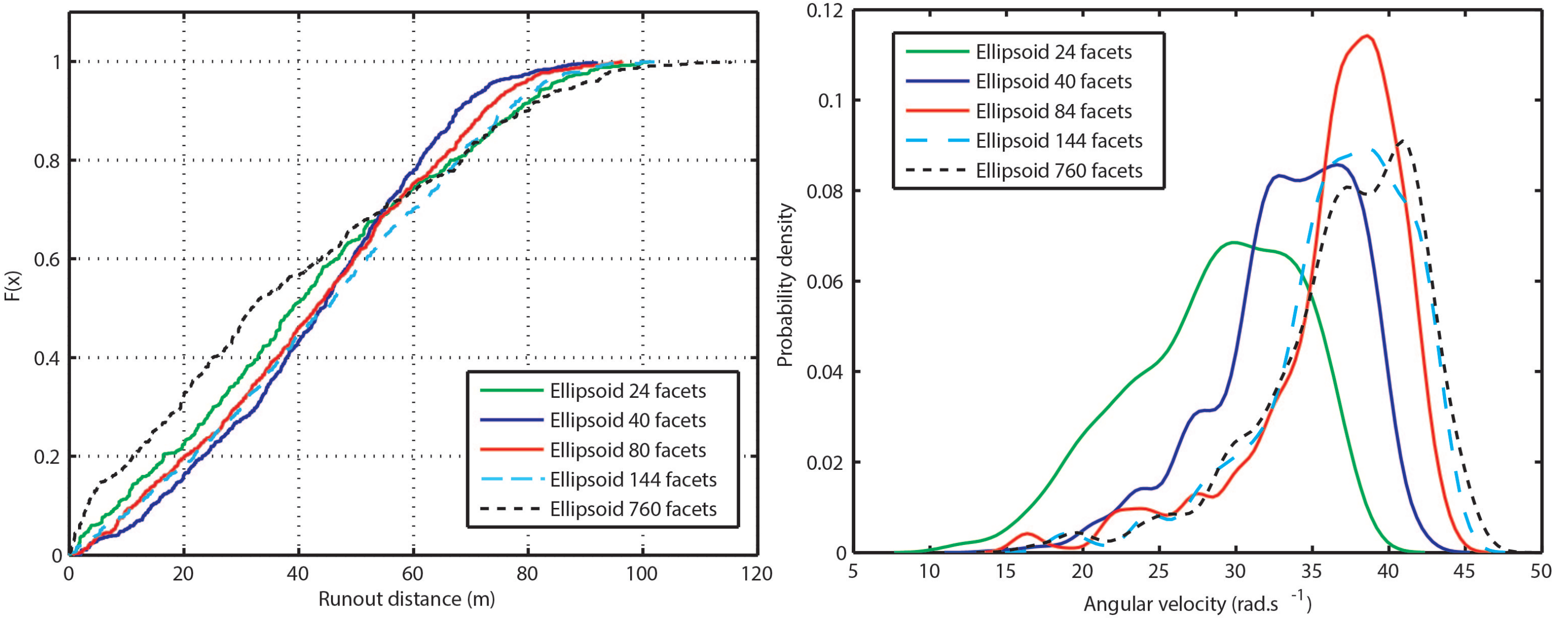

FIGURE 5.18: *Left* cumulative frequency (Fx) plot of the total runout distance for each shape sphericity. *Right* are the angular velocities according to sphericity.

The distribution of the dispersion factors (W/L) is shown in Figure 5.19. The trend indicates that with increasing sphericity there is a reduction in dispersion. However, the rock with the lowest sphericity does not produce the highest dispersion. This is perhaps because the facets are so large on this particular rock-shape; it is more like a rhombus form than the original ellipsoid form. It suggests that this form, with such large facets, is limiting to mobility.

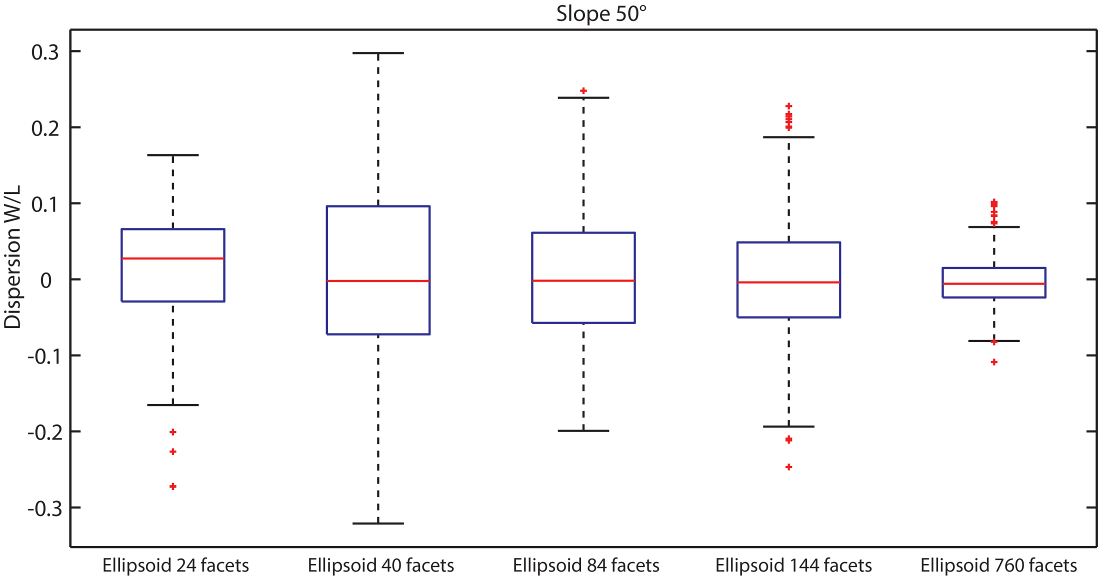

FIGURE 5.19: Boxplot showing the distribution of dispersion values as a function of the rock sphericity.

5.4.2 Rock sphericity and angular velocity Ω

Angular velocity recorded in this experimental series is on average between 30.0 rad·s^{-1} and 40.0 rad·s^{-1} (Figure. 5.18). The peaks in each distribution show an increase in angular velocity with increasing sphericity, a trend also reflected in the maximum values. Each distribution has a negative skew, and the weight of the tail increases with increasing angularity, i.e. there are a greater number of events with low angular velocity.

5.4.3 Rock sphericity Ψ and velocity and jump heights

The distributions of translational velocity and jump height are presented in Figure 5.20. Jump heights show a trend of decreasing jump height with increasing sphericity. This trend is well-pronounced for the initial three rock sphericities, while for the well rounded rock shapes the effect on jump heights becomes of less importance the ellipsoids with a greater number of facets than 84, or a sphericity of $\Psi = 0.95$. The distributions are positively skewed. Velocity shows distributions with very similar results: distributions are normally distributed and each focuses its peak between 26 m s^{-1} and 28 m s^{-1}. There does not appear to be a discernible trend in accordance with the degree of sphericity.

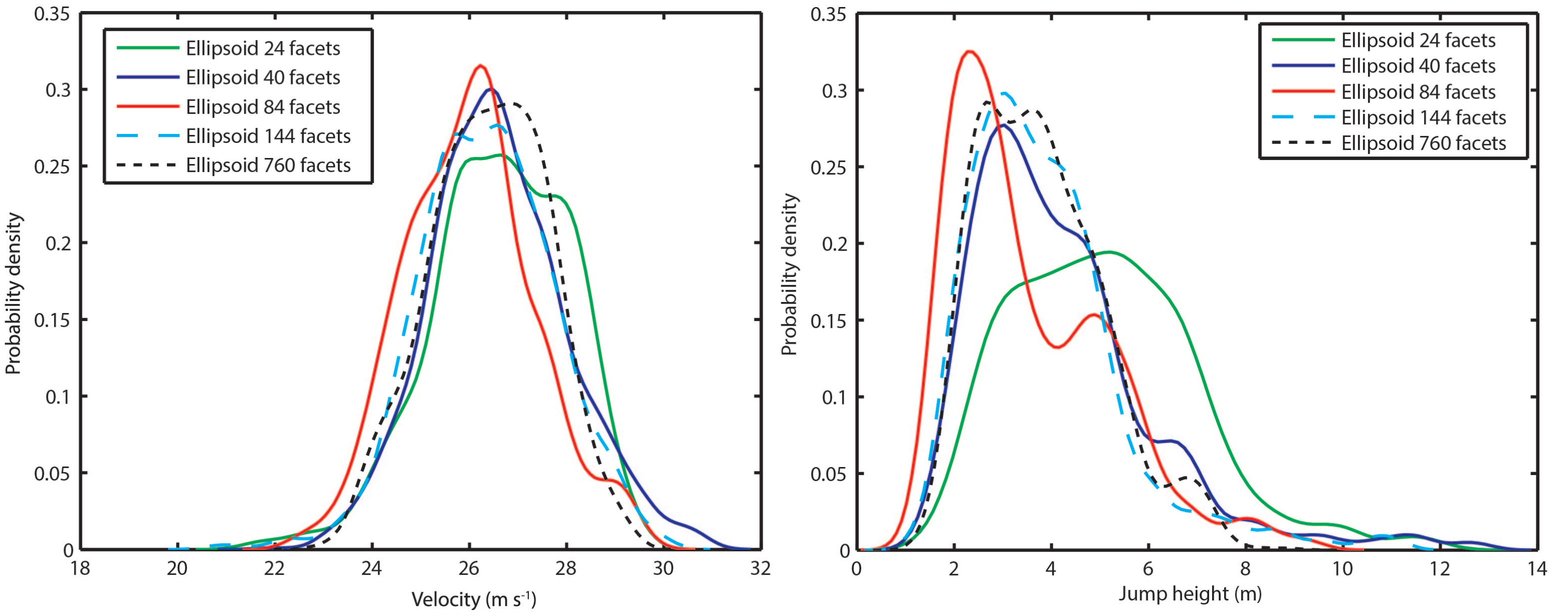

FIGURE 5.20: *Left*, probability densities of translational velocities, and *right* are jump heights. The different rock-shape sphericity is indicated by different coloured lines and dashes and is given in the legend.

5.4.4 Summary Sphericity

Summary statistics of the general trends in runout deposition patterns and dynamic runout behaviour according to changes in sphericity are presented in Figure 5.21. Runout distance and translational velocity of the different rocks (plots A and C Figure 5.21 respectively) appear little affected by changes in sphericity, while this may be due to the range of sphericity selected for the bodies, not including much lower sphericity. By expanding the range of sphericity values selected for these experiments, it is expected that runout distance and translational velocity may be greater. HHowever, by increasing the range of sphericity, one must also alter the form of the rock as sphericity and form are not independent of one another. Angular velocity on the other hand shows the strongest response to changes in sphericity (plot D Figure 5.21): With increasing sphericity there is an increase in angular velocity. This trend appears to tail off as sphericity approaches $\Psi = 1.0$. Both the responses of dispersion and jump heights show a decrease with increasing sphericity (plots B and E).

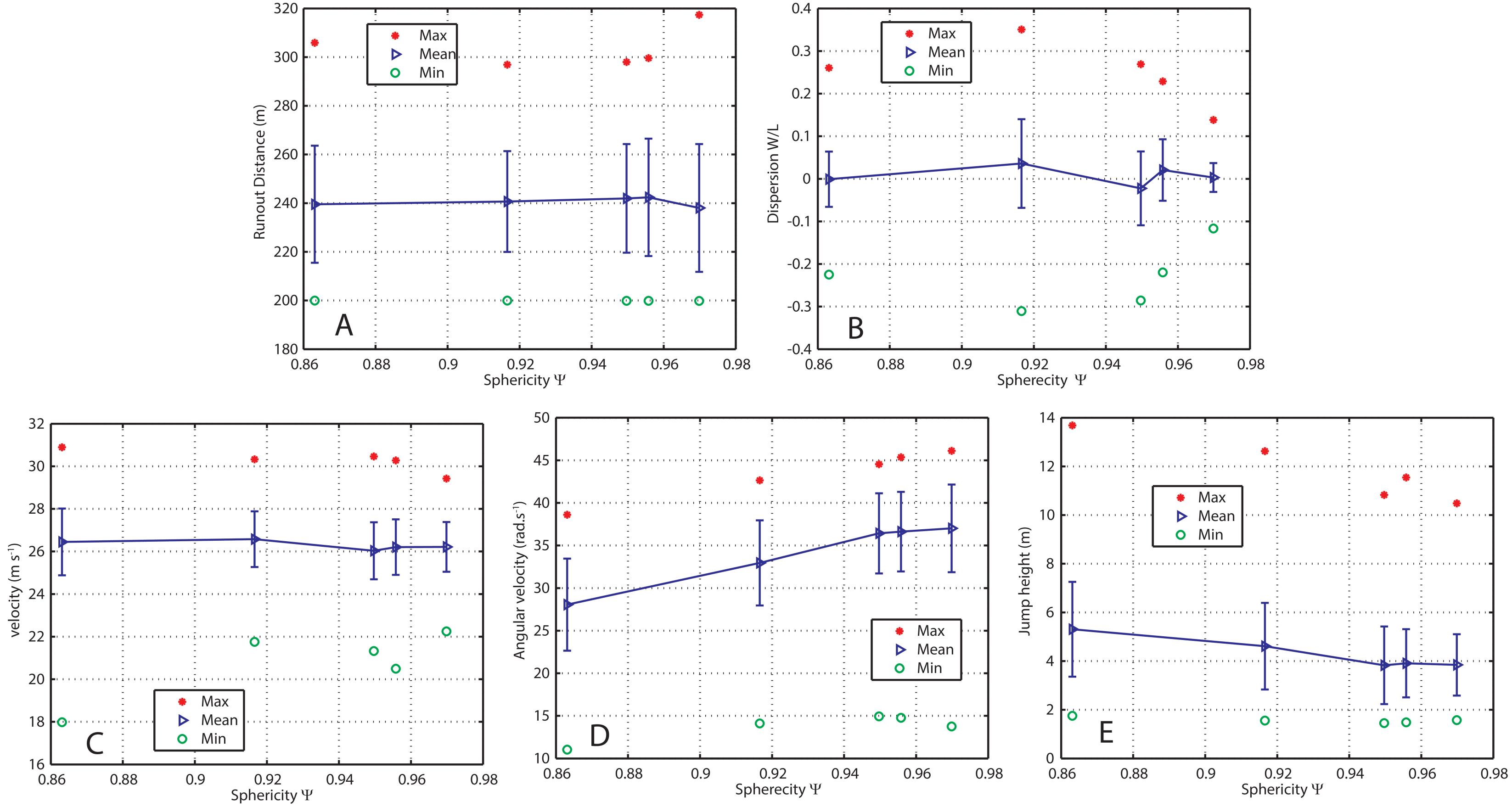

Figure 5.21: Summary statistics of; *A* runout distances in meters (m) as a function of sphericity (Ψ); *B* degree of dispersion (W/L); *C* the translational velocity; *D* angular velocity; *E* jump heights. Each point represents the statistics from $n = 1000$ simulations, where max values are the red stars, the mean values are the blue triangles and the minimum are the green squares. Standard deviations are indicated as the blue error bars on mean values.

5.5 Application to full-scale rock rolling experiments on a rock cut slope (St. Léonard, Switzerland)

An important application of rockfall modelling is the design and management of rock cut slopes (Duffy, 1992, Singh et al., 2013), see Figure, 5.22. The design and management of rock cut slopes is a demanding problem because it requires that detachable blocks are identified and their runout paths modelled. Rock cut engineering seeks the optimal slope angle for stability that requires the least excavation of ground material. Often there is a compromise between stability and slope angle and the rock cut can remain hazardous from precipitous rockfall. This is very much determined by the geological features of the rock cut, and therefore rockfall shape.

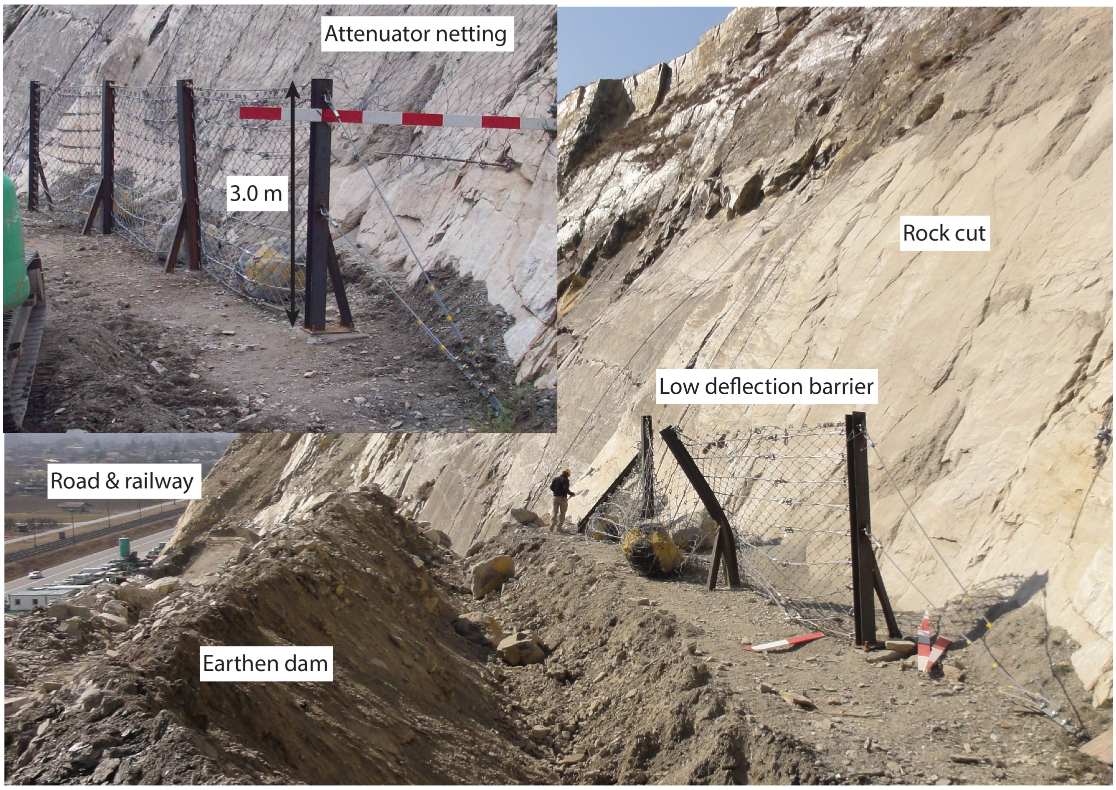

Figure 5.22: Situation of the rock cut test site at the St. Léonard quarry which was situated directly in front of a main road and railway. The rock cut was smoothed limestone rock cut at 50° down which the rocks were rolled. Experiments were conducted with netting lain on the rock slope. Rock rolling without the netting on the slope was also conducted. The main safety structures were the rockfall barrier and earthen dam at the foot of the slope.

The St. Léonard field test site (Figure. 3.9) was an ideal situation to explore the runout behaviour of full size rocks on a rock cut slope. The experiment test series at this site (Figure. 5.23) were initially intended to test the design of rockfall retaining structures, such as attenuator nets, catch fences and earthen dams (Figure. 5.22). These test series permitted the free rolling of rocks at full scale, and allowed insights into the detailed impact mechanics of rockfalls. Furthermore, it provided an opportunity to validate the rockfall model at full-scale.

Of the experiments that were conducted at this test site without the use of rockfall mitigation structures, a total of $n = 14$ rock rolls could be documented. The rocks varied in mass and shape (Table. 5.5). The rocks were released from the top of the rock cut with the use of a digger.

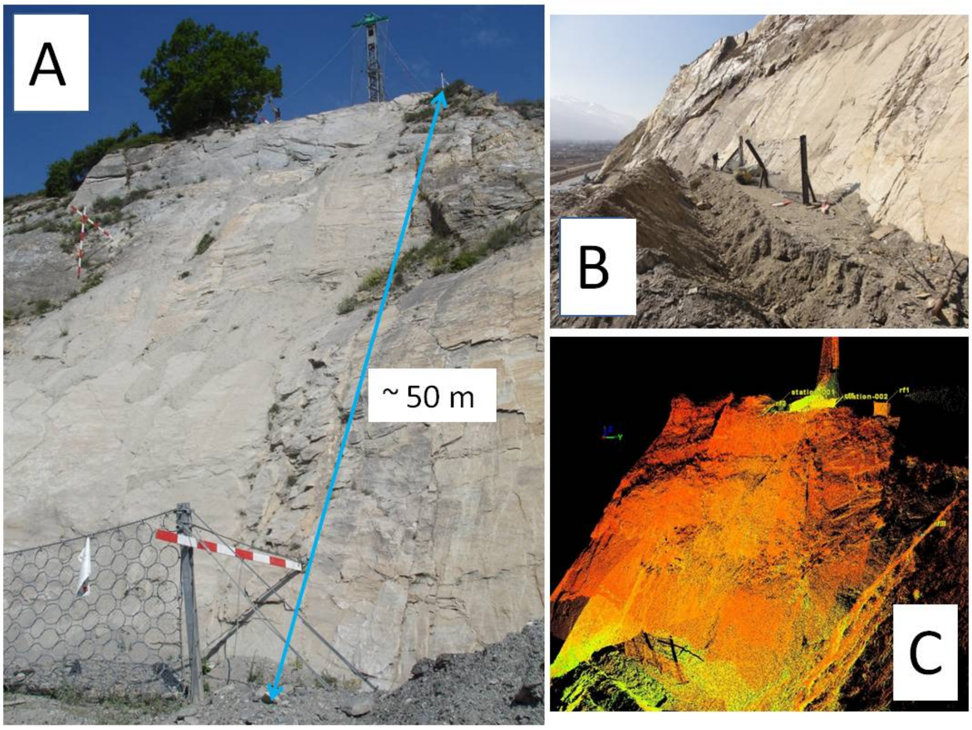

FIGURE 5.23: St Léonard rock rolling test site. A) presents the natural rock cut on which the experiments were conducted which was composed of solid limestone rock surface. B) is a picture of the dam at the toe of the rock cut composed of loos tailings and rock debris designed to contain the rocks as the rolled down the rock cut. C) is an image of the terrestrial laser scan conducted to extract a detailed terrain model of the rock cut for use in the modelling exercise and to aid the analysis of the video data of the rock rolling experiments.

The rock cut was scanned with a terrestrial laser scanner to generate an accurate high-resolution terrain model (Figure. 5.23). Rock velocities and angular velocities were determined using videogrammetric and geometric analysis (Glover et al., 2012). Both velocity extraction methods were explored and a comparison was made between the results (see Chapter 3, Section 3.4.1). The potential energies, velocities, angular velocities and jump heights are reported in (Table. 5.5). It should be noted that angular velocities in this case could only be measured using videogrammetry in 1-D, because at the time of these experiments the internal dynamic rock motion sensor was not available.

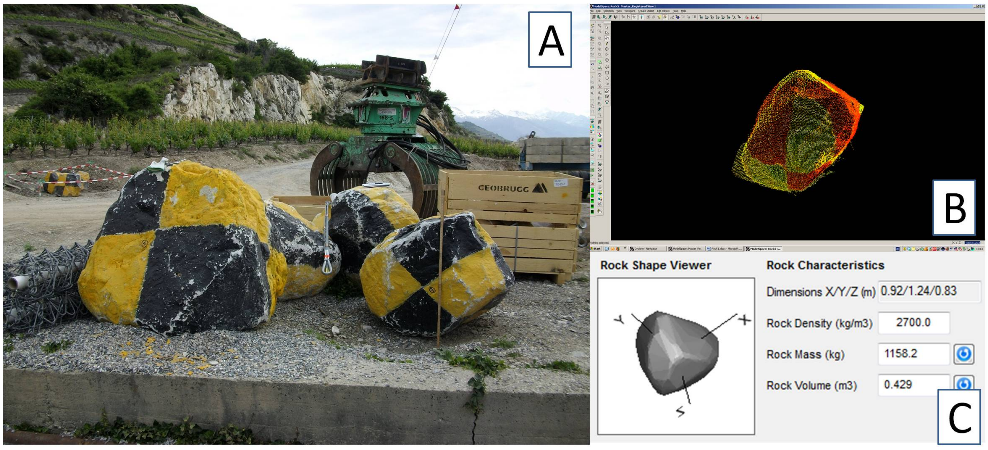

Dimensions X/Y/Z (m) 0.92/1.24/0.83
Rock Density (kg/m3) 2700.0
Rock Mass (kg) 1158.2
Rock Volume (m3) 0.429

FIGURE 5.24: *A*) gives an image of the rocks selected for the rock rolling exercise; they are painted with contrasting colours to assist in the video tracking analysis. *B*) shows an image of the scanned test rocks, the point clouds were used as input data to describe the test rock geometry for the rockfall simulation model *C*.

The rocks used in the experiments were scanned to provide the point cloud data which permitted the test rocks to be included into the rockfall model accurately accounting for their shape and volume (Figure. 5.24).The starting conditions were set to the observed dynamics of the rocks being released into the rock slope by the digger. For the experiments this release location was held constant creating a point release which permitted a quantification of the dispersion of the rocks from this point source.

Two terrain contact parameters were selected. The first modelled the hard contacts that the solid rock face created, while the second applied softer contacts parameters to represent the embankment at the base of the slope which was made of lose debris and rubble from the quarry. The parameter sets are presented in Table 5.4. The rock surface is modelled that it climbs relatively quickly to the max friction value with lower drag forces on the contacts. The embankment on the other hand has a broader frictional domain with a slower decay of friction after the contact allowing for greater kinetic losses through each contact, in addition to having a greater drag force which better represents the behaviour of the embankment material.

Table 5.4: St Léonard case study parameter selection. The parameter selection includes a rock terrain for the rock slope and a loose earth and debris parameter to model the embankment at the base of the slope.

Parameter set	Slippage-friction				Contact-impact		Drag
	μ_{min}	μ_{max}	$\kappa(m^{-1})$	$\beta(s^{-1})$	ϵ_t	ϵ_n	F
Rock slope	0.65	2.00	50.00	3.0	0.00	0.00	0.40
Embankment	0.25	2.00	175.00	1.5	0.00	0.00	0.70

Table 5.5: Results from rock rolling experiments St Léonard, Switzerland.

Test Nr.	Rock mass	Vel.	Ang.Vel.	Jh(f)	Axis(I)	I.Sphere	Trans.kE	Ang.kE	kE$_{tot}$	Pot.h	Pot.E	kE$_{tot}$/Pot.E
	(kg)	(m s^{-1})	(rad.s^{-1})	(m)	(m)	kg·m^2	(kJ)	(kJ)	(kJ)	(m)	(kJ)	%
1	490	20.11	24.73	1.45	0.70	96.04	99.06	29.36	128.43	37.00	177.86	72.21
2	360	21.47	27.19	2.23	0.65	60.84	82.93	22.49	105.43	37.00	130.67	80.68
3	500	22.86	18.33	0.44	0.70	98.00	130.62	16.46	147.08	37.00	181.49	81.04
4	690	23.43	16.02	1.43	0.60	99.36	189.40	12.76	202.16	37.00	250.45	80.72
5	820	22.40	19.63	3.14	0.77	194.47	205.68	37.49	243.16	42.00	337.86	71.97
6	950	20.87	16.73	1.21	0.85	274.55	206.98	38.40	245.38	42.00	391.42	62.69
7	1130	22.49	16.97	3.04	0.90	366.12	285.84	52.70	338.54	42.00	465.58	72.71
8	1270	18.41	14.08	0.55	0.95	458.47	215.13	45.42	260.55	42.00	523.27	49.79
9	1950	22.60	13.55	2.37	1.15	1031.55	497.97	94.67	592.64	42.00	803.44	73.76
10	490	18.47	38.48	1.60	0.70	96.04	83.57	71.12	154.69	42.00	201.89	76.62
11	820	19.10	17.09	2.84	0.77	194.47	149.65	28.40	178.04	37.00	297.64	59.82
12	950	18.00	16.56	1.34	0.85	274.55	153.86	37.64	191.50	37.00	344.82	55.54
13	1130	20.09	7.23	0.23	0.90	366.12	228.03	9.56	237.59	37.00	410.16	57.93
14	1270	18.52	18.53	1.90	0.95	458.47	217.88	78.69	296.57	37.00	460.97	64.34

An overview of the velocity simulation results at different time steps is displayed in Figure 5.25. The results indicate the natural dispersion of the rockfall from the single point release. In addition, 3 out of the 14 rocks were able to roll up and over the earthen dam, which is 21 % of the total released rocks, this compares well with the results of the simulation (93 of 500 simulated rocks, exceeded the earthen dam which is 19% of the total released rocks).

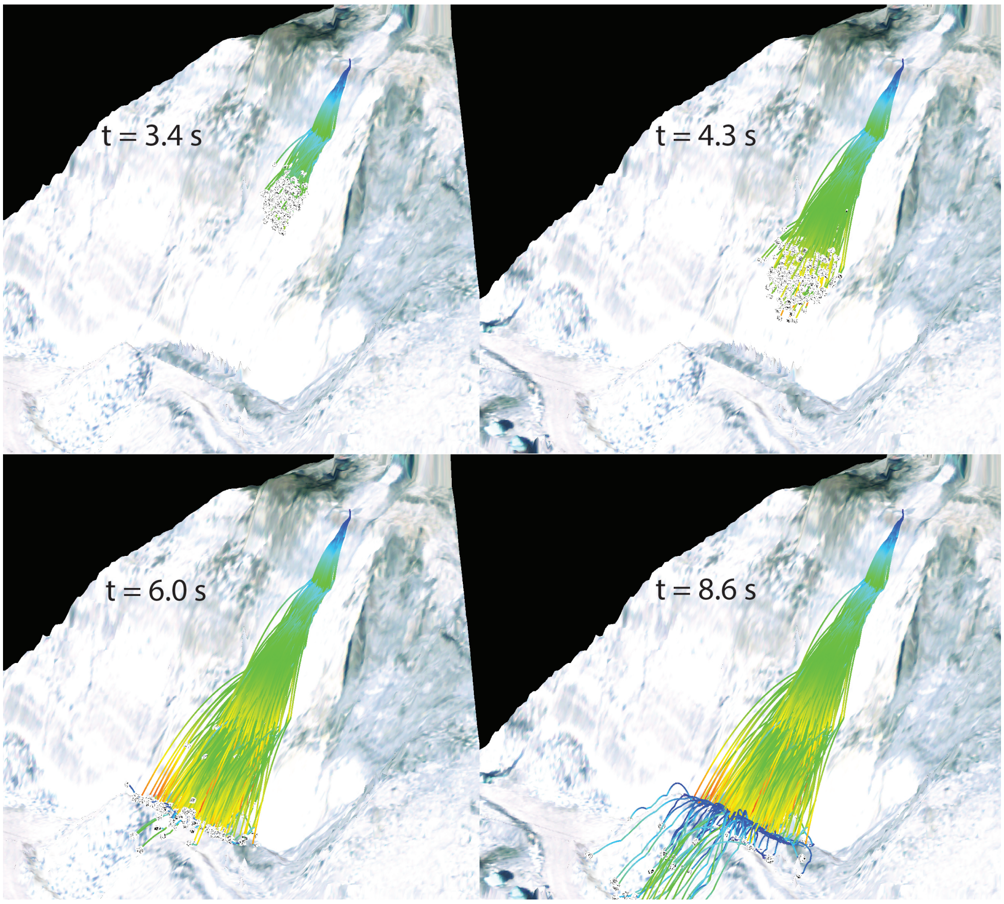

FIGURE 5.25: Sequence image of a rockfall simulation on the St Léonard test site rock cut. Images are sampled between t = 3.4 s to t = 8.6 s

Figure 5.26 compares the measured and calculated maximum jump heights, velocities, angular velocities and kinetic energies at the toe of the slope between simulations and experiments. The rockfall model is in good agreement with three of the measured values (jump heights, velocities and kinetic energy). There is a discrepancy between the measured and calculated angular velocities (Figure, 5.26C). The median values of the simulations are ≈30 rad·s^{-1}, whereas the median values of the measurements are ≈18 rad·s^{-1}. A likely explanation fo this is that it is an artefact of the data analysis of the real scale experiments which could only determine the one-dimensional angular velocity in the viewing plane of the video camera. The experimental results must therefore have lower angular velocities than the simulations which are delivered as an absolute value taken from the three rotational components. This indicates that there can be significant amount of energy in the remaining rotational components. The comparison between the calculated and experimental kinetic energies also reflects the missing energy of the rotational components (Figure, 5.26*D*). However, this cannot be fully varified with this dataset. To be sure of this, full three-dimensional measurements of the rocks rotations should be made. The newly develped internal motion sensor, the StoneNode, provides an opportunity in future experimentation to capture this.

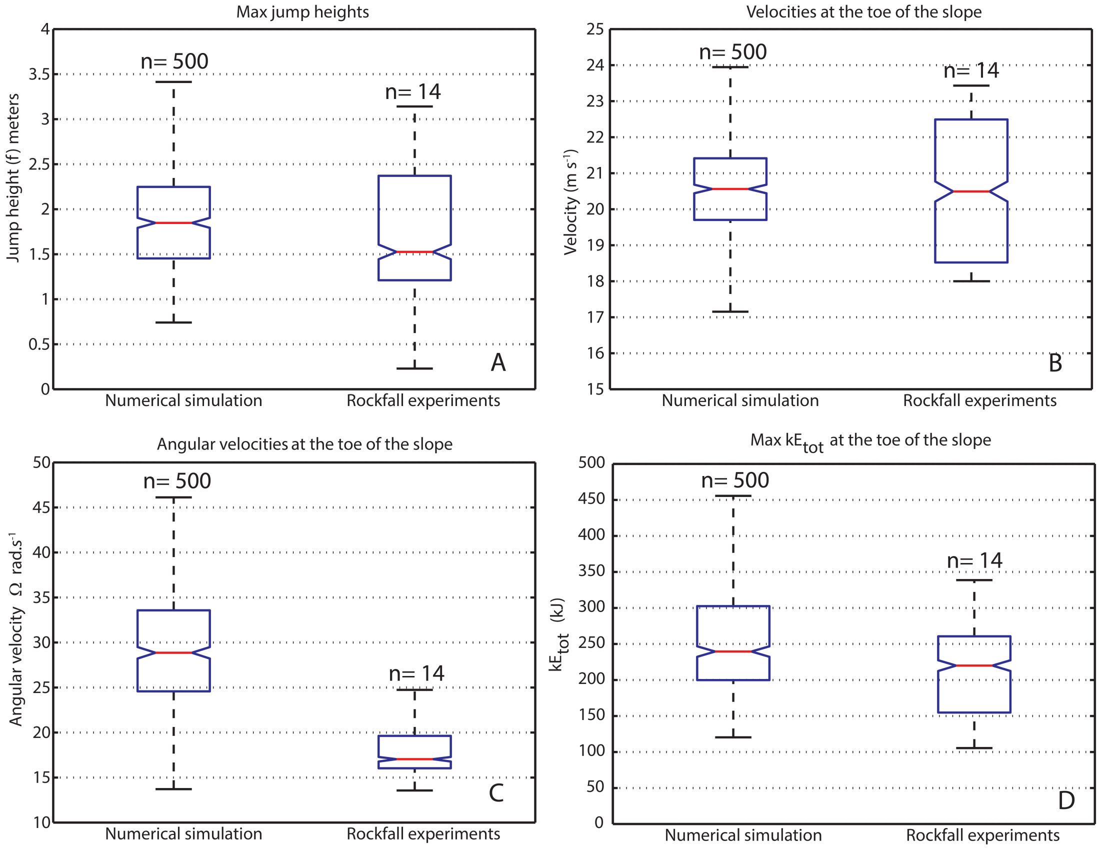

FIGURE 5.26: Box plots comparing the simulated and experimental maximum jump heights *A*), the velocities *B*), angular velocities *C*) and kinetic energies *D*) measured at the toe of the slope.

FIGURE 5.27: Rockfall damage following earthquake in 2011. A) Rock boulder travelled through a house, no persons were injured; B) rock boulder with a volume of 14.0 m^3 which passed through the house; C) *elongate* rock block coming to a stop in a drive way; D) Smaller rockfall approx 1.0 m^3 impacting a house.

5.6 Application to natural rockfall, case study Heathcote, New Zealand

On 22nd of February 2011 Christchurch, New Zealand experienced a Mw = 6.3 Earthquake which caused severe damages to buildings and infrastructure, through building collapse and liquefaction of ground induced by the strong ground acceleration in the area. The residential area of the Port Hills area of Christchurch was heavily affected by earthquake induced rockfalls, over 6000 single rock boulders were released from the basalt cliffs which ran out over the soft soil slopes and impacted over 200 houses and killed five people.

Although the earthquake and ensuing rockfalls were devastating events, this case provides an exemplary study for rockfall hazard. The entire Port Hills region was inundated by rockfalls (Figure. 5.27). The case study presented here focuses on the residential valley of Heathcote. In this area the location, size and the three principal axial dimensions of over 450 rocks could be mapped (Figure. 5.28) by local engineering offices. The distributions of the rock sizes and shapes are presented in Figures 5.29 and 5.30. Additionally to the mapped boulder locations, past deposits from rockfall events could be mapped from the orthophotography of the area.

5.6.1 Geology and rock characteristics

There were two distinct basalt lithologies which characterised the bluffs of the Heathcote Valley. An important geological feature of the basalt lava flows in the Heathcote Valley was the varying basalt compositions and cooling history between lava flows. This had a strong bearing on the nature of collapse and the rock shapes that were released during the earthquakes. The main bluffs were composed of large columnar jointed Trachyte basalts. Their slower cooling history generated massive elongate blocks (Figure. 5.31).

Figure 5.28 *(following page)*: Mapped boulder locations lain on an orthophoto taken of the area following the earthquake event (Orthophoto, GNS, 2011). Boulder positions that were mapped from the orthophoto include both pre and post earthquake rockfall deposits are displayed as blue triangles. Rocks that came down during the earthquakes are classified according to their volume estimate. The main of the boulder data are taken from GNS, single events and trajectories were recorded in this study to ground truth this data set.

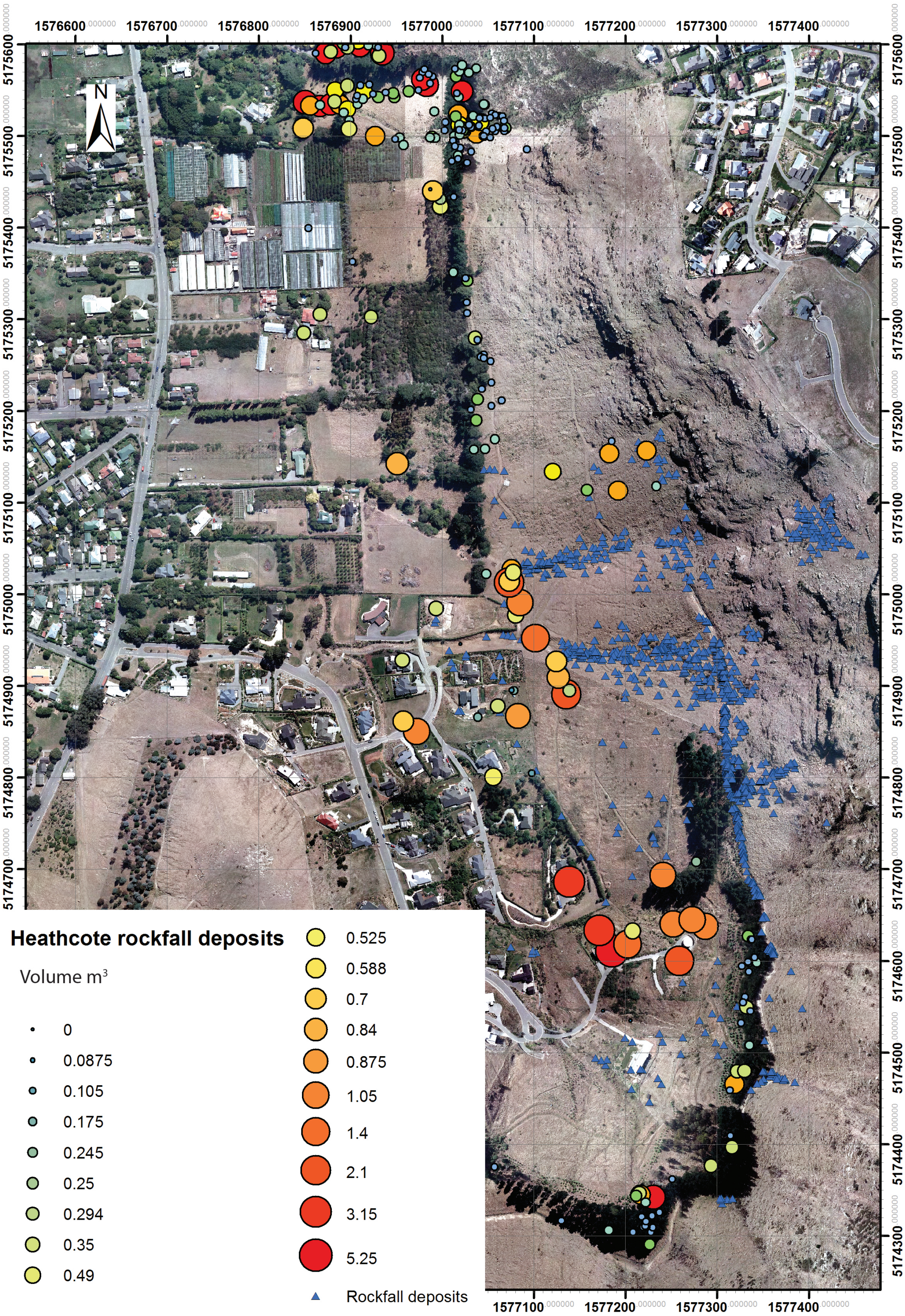
1576600
1576700
1576800
1576900
1577000
1577100
1577200
1577300
1577400
5175600
5175500
5175400
5175300
5175200
5175100
5175000
5174900
5174800
5174700
5174600
5174500
5174400
5174300
N
Heathcote rockfall deposits
Volume m³
0
0.0875
0.105
0.175
0.245
0.25
0.294
0.35
0.49
0.525
0.588
0.7
0.84
0.875
1.05
1.4
2.1
3.15
5.25
Rockfall deposits

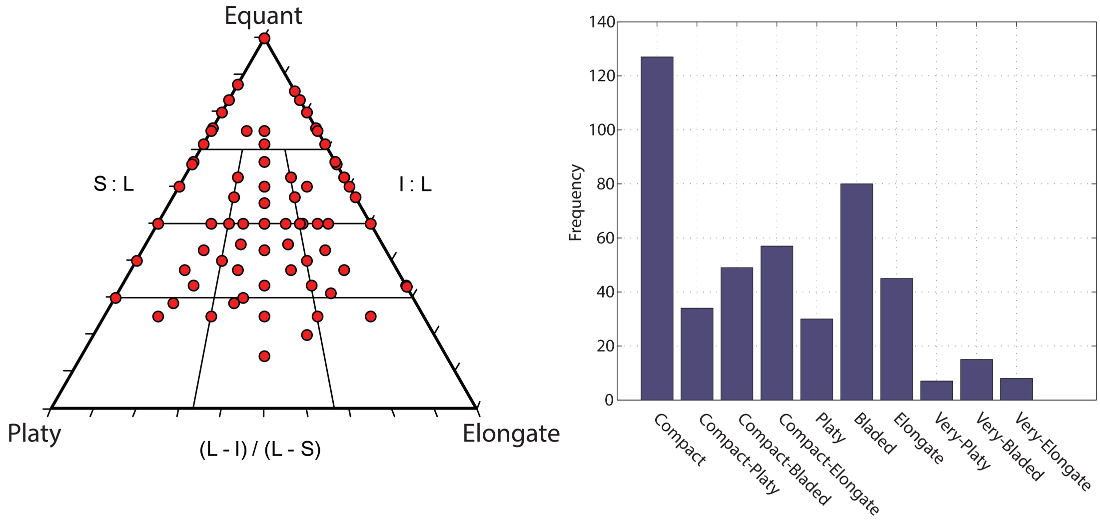

FIGURE 5.29: *Left* Tri-plot of the rock shapes sampled from the deposits of rockfalls during the 2011 earthquake event. The classification scheme is according Sneed and Folk. *Right* frequency histogram of the different shape classes of rockfall deposits sampled from the Heathcote valley.

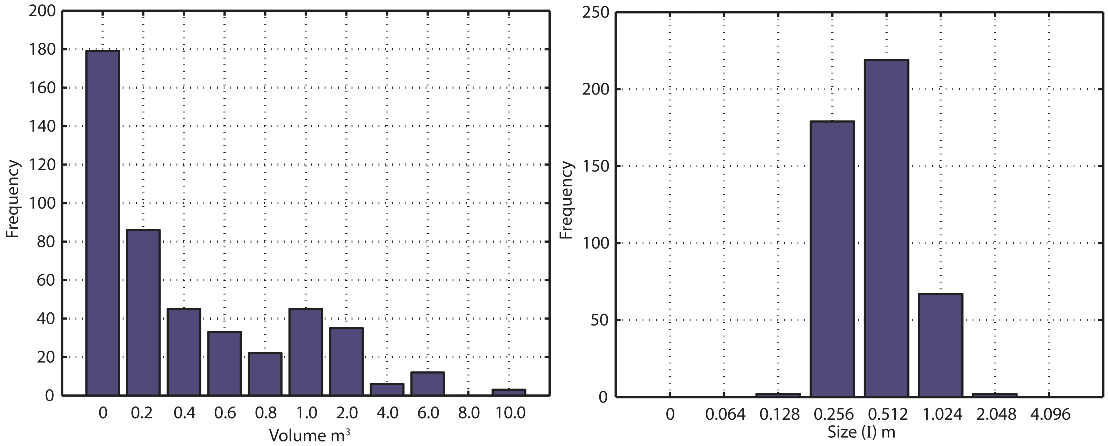

FIGURE 5.30: *Left*: frequency histogram of rockfall deposit boulder volumes (m^3) mapped in the Heathcote Valley area. *Right*: frequency histogram of the rockfall deposit boulder intermediate axis (I) length (m).

It was these particular blocks that travelled the farthest. The remaining bluffs were also a Trachyte composition. However, differences in the cooling history of these particular units lead to high foliations in the bulk rock mass. This produced flaky slabs, which although large in size, their propagation distance from the release zone was considerably smaller and less dispersed (see, Figure 5.32).

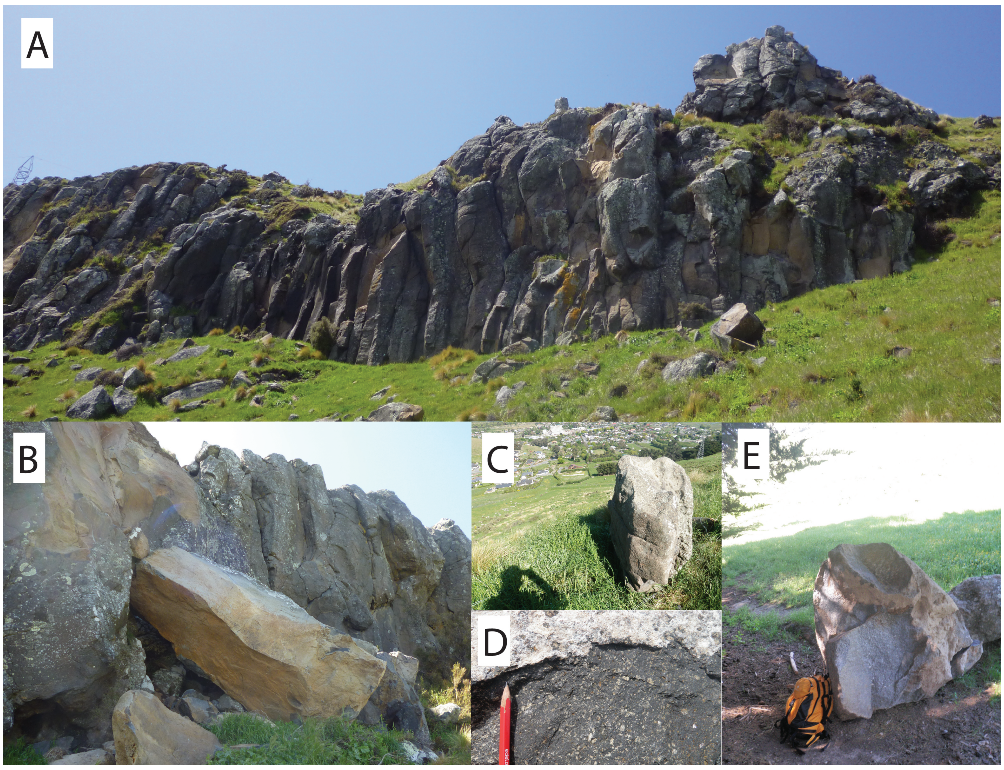

FIGURE 5.31: *A*) basalt bluffs outcropping in the Heathcote Valley with distinctive vertical jointing patterns. Brown weathered surfaces indicate regions from which rockfalls were released in the earthquake events. *B*) Columnar basalt block that has toppled from the outcrop, its large elongate form did not allow it to runout any further than the base of the bluff. *C*) Basalt boulder deposit lying in the runout slope looking down over the Heathcote residential area (has potential to be remobilised in an earthquake event). *D*) Fragment of a Trachyte basalt boulder. *E*) Boulder that has runout to the base of the valley.

5.6.2 Numerical simulations of the Heathcote rockfalls, New Zealand

The data of the rockfall deposits collated for the Heathcote area provide the opportunity to conduct numerical back calculations of the rockfall events and test the rockfall model. The simulation setup to back calculate the rockfall events used rock shapes and sizes to represent the data collated from the mapped boulders (Figures 5.29 and 5.30). Three different rocks representative of those encountered in the area were used. The release locations were selected from the base of the basalt bluffs found in the terrain, these were located by finding the break in slope in the terrain model and are also visible on the orthophoto in Figure 5.28. In total the release points along the bluffs produced 157 release locations for simulations in the studied area. From each location the three-dimension rocks were released from the same drop height of 0.5 m measured from the rock's centre of mass, while the orientation of the rock was varied at random in a total of 9 different start orientations. Through this approach it was possible to introduce

FIGURE 5.32: *A*) Buttress of a Trachyte basalt bluff show high degree of fracturing, the horizontal fabric is characteristic of this unit.*B*) Main Trachyte bluff with characteristic horizontal foliation fabric. A central collapse zone exposes the rusty brown weathered matrix of the lithology in this rock-mass; deposits are to the base of the bluff. *C*) Rubbly deposits at the base of the bluff illustrate how easily this unit disaggregates. *D*) Tabular platy formed fragment characteristic of this unit.

the variability in the simulations and produce the dispersive runouts. A total of 4239 simulations were initiated of which 4227 were successful and could be used to investigate the runout characteristics of rockfalls in the Heathcote valley.

TABLE 5.6: Best fit parameters selected for the back-calculation of the Heathcote rockfalls, New Zealand, with the rigid-body rockfall model.

Parameter set	Slippage-friction				Contact-impact		Drag
	μ_{min}	μ_{max}	$\kappa(m^{-1})$	$\beta(s^{-1})$	ϵ_t	ϵ_n	F
1	0.50	2.00	100.00	2.5	0.00	0.00	0.50

The parameter set was selected by assessing the simulations that stopped the closest to the runouts of the deposited rocks recorded for the Heathcote area (Figure. 5.28). The best fit parameter set selected for the simulations presented in the following results are presented in Table 5.6. These parameters have a larger additional drag force of $D = 0.5$

and a small β which are designed to simulate the longer release time of rocks penetrating the softer loess covered soil of the Heathcote area. In the field it was frequently observed that rocks would penetrate deep into the soil cover and slip to distances of 2.0 - 3.0 meters (e.g. Figure 2.7C). Important to note in the results presented hereafter is that the parameter set for the terrain parameters remained constant and was in no way made variable. The stochasticity observed in the results is entirely induced through a variation of the initial orientation of the rock before it is released into the simulation domain.

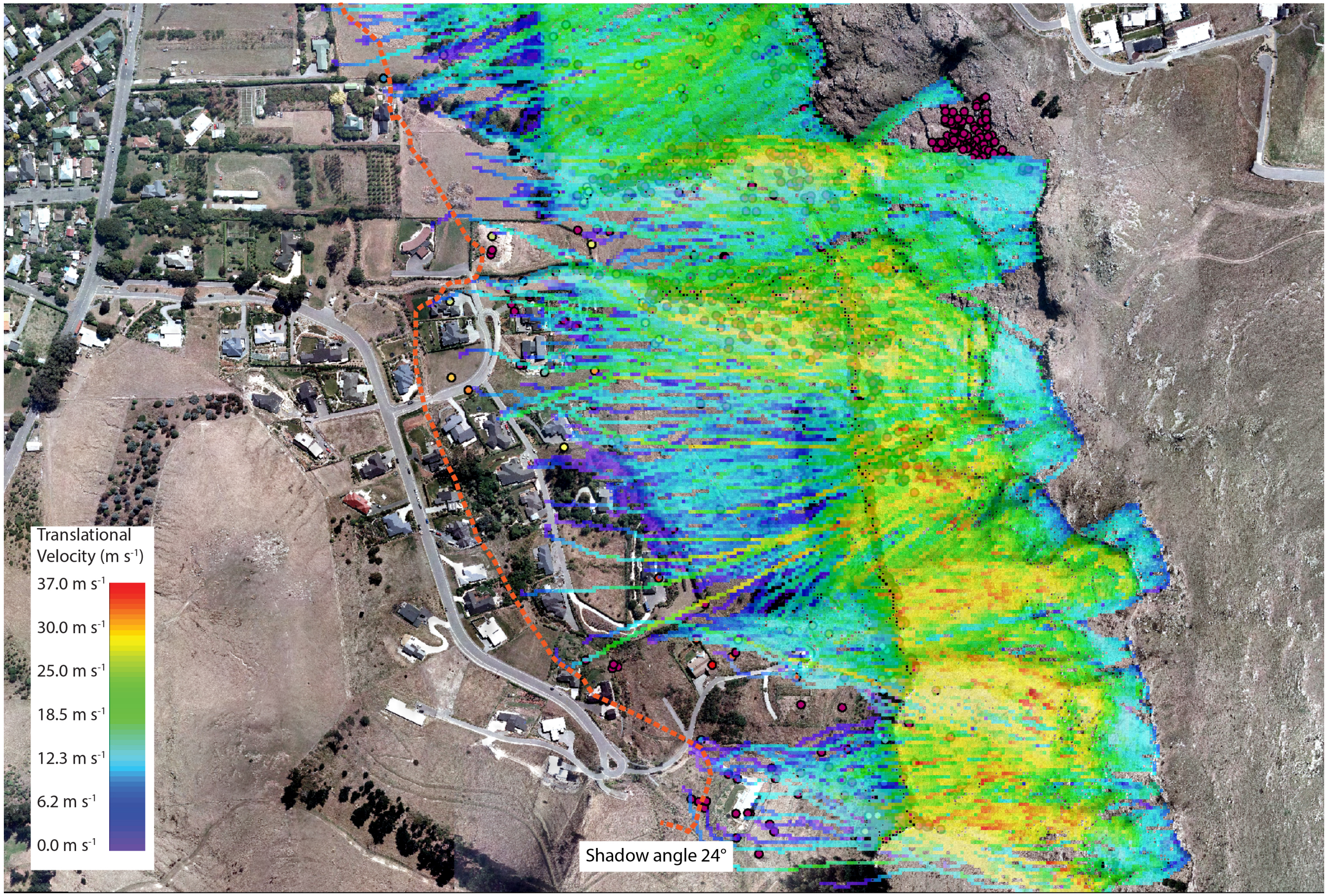

FIGURE 5.33: Velocity map sampled from rockfall simulations of the Heathcote valley area. 4227 single trajectory simulations compose this data set. The map plots the maximum velocity recorded for each (2.0 x 2.0 m) grid square that a simulated rock trajectory passes over. Grid squares are coloured according to the velocity intensity which is indicated in the legend. The rockfall shadow line for 24.0° (reflecting the most extreme runout for this area) is drawn with the dashed orange line.

5.6.3 Results of rockfall simulations for Heathcote

The results of rockfall trajectories simulated with the rock-shape and size distributions released from the cliff areas of the Heathcote Valley are presented. Of all the rocks shapes simulated and release points along the cliff lines, a total of 4227 single rocks could be displayed for the analysis. Figure 5.33 presents the maximum translational velocities passing through each grid square on the terrain model. It is noticeable that the high velocity regions of the trajectories are found in the cliff areas. Here the rocks spend a greater time in free fall than on the flatter portions of the terrain and are thus faster. Importantly, the velocity map delineates the rockfall inundation area of the Heathcote Valley. There is a good match of the runout trajectories with the extreme events that caused much of the damages to residential properties in this area (Figure. 5.27). In many cases simulated rockfall trajectories land upon the locations of the mapped deposits. Figure 5.33 also plots a dashed orange line indicating the extent rockfall runout according to the shadow angle method (Dorren (2003), see Figure, 2.1). The shadow angle applied was 24.0° taken from the most extreme runout observed in the field. The shadow angle projection is then taken from the base of the surrounding cliff sections in the Heathcote Valley. This indicates that the simulation results are in good agreement with the shadow angle method for predicting rockfall runout areas. Indeed while the shadow angle method predicting rockfall runout is of great use, it is lacking in providing the information of the dynamic behaviour of the potential rockfalls that a numerical simulation model can provide.

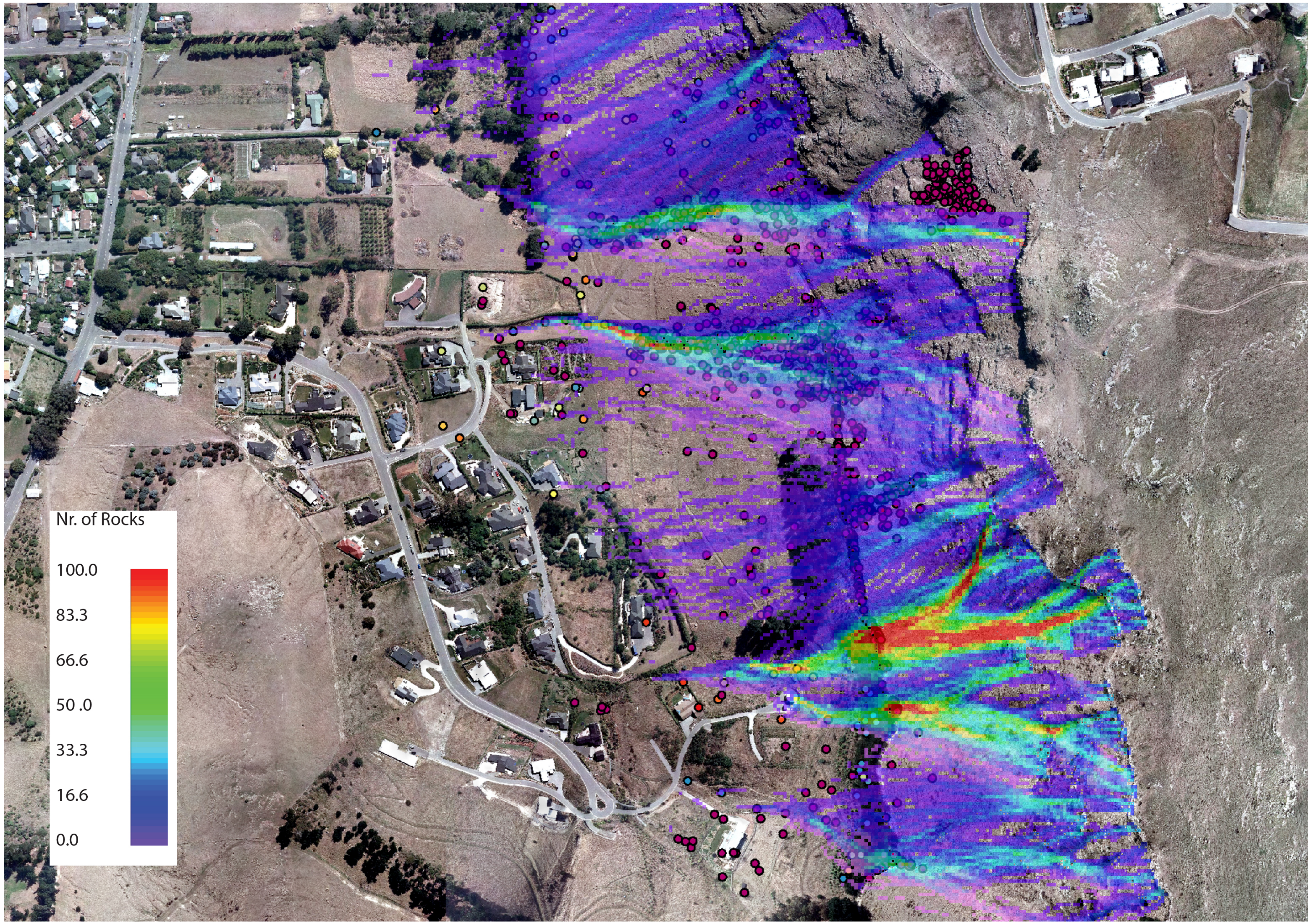

FIGURE 5.34: Map of the Heathcote valley rockfall simulations presenting the number of rocks passing through each (2.0 x 2.0 m) grid cell of the simulation domain. The legend indicates the number of rocks according to the grid square colour.

The number of simulated rocks that landed in each of terrain grid squares is counted and presented in Figure 5.34. Figure 5.34 illustrates the effects of terrain topography acting as channels and concentrating many of the rockfall trajectories into the gullies and terrain traps. Only a small portion of the entire simulated rockfall trajectories make it past the terrain traps and onwards towards the residential property. Although these events are few, it is evident from this case study that it is exactly these extreme events that have caused the most damage and disturbance to the residents of Heathcote Valley.

A noticeable feature of all the extreme events that make it past the terrain traps is the nominally straight nature of their trajectories. Along with a straight runout path, the trajectories can often cross-cut the topographic fall line. Contrasting this and reflecting the majority of trajectories which become stuck in the terrain traps, their paths are tortuous and often follow the fall line. With this in mind it is worthy of question as to what the dynamics are of the rocks that are causing this behaviour?

5.6.4 Dynamics of the Heathcote rockfalls

The purpose of this section is to assess if there are particular dynamics of the rocks that are responsible for the runout patterns obtained from the numerical simulations. As in the previous sections it has been seen that the runout distances are in agreement with the mapped deposits. Examining the dynamics observed in the model can assist in understanding the runout processes that may have occurred during the rockfall events, in particular the events that have lead to the longest runouts causing the most damage. Through this it is possible to identify important and hazardous rockfall behaviour.

In Figures 5.35, 5.36 and 5.37 the dynamic data of the simulation runout results are presented. Velocities (Figure. 5.35) range between 1.0 m s^{-1} and 37.0 m s^{-1}. Values are normally distributed with a mean velocity of 21.5m s^{-1} and a standard deviation of 6.4 m s^{-1}. Jump heights (Figure. 5.36) on the other hand have a positively skewed distribution, ranging between 0.0 m and 22.59 m, and on average jump heights are 6.4 m. Note that the jump height values are given here in free terrain are measured as a vertical line from the rocks centre of mass to the terrain surface, and therefore the extreme values often reflect when rocks have passed over a cliff section where the terrain naturally drops away.

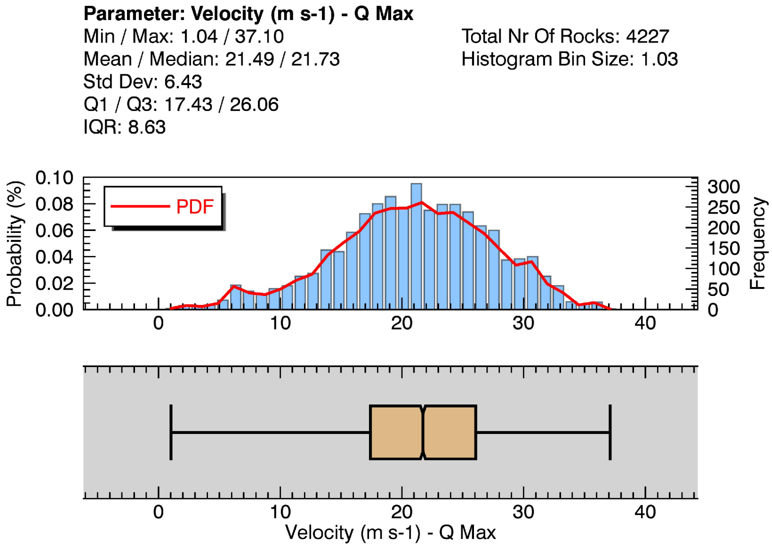

Parameter: Velocity (m s-1) - Q Max
Min / Max: 1.04 / 37.10
Mean / Median: 21.49 / 21.73
Std Dev: 6.43
Q1 / Q3: 17.43 / 26.06
IQR: 8.63

Total Nr Of Rocks: 4227
Histogram Bin Size: 1.03

FIGURE 5.35: Distribution of the maximum velocities attained by each trajectory within the simulation sample ($n = 4227$).

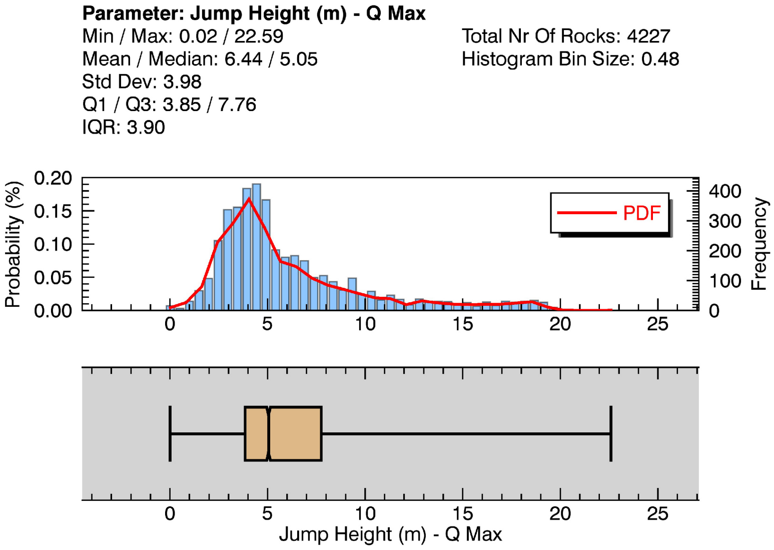

Parameter: Jump Height (m) - Q Max
Min / Max: 0.02 / 22.59
Mean / Median: 6.44 / 5.05
Std Dev: 3.98
Q1 / Q3: 3.85 / 7.76
IQR: 3.90

Total Nr Of Rocks: 4227
Histogram Bin Size: 0.48

FIGURE 5.36: Distribution of the maximum jump height (m) attained by each trajectory within the simulation sample ($n = 4227$).

Angular velocities are on average 30.0 rad·s^{-1} with a maximum of 82.0 rad·s^{-1} (Figure. 5.37). The distribution is bi-modal with a low angular velocity peak around 9.0 rad·s^{-1} and the higher angular velocity peak around 35.0 rad·s^{-1} which reflects the main data set (Figure. 5.37). The bi-modal split in the overall angular velocities can reflect the different rock shapes that were used to simulate the rock shapes and size distributions recorded in the field. Also this can reflect different modes or rotational motions preferred by each rock-shape.

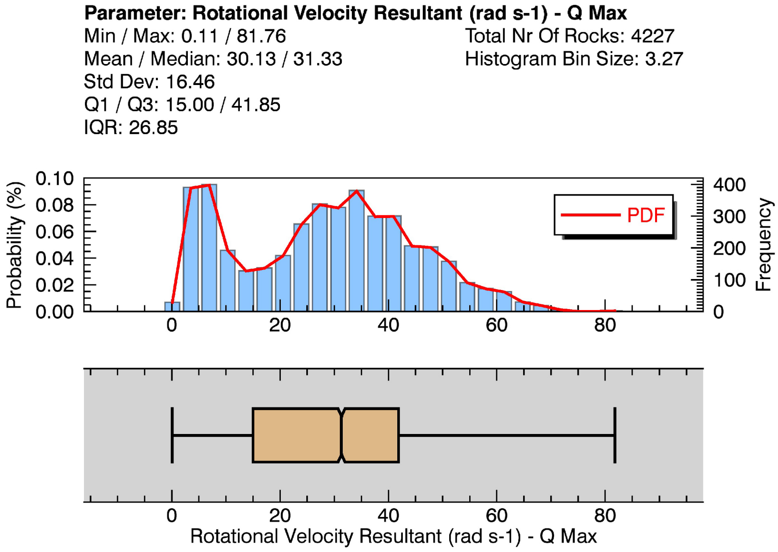

FIGURE 5.37: Distribution of the maximum angular velocities attained by each trajectory within the simulation sample ($n = 4227$).

5.6.5 Mechanisms of runout

In order to examine the observed runout patterns and dynamics that are responsible for the long runout distances, individual trajectories from the simulation series were investigated in closer detail. A sample of set of the trajectories that could be identified as having long and straight runout paths was selected, in addition to simulations where the rocks had tortuous paths and came to a rest further up slope.

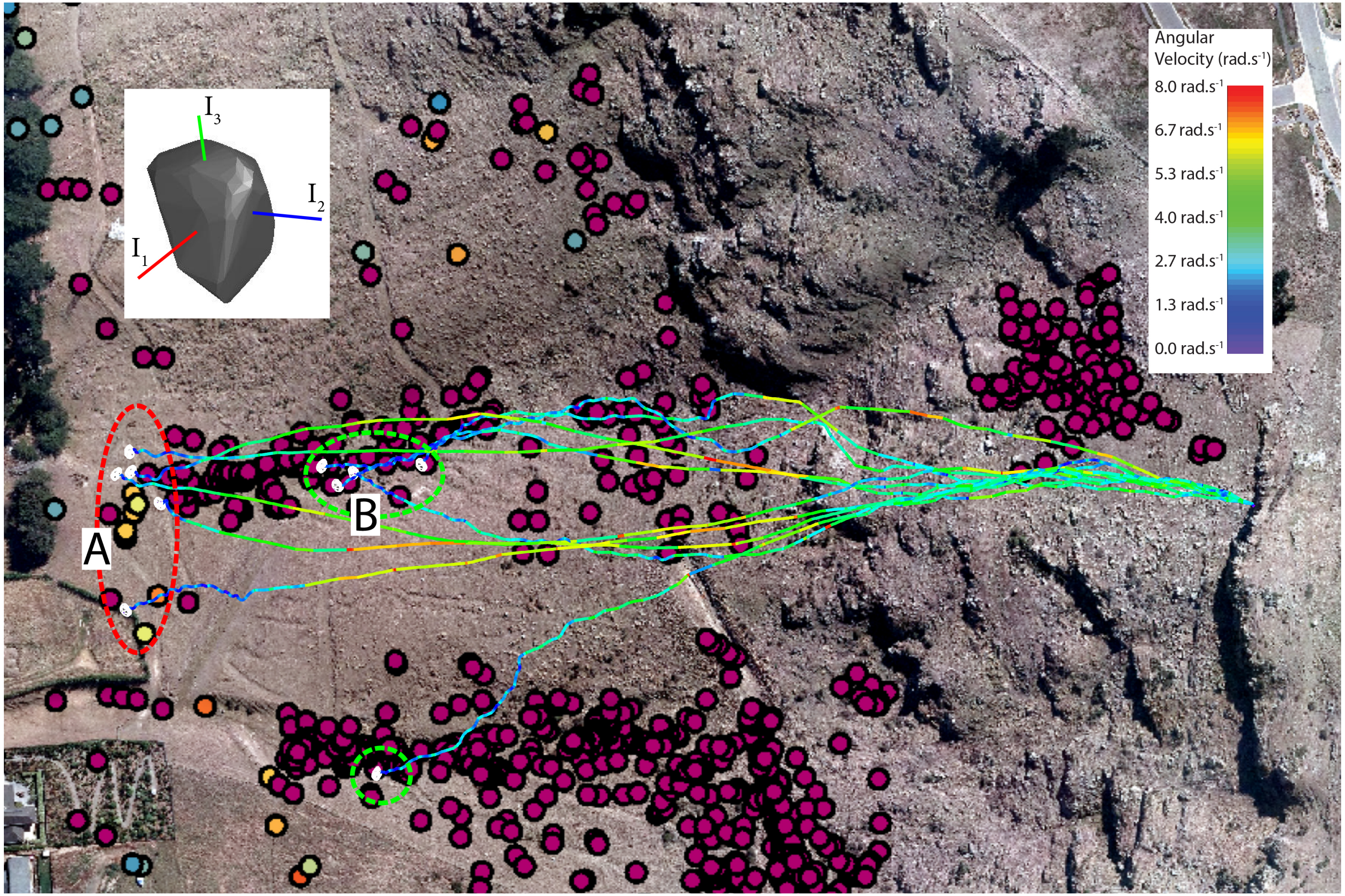

FIGURE 5.38: Simulation trajectories which show the two main rockfall runout cases *A* and *B*. Five examples of the type *A* runout paths have been selected and are circled in the dashed red line. The type *B* are circled in the green dashed line. In this particular plot the angular velocities are presented and colour the trajectory lines according to the magnitude of the angular velocity which is indicated in the legend. The red dots on the map are the locations of rock deposits from past rockfalls that were mapped from the orthophoto.

Of the simulations two main types of runout behaviour could be identified, type A runout and type B runout. Some example simulation trajectories are identified in Figure 5.38, and have been selected from the same release location using the same rock shape and size. Type A are the extreme events that follow a nominally straight path, can cross-cut the topographic fall line, runout the furthest and in most cases beyond collections of deposits in the gullies and terrain traps. Commonly type A runout paths show a tortuous track during the final portion of their runout path as their velocity slows. Type B reflect the majority of the rockfalls, mostly have tortuous runout paths throughout runout, do not runout the furthest and commonly are trapped in terrain features such as gullies and steps. Type B runout trajectories have kinetic momentum that is generally lower than type A.

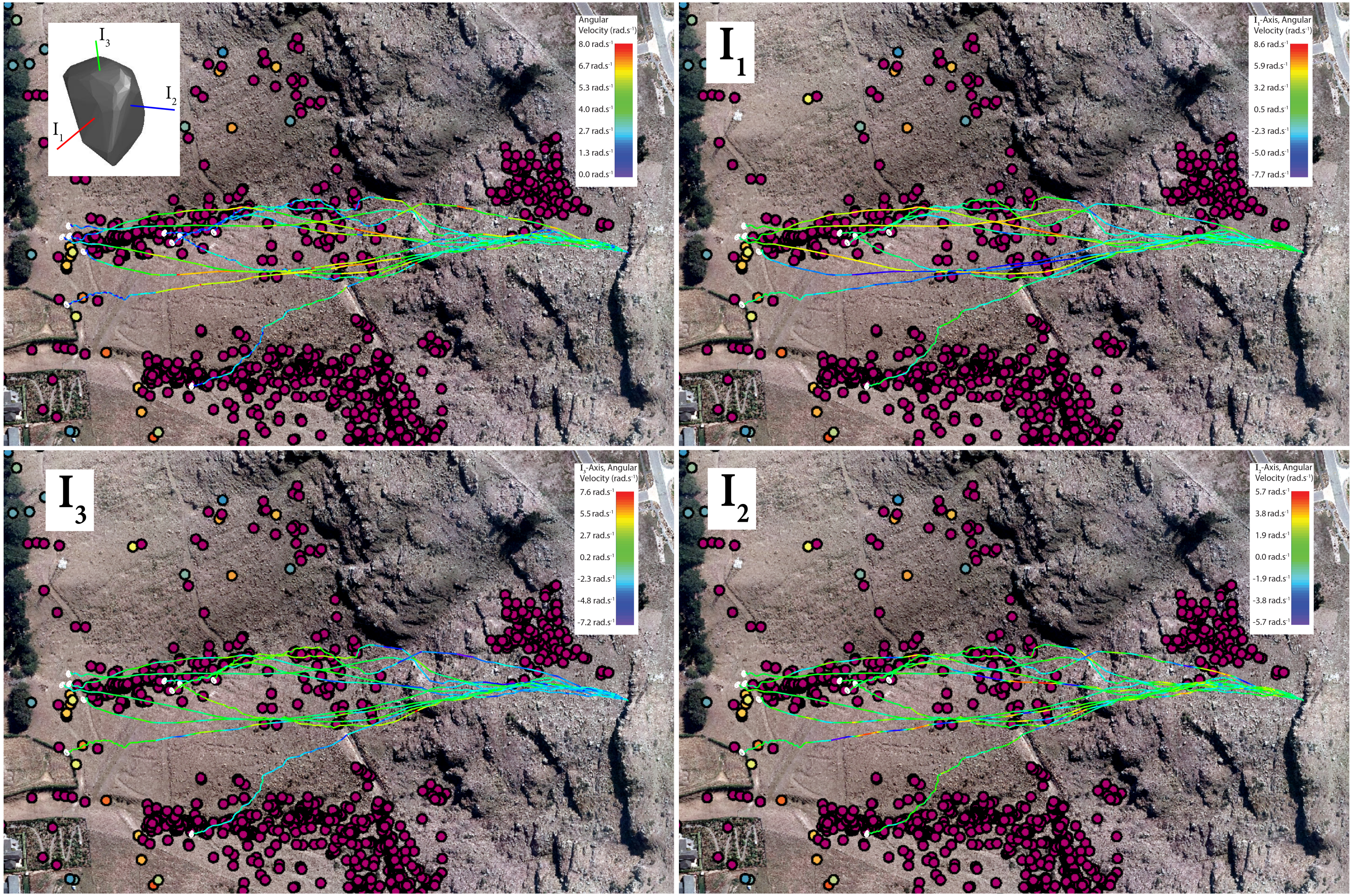

FIGURE 5.39: Maps showing the angular velocity of the rock about each principal axis of inertia.The red dots on the map are the locations of rock deposits from past rockfalls that were mapped from the orthophoto.

In order to investigate the reasons why there is a noticeably higher kinetic momentum in runout type A cases compared to type B, the rotational activity about each principal axis of inertia were mapped. This assisted in identifying the preferred axis of rotation for runout modes A and B. Figures 5.39 display the angular velocity of each principal inertial axis of the rocks inertia tensor. It can be seen that type A runout events are dominated by rotations about I_1 and I_2, while runout events of type B are dominated by rotations about I_3. This gives an indication as to the mode of motion during runout.

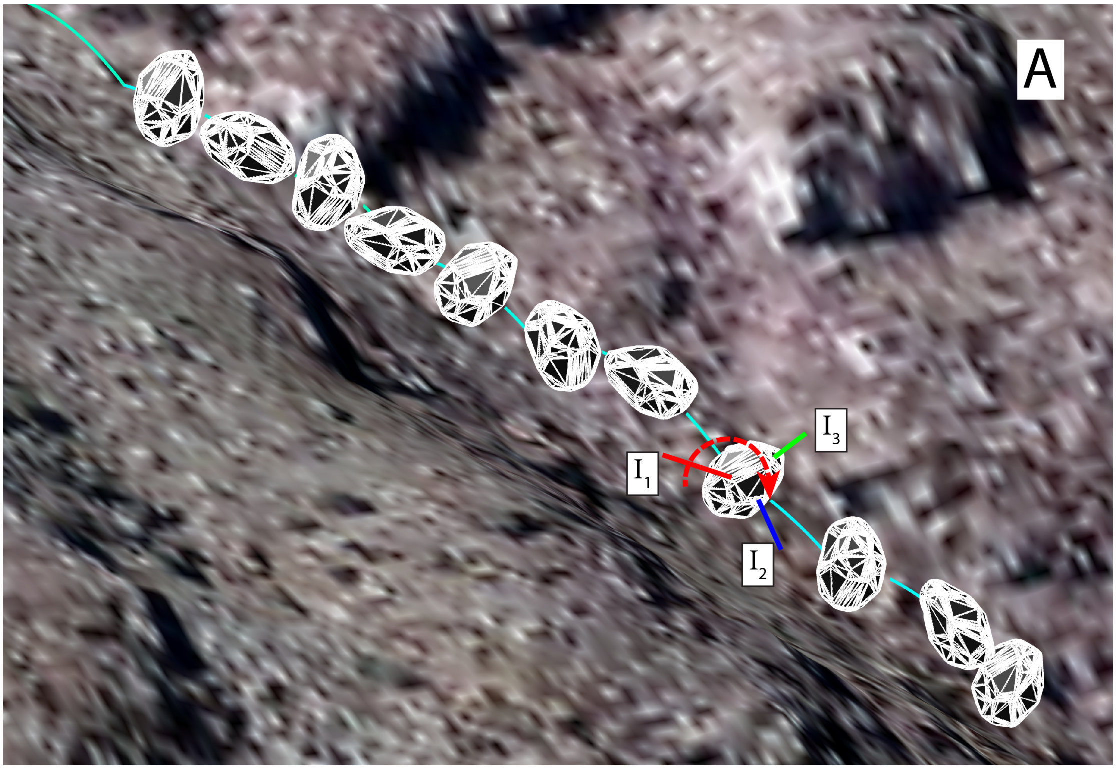

FIGURE 5.40: Rockfall simulation involving runout type A, rotations are focused about the largest axis of inertia. The rock is elongate and is travelling end over end standing up in its tallest position. The red dots on the map are the locations of rock deposits from past rockfalls that were mapped from the orthophoto.

Within the rockfall model individual simulations of type A and type B runout dynamics can be closely studied using the animation function of the model to observe how the rocks are rolling over the terrain. It can be seen that type A had a tendency to stand up on end and rotate about the axis of greatest inertia I_1, in particular for the *elongate* rocks (Figure. 5.40). While type B had a tendency to rotate about their axis of smallest inertia I_3 (Figure. 5.41). These features of rockfall runout motion were also identified in the physical experiments (Chapter 4, Section 4.7).

With respect to the rock's dynamics during runout there is a clear difference between

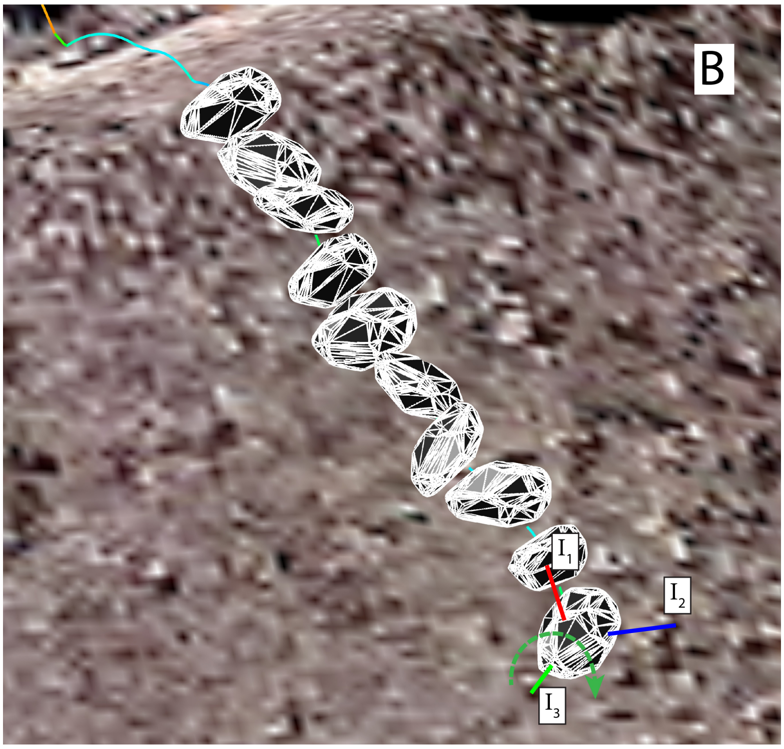

Figure 5.41: Rockfall simulation involving runout type *B*, rotation is centred about smallest axis of inertia. The rock can be seen to *wobble* off axis from side to side.

A and *B* types modes of runout. Figure 5.42 displays their runout trajectories coloured according to magnitude of angular and translational velocity, jump height and total kinetic energy. It is clearly shown that type *A* runout events runout with dynamics that are of greater intensity than type *B*. Higher values of angular and translational velocity along with jump heights are observed for the straight portions of the type *A* runout paths, this shows that for runout type *A* to be established and maintained, high momentum is required. It is shown that in this runout state rocks are capable of producing long runout with high kinetic energies that in many cases surpass topographic hindrances such as gullies and terrain traps as well as cross-cut the topographic fall line.

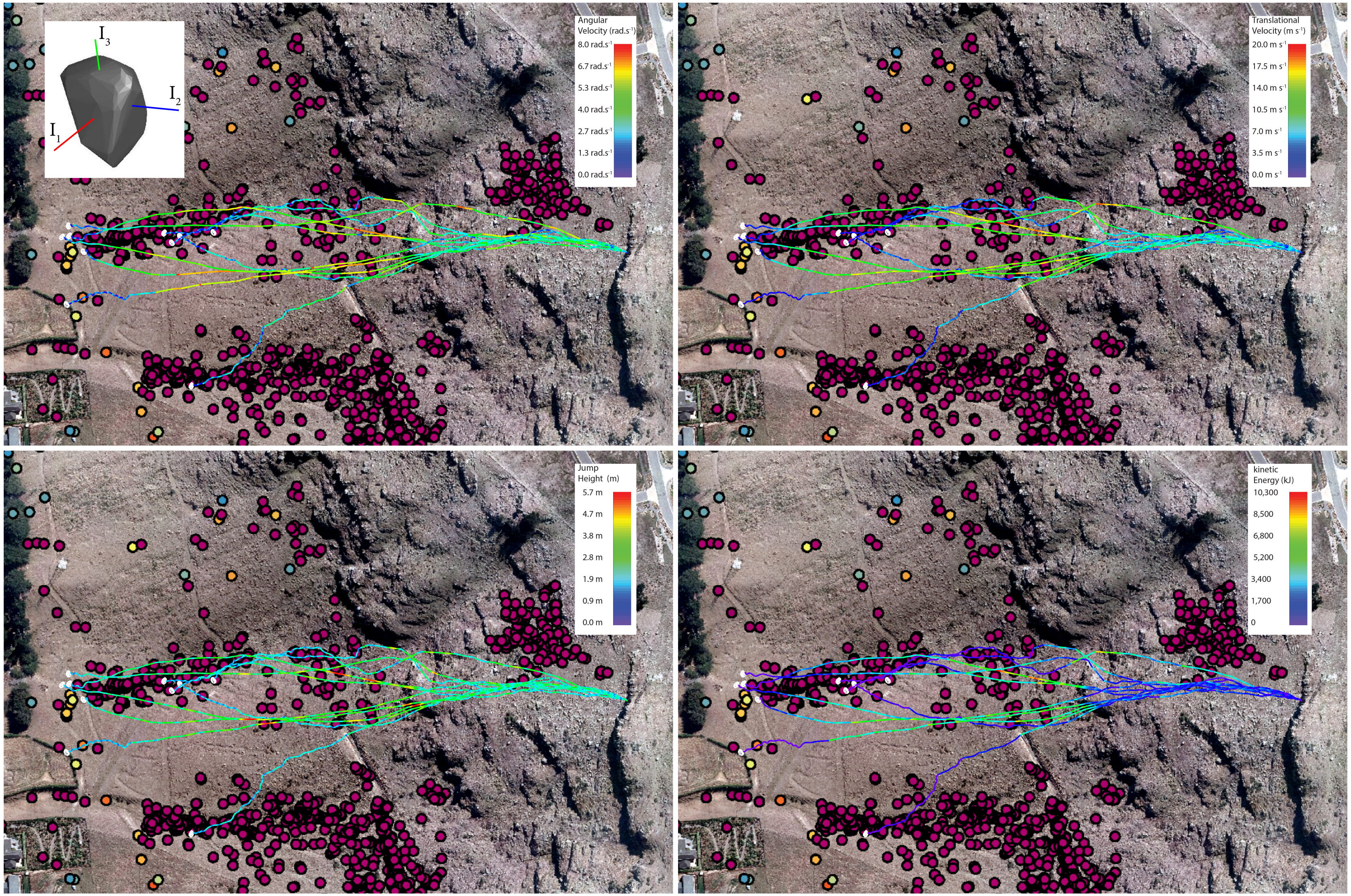

FIGURE 5.42: Comparison dynamic data of A and B type role out modes. *Top left*: Angular velocity. *Top right*: Translational velocity. *Bottom left*: jump height. *Bottom right*: Kinetic Energy (kJ). The red dots on the map are the locations of rock deposits from past rockfalls that were mapped from the orthophoto.

Importantly, it should be noted that while type A runout events are those that reach the farthest from the release zone with the greatest kinetic energy, and represent the extremities of the inundation area that form the rockfall shadow line, of the entire number of simulations, they represent only a small portion of the runout events. This can be seen in Figure 5.34 plotting the number of rocks found in each grid square of the simulation domain. In this respect the type A long runout events can be considered as extremes.

5.7 Summary and key findings

Applying the rigid-body rockfall model to back calculate the physical experiments has permitted a validation of the model and justified its application as a simulation domain to investigate further aspects of rock-shape in rockfall dynamics. The following key findings with the rockfall model were possible.

- The parameter study has revealed how the rate and magnitude in application (κ) and release (β) of friction to a contact of the rock's exterior surface with the ground is responsible for the interchange between translational and rotational kinetics and generation of rock jumps. This behaviour is responsible for the counter intuitive observation that with increases of the magnitude and rate with which friction is applied, rockfall runout distances are seen to increase. This point shows that the rotational and launch dynamics that are imparted to rocks during ground contact are more important to a rocks runout potential and mode of motion than friction alone. This is related to rock-ground contact time. In cases where friction is low the rocks commonly enter sliding and thus have long rock-ground contact periods for friction to act on the rock body and retard runout. Higher friction events better convert contact forces into angular velocity and assist departure from the slope surface effectively, reducing rock-ground contact time and producing angular velocity which promotes runout.
- Back calculations of the physical experiments have provided a model validation. Both runout patterns and dynamics have shown a good correlation with the physical data. Discrepancies between modelled and simulated results highlight the importance of correctly selecting the spatial impact condition and the question

of sample size. This is of particular pertinent of rockfalls where decisions about modelling parameters have to be made with limited historical data. The question is, how many rockfall simulations are required to represent the full spectrum of rockfall behaviour?

- The numerical simulation results have revealed that there are a number of preferred runout modes for each rock-shape. This is reflected in the multi-modal velocity and angular velocity distributions indicating that each rock as a number of runout speeds and rotations. This is likely to be attributed to the initial release orientation. *Equant* rocks are on average the fastest, while non-equant forms are slower, with the slowest being the elongate, whereby they demonstrate greater variability and present more cases of extreme behaviour.

- Apparent restitution coefficients calculated from the simulated trajectories shows they are, on the whole, in agreement with the measured data. R_n values show an increase in maximum and variability with increasing length of the principal inertial axis. However, there is a large amount of noise generated in these data, producing unrealistic values. This noise has highlighted the fundamental problem with defining the moment to sample pre- and post-impact velocities used to define apparent restitution coefficients, especially for the multiple and discrete contacts in simulation results that compose an entire rebound.

- Experiments with variable sphericity show that with increasing sphericity, angular velocity increases while jump heights decrease.

- Applying the rockfall model to real world examples of road-side rock cuts and rockfalls from cliffs in to open slopes has demonstrated the validity of the rockfall model for hazard analysis. The model predicts the runout patterns recorded in the field. It shows a common feature of rockfall where dominant terrain features such as gullies and terrain traps influence the main part of rockfall trajectories causing deposits to collect in this region. However, there are a number of rocks which escape these regions, running out further and overcoming the main influence of morphological terrain features. It is shown that such runout events are extreme event and occur due to particular motion dynamics that are established which promote stability of the rock bodies causing them to high kinetic momentum and follow a straight path.

Chapter 6

Discussion

In this thesis physical experiments were performed in conjunction with numerical modelling to investigate the role of rock shape in ground-rock interactions and rockfall runout. This work has revealed that any departure from an *equant* rock with high sphericity results in an increased variability of the runout dynamics and behaviour. This variability exists through all stages of the rockfall motion, starting from the 1^{st} impact to the runout zone. This geometric component gives rockfall dynamics its distinctive character for unusual events that are difficult to predict and mitigate. These findings are discussed in the context of current scientific literature and rockfall management practice. This chapter discusses the following key themes of rockfall runout dynamics in detail:

- The role of rock-shape in defining rockfall runout paths and the rockfall affected area, treating the implications of this for hazard management in the context of comparable scientific and engineering literature.
- The observed runout dynamics, in particular rebound mechanics, comparing this with the generalised apparent restitution model that has been widely used to predict the runout behaviour of rockfalls in models.
- The characteristic patterns and modes of rock motion derived from the experimental data of each rock shape, which links the mechanics of single rock-ground rebounds to their resultant runout path. This is discussed in the context of literature that deals with rockfall runout behaviour and modelling.

6.1 Runout trajectories and deposit patterns

Delineating the potential runout and inundation area of a rockfall zone is the primary task in rockfall hazard mapping. Empirical methods of estimating the runout zone, such as the shadow angle (Evans and Hungr, 1993, Dorren, 2003) are based on the statistical evaluation of the furthest runout blocks in a deposit zone from mapped historic events. The effect of particle size on runout length is well-known with many authors documenting size sorting effect of increasing runout distance with boulder size on rockfall scree and talus slopes (Copons et al., 2009, Evans and Hungr, 1993, Okura et al., 2000, Statham, 1976). While many authors report this fact, there remains a high degree of scatter in their data (Copons et al., 2009), suggesting other factors influence this process. The physical and numerical experiments in this work have clearly illustrated that rock shape is of key importance to runout distance and deposit patterns of rockfalls. It was found that *equant* forms were the most mobile, running out the farthest both slope-normal and laterally (Figure. 4.5), followed by the *elongate*, and then the *platy* rocks. This demonstrates that size alone cannot be used to determine runout potential of a rockfall zone.

Two explanations of rockfall particle size sorting are argued in the literature: i) larger rocks have greater mass and therefore kinetic energy to push past obstacles in its path; and, ii) particle sizes that are larger than the length scale of slope roughness are able to bridge the undulations and divots without getting caught, effectively smoothing the terrain (see Statham, 1976, and references therein). In the physical experiments of this work the influence of changing terrain roughness and material properties were neutralised while the rock-mass was held constant, and still there are marked differences in deposit patterns and dynamics according to rock shape. In terms of runout (Figure. 4.5), the mean distances were ranked by *equant, elongate* and *platy.* This shows that the mobility of a particle is related to its ability to maintain motion, and that a particle with equal axes of inertia is the most mobile compared to those with contrasting magnitudes of inertia. This suggests that runout potential is more related with the ability of a particle to maintain momentum, and that the mode of particle motion is an important factor in this.

The work of Fityus et al. (2013) alludes to the notion that different geologies of unstable rock-masses can produce characteristic rockfall activity. Additionally Statham (1976) reports differences in particle size runout distance relationships between study sites of contrasting geology. It is well known that the rock-mass character predetermines block shape and size (Calcaterra et al., 2010, Jaboyedoff, 2011) (Figure. 2.15), and thus, the runout distances and deposit patterns according to the different rock-shapes found in this work support this notion. Moreover, it suggests that particle shape generated by the two differing lithologies of Statham (1976) may have been a contributing factor to his observations.

6.1.1 Lateral dispersion of rockfall runout

A second feature in addition to runout distance observed in both physical and numerical experiments, was the lateral dispersion of rockfalls. This is important because, along with runout distance, this helps to define the inundation area of a rockfall zone. Although both physical and numerical experiments were performed on a planar slope with a single and straight fall line, each rock shape recorded lateral spreading of the test rocks from the point of release (Figures, 4.2 and 5.8). This observation alone brings into question the approach to rockfall modelling which assumes a rock will follow the path of steepest descent over terrain (e.g. Dorren and Seijmonsbergen, 2003, Van Dijke and van Westen, 1990). It is clear that the lateral dispersion of rockfalls is a dominant feature of their behaviour that should not be neglected in rockfall modelling.

While rock shape has demonstrated its key importance in the lateral dispersion of rockfalls, it is well known that topography also has a dominant role in determining the deposit locations of falling rocks. Terrain characteristics of morphology and roughness are the two main influencing factors. It is common knowledge that terrain features such as gullies and depressions act to channel and collect rocks as they runout, and was a feature of the field observations and numerical results in the New Zealand case study (Figures, 5.28 and 5.38). However, it was also observed that extreme runout events are those that are able to surpass such features, often cross-cutting the topographic fall line (Figure. 5.38). This aspect of rockfall appears to have much to do with the dynamics that a rock is capable of generating during runout, and is discussed in the following two sections (Sections, 6.3 and 6.2).

The terrain roughness is the second factor that can influence the dispersion of rockfalls. Roughness was explicitly excluded from this study, while many authors have explored the importance of terrain roughness in rockfall; e.g. Bourrier (2008) for single impacts, and Crosta and Agliardi (2004) for deposit patterns. In the work of Crosta and Agliardi (2004) the authors applied a numerical model to investigate the effects of surface roughness on the lateral dispersion of rockfalls using the ratio (W/L). Their experimental simulation domain was also a planar slope, as in the physical and numerical experiments of this study, while they used a spherical body and thus the effects of rock shape were neglected. They found that with increasing surface roughness dispersion increases, recording maximum dispersion values of $W/L = 0.4$. The values recorded in this work are comparable to those of Crosta and Agliardi (2004), indeed they fall within dispersion distributions of the physical experiments (see Figure 4.5). However, in the work of Crosta and Agliardi (2004) only a single value is given for dispersion, and this gives no idea of the likelihood of a rockfall reaching the extremities of an inundation area. The dispersion distributions of the physical experiments show peaks that are centred around low dispersion ($W/L = 0$), their inner shoulders give values that cover the range of values reported by Crosta and Agliardi (2004), while in all cases there are extended tails (with low probability) to the distributions, producing cases with high dispersion up to $W/L = 1.0$ (Figure. 4.2). This shows that such high dispersion values are possible, albeit unlikely. What this work has not covered is how the combined effects of rock shape and changes in terrain roughness might affect runout behaviour. It is anticipated that there will also be a distinct influence of the rock size relative to the terrain roughness that could also be explored in these studies. Whereby the greater the rock size relative to the terrain roughness the lower the influence of the roughness might be on runout.

An important feature of the measure of lateral dispersion in these experiments is that the value enables an assessment as to which side of the fall line the test rocks deviate. In all cases the peaks centre very closely around $W/L = 0$, while mean values do indicate slight tendency for deposits to favour either the left or the right side of the fall line (Figures, 4.2 and 4.11). There is no discernible trend that would suggest there may have been a bias (i.e. slanted slope) in the experimental set up. Under ideal conditions it is expected that a planar slope would produce distributions perfectly centred about the topographic fall line. A result indicating a slight tendency to the left or the right in these physical experiments is most likely to be a feature of the sample size selected, the back calculated numerical experiments have distributions that are more tightly centred (Figures, 5.7 and 5.8). In the work of Crosta and Agliardi (2004) however, all runout paths are weighted to the right and travel diagonally across the planar slope they generated. Because they used a perfect sphere which can only be influenced by surface roughness imposed onto their terrain model, this unexpected result is most likely to be a feature of how they induced the terrain roughness numerically. This fact underscores the dangers of attempting to induce variability and dispersion of rockfalls by artificially forcing features into terrain, or even stochastically changing terrain impact parameters (Bourrier et al., 2009b).

The experiments conducted in this work have looked at the role of rock form and sphericity in determining the runout trajectory of a rockfall on a planar slope. The numerical experiments exploring particle sphericity (Chapter 5, Section 5.4) found that with increasing sphericity there is a reduction in lateral dispersion (see Figure, 5.19) for runout on a smooth planar surface. Thus, there appears to be a close similarity between a smooth, spherical rock impacting a rough surface and an irregular shaped rock impacting a smooth, planar surface. The dispersion factors found in the physical experiments were shown to be governed by three main factors: i) slope angle; ii) the rock shape; and iii) release orientation. Similar to the work of Crosta and Agliardi (2004), this work finds a decrease in overall dispersion was observed with increasing slope angle. The numerical tests with the spherical rocks cannot be substituted to model rockfall in real terrain as the runout distances are not comparable. Moreover, spherical rocks continue rolling on an inclined plane and therefore ad-hoc stopping thresholds are implemented to stop them.

6.2 Modelling rockfall rebounds, apparent restitution coefficients and going ballistic

The main purpose of investigating rock-ground rebounds was to explore the influence of rock shape on this process. There has been much focus and attention in scientific and engineering literature on defining apparent restitution coefficients to model rock-ground rebounds (Chapter, 2, Section 2.5). This is mainly because rebound rockfall models which employ apparent restitution coefficients have been the common standard in rockfall modelling and engineering practice. It has been recognised that these values should be treated stochastically (Bourrier et al., 2009b), while a true understanding how to model this stochastic behaviour has been lacking, and an assessment whether it is actually realistic to average restitution coefficients to represent impacts on a terrain surface.

The results of this work have revealed a fundamental problem with the mathematical description of apparent restitution coefficients, rooted in the method of defining rock-ground contact periods of a rebound (Chapter. 3). The methodology for measuring apparent restitution coefficients of natural and controlled rockfalls can in itself induce great variability in the results, let alone the naturally occurring variability induced by material properties, terrain geometry, rock geometry, dynamics, and impact configuration.

Thus, the purpose of recording individual rock-ground rebounds was to quantify the variability of rebound behaviour and to gain insights into the mechanics of the process which can explain the variability, in particular considering the influence of rock-shape. This section discusses these findings in the context of past research that has focused on defining and quantifying apparent restitution coefficients, and the implications of this variability that has been observed.

6.2.1 Measured apparent restitution coefficients

In the analysis of the apparent restitution coefficients of the test rocks in the physical experiments an important distinction was made between: i) the first impacts (those which followed the initial period of free fall); and ii) rock-ground rebounds which occurred during runout. A general and important observation that can be made between the two datasets is that apparent restitution coefficients (R_t, R_n) of the first impacts all occur within the bounds of unity (i.e. $R_n, R_t < 1$ (see Figure 4.17)). This is within the bounds of R_t and R_n values reported commonly in literature (Labiouse and Heidenreich, 2009, and references therein). Whereas, apparent restitution coefficients measured during runout commonly exceed unity, R_n are on average above $R_n = 1$ and also generate very high restitution coefficients, in some cases reaching $R_n = 6.0$ (see Figure 4.18). It could be argued that this is a feature of the partly elastic nature of the wooden surface used in the planar slope of the physical experiments. However, it has been shown in this work that this is also a feature of how the restitution coefficients are measured with respect to the centre of mass and not the point of contact with the slope. When averaging the velocity of the impact over the centre of mass and decomposing it into normal and tangential velocity components, there can be situations where the normal velocity vector of the centre of mass is zero with respect to the impact surface. Through the mechanics of the impact as illustrated in this work, where edge points become pinned in the surface and a levering action projects the rock into rebound, it is then possible to induce a sudden and rapid change in velocity of the centre of mass. If this is computed into a restitution coefficient, the result is a very high value. See also (Vijayakumar et al., 2012) for a good description of this effect, who demonstrate this with a 2-D model. Currently, such high restitution coefficients are labelled "*extreme*" restitution coefficients in the literature (Buzzi et al., 2012) because it is not expected that restitution coefficients can exceed unity, as energetically this would be physically impossible. However, the restitution coefficients reported in this work and commonly applied in rockfall modelling are considered in terms of velocity. In this case such *extreme* R_n values reported from the physical experiments are highly plausible and are in range with those reported in literature (Bourrier et al., 2012, Buzzi et al., 2012, Cross, 2002, Spadari et al., 2012).

The simple distinction between apparent restitution coefficients recorded from first impacts and those during runout highlights the fact that the impact conditions determine the result, and not the terrain materials alone. Many studies investigating apparent restitution coefficients have employed simple drop tests (see: Chau et al., 2002, Haron and Ismail, 2012, Labiouse and Heidenreich, 2009, and references therein) attempting to provide averaged reference values for a given terrain material, or those pre-setting the impact condition with either rotational velocity or impact angle (Buzzi et al., 2012, Carré et al., 2006, Cross, 2010). Indeed, pre-conditioning the impact allows for experimental repeatability, and can reduce the experimental effort required to capture such measurements. Moreover, this has been seen in the results of Figure 4.17, and could have been used to characterise the runout behaviour of the experiments. However, it is clear that results fall into a confined range associated with the given impact condition. This illustrates the dangers of attempting to parameterise apparent restitution coefficients with the use of a single impact condition experiment and renders the pursuit of averaging representative restitution coefficients ineffective unless the full range of impact conditions is considered to gain a measure of the variability of the rebound process. The data of impacts recorded during the runout phase are clear testimony to the fact that the conditions of each rock-ground impact are highly variable.

6.2.2 Apparent restitution coefficients: measurement and definition

From video analysis of these experiments and observations of live rockfalls, it is evident that rock-ground rebounds are not always ideal single percussional events that best suit the definition of an apparent restitution coefficient. Often a contact period can involve a number of contacts, impacts, sliding and rolling phases (Figure. 6.1). It is common that a rock enters long period of downhill rolling and then suddenly catches an edge launching it into a ballistic trajectory. This exemplifies an extreme case in which the definition of a rocks rebound from the terrain surface cannot be predicted with the apparent restitution model. In such cases *extreme* R_n values are highly likely. This is because apparent restitution coefficients are defined by the velocity of the rocks centre of mass taken from the slope normal and tangential directions. In the case of a rolling rock entering into a ballistic trajectory, the situation arises where the pre-impact slope normal velocity is near zero, while the post-impact slope normal velocity is large resulting in *extreme* R_n values. This has been shown to be amplified when measuring the apparent restitution coefficients of rock-ground rebounds generated with a rigid-body rockfall model (Figure. 5.15), mainly because of the discrete time-stepping possible with such models.

Another important factor in the problem of the definition of apparent restitution coefficients, especially when considering that velocities are measured for the rocks mass centre, is that as soon as there is a departure from a perfect sphere, the velocity of the rocks mass centre is automatically variable through a contact phase if rotation is involved. This is a geometric shape feature that arises from the position vector r_i, (see Figure. 3.11), describing the location of a body's mass centre relative to the exterior rock-ground contact point. With this in mind, if a body's mass centre is tracked as it is rolled over a flat surface, the position of the mass centre will remain at constant height if the body is a perfect sphere, as r_i is in this case a constant. As soon as a different shape is introduced, the centre of mass will begin to move position when rolled, and this occurs to a lesser or greater degree according to shape (Figure. 6.2). With increasing departure of a rock away from a sphere toward an elongate form, the eccentricity of the centre of mass trajectory when rolled over a surface increases. This is a simple geometric effect, while ubiquitous to rock-shape. The position vector r_i can be considered as a moment arm. Because it is in this configuration of a fixed outer point that generates the

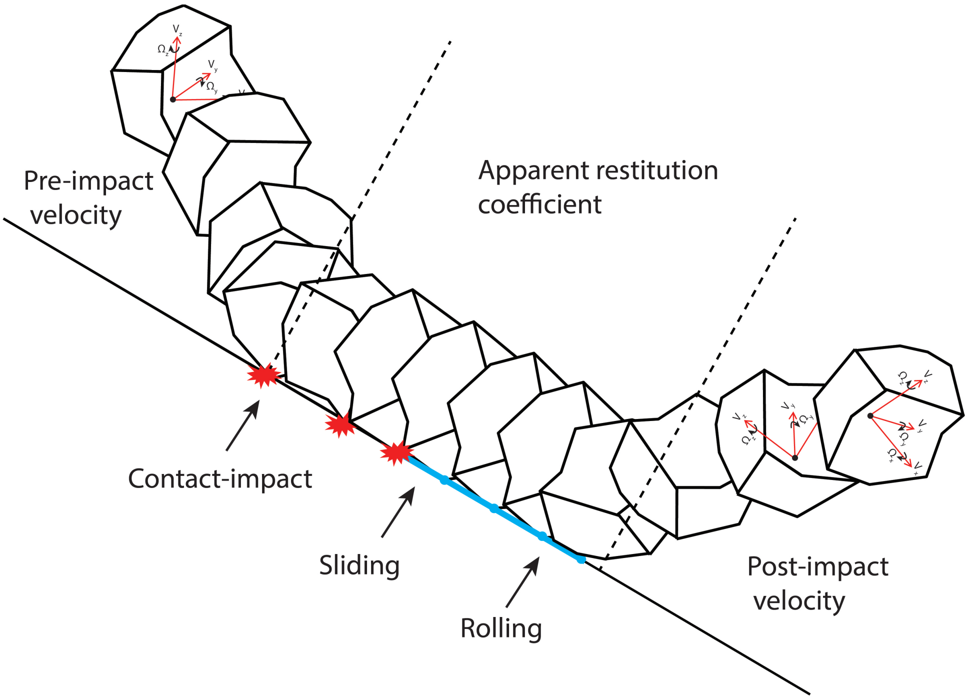

FIGURE 6.1: Sketch of full rock motion bundled into an apparent restitution coefficient. The ratio between the pre- and post impact velocities of this rock-ground contact event would represent the apparent restitution coefficient for this event. It consists of edge contacts sliding and rolling over a distance.

moment arm I_i, of length r_i and magnitude according to the body's mass distribution, that defines the work that must be done to lift the centre of mass in such situations. If considering the position vector r_i, during an impact it is a moment arm I_i which can lift the centre of mass.

6.2.3 Rebound mechanics, restitution coefficients and jump heights

The position vector r_i is an important factor in rock-ground rebound mechanics, due to the magnitude of the moment arm I_i that can be generated during a rock-ground contact. This is where rock-shape, its form and sphericity become of crucial importance in determining the rebound mechanics of a rock-ground impact. By altering the magnitude of the moment arm I_i through shape changes, one is effectively steering the amount of work that a given impact configuration must do to lift the centre of mass. It is also noted that there are periods where the mass centre is positioned in a state of free fall and is thus accelerating towards the ground. In terms of variability, if the principal inertial axes are considered, any departure from a sphere increases the contrast between the magnitudes of the principal inertial moments I_i of the body. This in itself increases

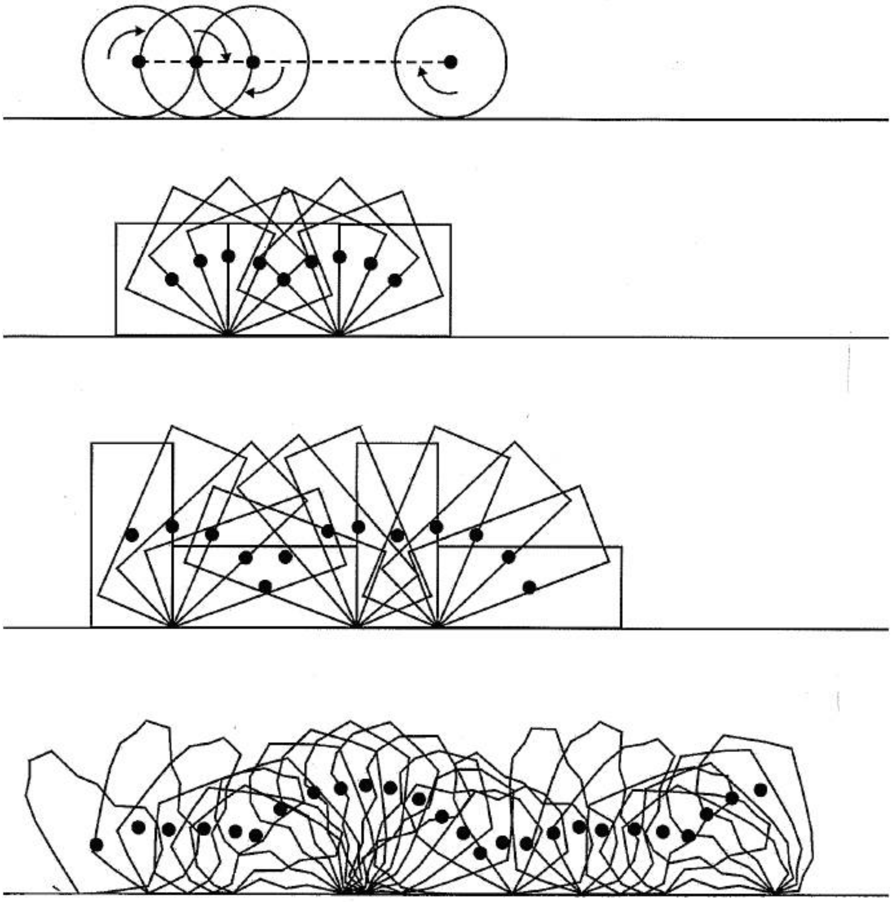

FIGURE 6.2: Sketch drawing depicting the trajectory of the centre of mass of four different shapes when it is tracked over one full rotation on a flat plane. The shapes are a sphere, a cube, an elongate cuboid and an arbitrary rock-shape.

the range of possible impact configurations and therefore the variability of a rebound. It has been seen in this work that this can 'make or break' the success of a rebound. This is an effect of rock-shape and impact configuration.

Investigating the orientation of the test rock's impact through the impact angle α of r_i in the physical experiments has shown that high jump heights f, trajectory ratios f/s and *extreme* R_n values are generated when the incident α angle is low (see Figures, 4.23 and 4.21). This observation is in accordance with the statements made by Buzzi et al. (2012). However, there is an important distinction that should be made between which incident α angle pertaining to the relative orientation of r_i, respectively the moment arm I_i at the point of contact; or the orientation γ of the absolute velocity vector $\overrightarrow{U^P}$ with the slope (see Figure, 3.11).

In the work of Buzzi et al. (2012), the authors refer to low impact angles in terms of angle γ of the incident velocity vector to the impacted surface. They suggest that with increasingly acute impact angles there is an increase in resultant R_n values. The findings of this work indicate an opposite trend. In fact, with increasing impact angle γ there is an increase in R_n (see Figure, 4.24). The observations of this work are in accordance with many other studies investigating the impacts of objects on inclined surfaces (see: Carré et al., 2004, Cross, 2002, 1999, Wallis, 1943b, 1942b), and observations of live rockfalls (Gerber and Jahn, 1989). The findings of Buzzi et al. (2012) that low angles generate high R_n values must therefore be referring to the impact configuration and the incident angle α of the position vector r_i. Because in the case of a low angle γ the force of the impact is directed closer and closer to slope parallel, the rock is more likely to enter sliding. In their work the authors correctly identify the position vector of the contact point r_i, in a coordinate frame d_x, d_y; and show the importance of angular velocity in the process of generating high rebound values of R_n, while they do not remark that it is the configuration of the impact point with the terrain in combination with the angular and translational velocities that is responsible for the mechanic that set the rebound trajectory and magnitude of the rebound.

For this rebound mechanic to occur it requires that an edge or corner point of the impacting rock becomes stuck or fixed to the terrain. This has been well-illustrated in the parameter study of the numerical model (Chapter, 5, Section, 5.2), where it was seen that by increasing μ_{max} and the rate κ with which is applied to a rock-ground contact point, there is an increase in jump heights, and respectively in angular velocity. This is in effect like a snatching action that works on the contact point when these values are high, allowing rapid transfer of translational velocity into angular momentum and the levering action required to project the rock away from the slope. Similar effects are observed by Cross (2000), and Nicolaides et al. (2013) who report that by increasing ball contact friction between surfaces and rackets, there is a marked increase in the angular velocity imparted to a ball following rebound. Bourrier (2008) also notes this effect for single rockfall impacts correlating it to an increase in terrain roughness.

Of all these observations made here, a central and key insight into the concept of a rebound is illustrated. This is that, in most cases, it is not a bounce that occurs during a rock-ground impact as it is commonly referred to in literature (Dorren, 2003, Ritchie, 1963). In fact very little if any bounce occurs during a rock-ground impact. It is the levering effect of the moment arm I_i rotating about a fixed corner point is responsible for the rock departing the ground and determining its jump height. The resultant rebound of this mechanism can be affected by both the rock-shape and terrain. For example Carré et al. (1999), and Cross (2002) show how the deformation of the ground during cricket ball impacts sets the attitude of the rebound trajectory. In rockfall this is also documented with reference to crater geometry, setting the rebound angle of the rock (Paronuzzi, 2009, Zinggeler and Pfeifer, 2009).

In the experiments of Buzzi et al. (2012) the required levering effect was achieved by introducing a terrain step, effectively a launching feature that enabled the required *low angle* α to be generated during impacts. What is observed in the physical experiments is that the lower the incident angle α and the greater the magnitude of the moment arm I_i, the more likely a high jump f, and a large high arched rebound trajectory f/s, or high R_n value are observed.

6.2.4 Impact configuration

The configuration of the position vector r_i with the slope effectively sets the amount of work that needs to be done in order to overcome the moment arm I_i, and also the potential trajectory of the centre of mass. This is because it defines if the centre of mass is in a situation climbing against gravity, or directed downwards toward the slope under a state of free fall. The rock body looses translational and angular velocity to overcome this work and launch the rock into a rebound ballistic trajectory. This indicates that there is a lift off velocity that can exist in which the centrifugal force generated by rotation about the fixed point is sufficient to cause lift off of the rock. The kinetic energy available to the rock-body to do work generating this force is drawn from the angular velocity and the translational velocity that can be converted to angular speed. This aspect of the rebound behaviour was not investigated in the analysis of this work. While this is possible from the measurements of angular velocity and impact configuration that were made, this remains future work. An important aspect of the findings related to the impact orientation angle α is that the results show a good linear correlations of the impact angle α with the arch of the rebound trajectory f/s. Low incident α angles produce high jumps, while large obtuse α produce flat f/s trajectories. Moreover, it was the *elongate* rock with the largest moment arm I_1 that produced the largest arched trajectories, while showed the greatest standard deviation and range in the data and therefore great variability (see Figure 4.15 and Table 4.2).

6.2.5 Rebound mechanics and rock-shape

An interesting observation of the experiments of Buzzi et al. (2012) is that they used different rock shapes, while they did not consider their classification. The shapes used had both differences in rock form and sphericity, using a disc, an ellipse, a square and a pentagon. Interestingly, the ellipsoid in their work had the greatest r_i length compared to the other shapes, which should have effectively produced the largest R_n values, when in fact they report the square shape as producing the largest R_n values. The difference in sphericity between the two shapes should be noted. The ellipsoid is smooth and allows rolling over contact points, while the square and the pentagon have long edges and points which can easily become stuck to cause the aforementioned rebound mechanism to occur. This distinction between the two types of rock-shape concerns the sphericity, and was investigated in the numerical experiments of Chapter 5. The results indicate that with increasing sphericity there is a reduction in the magnitude of rebound jump heights and restitution coefficients (Figure. 5.20).

In the physical experiments it could be seen that as the magnitude of I_i increased there was an increase in R_n values and jump heights (see Figures, 4.20 and 4.15). In addition there was an increase in range and variability of runout. This trend is also seen in the results of Buzzi et al. (2012), in the results comparing the square and the pentagonal shape.

A significant result that can be drawn from the point that R_n and jump heights show an increase with the increase in magnitude of I_i, is that the variability and range of this behaviour also increases in the values reported from the physical experiments. This emphasises the point that not only is it the orientation of the rock at the point of impact, but also the kinetics the rock holds at this moment. Should the angular velocity or available translational velocity be insufficient to overcome the moment arm generated by the orientation of r_i at the time of impact, then the rock body is likely to enter sliding, or could enter rolling. To this extent rock shapes with larger I_i, are by nature inherently unpredictable. Shapes with unequal magnitudes of principal inertial moments are in a dichotomous state of dynamic stability where on the one hand the success of a rebound can easily be terminated because the momentary kinetics at the point of impact is insufficient to overcome the large moment that is set by the rock- ground impact configuration. Equally, because these shapes possess large inertial moments, they have the potential to store large amounts of momentum and maintain stable and straight runout paths through a series of successive rock-ground impacts. The latter point was in fact why Wallis chose to use a cylindrical rather than a spherical shape for his bouncing bomb design. It was because the cylindrical shape could store greater momentum ensuring the greatest stability and range during the successive bounces of the bomb over water to its target (Wallis, 1944, 1943b).

It can be seen that it is the configuration of the rock position and dynamics at impact that determine the mode with which a rock will runout, it governs the success or failure of a rebound. As individual events, rebounds have been shown to be highly variable and to a large extent unpredictable. It is the combination of the series of rock-ground contacts (sliding, rolling and rebounds) that form a rockfall runout trajectory, which sum to form a rockfall affected area (see Figures, 2.3, and 2.11). In this work both the physical and numerical modelling of rockfalls has revealed that there are characteristic modes of motion and runout behaviour that can be assigned to each rock-shape which has an impact on the runout trajectories and resultant deposit inundation areas. The following section describes and defines these modes of motion that are associated with each rock-shape studied in this work.

6.3 Modes of rockfall motion

A widely accepted classification of modes of rockfall motion was first summarised in the work of Ritchie (1963), in which, from observation of rockfalls along road side rock cuts, the author was able to suggest particular slope angles at which a dominant mode of rockfall motion exists (i.e. sliding, rolling, jumping, or falling (see Figure, 2.2)). The physical experiments in this work covered slope angles from 20° - 55° with three principal rock shapes. The findings of this work are in general in agreement with these observations. However, it must be pointed out that Ritchie's proposed modes of rockfall motion are not exclusive to each of the slope angle categories suggested. In this work all modes of motions suggested by Ritchie (1963) were observed on each slope angle in the experimental series (with the exception of pure freefall). In particular, the case of rolling into sudden jumping, is mainly attributed to shape effects.

While the work of Ritchie (1963) has provided a suggestion of rockfall modes of motion according to slope angle, a description of the entire runout process is lacking. Moreover, Ritchie (1963) suggests that rock-shape is negligible, while his data are based on basaltic rock cuts from which the dominant rock form was *equant*. This section draws together the findings of deposition patterns and dynamic runout behaviour to provide a description of the runout process, to demonstrate how it is influenced by shape.

6.3.1 Initial impact configuration and lateral dispersion

From the physical experiments, the deposit mapping has shows a clear dependency of runout on rock-shape (Figure. 4.5), and equally interesting was a pronounced dependence of this result on the release orientation of the test rocks. In particular this was related to the orientation of the principal inertial axes with respect to the central fall line of the experiments (Figure. 4.9). It was found that high lateral dispersion correlated to release orientations that held the rocks with their axis of smallest inertia aligned perpendicular to the central fall line of the slope. While runout events that aligned the axis of largest inertia perpendicular to the central fall line resulted in low dispersion long runout events (see Figure, 4.11).

The fact that the release orientation produced such distinct deposition patterns according to the relative magnitude of the principal inertial axes I_i, indicates that the initial impact configuration is instrumental in setting the outcome of a runout event. This is particularly important when considering that not only does the geological condition of a rock-mass pre-determine the size and shape of detachable rocks, but also the mechanism of failure and orientation with which they enter the slope. With this it is perfectly plausible to elaborate upon the notion of Fityus et al. (2013) that rock-masses produce characteristic rockfall behaviour, and state that this behaviour is preset by both the different rock-shapes produced as well as the mode and orientation of their release.

6.3.2 Rotational behaviour and runout path

The simple observation that rockfall runout patterns and lateral dispersion is shown to be related to the rocks initial slope impact configuration generated the question as to what particular runout dynamics followed, and how this initial orientation in addition to the shape affected the ensuing runout. It is during this starting phase in the rockfall release zone that a rock will gather momentum and initiate a dominant mode of rockfall motion given the boundary conditions of the initial impact. In the previous section (Section. 6.2) it has been shown that for single rebound conditions of low α impact angles and large moment arm lead to large rebound jump heights and large R_n values, while in these impact configurations the likelihood that a rock will rebound and its magnitude are highly variable. This suggests that for runout to be persistent a state of continuing rebounds must be established in the release zone acceleration phase. Thus, what was searched for in the dynamic runout data was a state of runout stability, a condition where rock-ground impacts could continue in succession. This is because the main variable altering the orientation of the rock during a ballistic trajectory is the rock's rotational behaviour. It effectively sets the impact configuration and its variability. A state of rotational stability or instability was sought in the angular velocity measurements of the three principal inertial axes.

It is a well know physical phenomena that there are two stable inertial axes (I_1 and I_3) of a body as it rotates, while the third (I_2) in inherently unstable (see Section, 2.3.6 Figure, 2.20, and Pettit (2009)). Leine et al. (2014) show that a rotating *Plate* shaped block if left to accelerate down an infinite slope will seek a state of rotation about its axis of largest inertia. The novel high-resolution dynamic motion sensor developed in this work has facilitated the examination of the rock's rotational behaviour to investigate the concept of rotational stability and runout propagation based on the results of physical experiments. This was achieved by taking the measurements of rotational activity about each principal inertial axis and determining the most dominant axis during each runout event.

In all it can be shown that the *equant* rock had no particular preferred axis of rotation, as the inertial axes are all of equal magnitude, the *platy* rock was dominated by rotations about the largest axis of inertia, and the *elongate* was dominated by rotations about smallest axis of inertia (Table. 4.3). This shows that shapes do not necessairly end up with rotations that are dominated by the largest axis of inertia. It could be shown that for all shapes in cases where rotations were dominated by the largest axis of inertia, runout tended to be long and of low dispersion (Figure. 4.32). This is an important result because it indicates that attaining the rotational state about the largest axis of inertia promotes low dispersion. This is likely to be because there can be a large amount of rotational kinetic energy stored in rotations about this axis which can make the trajectory stable against perturbations, holding it on course. It is such events that can lead to extreme runout, which from a hazard perspective are unusual and can be catastrophic. These findings are supported with the observations of Statham (1976), who makes reference to the runout mode of elongate scree particles, noting they are most efficient and runout the farthest when skipping end over end; in this state an elongate particle is rotating about its axis of largest inertia.

The issue for non-equant rock particles is, how do they enter into this state of rotational stability? The findings of Leine et al. (2014) suggest that all bodies tend towards rotation about the largest axis of inertia. While from these experiments this can only truly be said for the *platy* rock, the *elongate* rock data provides evidence that this form seeks to be in this state but cannot always achieve it. This is confirmed by the observation that, for the *elongate* rock, when rotations are dominated by the smalest axis of inertia I_3, there was in each case no less than 10.0% rotational activity about the additional axes (see Figure, 4.32), while for the other shapes (*equant* and *platy*) rotations were often dominated by near 100% activity. This is an indication that the rock body is trying to stand up and enter rotation about the largest axis of inertia, but cannot always achieve this. This could be because the momentum is not sufficient, while also shows similarities with the classical spinning egg demonstration described by Moffatt and Shimomura (2002).

It has been shown in this work, in particular from the video evidence, that transitions between rotational axes and the mechanism of a rock-body standing up to rotate about its axis of greatest inertia can lead to a degree of instability or “wobble” in rotation (see Figures, 4.30, and 4.29). This is similar to the remarks of Pfeiffer and Bowen (1989) who suggest that it is in the transition states of rockfall modes of motion that the rock is most unstable. In addition to the analysis of the rotational velocity signal of each axis which measured the combined rotational activity to assess for order or disorder (see Section, 3.6 Chapter, 3, and Table, 4.3). This suggest that in such states of seeking rotation about the axis of largest inertia, especially if a change of rotational axes is required, this leads to a large degree of rotational instability. With high rotational instability it has been shown that this leads to the high lateral dispersion of rockfalls (Figure. 4.32).

6.4 Synthesis

The role of rock-shape in rockfall dynamics has been shown to be persistent throughout all stages of runout, from release to deposition. This is evident from the stage of individual rock-ground impacts, the rotational dynamics between the ballistic trajectories that link the impacts, and ultimately are reflected in the runout paths and deposition patterns attributed to each shape.

Of importance in determining the characteristic runout dynamics is the magnitude of the principal inertial axes and their relative orientation with the slope at impact, the impact configuration. Rock-shape changes result in contrasting magnitudes of the principal inertial moments and respectively expand the potential for variability in the impact orientation and amount of work to be done to overcome the impact phase with a successful rebound. This leads to the 'make or break' condition of rockfall rebounds, producing both impacts that directly enter sliding, and those that produce *extreme* rebound events. This is particularly the case when the rebound is measured under the apparent restitution coefficient model. The variability and range of this behaviour is exacerbated with an increasing departure from an equant spherical body.

Secondly, it can be shown that rock-shape and mass distribution being rooted in the principal inertial axes has a key bearing on the rotational dynamics of a rock body. The application of the StoneNode has facilitated the capture of the three-dimensional accelerations and rotations of a rock body. The sensor has revealed that the three principal rock forms each have characteristic rotational dynamics, and a tendency towards rotation about the largest axis of inertia. It is found that if rotations about the largest axis of inertia are established, then the rock is in its most stable and mobile state leading to long runout distances with the lowest dispersion. However, the acceleration phase following its release into the slope, along with the deceleration phase in the stopping zones are shown to be the most unstable as the rock-body is initiating or falling from a state of rotational stability. It is these *"wobble"* periods of runout that are instrumental in setting a rocks trajectory which leads to the dispersive nature of rockfall runout paths, and deposition patterns. With this, the following key statements can be drawn from this research:

1) This research demonstrates that size alone cannot be used to determine runout potential of a rockfall zone.

2) The highly variable restitution coefficients measured during this work and the influence of rock-shape on rebound mechanics underscores the dangers of attempting to induce variability and dispersion of rockfalls by artificially forcing features into terrain, or even stochastically changing terrain impact parameters (Bourrier et al., 2009b).

3) The data of impact recorded from the runout phase are clear testimony to the fact that the conditions of each rock-ground impact are highly variable. This illustrates the dangers of attempting to parameterise apparent restitution coefficients with the use of a single impact condition experiment and renders the pursuit of averaging representative restitution coefficients ineffective unless the full range of impact conditions is considered to gain a measure of the variability of the rebound process.

4) The position vector r_i is an important factor in rock-ground rebound mechanics because of the magnitude of the moment arm I_i that can be generated during a rock-ground contact. This is where rock-shape, its form and sphericity, become of crucial importance in determining the rebound mechanics of a rock-ground impact.

5) Given the clear differences in runout behaviour according to rock-shape, it is perfectly plausible to elaborate upon the notion of Fityus et al. (2013) that rock-masses produce characteristic rockfall behaviour, and state that this behaviour is preset by both the different rock-shapes produce as well as the mode and orientation of their release.

Chapter 7

Conclusions

This thesis has explored the role of rock-shape in rockfall dynamics from the detailed mechanics of rock-ground rebounds, to the resultant runout trajectories and deposit patterns attributed to rock form and sphericity. Data were obtained from an extensive series of physical runout experiments conducted on a planar slope releasing three end-member rock shapes (*equant, platy,* and *elongate*) embedded with a novel motion sensor. These experiments were supported with numerical experiments using a rigid-body rockfall model capable of simulating rock-shapes.

Rockfall is a gravity driven process that is pervasively variable which makes the task of predicting and observing runout particularly challenging. This variability exists at all stages of rockfall which can influence the outcome. These are: i) the initial release conditions; ii) the changing terrain feature, morphology and ground properties; and, iii) the rock-shape, size and strength. The abundance of potential combinations of these influencing parameters demands probabilistic data of likely events which can be associated to these characteristic parameters and makes the task of understanding the rockfall runout all the more difficult.

In pursuit of a deeper understanding of this complex process this study applied an approach which isolated and quantified the influence of rock-shape on rockfall runout dynamics. It is one of the first studies to have examined the detailed mechanics of rock-ground impacts according to rock-shape and go on to link this to the ensuing rotational runout dynamics and resultant deposition patterns of rockfalls. The concepts and findings of this work provided key insights into the nature of rockfall runout mechanics according to rock-shape, and serve to have advanced the state of rockfall hazard assessment and understanding of the morphology of rockfall deposits. This work has enabled a better inclusion of the rock-mass characteristics into the rockfall problem.

7.1 Origional contribution to knowledge

7.1.1 Rock-ground rebounds

Condensing the rock-ground rebound problem using apparent restitution coefficients and simplifying the rock description to spheres or point masses has been popularised by ease of use and application in rockfall modelling (Volkwein et al., 2011), which is understandable given the complexity of the rock-ground rebound process. However, the task of quantifying apparent restitution coefficients with sufficient rigour and quantity to capture all likely results is hampered by the shear effort and processing time required (Cross, 2002), and in most cases studies investigating rebound behaviour have been limited to single impact tests (e.g. Labiouse and Heidenreich, 2009) or large scale experiments with limited data (e.g. Dorren et al., 2006). The physical experimentation conducted with small sized rocks have enabled the capture of the high-resolution dynamic data of rockfall rebounds with sufficient quantity to statistically describe the rebound behaviour of three end-member rock shapes.

It can be shown that because of the definition of apparent restitution coefficients with respect to slope normal and tangential velocity vectors of a rock's centre of mass, the so called *extreme* restitution coefficients are highly likely. The reason for this is because the definition takes the velocity of the rock's mass centre and fails to account for the disparity in velocity between the true ground contact point and the mass centre. The observation in the literature of *extreme* restitution coefficients (Buzzi et al., 2012) and their stochastic behaviour (Bourrier et al., 2009b) is corroborated by the findings of this work. More importantly the findings of this work could show that the *extreme* rebounds and stochastic behaviour are a function of rock-shape. Any departure from a spherical body increases the variability and potential for extreme rebound events. The *elongate* rock form was shown to produce the greatest variability and range in rebound behaviour. This has strong implications for practitioners implementing rockfall models which employ apparent restitution coefficients to model rock-ground impacts.

Contrary to the popular concept of a rock *bouncing* down a slope (Dorren, 2003), the analysis has revealed that rock-ground rebounds require that the rock's edge or corner point becomes stuck or fixed to the terrain about which the rock rotates over the moment arm which is set between the contact point and the centre of mass, effectively levering the rock into ballistic trajectory. Importantly, the rock-shape is instrumental in setting the work that must be done to overcome the terrain contact. This is achieved through the contrasting principal moments of inertia according to rock-shape and the impact configuration (i.e. the impact angel α). This mechanism leads to the 'make or break' situation of a rebound. In conclusion, levering effects and the variability of the impact configuration do not allow a consistent definition of apparent restitution coefficients, and are fundamentally rooted in rock-shape.

7.1.2 Runout paths and rotational dynamics

The erratic behaviour of rocks as they runout over terrain has been particularly difficult to capture or quantify, and exists mostly as descriptive anecdotes of the behaviour. A sophisticated signal analysis of the angular velocity measurements to reveal the relative rotational activity about each principal inertial axis of the test rocks has provided a quantification of this behaviour and enabled the identification of distinctive patterns of rotation which explain the nature of rockfall runout paths. It could be shown that where rotations were chaotic and interchanging between principal axes of inertia the rock was unstable in a "wobble" state, this lead to short runout and frequently high lateral dispersion. It was found that with increasing momentum a rock tends towards a stable rotation state about its axis of largest inertia corroborating the hypothesis of Leine et al. (2014). It was shown that in these rotation states runout tended to be straight and long. While it was also shown that the phase of transition between a rotationally unstable and stable state sets the rocks trajectory and corroborates the suggestion of Pfeiffer and Bowen (1989) that transitions between modes of motion are responsible for the erratic behaviour of rockfalls. To summarise the behaviour of the three rock forms:

- *Equant* rocks have no preferred rotational axis, and cannot store large amounts momentum in rotations and are thus easily thrown off a rotation axis. Because of this, *equant* rocks are more susceptible to sphericity.

- *Platy* rocks attain rotation about the largest axis of inertia more easily, rotating like a wheel. If they attain this stable rotation state they can have long and straight runout paths. If in a state of ”wobble” they are highly erratic.
- *Elongate* rock forms have a tendency to rotate about the smallest axis of inertia, but seek rotation about the largest. Because of this they are inherently unstable and have ”wobble” motion that leads to high dispersive runout.

These conclusions, based on both the physical and numerical modelling, have led to the conceptual model of a runout trajectory which composes of three phases and is strongly influenced by rock-shape;

1. *Acceleration phase*, the rock gains momentum and is seeking rotation about the largest moment of inertia. During this phase the rock is inherently unstable; it can have ”wobbly” rotations and because of the levering effect and impact configuration is in a state of ’make or break’ rebounds. During this phase the main runout direction is set.
2. *Transition phase* exists once the rock has gained momentum sufficient to establish a stable rotation state, the trajectory tends to be straight and follows the initial direction set during the *Acceleration phase.*
3. *Deceleration phase*, involves the rock coming to a stop, it is falling out of rotational stability and has a tendency to veer off track towards the direction of topple. This often leads to the curved hooked trajectories at the end of runout seen in both the physical and numerical modelling of rockfalls.

7.1.3 Deposition patterns

The systematic approach applied in these physical experiments identifed the underlying trends in runout behaviour associated with rock-shape and its release orientation. This is of particular importance because these trends provide the link between the characteristics rock shapes of an unstable rock-mass with the characteristic dynamics of a rockfall runout behaviour and deposition patterns. The results indicate that rock-shape greatly affects runout, due to the typical impact and rotational behaviour associated with each rock-shape. The *equant* rock is shown to produce long and moderately dispersed deposit patterns, while the *platy* and *elongate* rocks have a tendency for short and highly disperse deposit patterns. This alone corroborates the hypothesis of Fityus et al. (2013), who suggest that rockfalls have characteristic runout behaviour.

In this work the typical deposit patterns could be further associated with the rock release orientation. This was shown to be linked to the initial dynamic created as the rock first entered the slope. Situations where rotations were initiated about the axis of smallest inertia as the rock entered the slope resulted in the largest lateral dispersion. While initial releases which initiated rotations about an axis of largest inertia produced the least lateral dispersion and the longest runout distances. Considering this in the context of unstable rock-masses, there are characteristic failure mechanisms (e.g. wedge, toppling, and plane failure) which can preset the initial impact orientation of rocks as they enter the rock slope. To this end this work allows an extension of the hypothesis (Fityus et al., 2013) to suggest that along with rock-shape it is the rock-mass failure mechanism that initiates the runout which define the characteristics rockfall behaviour associated with a given rock-mass. This permits a better inclusion of rock-mass characteristics in rockfall runout modelling.

7.2 Recommendations for further research

One of the biggest challenges in pursuing the aim of this research was being able to devise an experimental approach that focused on the role of rock-shape in rockfall dynamics, amid numerous additional influencing factors. The findings of this research have raised a number of questions to be addressed in further research which can advance the state of knowledge in rockfall mechanics.

7.2.1 Application of embedded rock motion sensor

The development of the embedded rock motion sensor in this work opened up a broad field of research potential in the dynamics of rockfall. The experimental study of rockfall behaviour has previously been limited to laborious videogrammetric techniques. This technology offers the chance to focus in on the following main themes:

1. Detailed trajectory tracking to resolve the entire rockfall path. A limitation of the experimental setup in these experiments was that only the terminus deposit locations were mapped. There was no indication of how tortuous or straight the rockfall path was, this could only be resolved with the dispersion measure W/L. By integrating the three-dimensional accelerations of the rock body the detailed trajectory of the rock could be resolved. This would enable a verification of the conceptual three-phase runout model presented in this work. Moreover, it could provide detailed vector data in three-dimensions of the resultant takeoff trajectory following each rebound, and would further advance the stiction levering model for rock-ground rebounds described through this work. One of the biggest challenges with this approach is resolving the rock position over time; this requires complex integration which is unfortunately highly prone to numerical drift.

2. Through this work it could be suggested that there was an optimal take-off speed that is brought about by the centrifugal force of the rock as it rotates about a pinned edge point in the terrain. This would have close relation to the magnitude of the moment arm I_i set by the rock-shape and its configuration at impact. The angular velocity signal recorded in this work could be used to identify the required take-off rotational velocity. This would be of great use in identifying the transition dynamic between rolling and ballistic trajectory rebounds.

3. With the use of the acceleration data a more detailed inspection of the rock-ground impact phase could be performed to resolve contact forces during an impact and assess in more detail the mechanisms of terrain scaring.

7.2.2 Fragmentation of rockfalls

In addition to rock-shape it is known that rocks also have a tendency to fragment during runout, and contrary to the assumption that rocks mostly fragment on first impact with the rock slope (Hungr and Evans, 1988), rock fragmentation is a dynamic process that is a result of compounded damage during runout and can occur during all phases of runout over the slope. This work has identified that the *equant* rock form is the most mobile. Thus, fragmentation of rock forms can play a role in chipping corner and edge pieces, tending towards a *equant* form, enhancing mobility. Further to this concept, the idea that fragmentation can enhance rockfall dispersion, whereby large rock boulders runout over terrain and fragment scattering smaller rock fragments with high dispersion (e.g. Nocilla et al., 2009). With this research it could be assessed to what extent rock-shape or fragmentation is responsible for the dispersive nature of rockfalls.

For fragmentation to occur a rock must be exposed to sufficient impact force, to overcome rock strength. Rock fragmentation experiments using single impact drop test are steps towards defining fragmentation energy thresholds (Giacomini et al., 2009), while the idea that there is a cumulative damage effect as the rock runs out over terrain has yet to be resolved. Using both the embedded rock motion sensor and the numerical model, the cumulative impact force over the period of runout could be quantified and a fragmentation threshold defined.

7.2.3 Rockfall protection structures and trees

The design of rockfall protection structures and the protective effect of forests against rockfall have been carried out only with the consideration of impact force, rock-shape and rotational dynamics have been neglected from this problem. Given the influence of rock-shape on the runout over simple terrain highlighted in this work, it is perfectly reasonable to expect that rock-shape will be of importance in impact with rockfall protection structures and trees. This is particularly the case for the testing of rockfall protection measures where a single drop test is conducted with a cubed rock. Angular spinning rocks are not considered in these problems, while they have the potential to cause considerable damage to such structures and trees through lacerations and high punctual forces. Both the rock motion sensor and rockfall model can be used to provide the required input data to define characteristic rotational velocities of rocks according to their shape.

7.2.4 Rockfall modelling

The validation of the rigid-body rockfall model in through this work has established this approach both as a practical tool for engineers to assess rockfall hazard and design rockfall protection structures, and has also proved itself as an experimental platform with which to carry out detailed investigations of problems in rockfall mechanics.

One of the key issues is the definition of terrain parameters over large spatial extents that are consistent and physically based. This is an ongoing problem in rockfall research. From a perspective of existing rockfall models the use of rigid body mechanics rockfall modelling offers insight on rebound models in defining the stochastic bracket of rebound parameters applied.

The findings of this research have highlighted the parity between modelling a rock as a sphere on a terrain with forced terrain roughness and variable impact coefficients, and modelling true rock-shape with consistent impact parameters on a planar slope. The rockfall model presented in this work offers the opportunity to unite these problems and investigate the effects of terrain roughness on the behaviour or rockfalls with realistic shapes, and in doing so extend the work of Crosta and Agliardi (2004). Moreover, it offers the opportunity to also explore how rock size would affect these trends, and answer the question as to whether there is a scale effect to these processes.

An application of the rigid body rockfall model would be to simulate the deposition patterns of talus slopes, and would support the theme of characteristic runout patterns of different rock shapes (e.g. Fityus et al. (2013)).

Bibliography

Andrew, R., Hume, H., Bartingale, R., Rock, A., and Zhang, R. (2012). *CRSP-3D Users Manual Colorado Rockfall Simulation Program.*

ASTRA (1998). Amt für Strassen, Bereich Kunstbauten, Planung, Bau und Unterhalt von Schutzgalerien gegen Steinschlag - und Lawineneinwirkunggen. *Bern.*

Azzoni, A. and Freitas, M. (1995). Experimentally gained parameters, decisive for rock fall analysis. *Rock Mechanics and Rock Engineering*, 28:111–124.

Azzoni, A., La Barbera, G., and Zaninetti, A. (1995). Analysis and prediction of rockfalls using a mathematical model. *International Journal of Rock Mechanics and Mining Science & Geomechanics Abstracts*, 32(7):709 – 724.

Baillifard, F., Jaboyedoff, M., and Sartori, M. (2003). Rockfall hazard mapping along a mountainous road in switzerland using a gis-based parameter rating approach. *Natural Hazards and Earth System Sciences*, 3:431 438.

Basson, F. R. P. (2012). Rigid body dynamics for rock fall trajectory simulation. *American Rock Mechanics Association, 46th US Rock Mechanics / Geomechanics Symposium, Chicago, IL, USA*, pages 1–7.

Benn, D. I. and Ballantyne, C. K. (1993). The description and representation of particle shape. *Earth Surface Processes and Landforms*, 18(7):665–672.

Bennett, G., Molnar, P., McArdell, B., Schlunegger, F., and Burlando, P. (2013). Patterns and controls of sediment production, transfer and yield in the illgraben. *Geomorphology*, 188:68 – 82.

Blott, S. J. and Pye, K. (2008). Particle shape: a review and new methods of characterization and classification. *Sedimentology*, 55(1):31–63.

Bourrier, F. (2008). Modlisation de l'impact d'un bloc rocheux sur un terrain naturel, application la trajectographie des chutes de blocs. *PhD thesis L'Institut polytechnique de Grenoble*, pages 1–247.

Bourrier, F., Berger, F., Tardif, P., Dorren, L., and Hungr, O. (2012). Rockfall rebound: comparison of detailed field experiments and alternative modelling approaches. *Earth Surface Processes and Landforms*, 37(6):656–665.

Bourrier, F., Dorren, L., and Hungr, O. (2013). The use of ballistic trajectory and granular flow models in predicting rockfall propagation. *Earth Surface Processes and Landforms*, 38(4):435–440.

Bourrier, F., Dorren, L., Nicot, F., Berger, F., and Darve, F. (2009a). Toward objective rockfall trajectory simulation using a stochastic impact model. *Geomorphology*, 110(3-4):68 – 79.

Bourrier, F., Eckert, N., Nicot, F., and Darve, F. (2009b). Bayesian stochastic modeling of a spherical rock bouncing on a coarse soil. *Natural Hazards and Earth System Sciences*, 9:831 – 846.

Bozzolo, D. and Pamini, R. (1986). Simulation of rock falls down a valley side. *Acta Mechanica*, 63:113–130. 10.1007/BF01182543.

Brewer, R. (1965). Fabric and mineral analysis of soils. *Wiley, Chichester*, 148(3668):355–356.

Bühler, Y., Glover, J., Christen, M., and Bartelt, P. (2014). Digital elevation models in numerical rockfall simulations. *[Abstract] Geophys. Res. Abstr. 16: EGU2014-2109.*

Buzzi, O., Giacomini, A., and Spadari, M. (2012). Laboratory investigation on high values of restitution coefficients. *Rock Mechanics and Rock Engineering*, 45:35–43.

Calcaterra, D., Parise, M., and of London, G. S. (2010). *Weathering As a Predisposing Factor to Slope Movements.* Geological Society Engineering Geology Special Publication. Geological Society.

Carré, Baker, Newell, and J., H. (1999). The dynamic behaviour of cricket balls during impact and variations due to grass and soil type. *Sports Engineering*, 2(3):145–160.

Carré, M. J., James, D., and Haake, S. J. (2006). Hybrid method for assessing the performance of sports surfaces during ball impacts. *Proceedings of the Institution of Mechanical Engineers, Part L: Journal of Materials Design and Applications*, 220:31–39.

Carré, M. J., James, D. M., and Haake, S. J. (2004). Impact of a non-homogeneous sphere on a rigid surface. *Proceedings of the Institute of Mechanical Engineers, Part C: Journal of Mechanical Engineering Science*, 218:273–281.

Chau, K., Wong, R., Liu, J., Wu, J., and Lee, C. (1999). Shape effects on the coefficient of restitution during rockfall impacts. *Ninth International Congress on Rock Mechanics , ISRM Congress, Paris*, 1:541 – 44.

Chau, K. T., Wong, R., Liu, J., and Lee, C. F. (2003). Rockfall hazard analysis for hong kong based on rockfall inventory. *Rock Mechanics and Rock Engineering*, 36(5):383408.

Chau, K. T., Wong, R. H. C., and Wu, J. J. (2002). Coefficient of restitution and rotational motions of rockfall impacts. *International Journal of Rock Mechanics and Mining Sciences*, 39(1):69 – 77.

Christen, M., Bühler, Y., Bartelt, P., Leine, R., Glover, J., Schweizer, A., Graf, C., McArdell, B., Gerber, W., Deubelbeiss, Y., Feistl, T., and Volkwein, A. (2012). Integral hazard management using a unified software environment: numerical simulation tool "RAMMS" for gravitational natural hazards. *In: Koboltschnig, G.; Hbl, J.; Braun, J. (eds) 12th Congress INTERPRAEVENT, 23-26 April 2012 Grenoble - France. Proceedings. Vol. 1. Klagenfurt, International Research Society INTERPRAEVENT.*, pages 77–86.

Coe, J. A. and Harp, E. L. (2007). Influence of tectonic folding on rockfall susceptibility, American Fork Canyon, Utah, USA. *Natural Hazards and Earth System Science*, 7(1):1–14.

Copons, R., Vilaplana, J. M., and Linares, R. (2009). Rockfall travel distance analysis by using empirical models (Solà d'Andorra la Vella, Central Pyrenees). *Natural Hazards and Earth System Science*, 9(6):2107–2118.

Craig, C. M., Berton, E., Rao, G., Fernandez, L., and Bootsma, R. J. (2006). Judging where a ball will go: the case of curved free kicks in football. *Naturwissenschaften*, 93(2):97–101.

Cross, R. (1999). The bounce of a ball. *American Journal of Physics*, 67(3):222–227.

Cross, R. (2000). Effects of friction between the ball and strings in tennis. *Sports Engineering*, 3(2):85–97.

Cross, R. (2002). Measurements of the horizontal coefficient of restitution for a superball and a tennis ball. *American Journal of Physics*, 70(5):482–489.

Cross, R. (2010). Bounce of an oval shaped football. *Sports Technology*, 3(3):168–180.

Crosta, G. B. and Agliardi, F. (2004). Parametric evaluation of 3D dispersion of rockfall trajectories. *Natural Hazards and Earth System Sciences*, 4:583–598.

Crosta, G. B., Agliardi, F., Frattini, P., and Imposimato, S. (2004). A three-dimensional hybrid numerical model for rockfall simulation. *Geophys. Res. Abstr.*, 6.

Cruden, D. and Varnes, D. (1996). Landslide types and processes. *In Special Report 247: Landslides: Investigation and Mitigation, Transportation Research Board, Washington D.C.*

Cundall, P. A. (1971). A computer model for simulating progressive, large-scale movements in blocky rock systems. In *Proc. Symp. Int. Rock Mech.*, volume 2, Nancy.

Demir, T. (2000). *The infuence of particle shape on bed load transport in coarse-bed river channels.* PhD thesis, Durham University, Department of Geography. Available at Durham E-Theses Online: http://etheses.dur.ac.uk/4375/.

Descoeudres, F. and Zimmermann, T. (1987). Three-dimensional dynamic calculation of rockfalls. *In: Proceedings of the Sixth International congress of Rock Mechanics, Montreal, Canada*, pages 337 – 342.

Dewez, T., Mathon, C., Kobayashi, H., Nachbaur, A., Sedan, O., Berger, F., Nowak, E., and Des Garets, E. (2011). Real-size rockfall trajectory and derived mechanical quantities from close-range stereo video experiment in tahiti, french polynesia. *Geophysical Research Abstracts, EGU2011*, 13:3631.

Dimnet, E. (2002). *Mouvement et collisions de solides rigides ou deformables.* PhD thesis, Ecole Nationale des Ponts et Chaussées, Paris.

Djordjevic, N. (2010). Improvement of energy efficiency of rock comminution through reduction of thermal losses. *Minerals Engineering*, 23(15):1237–1244.

Dorren, L. (2003). A review of rockfall mechanics and modelling approaches. *Progress in Physical Geography*, 27(1):6987.

Dorren, L., Berger, F., and Putters, U. S. (2006). Real-size experiments and 3-D simulation of rockfall on forested and non-forested slopes. *Natural Hazards and Earth System Sciences*, 6:145 – 153.

Dorren, L. K. A. (2010). Rockyfor3D revealed - description of the complete 3D rockfall model. *Tech. rep., EcorisQ, http://www.ecorisq.org, Date accessed: 09.06.13.*

Dorren, L. K. A. and Seijmonsbergen, A. C. (2003). Comparison of three GIS-based models for predicting rockfall runout zones at a regional scale. *Geomorphology*, 56(1-2):49 – 64.

Duarte, R. M. and Marqunez, J. (2002). The influence of environmental and lithologic factors on rockfall at a regional scale: an evaluation using GIS. *Geomorphology*, 43(1-2):117 – 136.

Duffy, J. D. (1992). Flexible wire rope rockfall nets, in: Soils, geology, and foundations rockfall prediction and control and landslide case histories. *Transportation Research Record*, No. 1343:3035.

Eberhardt, E. (2006). From Cause to Effect: Using Numerical Modelling to Understand Rock Slope Instability Mechanisms. In Evans, S., Mugnozza, G., Strom, A., and Hermanns, R., editors, *Landslides from Massive Rock Slope Failure*, volume 49 of *NATO Science Series*, pages 85–101. Springer Netherlands.

EOTA (2008). European Organisation for Technical Assessment, Guidelines for European technical approval of falling rock protection kits (ETAG 027). *Brussels.*

Erismann, T. and Abele, G. (2001). *Dynamics of Rockslides and Rockfalls.* Springer Verlag Berlin.

Evans, S. and Hungr, O. (1993). The assessment of rockfall hazard at the base of talus slopes. *Canadian geotechnical Journal*, 30:620 – 636.

Fischer, L., Purves, R. S., Huggel, C., Noetzli, J., and Haeberli, W. (2012). On the influence of topographic, geological and cryospheric factors on rock avalanches and rockfalls in high-mountain areas. *Natural Hazards and Earth System Science*, 12(1):241–254.

Fityus, S., Giacomini, A., and Buzzi, O. (2013). The significance of geology for the morphology of potentially unstable rocks. *Engineering Geology*, 162:43–52.

Fornaro, M., P. D. and Nebbia, M. (1990). Block falls on rock slopes application of a numerical simulation program to some real cases. *6th Int. Congress IAEG, Rotterdam*, pages 2173–2180.

Frattini, P., Crosta, G., Carrara, A., and Agliardis, F. (2008). Assessment of rockfall susceptibility by integrating statistical and physically-based approaches. *Geomorphology*, 94:419 – 437.

Fuss, F. K., Smith, R. M., and Subic, A. (2012). Determination of spin rate and axes with an instrumented cricket ball. *Procedia Engineering*, 34:128 – 133.

Garber, T. B. (1959). On the rotational motion of a body re-entering the atmosphere. *Journal of the Aerospace Sciences*, 26:7:443–449.

Gerber, W. (2001). Richtlinie über die Typenprüfung von Schutznetzen gegen Steinschlag. *Tech. rep., Bundesamt für Umwelt,Wald und Landschaft (BUWAL), Eidgenössische Forschungsanstalt WSL*, Bern.

Gerber, W. (2008). Einwirkungen bei steinschlag. *FAN Herstkurs Fachleute Naturgefahren Schweiz, Bellinzona.*

Gerber, W. and Jahn, J. (1989). Video Auswerrtung von Steinschlagversuchs, Bechenried (SZ), Switzerland. Technical report, Bundesamt für Umwelt,Wald und Landschaft (BUWAL), Eidgenössische Forschungsanstalt WSL.

Giacomini, A., Buzzi, O., Renard, B., and Giani, G. (2009). Experimental studies on fragmentation of rock falls on impact with rock surfaces. *International Journal of Rock Mechanics and Mining Sciences*, 46(4):708 – 715.

Giani, G. (1992). *Rock Slope Stability Analysis.* Taylor & Francis.

Glover, J., Denk, M., Bourrier, F., Volkwein, A., and Gerber, W. (2012). Measuring the kinetic energy dissipation effects of rock fall attenuating systems with video analysis. *In: Koboltschnig, G.; Hbl, J.; Braun, J. (eds) 12th Congress INTERPRAEVENT, 23-26 April 2012 Grenoble - France. Proceedings.*, 1. Klagenfurt, International Research Society INTERPRAEVENT:151–160.

Glover, J., Volkwein, A., Dufour, F., Denk, M., and Roth, A. (2010). Rockfall attenuator and hybrid drape systems design and testing considerations. *In: Darve, F.; Doghri, I.; El Fatmi, R.; Hassis, H.; Zenzri, H. (eds) Euromediterranean Symposium on Advances in Geomaterials and Structures. Third Edition, Djerba.*

Glover, L. S. (1965). Effects on roll rate of mass and aerodynamic asymmetries for ballistic re-entry bodies. *Journal of Spacecraft and Rockets*, 2:2:220–225.

Guzzetti, F., Crosta, G., Detti, R., and Agliardi, F. (2002). STONE: a computer program for the three-dimensional simulation of rock-falls. *Computers & Geosciences*, 28(9):1079 – 1093.

Haron, A. and Ismail, K. A. (2012). Coefficient of restitution of sports balls: A normal drop test. *IOP Conference Series: Materials Science and Engineering*, 36(1):012038.

Heim, A. (1932). *Bergsturz und Menschenleben.* Vierteljahrsschrift der Naturforschenden Gesellschaft in Zürich. Fretz and Wasmuth.

Holm, K. and Jakob, M. (2009). Long Rockfall runout, Pascua Lama, Chile. *Canadian geotechnical Journal*, 46:225–230.

Hungr, O. and Evans, S. (1988). Engineering evaluation of fragmental rockfall hazards. *5th International Symposium on Landslides, Balkema, Rotterdam, Lausanne, Switzerland*, 1:685–690.

Hungr, O., Evans, S. G., Bovis, M. J., and Hutchinson, J. N. (2001). A review of the classification of landslides of the flow type. *Environmental & Engineering Geoscience*, 7(3):221–238.

Hutchinson, J. N. (1988). General report: Morphological and geotechnical parameters of landslides in relation to geology and hydrogeology. *Proceedings, Fifth International Symposium on Landslides (Ed: Bonnard, C.) Rotterdam: Balkema*, 1:3–35.

Jaboyedoff, M. (2011). Slope tectonics. *Geological Society London.*

Jaboyedoff, M. and Labiouse, V. (2011). Technical note: Preliminary estimation of rockfall runout zones. *Natural Hazards and Earth System Science*, 11(3):819–828.

James, D. and Haake, S. (2008). The spin decay of sports balls in flight. In *The Engineering of Sport 7*, pages 165–170. Springer Paris.

Jonsson, M, J. O. (2007). *Energy absorption of trees in a rockfall protection forest.* PhD thesis, Eidgenssische Technische Hochschule, Switzerland.

Kalenchuk, K. S., Diederichs, M. S., and McKinnon, S. (2006). Characterizing block geometry in jointed rockmasses. *International Journal of Rock Mechanics and Mining Sciences*, 43(8):1212 – 1225.

Kalenchuk, K. S., McKinnon, S., and Diederichs, M. S. (2008). Block geometry and rockmass characterization for prediction of dilution potential into sub-level cave mine voids. *International Journal of Rock Mechanics and Mining Sciences*, 45(6):929 – 940.

Keefer, D. K. (1984). Landslides caused by earthquakes. *Geological Society of America Bulletin,*, 95:406–421.

Kim, Y.-S., Peacock, D. C. P., and Sanderson, D. J. (2004). Fault damage zones. *Journal of Structural Geology*, 26(3):503 – 517.

King., K., C., P. N., Churchill., H., McGinnis., R., Doss., R., and Hickland, R. (2011). Bowling ball dynamics revealed by miniature wireless MEMS inertial measurement unit. *Sports Engineering (Online)*, 13(2):95–104.

Krumbein, W. (1941). Measurement and geological significance of shape and roundness of sedimentary particles. *Journal of Sedimentary Petrology*, 11:64–72.

Labiouse, V. and Heidenreich, B. (2009). Half-scale experimental study of rockfall impacts on sandy slopes. *Natural Hazards and Earth System Science*, 9(6):1981–1993.

Lambert, S. and Bourrier, F. (2013). Design of rockfall protection embankments: A review. *Engineering Geology*, 154:77–88.

Lambert, S., Bourrier, F., and Toe, D. (2013). Improving three-dimensional rockfall trajectory simulation codes for assessing the efficiency of protective embankments. *International Journal of Rock Mechanics and Mining Sciences*, 60:26–36.

Lambert, S. and Nicot, F. (2011). Rockfall engineering. *(ed) ISTE Ltd and Wiley & Sons Inc.*

Lan, H., Martin, D., and Lim, C. (2007). RockFall analyst: A GIS extension for three-dimensional and spatially distributed rockfall hazard modeling. *Computers & Geosciences*, 33(2):262 – 279.

Latham, J.-P., Munjiza, A., Garcia, X., Xiang, J., and Guises, R. (2008). Three-dimensional particle shape acquisition and use of shape library for {DEM} and FEM/-DEM simulation. *Minerals Engineering*, 21(11):797 – 805.

Leine, R., Schweizer, A., Christen, M., Glover, J., Bartelt, P., and Gerber, W. (2014). Simulation of rockfall trajectories with consideration of rock shape. *Multibody System Dynamics*, 32:241–271.

Lock, G. D., Edwards, S., and Almond, D. P. (2010). Flow visualization experiments demonstrating the reverse swing of a cricket ball. *Proceedings of the Institution of Mechanical Engineers, Part P: Journal of Sports Engineering and Technology*, 224 no. 3:191–199.

Magnus, G. (1852). Über die abweichung der geschosse. *Abhandlungen der Königlichen Akademie der Wissenschaften zu Berlin*, pages 1–23.

McGinnis, R. S. and Perkins, N. C. (2012). A highly miniaturized, wireless inertial measurement unit for characterizing the dynamics of pitched baseballs and softballs. *Sensors*, 12(9):11933–11945.

McPherson, T. . J. (1999). Grain size and textural classification of coarse sedimentary particles. *Journal of Sedimentary Research*, 69:6–19.

Mehta, R. (2005). An overview of cricket ball swing. *Sports Engineering*, 8(4):181–192.

Moffatt, H. K. and Shimomura, Y. (2002). Classical dynamics: Spinning eggs - a paradox resolved. *Nature*, 416(6879):385–386.

Nicolaides, A., Elliott, N., Kelley, J., Pinaffo, M., and Allen, T. (2013). Effect of string bed pattern on ball spin generation from a tennis racket. *Sports Engineering*, 16(3):181–188.

Nocilla, N., Evangelista, A., and Santolo, A. S. (2009). Fragmentation during rockfalls: Two italian case studies of hard and soft rocks. *Rock Mechanics and Rock Engineering*, 42:815 – 833.

Okura, Y., Kitahara, H., Sammori, T., and Kawanami, A. (2000). The effects of rockfall volume on runout distance. *Engineering Geology*, 58(2):109 – 124.

Palmström, A. (1995). *RMi - a rock mass characterisation system for rock engineering purposes.* PhD thesis, University of Oslo, Department of Geology, 400 pp.

Palmström, A. (2005). Measurements of and correlations between block size and rock quality designation (RQD). *Tunnelling and Underground Space Technology*, 20(4):362 – 377.

Paronuzzi, P. (2009). Rockfall-induced block propagation on a soil slope, northern Italy. *Environmental Geology*, 58:1451–1466.

Petley, D. N. (2013). Characterizing giant landslides. *Science*, 339(6126):1395–1396.

Petley, David, N. (2012). Global patterns of loss of life from landslides. *Geology*, 40(10):927–930.

Pettit, R. D. (2009). Solid body rotation, NASA, International Space Station (ISS). http://www.youtube.com/watch?v=GgVpOorcKqc. Date accessed: 16.11.13.

Pfeiffer, T. and Bowen, T. (1989). Computer simulation of rockfalls. *Bulletin of the Association of Engineering Geologists*, 26:135–146.

Pierson, L. A., Gullixson, C. F., and Chassie, R. G. (2001). Rockfall catchment area design guide. Technical Report SRP-3(032), Oregon Department of Transport.

Platus, D. H. (1970). Dynamic instability of finned missiles caused by unbalanced fin forces. *AIAA Journal, American Institute of Aeronautics and Astronautics*, 9, No. 3.

Radtke, A., Toe, D., Berger, F., Zerbe, S., and Bourrier, F. (2014). Managing coppice forests for rockfall protection: lessons from modeling. *Annals of Forest Science*, 71:485–495.

Rayleigh, L. (1877). On the irregular flight of a tennis ball. *Messenger of Mathematics*, 7:1416.

Rheinberger, C. (2011). A mixed logit approach to study preferences for safety on alpine roads. *Environmental and Resource Economics*, 49(1):121–146.

Riley, N, A. (1941). Projection sphericity. *Journal of Sedimentary Research*, 11(2):94–95.

Ritchie, A. (1963). Evaluation of rockfall and its control. *Highway Research Record*, 17:13 – 28.

Rochet, L. (1987). Development of numerical models for the analysis of propagation of rock-falls. *6th Int. Congress on Rock Mech*, 1:479–484.

Rosser, N. J., Brain, M. J., Petley, D. N., Lim, M., and Norman, E. C. (2013). Coastline retreat via progressive failure of rocky coastal cliffs. *Geology*, 41(8):939–942.

Rosser, N. J., Petley, D. N., Lim, M., Dunning, S. A., and Allison, R. J. (2005). Terrestrial laser scanning for monitoring the process of hard rock coastal cliff erosion. *Quarterly Journal of Engineering Geology and Hydrogeology*, 38:363–375.

Santi, P. M., Russell, C. P., Higgins, J. D., and Spriet, J. I. (2009). Modification and statistical analysis of the colorado rockfall hazard rating system. *Engineering Geology*, 104(1-2):55 – 65.

Schweizer, A. (2008). Kontakt zwischen körpern mit triangularisierter oberflächenrepräsentation. *Master thesis at the Center of Mechanics, ETH Zurich.*

Schweizer, A., Leine, R. I., and Glocker, C. (2011). Simulation of rockfall using the non-smooth contact dynamics approach. *Proceedings of the EUROMECH Colloquium Nonsmooth contact and impact laws in mechanics, Grenoble, France.*

Selby, M. J. (1982). *Hillslope Materials and Processes.* Oxford University Press.

Singh, R., Umrao, R., and Singh, T. (2013). Stability evaluation of road-cut slopes in the lesser himalaya of uttarakhand, india: conventional and numerical approaches. *Bulletin of Engineering Geology and the Environment*, 73:845–857.

Sneed, E. D. and Folk, R. L. (1958). Pebbles in the lower colorado river, texas, a study in particle morphogenesis. *Journal of Geology*, 66 (2):114–150.

Spadari, M., Giacomini, A., Buzzi, O., Fityus, S., and Giani, G. (2012). In situ rockfall testing in New South Wales, Australia. *International Journal of Rock Mechanics and Mining Sciences*, 49(0):84 – 93.

Spang, R. and Sönser, T. (1995). Optimized rockfall protection by 'rockfall'. *Proceedings of the 8th International Conference on Rock Mechanics, Rotterdam: A.A. Balkema, Tokyo*, pages 1233–1242.

Statham, I. (1976). A scree slope rockfall model. *Earth Surface Processes*, 1(1):43–62.

Stevens, Warren, D. (1998). Rocfall: A tool for probablistic analysis, design of remedial measures and prediction of rockfalls. Master's thesis, University of Toronto.

Stoffel, M. and Perret, S. (2006). Reconstructing past rockfall activity with tree rings: Some methodological considerations. *Dendrochronologia*, 24(1):1 – 15.

Stoffel, M., Wehrli, A., Khne, R., Dorren, L. K., Perret, S., and Kienholz, H. (2006). Assessing the protective effect of mountain forests against rockfall using a 3D simulation model. *Forest Ecology and Management*, 225(1-3):113 – 122.

Sturzenegger, M., Sartori, M., Jaboyedoff, M., and Stead, D. (2007). Regional deterministic characterization of fracture networks and its application to GIS-based rock fall risk assessment. *Engineering Geology*, 94(3-4):201 – 214.

Sturzenegger, M. and Stead, D. (2009). Close-range terrestrial digital photogrammetry and terrestrial laser scanning for discontinuity characterization on rock cuts. *Engineering Geology*, 106(34):163 – 182.

Van Dijke, J. and van Westen, C. (1990). Rockfall hazard: a geomorphological application of neighbourhood analysis with ILWIS. *ITC Journal*, 1:40–44.

Vijayakumar, S., Yacoub, T., Ranjram, M., Curran, J., et al. (2012). Effect of rockfall shape on normal coefficient of restitution. *American Rock Mechanics Association.*

Volkwein, A., Fritschi, B., Schaedler, S., and Grassl, H. (2006). Posterior trajectory analysis of an artificial instrumented boulder. *[Abstract] Geophys. Res. Abstr.*, 8:03856.

Volkwein, A., Schellenberg, K., Labiouse, V., Agliardi, F., Berger, F., Bourrier, F., Dorren, L. K. A., Gerber, W., and Jaboyedoff, M. (2011). Rockfall characterisation and structural protection - a review. *Natural Hazards and Earth System Science*, 11(9):2617–2651.

Wadell, H. (1935). Volume, shape and roundness of quartz particles. *Journal of Geology*, 43(3):250–280.

Wallis, B. (1942a). Manufacture of spherical (bouncing) bomb, coating to make impervious to seawater; highball and spherical bomb test reports. Technical Report 97D, The Papers of Sir Barnes Wallis, Science Museum Library, (D2/5).

Wallis, B. (1942b). A note on a method of attacking the axis powers. Technical report, The Papers of Sir Barnes Wallis, Science Museum Library, (D1).

Wallis, B. (1943a). Upkeep manufacture and trials. Technical Report 97H, The Papers of Sir Barnes Wallis, Science Museum Library, (D2/10).

Wallis, B. (1943b). Upkeep trials; spinning trials. Technical Report 97I, The Papers of Sir Barnes Wallis, Science Museum Library, (D2/11).

Wallis, B. (1944). Dynamic unbalance of spinning shells. Technical Report 97M, The Papers of Sir Barnes Wallis, Science Museum Library, (D2/15).

Wang, L., Park, J.-Y., and Fu, Y. (2007). Representation of real particles for {DEM} simulation using X-ray tomography. *Construction and Building Materials*, 21(2):338 – 346.

Wentworth, C. K. (1922). A scale of grade and class terms for clastic sediments. *The Journal of Geology*, 30(5):377–392.

Wu, S. (1985). Rockfall evaluation by computer simulation. *Transport Research Record*, 1031:1–5.

Wyllie, D. and Mah, C. W. (2004). *Rock Slope Engineering: Civil and Mining 4th edt.* Spon Press, Taylor & Francis Group, London and New York.

Zingg, T. (1935). Beitrag zur schotteranalyse: Die schotteranalyse und ihre anwendung auf die glattalschotter. *Schweizerische Mineralogische und Petrographische Mitteilungen*, 15:39–140.

Zinggeler, A. and Pfeifer, R. (2009). Steinschlagmodellierung GEOTEST+Zinggeler Modellbeschreibung. pages 1–22.